Local instabilities in differentially rotating stars

Robert W Dymott

Submitted in accordance with the requirements for the degree of

Doctor of Philosophy

The University of Leeds

Faculty of Engineering and Physical Sciences

School of Mathematics

July 2024

Intellectual Property Statement

The candidate confirms that the work submitted is their own, except where work which has formed part of jointly authored publications has been included. The contribution of the candidate and the other authors to this work has been explicitly indicated below. The candidate confirms that appropriate credit has been given within the thesis where reference has been made to the work of others.

Chs. 3, 4, contain material from the jointly authored publication (Dymott et al., 2023): **Dymott, R. W., Barker, A. J., Jones, C., & Tobias, S.** (2023). Linear and nonlinear properties of the Goldreich-Schubert-Fricke instability in stellar interiors with arbitrary local radial and latitudinal differential rotation. *Monthly Notices of the Royal Astronomical Society*, *524* (2), 2857–2882.

Ch. 5, contains material from the jointly authored paper in preparation: Local stability of differential rotation in magnetised radiation zones, with applications to the solar tachocline

Dymott, R. W., Barker, A. J., Jones, C., & Tobias, S. (2024).

This paper is in preparation for submission to *Monthly Notices of the Royal Astronomical Society.*

Ch. 6 represents an ongoing project of as-yet unpublished work.

The above papers were authored by R. W. Dymott, who executed all nonlinear simulations, performed the linear analysis and wrote the draft manuscript. C. Jones provided the MATLAB code used for several of the numerical linear figures seen in Chs. 3 and 5, and contributed to the asymptotic analysis in the appendix. The SNOOPY code was supplied by A. J. Barker. Other contributions from the authors were through advisory and editorial roles.

A gift to my mother

Acknowledgements

First and foremost, I would like to thank my supervisors Adrian Barker, Chris Jones, and Steven Tobias. Adrian's patience, support, and advice have unquestionably been the defining factors in the completion of this work. I am grateful for Chris's advice and contributions, including the MATLAB code used to produce many of the figures in Chapters 3 and 4, the asymptotic analysis in Appendix A, and the help I received in preparation for my Viridien interview. I would also like to acknowledge the endless source of expert advice and creative ideas that Steve has provided throughout my time at Leeds; without these, you would undoubtedly be reading a very different thesis. I would also like to thank my examiners, Rainer Hollerbach and Junho Park, for their valuable comments and thought-provoking discussions.

Perhaps the greatest pleasure during my time at Leeds has been the people I've met. I am grateful to all members of the Mathematics department with whom I have had the pleasure of speaking. Specifically, I would like to mention Alexander Kimbley for his treasured support, Luke Gostelow for humbling me endlessly with our games of chess, and Sam Myers for his friendship; you will be greatly missed. Additionally, my office companion, Nils de Vries, with whom I've shared my PhD experience, deserves an exclusive mention for his years of invaluable advice and true friendship.

I am especially grateful to Ellie for the continuous supply of delicious meals and excellent books; I can't imagine the last few months without you.

I also greatly appreciate the three and a half years of funding I've received from the STFC, which made this research possible.

I would like to acknowledge all those whom I've met and trained with at GameFight over the last few years. A group of truly amazing people and an experience I'll never

forget—thank you all.

I am grateful to all members of the Dymott, Dannatt, and Harvey families who have supported me over the last 26 years. It never ceases to amaze me how much of an influence a simple visit to the pub, a football match, or a late-night conversation in the kitchen can have on us.

In particular, I'd like to thank my grandfather, Brian Dymott, for his inspiration and continual encouragement, my sister, Sadie Dannatt, for being a constant source of love and support throughout my life, particularly over the last few years, and my father, David Dymott, whose role in my life and the completion of this work cannot be overstated; thank you all for always believing in me.

Finally, to my nephews, Henry, George, and Reuben Dannatt, thank you for being a constant source of joy; I hope that one day you find this work inspiring.

Abstract

Advancements in cutting-edge observational technologies, combined with refined helioseismic techniques, have revealed that the surface differential rotation (which has been observed for hundreds of years) permeates throughout the convection zone of the Sun, below which the radiative zone rotates approximately as a solid body. The thin layer bounding these two regions is known as the solar tachocline and is expected to play a vital role in many of the most interesting and least understood solar mechanisms.

This thesis studies the local instabilities of differentially rotating, stably stratified, magnetised stellar interiors, which are relevant for the lower regions of the tachocline among many other astrophysical contexts. Our primary focus is on the ability of these instabilities to transport angular momentum in the regions where they operate. We use a local box model to analyse and simulate a small patch of the stellar radiative zone within the tachocline.

Initially, we systematically explore the hydrodynamic regime, derive the dispersion relation for axisymmetric modes, and identify key stability criteria. Our findings reveal two dominant instabilities: an adiabatic centrifugal instability and the diffusive Goldreich-Schubert-Fricke (GSF) instability. Nonlinear simulations with generalised differential rotation profiles show that these instabilities lead to the formation of ‘zonal jets’, whose orientation and angular momentum transport properties depend heavily on the local rotation profile.

Transitioning to the magnetohydrodynamic system, we introduce a poloidal magnetic field and observe its interaction with the centrifugal and GSF instabilities, as well as the new axisymmetric instabilities enabled by its presence, in particular the magnetorotational instability. We use linear theory in combination with an analysis of the energetic properties of the system to derive stability criteria and better understand the instabilities in the magnetised system. Nonlinear simulations provide insights into the dynamo-generating and angular momentum-transporting capabilities of such flows in the presence of a magnetic field.

Contents

List of Figures

List of Tables

Chapter 1

Introduction

1.1 A brief history of sunspots and rotation

Since antiquity mankind has gazed to the heavens in the hope of a better understanding of our place in the universe. Cultures worldwide have revered the Sun as a deity, symbol of life, and source of light, warmth, and energy. Ancient civilizations built monuments and temples aligned with the Sun's movements, such as Stonehenge in England and the temples of ancient Egypt. Sun worship was prevalent in societies like the Inca, Egyptian, and Aztec civilizations. Moreover, solar calendars, based on the Sun's annual journey, were developed by numerous cultures to track time and seasons, influencing agricultural practices and societal events. In modern times, the Sun's energy is harnessed through solar technologies for electricity generation, heating, and other applications, playing a crucial role in efforts to combat climate change and transition to renewable energy sources.

In terms of scientific observations, the earliest documented sightings of sunspots can be traced back to 165 BC in the far east (Yau and Stephenson, 1988), mainly in what is now China, where over a hundred pre-telescopic records exist (Wittmann and Xu, 1987; Yau and Stephenson, 1988; Eddy et al., 1989). Sunspots are characterized as dark patches on the surface of the Sun, formed by an intense concentration of

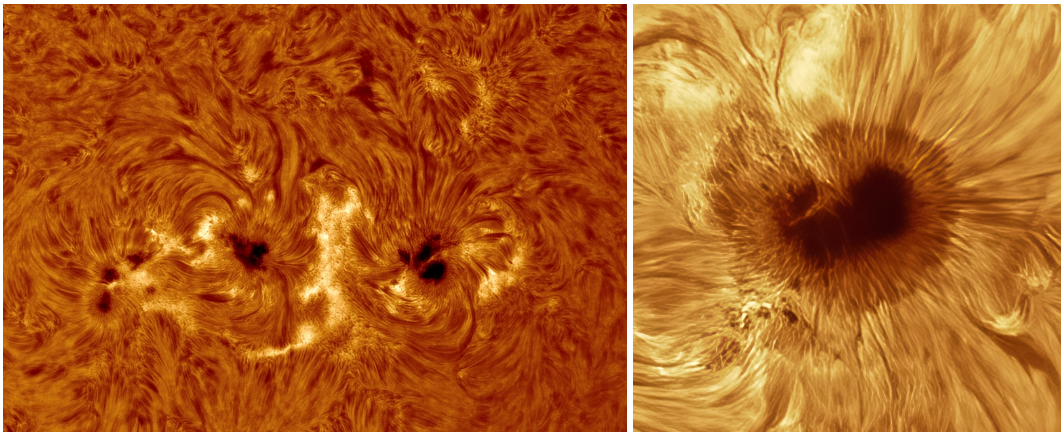

Figure 1.1: Two high-resolution images of sunspots on the solar surface. On the right-hand side, we can clearly see the distinction between the center, known as the umbra, and the slightly lighter region just outside of it, known as the penumbra, which is surrounded by the solar surface (BBC, 2022).

magnetic fields (Weiss, 2007). The apparent darkness of sunspots results from these magnetic fields inhibiting convection beneath the Sun's surface, which leads to a decrease in temperature locally (Solanki, 2003). Sunspot sizes can vary widely, ranging from around $2,000$km to $100,000$ km in diameter, with most being on the order of 10,000 km in diameter. The magnetic field's loop-like structure often causes sunspots to appear in pairs, with one spot exhibiting positive polarity (outward-directed) and its corresponding spot displaying negative polarity (inward-directed).

Before Doppler measurements became feasible, scientists studied the Sun's differential rotation by tracking sunspots and documenting their changes over time. Carrington's meticulous observations from 1853 to 1861 (Carrington, 1863) revealed that sunspots at mid-latitudes exhibited slower rotation compared to those nearer to the equator, thus establishing that the solar surface rotates differentially. Since sunspots are absent near the poles, determining the very slow polar rotation required the use of Doppler measurements, a more recent discovery. The number and location of sunspots heavily depends on the level of magnetic activity and evolves over time (Harvey, 1992). The evolution of the location and quantity of sunspots is illustrated by the renowned "Butterfly diagram" (see Fig. 1.2), which showcases the cyclic nature of sunspot occurrence over an 11-year period, along with a ten-

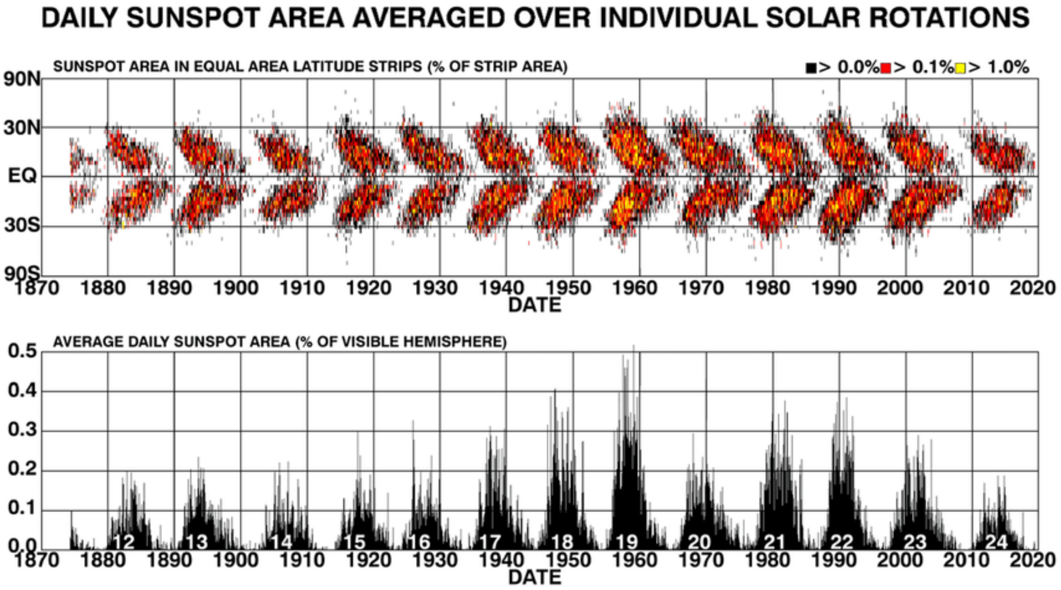

Figure 1.2: The so-called "Butterfly diagram" consists of two panels: an upper panel representing solar latitude on the vertical axis and time on the horizontal axis, and a lower panel which records the relative solar surface area covered by sunspots over time. Both figures illustrate the 11-year cyclic nature of the Sun's magnetic activity and in turn the number of sunspots, which we refer to as the solar cycle. Figure courtesy of Hathaway (2015).

dency for sunspots to migrate towards the equator as time progresses. This diagram provides valuable insights into the dynamic behavior of the Sun's magnetic activity and its influence on sunspot formation and movement (Tobias, 2002).

Understanding the origin of the butterfly diagram requires us to unveil the secrets of the solar cycle. The term 'solar cycle' refers to the time it takes for the Sun's magnetic field to flip polarity, and as a dynamical system, it is not yet fully understood (Wilson, 1994). The Sun's magnetic field is generated by a dynamo, a phenomenon that occurs when plasma flow generates a magnetic field. While not all stars are necessarily expected to possess a dynamo, the Sun certainly does. Some low to medium mass stars ($0.5M_\odot \lesssim M \lesssim 1.1M_\odot$, see 1.1)[1] such as the Sun are comprised of multiple distinct regions, several of which could potentially host a dynamo. In the case of the Sun, most astrophysicists studying this problem now believe the dynamo primarily operates in a region of the Sun known as the "tachocline" (Tobias,

---

[1] Where $M_\odot$ is defined to be one solar mass.

2002; Jones et al., 2010; Weiss, 2010), a region of strong shear at the bottom of the convection zone, which was discovered thanks to helioseismology.

Stars vs mass

The mass of a star is arguably its most fundamental parameter. Whilst there is some variation, stars are normally categorised into: low-mass stars ($M \lesssim 1.1M_{\odot}$) containing a radiative core whilst on the main sequence (MS) and ending their lives as white dwarfs, intermediate-mass stars that have a convective core whilst on the MS ($1.1M_{\odot} \lesssim M \lesssim 8M_{\odot}$), which also end their lives as white dwarfs, and then high-mass stars which have a mass ($8M_{\odot} \lesssim M$) sufficient to end as a supernova explosion, leading to either a neutron star or a black hole (Chiosi and Maeder, 1986). Note there are also some very low mass stars ($M \lesssim 0.5M_{\odot}$) which are fully convective and live so long that none have yet reached their final stages of life, but we also expect these to end up as white dwarfs (Eddy et al., 1989; Tayler, 1994; Schwarzschild, 2015).

The Sun is a low mass star, meaning its inner core is surrounded by a radiative region, which rotates nearly as a solid body and where energy is transported primarily through the absorption and re-emission of photons which gradually diffuse outwards. This zone is characterized by high temperatures and densities but low opacities. This inner $\sim 70\%$ of the star by radius also contains 98% of the mass of the star and 90% of the angular momentum (AM) resides here (Hughes et al., 2007). Beyond the radiative zone, there exists a region unstable to convection whose rotation rate depends on radius and latitude; this is known as differential rotation.

1.2 Helioseismology

New technologies are paving the way for cutting-edge observational techniques, allowing us to verify previously uncalibrated stellar evolution models (Eggenberger et al., 2008). At the forefront of these methods is helioseismology (Charbonneau et al., 1999; Corbard et al., 1999), or more generally asteroseismology. Thanks to state-of-the-art observational facilities such as GONG (Global Oscillation Network Group) and IRIS (International Research on the Interior of the SUN) whose sole focus is directed towards the solar surface, we are now inundated with data. What we see are millions of modes simultaneously oscillating throughout the Sun, typically possessing periods between 3 and 10 minutes (Kosovichev, 2003).

The first reliable observations of solar oscillations were taken in the early 1960s (Noyes & Leighton, 1963; Leighton et al., 2018). Initially believed to be a surface phenomenon, it was only when Frazier (1968) thought to take Fourier transforms of this data and create a power spectrum with it that its true nature became apparent. Some significant progress quickly followed (Ulrich & Rhodes Jr., 1977; Leibacher & Stein, 2018), with the key breakthrough occurring in 1975 thanks to Deubner (1975), who, for the first time, identified ridges in the wave-number frequency diagram, reflecting the modal structure of the oscillations. Rhodes Jr. et al. (1977) reported similar findings, comparing the observed frequencies with computational models to obtain constraints on the properties of the solar convection zone.

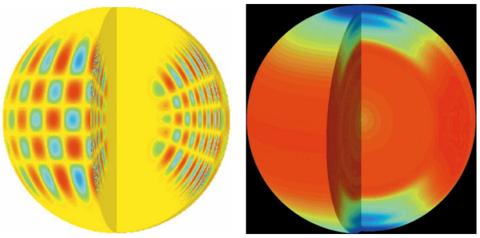

Figure 1.3: A pair of figures: The left figure illustrates solar p-mode oscillations in the solar interior, while the right figure shows the inferred differential rotation, with red indicating faster rotation (minimum ∼ 25 day period) and blue indicating slower rotation (maximum ∼ 29 day period) (Engvold et al., 2018).

The modes unambiguously observed in the sun are p-modes (see Fig. 1.3) and f-modes; along with some hopeful attempts at resolving g-modes (Wolff, 1983). Pressure modes (p-modes) are acoustic waves that propagate the interior of a star within the region known as the acoustic cavity. This region ranges from the surface of the star to the radius at which point the phase speed equals the adiabatic sound speed; this is the lower turning point of the mode. The f-modes are standing waves, which at high degree resemble surface gravity waves (Christensen-Dalsgaard and Thompson, 2007). Gravity modes or ‘g-modes’ are expected to occur in the radiative interiors of stars but, likely due to the convection zone, have yet to be unambiguously identified in the Sun.

Efficient analysis of this data is made far easier thanks to spherical harmonics. Just as a Fourier series represents a function as the sum of sinusoidal waves, spherical harmonics represent a function on a sphere as the sum of spherical harmonics. The spherical harmonics themselves are eigenfunctions of the Laplace operator on the surface of a sphere. This means that when you apply the Laplace operator to a spherical harmonic, you get back a multiple of the same function. Together the spherical harmonics form an orthogonal and complete basis embedded into the surface of a sphere, meaning any function defined on the sphere can be expressed as a linear combination of these spherical harmonics.

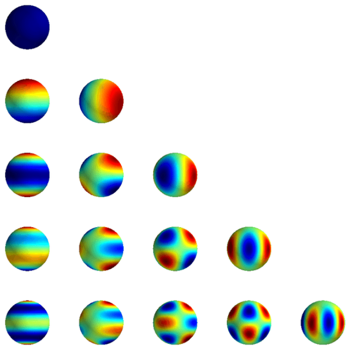

Figure 1.4: An illustration of the spherical harmonics, with azimuthal order (m) along the $x-$axis, and latitudinal order ($l-m$) along the $y-$axis, with $l = n + m \leq 4$ fixed (Hollebon & Fazi, 2020).

The general idea in analysing the raw data is to consider the governing equations in a spherical geometry, after which the oscillations are considered to be small perturbations around the equilibrium sphere. After forming and separating the eigenvalue problem into horizontal and radial components the equations of motion are described in terms of spherical harmonics, namely,

$$Y_l^m(\theta, \phi) = c_{lm} P_l^m(\cos\theta) \exp(im\phi). \quad (1.1)$$

The coefficients c_{lm} are chosen to make the spherical harmonics orthonormal so that any oscillation can be written as a sum of spherical harmonics each with its coefficient. These $Y_l^m(\theta, \phi)$ are known as the spherical harmonics, which are functions of co-latitude θ and longitude ϕ, and the P_l^m are the associated Legendre polynomials.

A non-radial mode in a non-rotating star is characterized by three wave numbers:

the degree l and the azimuthal order m which determine the behavior of the modes across the surface of the star, and the radial order n determines the number of nodes radially. In general the frequencies ω_{nlm} of stellar oscillations depend on all three of these numbers. The dependence on time of an arbitrary oscillation can be written $\exp(-\mathrm{i}\omega_{nlm}t)$, so in general a radial displacement is described by the real part of the sum over all of these individual mode oscillations.

Once we have obtained the nature of these oscillations what follows is an inverse problem to obtain the properties of the interior of the star, or in the case of helioseismology, the Sun.

1.2.1 Helioseismology as an inverse problem

Helioseismology is an inverse problem in the sense that to calculate the internal structure from observational modal data, we must first assume a structure and then iteratively converge towards the true solution. Several methods can perform these types of inversions, such as "Regularized Least Squares" (Eff-Darwich & Hernández, 1997) or more modern techniques like "Full Waveform Inversion" (Hanasoge, 2014). While the theory for the latter is currently incomplete in a helioseismic context, it holds promise for much more detailed observational images in the future. The general algorithm for such an inverse method involves assuming a starting model resembling the internal structure. Then, we forward propagate this model to predict its output based on the assumed properties. Next, we compare this output with observational data and, using our chosen algorithm, update and improve our starting model iteratively. These iterations are repeated until the residual (the difference between observational and modeled data) is sufficiently small.

1.2.2 Rotation and rotational splitting

If a model of the Sun is perfectly spherical, modes with different azimuthal orders m would exhibit identical frequencies. However, rotation breaks this symmetry, causing the modal frequencies to be altered by the effect of rotational splitting. In the Sun this effect is described to first-order (i.e. weak rotation relative to mode frequency) by:

$$\omega_{nlm} = \omega_{nl0} + m \int_0^R \int_0^\pi K_{mln}(r,\theta)\Omega(r,\theta) r dr d\theta, \tag{1.2}$$

here r is the spherical radius and the modes with no azimuthal dependence (and so don't experience rotational splitting) are given by ω_{nl0} (Christensen-Dalsgaard & Thompson, 2007). This is an odd function of m. The fact that different m's have different frequencies means it's possible to distinguish between $+m$ and $-m$ modes in the data, allowing the rotation to be observed. K_{nlm} are functions of the spherically symmetric structure of the Sun and are generally assumed to be known to an adequate degree of accuracy so that the above equation gives restrictions on the unknown angular velocity profile $\Omega(r, \theta)$ in the Sun.

In terms of rotational properties, helioseismology has revealed:

- The presence of a thin shear layer, known as the tachocline, demarcating the rigidly-rotating interior from the differentially-rotating convective envelope.
- Variations in rotation rate with depth and latitude within the convective envelope - known as differential rotation.
- A thin shear layer just beneath the surface, where the rotation rate gradually decreases towards the surface.

1.3 Stellar rotation

Stars are born from interstellar gas clouds, and much like how an ice-skater will spin faster as they bring their arms inward, as a cloud becomes smaller and more compact, the conservation of angular momentum acts to spin up the protostar (McKee & Ostriker, 2007). This inherited rotation often evolves intrinsically with the magnetic field, which, neglecting non-ideal effects, is frozen into the star's conducting plasma. This interaction amplifies during the star's formation, arguably making rotation one

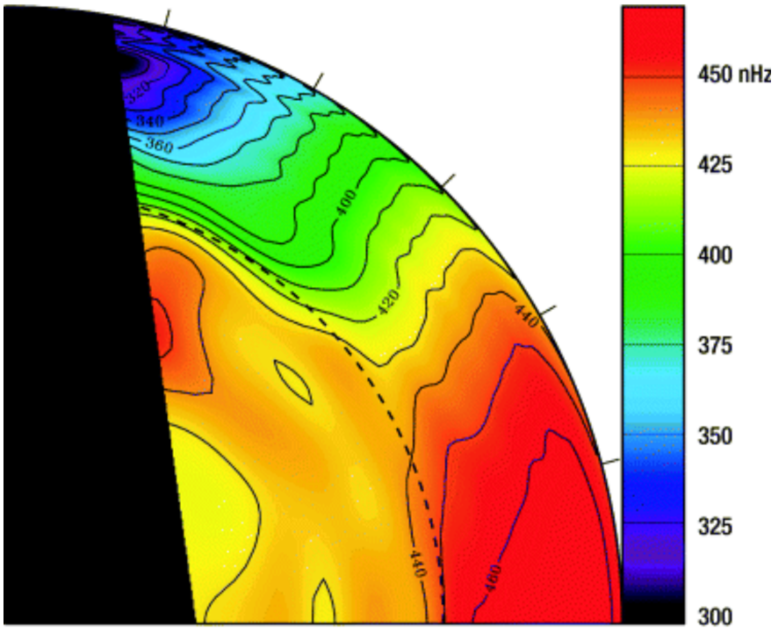

Figure 1.5: Solar differential rotation as inferred by helioseismology. This figure illustrates the surface and convection zone of the Sun rotating faster at the equator, with a period of approximately 25 days, compared to the poles, where it has a period of approximately 29 days (Thompson, 2004).

of the most influential mechanisms governing the star's subsequent evolution.

Once formed, the subsequent evolution of its rotation is governed by the interplay of angular momentum lost through its external, magnetically dominated stellar wind, and the redistribution within its interior. In the case of the Sun, the redistribution of angular momentum, particularly throughout the convection zone, leads to a differentially rotating configuration where the equator of the star rotates more rapidly than the poles (Goldreich & Schubert, 1967; Rüdiger, 1989; Balbus et al., 2009).

Differentially rotating configurations give birth to a whole new landscape of important mechanisms that drastically alter the evolutionary trajectory of a star (Spiegel & Zahn, 1970; Knobloch & Spruit, 1982), including the redistribution of chemical elements and angular momentum transport via meridional circulations, magnetic effects, waves, and instabilities (Hughes et al., 2007; Maeder, 2008; Aerts et al., 2019), all of which will be discussed shortly.

In essence, despite its great importance, the details of stellar rotation (and linked mechanisms) remain poorly understood. Thus, in order to elevate our understanding, it is imperative to learn more about the mechanisms involved, with the goal of understanding the underlying physics in a way that allows us to better parameterise their effects and include such parameterisations in future, more accurate stellar evolution codes (Eggenberger et al., 2008; Aerts et al., 2019; Buldgen, 2019b).

1.4 The solar tachocline

The tachocline is a thin layer of strong shear joining the differentially rotating convection zone to the solid rotation of the radiative zone (Tobias, 2005). It was initially discovered after the advent of helioseismology (Charbonneau et al., 1999; Corbard et al., 1999), which, for the first time, has given us the ability to probe the internal structure and rotation of the Sun.

Through analysis of surface oscillations, primarily driven by pressure waves in the Sun's interior, researchers have identified the tachocline as a prolate shell (Tobias, 2005; Miesch et al., 2007), slightly thicker at the equator than at the poles (Charbonneau et al., 1999). It exhibits a complex rotation profile, with its outer boundary placed within the differentially rotating convection zone, and its stably stratified interior rotating nearly uniformly (Charbonneau et al., 1999) (see Fig. 1.5).

As the tachocline connects the dense radiative interior, housing approximately 95% of the Sun's AM (Hughes et al., 2007), to the convective envelope, characterised by a complex AM profile and mass loss through the solar wind and associated magnetic braking (Mestel, 1968), its role in the Sun's AM evolution is crucial.

Given the solid body rotation of the radiative interior juxtaposed with the strong differential rotation exterior to it, force imbalances within the tachocline induce a meridional circulation that transports AM towards latitudes where the exterior rotates faster than the interior (Sule et al., 2005). This circulation likely includes a smaller radial component, allowing for leakage into the convection zone or, to a lesser extent, the denser radiative zone, albeit over a timescale where thermal diffusion counters opposing buoyancy forces (Hughes et al., 2007).

Convective overshoot at the tachocline's outer boundary occurs when convective plumes with sufficient AM penetrate its upper reaches (Miesch, 2005), leading to a complex interplay between convection and shear, contributing to the excitation of gravity waves in the radiative zone (Rogers & Glatzmaier, 2006) that produce AM transport (Brummell et al., 2002), compositional mixing, and modifications to the magnetic field.

The tachocline is suspected to experience a range of hydrodynamic and magnetohydrodynamic (MHD) instabilities (Rashid et al., 2008; Gilman, 2018), which can drive turbulent motions and various forms of mixing. These instabilities can draw energy from kinetic, gravitational, and magnetic sources, or a combination thereof. The complexity of the dynamics within the tachocline, and radiative zones more broadly, presents challenges in parameterising its role in stellar evolution codes. This is especially evident in red and sub-giant stars, where discrepancies between core-envelope differential rotations inferred from asteroseismology and existing models highlight this difficulty, particularly in terms of missing angular momentum (e.g., Eggenberger et al., 2008; Aerts et al., 2019). Further research is needed to address these discrepancies and improve parameterizations. By gaining a deeper understanding of these dynamics, more accurate parameterisations can be integrated into stellar evolution codes, enhancing their predictive capabilities and leading to improved results that may better explain observations.

1.5 Modelling stars

We turn to the introduction of stellar evolution models by first discussing some important timescales of interest.

1.5.1 Timescales

Even with accelerating advancements in computational technology, quantum computing, and AI, realistic simulations of stars still seem at best improbable in the near future.

Perhaps the most fundamental issue surrounding this development is the vast range of both spatial and temporal scales at play. Examples range from oscillations and instabilities spanning only hundreds or thousands of kilometers, and fluctuating over minutes and days, to global properties that evolve over several billion years.

One of the shortest relevant timescales, equating to around half an hour in the Sun is the dynamical timescale (Kippenhahn et al., 1990; Prialnik, 2000; Maeder, 2008). This is on the order of time required, if thermal pressure supporting the gas against the pull of gravity were to suddenly vanish, for the star to collapse in upon itself. Characteristically, we expect this timescale to be roughly $\sqrt{R/g}$, where R is the stellar radius and $g \sim GM/R^2$ is the gravitational acceleration at the surface, $G \sim 6.67 \times 10^{-11}$ being the Newtonian constant of gravitation (with the value in SI units) and M is the total mass. Hence

$$t_{dyn} \sim \sqrt{\frac{R^3}{GM}}. \tag{1.3}$$

If a star is dynamically stable this is the timescale on which a small perturbation would be restored to its equilibrium position. Whilst a star remains on the main sequence phase it is typically be considered very close to being dynamically stable.

Another important timescale used when characterising a star is the thermal or Kelvin-Helmholtz timescale t_{KH}, with a value around 10^7 years for the Sun (Prialnik, 2000; Maeder, 2008; Pols, 2011), named after the two physicists who first described it as the evolutionary timescale of a star generating its energy output solely by gravitational contraction. This is given by the gravitational binding energy $E_g \sim GM^2/R$ divided by the luminosity L. Such that,

$$t_{KH} \sim \frac{GM^2}{RL}. \tag{1.4}$$

The largest of the timescales is that of the nuclear timescale t_{nuc}, which is the total energy sources of the star divided by the rate of energy loss. $t_{nuc} \sim 10^{10}$ years for the Sun (Kippenhahn et al., 1990; Pols, 2011).

1.5.2 Solving for stellar structure - 1D stellar models

The construction of a stellar model involves solving a set of differential equations rooted in fundamental physical principles, alongside appropriate boundary conditions for both the star's core and its surface. These equations must account for various microscopic properties of stellar matter, such as the behaviour of gases, nuclear reactions, and interactions between radiation and matter (Prialnik, 2000; Maeder, 2008). Despite considerable advancements in computational capabilities, achieving comprehensive three-dimensional models throughout a star's evolutionary stages remains seemingly impossible, primarily due to the vast range of timescales involved (Pols, 2011).

As a result, either significant simplifications must be adopted to reduce computational complexity, or alternative modeling methods, such as a local box model (Hawley & Balbus, 1992; Hawley et al., 1995; Barker et al., 2019) can be employed to study a particular aspect of the problem. Simplifications can involve ignoring fundamental effects like rotation and magnetism, resulting in a spherically symmetric system devoid of many observed waves, instabilities, and flows.

Since it is not yet feasible to include all important physical processes in stellar evolution models, a common approach is to study a particular phenomena in isolation to understand its dynamical properties, such as its role in mixing chemical elements, driving flows or magnetic fields, and transporting angular momentum. These insights are then used to parameterize their effects, unfortunately often through ad-hoc diffusive coefficients, which are then incorporated into stellar models (Eggenberger et al., 2008; Aerts et al., 2019).

The relevance of a particular physical phenomenon in computational models depends on the specific characteristics of the type of star being studied, which can vary from slow rotators or those with hardly detectable magnetic fields to rapidly rotating stars and/or with dominating magnetic fields (Maeder & Meynet, 2000; Donati & Landstreet, 2009).

Typically, deforming effects such as those from centrifugal forces, magnetic fields, and tidal interactions are ignored, resulting in spherically symmetric models, which are a good first global approximation given the oblateness of the Sun is very small (Dicke & Goldenberg, 1974). This simplifies the governing equations, which are often expressed in terms of global spherical polar coordinates, with the radial coordinate (r) representing the distance from the star's center and m_r representing the mass enclosed within that radius.

In terms of global evolution, it is instructive to consider the simplest case of a spherically symmetric star with no magnetic field or rotation in dynamical equilibrium. To describe this scenario, we require four equations: conservation of momentum, mass, energy, and one describing the nature of heat transport.

Here the momentum equation expresses the acceleration in terms of two components: the outward acceleration due its pressure gradient, and the inward acceleration due to gravity. These are the most fundamental forces, and additional forces may be included depending on the specific problem being analysed. Whilst in its main stage we consider a star to be in hydrostatic equilibrium, where the total radial acceleration is zero, indicating a balance between these forces.

If we consider a fluid element with $dm_r = \rho dr dS$ as seen in Fig. 1.6, then we can equate forces acting on the fluid element and note that they must balance such that,

$$\frac{\partial^2 r}{\partial t^2} = -g \ dm_r + P(r)ds - P(r+dr)ds. \tag{1.5}$$

From here we can note $P(r+dr) = P(r) + \frac{\partial P}{\partial r}dr$ and use $dm_r = \rho dr dS$ along with the standard form for the gravitational potential in a spherical body ($g = \frac{Gm_r}{r^2}$) to give,

$$\frac{\partial^2 r}{\partial t^2} = -\frac{1}{\rho}\frac{\partial P}{\partial r} - \frac{Gm_r}{r^2}, \tag{1.6}$$

whilst in equilibrium, $\frac{\partial^2 r}{\partial t^2} = 0$, so

$$\frac{dP}{dr} = -\frac{G\rho m_r}{r^2}. \tag{1.7}$$

This is a simplified form of the Navier-Stokes momentum equation governing an inviscid, compressible, non-magnetic fluid in a gravitational field describing hydrostatic balance.

To obtain our next fundamental equation we consider the conservation of mass acting on some shell element dS. Under the same forces as seen in Fig. 1.6, this gives

$$dm(r,t) = 4\pi r^2 \rho dr - 4\pi r^2 \rho v dt, \tag{1.8}$$

where v is the radial acceleration ($v = 0$ in hydrostatic equilibrium). We can then take derivatives with respect to dr and dt, which yield,

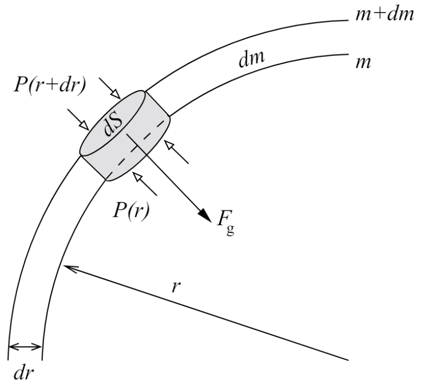

Figure 1.6: A shell of mass dm inside a spherically symmetric star, at radius r and with thickness dr. The mass of the shell is $dm = 4\pi r\rho dr$. The pressure and gravitational forces acting on the cylindrical mass element are also indicated. Figure courtesy of (Pols, 2011).

$$\frac{\partial m}{\partial t} = -4\pi r^2 \rho v, \tag{1.9}$$
$$\frac{\partial m}{\partial r} = 4\pi r^2 \rho. \tag{1.10}$$

Cross-differentiating and equating the above equations leads to the spherical form of the mass continuity equation,

$$\frac{\partial \rho}{\partial t} = -\frac{1}{r^2}\frac{\partial}{\partial r}(\rho r^2 v). \tag{1.11}$$

Note that if this shell was located at the surface of the star, $v > 0$ in 1.9 would correspond to a solar wind (loss of mass), and $v < 0$ would correspond to accretion (mass gain), however as mentioned we'll be taking $v = 0$ since this corresponds to hydrostatic equilibrium. When we take $v = 0$ the second equation, 1.10, becomes $dm_r/dr = 4\pi r^2 \rho$. In general this equation relates the mass to the radius of the star, in turn giving us the second fundamental equation of stellar structure.

The next equation comes from the conservation of energy. If we define L_r as the energy passing through the sphere of radius r per unit time, aka the Luminosity, we have

$$\frac{\partial L_r}{\partial m_r} = \epsilon - \frac{\partial q}{\partial t}, \tag{1.12}$$

where ϵ is the sum of the energy generated via nuclear processes per unit time, per unit mass, at a radius r, including losses associated with neutrino emissions, and dq corresponds to the heat per unit mass exchanged between the shell and its adjacent layers within the time dt.

Lastly we have the temperature distribution which depends on the efficiency of the radiative transport, the scales associated with which are typically much less than the stellar radius for most of the interior of a star. In convectively stable zones the radiative energy flux, F, is given in terms of the temperature, T, by

$$F = -\frac{4acT^3}{3\kappa\rho}\frac{\partial T}{\partial r}, \tag{1.13}$$

where ρ is the density, c the speed of light, a the radiation-density constant, and κ is the Rosseland mean opacity. Since $L_r = 4\pi r^2 F$, this leads to

$$\frac{\partial T}{\partial r} = -\frac{3\kappa\rho L_r}{16\pi acr^2T^3}, \tag{1.14}$$

in radiative regions. Convectively unstable regions are less straightforward and require the introduction of a theory for convection, such as mixing length theory. This invokes a 'mixing length', representing the mean free path of a macroscopic parcel in a fluid. In this case our energy transport equation takes the more general form

$$\frac{\partial T}{\partial m_r} = -\frac{G m_r T}{4\pi r^4 p}\nabla, \tag{1.15}$$

where $\nabla \equiv \partial \ln T / \ln p$ depends on the particular choice of mixing length theory employed.

Hence, the four equations governing the properties of a star's internal structure whilst on the main sequence are,

$$\frac{\partial m_r}{\partial r} = 4\pi r^2 \rho, \tag{1.16}$$

$$\frac{\partial p}{\partial r} = -\frac{G m_r \rho}{r^2}, \tag{1.17}$$

$$\frac{\partial L_r}{\partial r} = 4\pi r^2 \rho(\epsilon - \frac{\partial q}{\partial t}), \tag{1.18}$$

$$\frac{\partial T}{\partial r} = -\frac{G m_r T \rho}{r^2 p}\nabla, \tag{1.19}$$

representing the continuity of mass, hydrostatic balance, energy and heat transport equations, respectively.

In reality hydrostatic equilibrium is the standard configuration for a star to be in whilst along the main sequence, however during the early stages of its formation and the latter stages of its life this approximation won't be valid. As previously mentioned these equations govern a very idealised situation and improving their accuracy requires the inclusion of additional information in the governing equations. Due to the difficulties involved in resolving dynamics such as waves or turbulence in such models, they're often included in very sub-optimal ways (Eggenberger et al., 2008; Aerts et al., 2019). For example many types of waves and instabilities transport angular momentum and in turn can evolve the internal rotation profile of a star (Maeder & Meynet, 2000; Prialnik, 2000; Rogers & Glatzmaier, 2006), yet these are often included in models as isotropic diffusive coefficients. This is a significant simplification over reality and ignores all nontrivial orientation properties of these phenomena. Our hope is that refining our understanding of the transport induced by such instabilities will lead to more accurate parameterisations, hence enhancing stellar evolution models, and ultimately progressing our understanding of stellar evolution.

1.5.3 The evolution of stellar rotation profiles

Stellar rotation opens the door to a zoo of new dynamical processes that regulate the transportation of angular momentum and, in turn, evolve the star's rotation profile (and possibly affect mixing of chemical elements). These numerous processes necessitate modifications to the basic equations of stellar structure. In particular, we require an additional equation to govern the transport of angular momentum. Due to the strong stable stratification, the transport of angular momentum is thought to be considerably horizontally dominated. Zahn (1992) argued that due to this strong stratification, the dominating horizontal transport will mix the rotation rate efficiently in the horizontal direction unimpeded by the stable stratification, leading to rotation that is approximately constant with radius, $\Omega(r)$, commonly refereed to as 'shellular rotation' (though this view has also been disputed e.g. Gough and McIntyre, 1998).

For a shellularly rotating configuration, the equation of angular momentum transport in the vertical direction is, in Lagrangian coordinates (following e.g. Zahn, 1992; Meynet and Maeder, 2000), given by:

$$\rho \frac{d}{dt}\left(r^2\Omega\right)_{M_r} = \frac{1}{r^2}\frac{\partial}{\partial r}\left(\rho D r^4 \frac{\partial \Omega}{\partial r}\right) + \dots \, . \tag{1.20}$$

Here D is the total diffusion coefficient representing the effects of various instabilities that operate and transport angular momentum, assuming they act like a simple isotropic viscous diffusive process. The dots indicate terms that we have omitted from discussion here, such as transport of angular momentum by meridional circulations. However, a lackluster understanding of the fundamental processes—including the transport of angular momentum via instabilities—means that such equations can lack precision and lead to errors in models that use these approaches. Our hope is that through developing better understanding and generating improved parameterisations of such phenomena, we can develop more accurate stellar evolution models that better match asteroseismic observations (Aerts et al., 2019).

It's also worth briefly noting that the evolution of a star's rotation profile is heavily influenced by the mass loss that it experiences through its stellar wind (Maeder & Meynet, 2000). The effect of a stellar wind on its rotation profile comes not only from the outward loss of mass but also as a result of magnetic braking. This means that the transport of angular momentum itself is heavily dependent on the rotation properties of the star (Meynet & Maeder, 2000).

1.6 Angular momentum transport in the solar tachocline

In the Sun, the radiative interior contains approximately 98% of its mass (Hughes et al., 2007), and the vast majority (95%) of its angular momentum. It is standard practice in the treatment of the structure and evolution of such stars to assume radiative regions are quiescent. However, in reality, they likely host an array of interesting dynamics, many of which are potential mechanisms for angular momentum transport; and hence may address some of the shortcomings of our current theories.

In the Sun, the tachocline is a particularly interesting region for angular momentum transport. Serving as the boundary between the radiative interior where the majority of angular momentum resides, and the convective zone, which continually sheds angular momentum through its stellar wind (Mestel, 1968), it plays a crucial role in the evolution of the Sun's rotation profile. Its significant shear, buoyancy, and magnetic fields offer a variety of potential mechanisms for transporting angular momentum, including instabilities, waves, and transport along magnetic field lines (Tobias, 2005; Gilman, 2018; Aerts et al., 2019). Furthermore, the anisotropic nature of these forces can induce meridional circulations, further influencing the redistribution of angular momentum within the star (Sule et al., 2005; Balbus et al., 2009).

The following sections will focus on the four main mechanisms of AM transport as identified by e.g. Marques et al. (2013) and Aerts et al. (2019): meridional circulation, waves, magnetism and the key topic of this thesis, instabilities.

1.6.1 Meridional Circulation

Meridional circulation is the large-scale flow along meridional lines (i.e. lines of constant longitude), and acts to stir stellar radiative zones (Sule et al., 2005). Such circulations are attributed to the centrifugal effects rotation has on the star's isobars, the Lorentz forces if a magnetic field is present, and in the case of a binary system, the tidal forcing present. The most modern assessment of the loop of angular momentum transport via meridional circulation is as follows (Decressin et al., 2009; Rieutord & Espinosa Lara, 2009): meridional currents are first sustained by internal stresses (such as those from instabilities) as well as from torques at the surface due to magnetic braking and the stellar wind (Mestel, 1968). The temperature profile then changes to balance the advection of entropy due to the circulation, and finally, due to the baroclinic torques induced by the latitudinal distribution of temperature fluctuations on the isobar, a new differential rotation profile is formed. This can in turn generate new flows, thus closing the loop.

1.6.2 Waves

Waves arise from the presence of restoring forces within a system. In an astrophysical context, these forces include compressibility, stratification, magnetic fields, rotation, or tidal effects, giving rise to sound waves, internal gravity waves (IGWs), Alfvén waves, and inertial waves, respectively. In reality it is often more complex waves that emerge as a result of a combination of these restoring forces. In general waves can be effective transporters of angular momentum, but in particular IGWs and Alfvén waves are two particularly common and efficient propagators of AM (Schatzman, 1993; Kumar et al., 1999; Rogers & Glatzmaier, 2006; Bühler, 2014).

Internal gravity waves

In a stellar context, the most common and efficient mechanisms of IGW generation stem from either a tidal forcing due to a companion star (or planet), or from the adjacent convective zone. Tidal generation of waves occurs primarily at the radiative-convective interface. Subsequently, mechanisms such as thermal diffusion, nonlinear breaking, and critical layers act to dissipate the waves, in turn facilitating the transfer of angular momentum between the interacting bodies (Goodman & Dickson, 1998; Barker & Ogilvie, 2010, 2011; Weinberg et al., 2012; Essick et al., 2016). In the solar case however the planets are too far away and so the gravitational force between them is too small to generate IGWs efficiently. Internal gravity waves (IGWs) propagate when their frequency, represented by ω, is lower than the surrounding buoyancy frequency, $\mathcal{N}$. The extent to which thermal diffusion affects the wave depends heavily on its frequency and wavelength (Staquet & Sommeria, 2002). Essentially, thermal diffusion extracts energy from within the wave and diffuses it into the local surroundings, especially when the waves have a low frequency (and hence for short radial wavelengths). The dispersion relation for short wavelength IGWs, without shear or rotation, is given by,

$$\omega^2 = \mathcal{N}^2 \frac{k_\perp^2}{k^2}. \tag{1.21}$$

Nonlinear wave breaking can result from the overturning of stratification surfaces, leading to convective instability, or from the shear of the wave itself, known as the Kelvin-Helmholtz instability.

In singular stars, the primary source for IGW generation is through their neighbouring convection zones, and occur as a result of two primary mechanisms: bulk excitation through Reynolds stresses in the convection zone and directly through convective plumes (Staquet & Sommeria, 2002). In rotating systems the Coriolis force can lead to so-called inertial waves (Rieutord & Valdettaro, 1997; Zhang et al., 2001). These can also be excited through tidal interactions or by convection (Astoul et al., 2021; Astoul & Barker, 2023; De Vries et al., 2023), and in both cases these waves can transport AM.

In a frame rotating at the rate $\boldsymbol{\Omega}$ the momentum equation for an incompressible inviscid fluid (after removing the viscous term) can be written,

$$\frac{\partial \boldsymbol{u}}{\partial t} + (\boldsymbol{u} \cdot \nabla)\boldsymbol{u} + 2\boldsymbol{\Omega} \times \boldsymbol{u} = -\frac{1}{\rho}\nabla p, \tag{1.22}$$

which after linearisation and seeking exponential solutions of the form $\exp(\mathrm{i}\boldsymbol{k} \cdot \boldsymbol{x} - \mathrm{i}\omega t)$ we obtain the following simple dispersion relation,

$$\omega = \pm \frac{2(\boldsymbol{k} \cdot \boldsymbol{\Omega})}{|\boldsymbol{k}|}, \tag{1.23}$$

or equivalently

$$\omega = \pm 2\Omega \cos\theta, \tag{1.24}$$

where θ is the angle between the rotation axis and the direction of the phase velocity. Note the interesting property that the group velocity of an IGW, given by $d\omega/dk$, is always perpendicular to its phase velocity, ω/k.

1.6.3 Magnetic fields

Under the extreme conditions in stellar interiors, electrons are stripped from their parent atoms, thereby creating a soup of free flowing electrically charged particles, commonly referred to as plasma. When a plasma flows the motion of charged particles generates a corresponding magnetic field, which itself interacts with the fluid, leading to a wide array of complex dynamics, including solar flares (see Fig. 1.7), prominences, and sunspots (Sweet, 1969; Van Ballegooijen & Martens, 1989; Svestka, 2012). Such configurations require a more sophisticated set of equations, necessitating the combination of Maxwell's Laws of Electromagnetism with the Navier-Stokes equations. Alfvén (1942) made important contributions to the field known as Magnetohydrodynamics (MHD), for which he was awarded the 1970 Nobel Prize in Physics.

Alfvén waves

From these equations we can see another type of wave that is extremely prevalent in astrophysical contexts are Alfvén waves (Alfvén, 1942). These waves occur in magnetohydrodynamic systems due to the Lorentz force linking the momentum and magnetic induction equations. Here the magnetic tension in the field lines can act as a restoring force to perturbations in the fluid. Like other waves, Alfvén waves generate Reynolds stresses and so can transport angular momentum that way, however they also lead to magnetic internal stresses that transport AM (known as Maxwell stresses), which must also be taken into account.

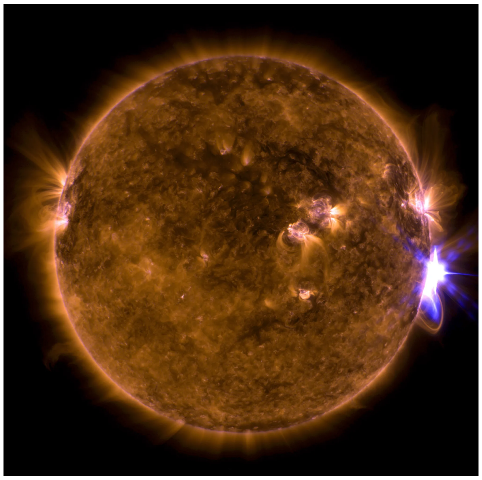

Figure 1.7: Image captured by NASA's Solar Dynamics Observatory (2017) of a solar flare – as seen in the bright flash on the right side – on Sept. 10, 2017. On the left hand side of the image we can also see a solar prominence protruding out at roughly latitude 30°.

In the simplest case of an incompressible magnetic fluid with no diffusion or gravity, the full system of governing equations would be,

$$\rho_0(\frac{\partial \boldsymbol{u}}{\partial t} + \boldsymbol{u} \cdot \nabla \boldsymbol{u}) = -\nabla p + \frac{1}{\mu_0}(\nabla \times \boldsymbol{B}) \times \boldsymbol{B}, \tag{1.25}$$

$$\nabla \cdot \boldsymbol{u} = 0, \tag{1.26}$$

$$\frac{\partial \boldsymbol{B}}{\partial t} = \nabla \times (\boldsymbol{u} \times \boldsymbol{B}), \tag{1.27}$$

$$\nabla \cdot \boldsymbol{B} = 0, \tag{1.28}$$

where 1.25 contains the Lorentz force (in which μ_0 is the magnetic permeability) in the final term, 1.27 is the induction equation and 1.28 is the solenoidal constraint on $\boldsymbol{B}$. Performing a linear analysis on this set of equations in a similar manner to the above, with $\boldsymbol{B} = \boldsymbol{B}_0 + \boldsymbol{b}$ (where $\boldsymbol{B}_0$ is the imposed background field and $\boldsymbol{b}$ is the perturbation to the magnetic field), we find the dispersion relation for Alfvén waves:

$$\omega^2 = \frac{(\boldsymbol{B}_0 \cdot \boldsymbol{k})^2}{\mu_0 \rho_0}. \tag{1.29}$$

If we define $v_A = B_0/\sqrt{\mu_0 \rho_0}$ as the Alfvén speed, and θ as the angle between $\boldsymbol{k}$ and $\boldsymbol{B}_0$ (in this section), then it follows,

$$\omega^2 = v_A^2 k^2 \cos^2 \theta. \tag{1.30}$$

Dynamos

A dynamo is a mechanism that sustains a magnetic field against diffusive decay. Low to medium mass solar-type stars, which possess convective envelopes like the Sun, are thought to generate dynamos. Additionally, around 10% of intermediate to high-mass stars retain stable large-scale fossil magnetic fields from their formation (Aerts et al., 2019). It is possible even stars with undetectable dynamos in their convective interiors are affected by the dynamics and evolution of their fields. Coupling a star's stellar wind and magnetic field also leads to the redistribution of angular momentum through a mechanism known as magnetic braking, which acts to 'spin down' the star over the course of its evolution.

Magnetic fields also offer additional mechanisms for the transport of angular momentum (Moyano et al., 2023), beyond their interactions with the stellar wind. In stably stratified regions with differential rotation, the shear flows lead to a stretching of the field lines, which through the Lorentz force ultimately causes the field to act back on the flow, leading to an exchange of momentum. This process generally acts to enforce uniform rotation (Mestel & Weiss, 1987). Furthermore, if a fossil magnetic field connects adjacent radiative and convective zones, some differential rotation can be transferred to the radiative zone via the field lines e.g. Strugarek et al. (2011).

Magnetic fields can also introduce numerous additional instabilities, with two of the best studied being the magnetorotational instability (MRI), and the Tayler instability, which have both proven to be promising methods of enhancing angular momentum transport as well as being mechanisms of dynamo generation (Spruit, 2002; Cantiello et al., 2014; Goldstein et al., 2019).

1.6.4 Instabilities

Some of the primary physical mechanisms enhancing angular momentum (AM) transport in stars involve (magneto-)hydrodynamic instabilities e.g., Maeder, 2008; Meynet et al., 2013; Kitchatinov, 2014; Aerts et al., 2019. When a system becomes unstable, turbulence can be induced, and depending on the properties of the Reynolds and Maxwells stresses, can either enhance or restrict the flow of angular momentum in a particular direction. The timescales governing the evolution a given instability depend on the dominant mechanism driving the instability and the limiting mechanisms involved.

Differential rotation can induce instabilities in regions of stars that are convectively stable, such as the solar radiation zone (Spiegel & Zahn, 1970; Watson, 1980; Knobloch & Spruit, 1982). Apart from transporting angular momentum, these instabilities can also mix chemical elements, which is thought to be an important factor in a star's evolution (Aerts et al., 2019). There are several canonical hydrodynamic instabilities that could occur within radiation zones, arising from rotational kinetic energy, misalignment of equipotentials, shear flows, compositional gradients, and magnetic fields. Here I will touch on those most relevant to this thesis.

Centrifugal instability of differentially-rotating flows

Centrifugal instabilities were first studied by Rayleigh (1917) and shortly after in the viscous regime by Taylor (1923). Their results ultimately depended on the

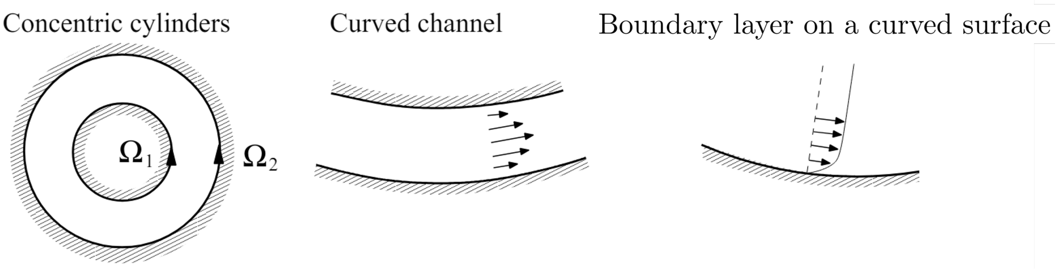

Figure 1.8: A selection of the canonical centrifugally unstable flows (Fielding, 2020).

epicyclic frequency, also known as the Rayleigh frequency, which corresponds to the frequency at which a radially displaced fluid ring will axisymmetrically oscillate about its equilibrium position in a differentially rotating flow. It's worth noting that this frequency is analogous to the Brunt-Väisälä frequency for the case of buoyancy. It was found that for an epicyclic frequency defined as

$$\mathcal{F}_\Omega^2 = \frac{1}{\varpi^3}\frac{d}{d\varpi}(\varpi^2\Omega)^2, \tag{1.31}$$

where ϖ is the distance from the axis of rotation in cylindrical coordinates, that the differentially rotating flow can be unstable to this instability if $\mathcal{F}_\Omega^2 < 0$ but stable if $\mathcal{F}_\Omega^2 > 0$. This is equivalent to saying that for instability to occur the angular momentum per unit mass must decrease as we move away from the rotation axis.

Later works by Solberg (1936) and Høiland (1941) generalised this to systems with stable stratification. When entropy surfaces are constant along cylinders, a stronger criterion was found: for instability, we require $\mathcal{N}^2 + \mathcal{F}_\Omega^2 < 0$, in addition to the previous requirement that angular momentum per unit mass must decrease whilst moving away from the rotation axis. $\mathcal{N}$ is typically large in stellar radiative zones, so strong differential rotation is generally required for this instability to operate.

There are several types of canonical flows that produce centrifugal instabilities (see Fig. 1.8), including the well-known Taylor-Couette flow, boundary layer flows, and curved channel flows.

Baroclinic instabilities

Instabilities can also arise in differentially rotating stars as a result of the misalignment between their surfaces of constant pressure and density, a configuration referred to as baroclinic. In a baroclinic equilibrium, we require an additional equation, known as the thermal wind equation (TWE), to describe the properties of this balance.

When there is a misalignment between the surfaces of constant pressure and density, it becomes possible for a parcel of fluid to move perpendicular to gravity (without doing any work against it) while simultaneously moving into a denser medium, thereby developing upward buoyancy and potentially becoming unstable (Spruit & Knobloch, 1984; Gilman & Dikpati, 2014; Kitchatinov, 2014). Baroclinic instabilities are generally inhibited (if not fully damped) by stable stratification but can become unstable when, for example, thermal diffusion is strong enough to reduce the restoring effects of buoyancy (Knobloch & Spruit, 1982). Baroclinically unstable displacements exist within the wedge separating the lines of constant pressure and density. As the strength of the stratification increases, the wedge becomes smaller (as will be seen when we discuss the thermal wind equation in Chapter 2), and the minimum horizontal wavelength λ_m increases. Stability is then achieved when λ_m exceeds the size of the volume considered, here, the stellar radius (Knobloch & Spruit, 1982).

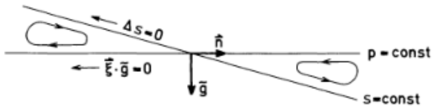

Figure 1.9: Baroclinic instability where p = pressure and s = entropy. Figure courtesy of Knobloch and Spruit (1982).

Shear instabilities

Another family of instabilities we expect to operate in the tachocline are those triggered by horizontal and vertical shears (Maeder, 1995; Brüggen & Hillebrandt, 2001; Mathis et al., 2004; Garaud, 2020b) (see Fig. 1.10 for a snapshot of a nonlinear simulation of such an instability).

The stability of shear flows was first studied theoretically by Rayleigh (1880) who considered an unstratified unidirectional shear flow between two rigid boundaries. When studying the inviscid, non-rotating, unstratified flow, he found that for the shear flow $U(z)\hat{\boldsymbol{x}}$, a necessary condition for instability is the requirement of an inflection point in its domain, i.e., $\frac{d^2U(z)}{dz^2} = 0$ somewhere in the flow.

Subsequently, it was discovered that for a shear flow with gravity in the z-direction, buoyancy acts to inhibit the instability, and a sufficient condition for adiabatic stability can be derived (Howard, 1961; Miles, 1961). They determined that $Ri = \frac{N^2}{(U'(z))^2} < \frac{1}{4}$ is a necessary condition for instability of a plane parallel shear flow with aligned stratification, i.e., a horizontal flow varying with z in a fluid with density decreasing with height z.

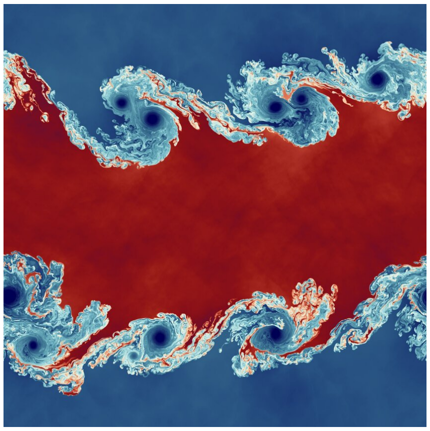

Figure 1.10: A snapshot from a nonlinear simulation by Dzanic and Witherden (2022) of the Kelvin-Helmholtz instability (a classical shear instability).

Double diffusive instabilities

When the density of a fluid depends on two separate components that diffuse at different rates, such as salinity and temperature, a fluid can become unstable even if its density decreases upwards, e.g. Knobloch (1982) and Garaud (2018, 2021). The dynamics of this type of convection depend heavily on whether the faster or slower diffusing component is responsible for driving the instability. For temperature and salinity a configuration in which the energy is supplied from the slower diffuser is called a fingering instability. The alternative case, in which the faster diffusing component drives the instability, is referred to as diffusive convection. If both diffusing quantities are responsible for the instability, then the total density stratification is unstable, resulting in top-heavy convection.

The canonical example of a fingering instability is salt fingers, which commonly occur in the upper kilometer of tropical and sub-tropical oceans, where warm-salty waters sits on top of cold-fresh waters (Schmitt, 1995; Kunze, 2003). As shown in Fig. 1.11, if a fluid parcel is displaced upwards, because thermal diffusion is quicker than the diffusion of salinity, the parcel will heat up and gain buoyancy at a quicker rate than it will gain weight from the extra salinity, creating an unstable upwards motion. This leads to finger-like plumes, which can then become unstable themselves via parasitic instabilities, leading to turbulence.

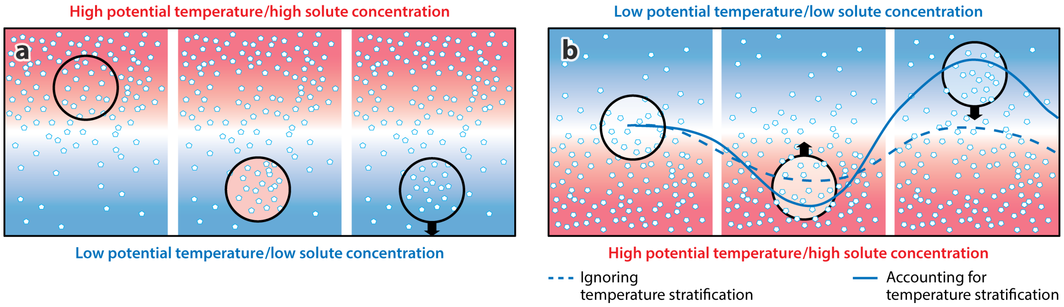

Figure 1.11: Diagram showing the two main types of double diffusive instability, from (Garaud, 2018). A fingering instability on the left, and diffusive convection on the right.

On the other hand, a cold-fresh over warm-salty configuration offers another potential double-diffusive instability (Garaud, 2013; Garaud, 2020a). If we consider perturbing a fluid element downwards, similar to the salt-fingering case, its temperature rapidly adjusts whilst it remains at a similar salinity. Since the salinity now increases with depth, the parcel becomes lighter than the ambient fluid surrounding it, and buoyancy forces start to drive it upwards. The parcel is now not only lighter than its surroundings but, because of the heat gained, it is now lighter than it was originally. Hence, on its way back up, it will overshoot its original starting point. At its new equilibrium position, the parcel again quickly adjusts its temperature, but because of the slow salinity diffusion rate, it is now saltier and heavier than its surroundings. This process repeats itself, and the overshooting distance gradually becomes larger and larger, resulting in a so-called ‘overstable’ mode, which is itself unstable.

The application of these instabilities to stars can involve viscosity (ν), thermal diffusion (κ), magnetic diffusion (η) or diffusion of chemical elements to destabilise an otherwise stable flow. We'll be particularly interested in the quantities $\mathrm{Pr} = \nu/\kappa$ and $\mathrm{Pm} = \nu/\eta$. For the tachocline, Gough (2007) and Caleo et al. (2016) predict $\nu = 2.7 \times 10^1\,\mathrm{cm}^2\,\mathrm{s}^{-1}$, $\kappa = 1.4 \times 10^7\,\mathrm{cm}^2\,\mathrm{s}^{-1}$, and $\eta = 4.1 \times 10^2\,\mathrm{cm}^2\,\mathrm{s}^{-1}$, which implies $\mathrm{Pr} = 2 \times 10^{-6}$ and $\mathrm{Pm} = 0.7 \times 10^{-2}$ (both very small), suggesting that secular instabilities may be quite common in astrophysical contexts.

Goldreich-Schubert-Fricke instability (GSF)

The GSF instability brings together many of the instabilities previously discussed. It is a doubly-diffusive instability of differential rotation, where the action of thermal diffusion on sufficiently small lengthscales reduces the stabilising effects of buoyancy, allowing for the development of a fingering-type instability (analogous to the thermohaline instability e.g. Garaud, 2018). In a rotating shear flow where the thermal gradient is stabilising (a radiative region) a reduction in thermal effects can allow AM fingers to develop and grow exponentially. Subsequently, these non-linearly saturate, e.g. by secondary parasitic shear instabilities, which grow until turbulence develops. This configuration is visually analogous to salt fingering, and formally analogous for axisymmetric (2D 3-component) simulations performed with purely radial shear at the equator (for a certain choice of diffusivity ratio, Barker et al., 2019). The GSF instability belongs to a family of instabilities referred to as 'secular' shear instabilities. Standard shear instabilities, for which perturbations are usually assumed to be adiabatic, are not typically expected to develop in stellar radiation zones, thanks to the strong stabilising effects of the stratification, which ensures that $\mathrm{Ri} \gg 1$.

On the other hand, finite-amplitude 'secular' (or diffusive) shear instabilities (e.g. Zahn, 1974; Zahn, 1992), are believed to be important by producing thermally-diffusive shear-induced turbulence when the Richardson number Ri of the flow is large, provided the Peclet number Pe (which measures the ratio of thermal diffusion to advection timescales) is sufficiently small (e.g. Prat & Lignières, 2013; Garaud et al., 2017; Gagnier & Garaud, 2018; Kulenthirarajah & Garaud, 2018; Cope et al., 2020; Garaud, 2020a). The GSF instability is distinct from these in that it is a linear instability that only operates in the presence of rotation, but it is related in that it requires strong thermal diffusion to operate. When shear and GSF instabilities operate simultaneously they can interact, leading to interesting nonlinear dynamics (Chang & Garaud, 2021). The GSF instability and its co-existence with inflection-point instabilities has also been analysed in linear theory for horizontal shears with a tanh profile by Park et al. (2020), Park et al. (2021). They referred to the GSF instability as the "inertial instability" (e.g. Park et al. (2019)) following its relation to this instability in the geophysical literature.

Interestingly, the nonlinear development of the instability does not lead to a homogeneous turbulent state in general, and other interesting dynamics, such as the formation of layering in AM (often referred to as 'zonal jets') has previously been observed, which can enhance turbulent transport (particularly at non-equatorial latitudes, in the case with radial shear, Barker et al., 2020).

The GSF instability is considered in this thesis and will be covered in much more detail in Chapters 3 and 4.

Magneto-rotational instability (MRI)

The final instability we discuss in this section delves into the realm of magnetohydrodynamics (MHD). As previously mentioned, the introduction of a magnetic field significantly alters the potential dynamics within a system. New magnetic pressure and tension forces come into play, magnetic buoyancy emerges, and questions regarding dynamo generation and magnetic heating become highly relevant (Velikhov, 1959; Chandrasekhar, 1961; Hughes, 1988; Spruit, 2002; Jones et al., 2010; Cantiello et al., 2014). One key MHD instability, which has seen extensive interest, is the Magnetorotational Instability (MRI) (e.g. Acheson & Gibbons, 1978; Balbus & Hawley, 1991, 1994; Balbus, 1995; Spruit, 1999; Menou et al., 2004; Menou & Le

Mer, 2006; Ogilvie, 2007; Parfrey & Menou, 2007; Balbus, 2009; Guilet & Müller, 2015).

The MRI instability can be described using the following physical argument: consider two fluid elements with masses m_1 and m_2 orbiting some rotation axis at different radii ($r_1 < r_2$), joined by a weak elastic tether as seen in Fig. 1.12. Assuming the angular velocity decreases as a function of radius, the mass at radius r_1 will move ahead, stretching the tether. As a result, angular momentum is transferred from m_1 to m_2. The fluid elements then adjust to an orbit compatible with their new angular momenta, where m_1 moves inwards and m_2 outwards. Since $\partial\Omega/\partial r < 0$, the difference in angular velocity increases, which leads to a repeated process that exponentially separates the fluid elements over time. It's important to note that this argument fails if our magnetic tether is too strong, since then the fluid elements are kept tightly together. Thus, the MRI commonly occurs for weak magnetic fields. We shall discuss the MRI in more detail in Chapter 5.

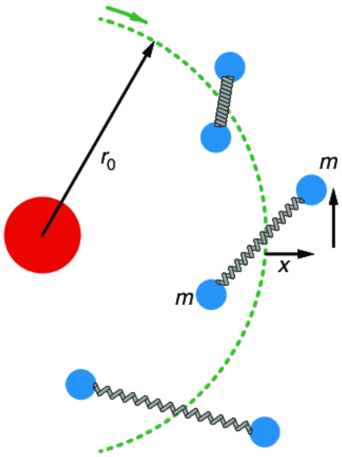

Figure 1.12: An illustration of the physical argument describing the magnetorotational instability (MRI). Figure courtesy of Hung et al. (2019).

1.7 Motivation

The overarching goal of astrophysical fluid dynamics is to understand the mechanisms driving the evolution of astrophysical objects such as accretion disks, planets, stars, and galaxies. Despite significant technological and theoretical advancements, our understanding remains incomplete. Even the most advanced simulations struggle to accurately replicate key phenomena like differential rotation, the formation of the tachocline, and dynamo processes within the Sun. Identifying the precise physical mechanisms responsible for these phenomena continues to be a major challenge. This thesis aims to bridge this gap by enhancing our understanding of the role of instabilities in transporting angular momentum within stably stratified radiative zones, an area still poorly understood.

The following research is conducted with a particular focus on the solar tachocline, a region with extreme parameters conducive to various instabilities. The tachocline is crucial as it links the radiative interior, containing the majority of the Sun's angular momentum, to the convective zone. All angular momentum in the convective zone, as well as that lost through interactions with the solar wind, must have ultimately crossed the tachocline. Thus, a better understanding of the tachocline is essential for comprehending the Sun's evolution, its magnetic dynamo, and for improving boundary conditions in simulations of turbulent convection in its envelope. Furthermore, insights gained from studying differential rotation profiles in stably stratified, potentially magnetized fluids, have broad applications across various astrophysical contexts.

For example, giant planets like Jupiter, which have radiative regions, exhibit unexplained phenomena such as polar vortices and striking zonal jets. Nonlinear simulations suggest that instabilities like the GSF instability can lead to the formation of similar jet-type structures (Barker et al., 2020). Additionally, there are challenges in reproducing the rotation profiles of red giant and subgiant stars. Missing angular momentum transfer from the inner to outer regions may account for discrepancies between observations and simulations in these cases.

1.8 Thesis structure

Much of the work presented in this thesis has been published in MNRAS (DBJT3), or is being prepared for submission (Chapter 5) and builds directly upon previous studies by Barker et al., 2019, 2020 (hereafter BJT1 and BJT2). BJT1 and BJT2 utilize a local Cartesian box setup to study a small patch of a stably stratified, differentially rotating radiative zone, modeling a global 'shellular' (or 'vertical') differential rotation that varies only with spherical radius. The primary aim of this work is first to generalise this to include arbitrary differential rotation profiles, and then to study the problem in the MHD context through the incorporation of a poloidal magnetic field.

BJT1: Radial shear at the equator The initial paper by Barker et al. (2019) examined the case where $\Lambda = 0$ and $\phi = 0$, corresponding to cylindrical rotation at the equator. 3D equatorial simulations with vertical shear revealed homogeneous turbulence alongside enhanced and sustained AM transport. A simple and easily implementable theory was proposed to model AM transport in stars.

BJT2: Moving away from the equator Generalising the initial model to an arbitrary latitude, their second paper found enhanced AM transport, with further increases typically seen away from the equator. Notably, zonal jets (or layering in AM) were observed in nonlinear simulations. A simple criterion for the onset of (diffusive) axisymmetric instability at a general latitude for radial differential rotation was derived: $\mathrm{RiPr} < 1/4$.

DBJT3: The study of general differential rotation profiles The model is proposed and discussed in Chapter 2, after which the results of the third paper are outlined in Chapters 3 and 4, where we investigate the GSF instability in stellar radiative zones with arbitrary local differential rotation (building also upon Knobloch (1982) and Knobloch and Spruit (1982)). In Chapter 2 we first justify the use of our local Boussinesq model and derive several key equations including the thermal wind equation and the relevant dispersion relations for adiabatic and diffusive axisymmetric modes.

Chapter 3 conducts an axisymmetric linear analysis probing the stability properties of general rotation profiles (through varying ϕ). We analytically derive key criteria in both the diffusive and non-diffusive regimes, identifying two key instabilities along with a set of weaker oscillatory modes. We complement this with a numerical analysis of the dispersion relation to develop an understanding of the regions of instability and the properties of the most unstable modes.

Chapter 4 explores the nonlinear hydrodynamical evolution in three dimensions using the pseudo-spectral code Snoopy in a modified shearing box. Various latitudes and rotation profiles were investigated, encompassing cases from both the GSF and adiabatically unstable regimes identified in Chapter 3. The emergence of robust nonlinear zonal jets, indicative of "layering" in angular momentum, is observed. Mixed radial and latitudinal shears are found to transport angular momentum more effectively compared to cases with purely radial shear. We also conduct simulations for various shear strengths to probe the effects of the background shear on the nonlinear evolution of the instability, as well as simulations in a variety of box sizes to ensure that the properties of the instability don't depend on the dimensions of the box. We find that the nonlinear properties of the GSF instability are largely independent of box size, suggesting our results could be extrapolated meaningfully into an astrophysical context.

Effects of a poloidal magnetic field on the linear problem Chapter 5 investigates the system's behavior in the presence of a poloidal field. The linear stability of the system to axisymmetric perturbations is analysed both analytically and numerically, where we identify instabilities with and without diffusion. The GSF, MRI, Solberg-Høiland instability, and weakly unstable inertial gravity waves are observed under certain parameter regimes.

Nonlinear Evolution of the Magnetic System The final section, Chapter 6, examines the nonlinear evolution of the magnetohydrodynamic system considered in Chapter 5. Nonlinear simulations reveal that here instabilities not only have the ability to enhance angular momentum transport but can also significantly enhance the strength of the magnetic field. These simulations allow us to build a deeper understanding of how poloidal fields of various strengths alter the dynamical and transport properties of the various instabilities. Several simulations probing the dependence of each instability on the size of the computational domain (L_x, L_y, L_z), reveal which of our results could be meaningfully extrapolated into an astrophysical context.

Chapter 2

Local modelling of stellar interiors

This chapter introduces the local model adopted throughout this thesis to study the stability of differential rotation in stellar (or planetary) interiors. We present our governing equations and the modelling approximations employed, discussing their validity and suitability for the problems at hand. We shall also derive and discuss both the thermal wind equation and the dispersion relation describing axisymmetric perturbations to the hydrodynamic system.

This sets the stage for a detailed exploration of our system in Chapters 3 and 4. We focus in those chapters on the effects of varying the parameter ϕ – the angle between the effective gravity and local angular velocity gradient – which enables us to build upon and generalise the results of Barker et al. (2019) and Barker et al. (2020) for arbitrary differential rotation profiles. Whilst the effects of shear orientation on the stability properties of this system have previously been investigated previously by Knobloch and Spruit (1982), albeit using different notation, the following work in Chapters 3 both verifies and builds upon their results.

2.1 Global or Local?

Processes occurring inside stars happen on a vast range of length and time scales. So the appropriate strategy to modelling different processes can vary widely.

Global models ignore much of the small scale dynamics in exchange for the ability to probe phenomena on a global scale, meaning on scales comparable with the size of a given star (or a significant portion of them). This approach has proven effective at modelling large-scale dynamo action, meridional circulations, modelling star formation, and for producing 1D stellar models, as seen in for example Dikpati and Gilman (2008), Miesch et al. (2010), Mordasini et al. (2015), Buldgen (2019a), and Charbonneau (2020). However, due to computational limitations, global simulations often lack some detailed physics and also fail to resolve effects occurring on small scales – particularly effects smaller than any grid scales.

In contrast, the local modelling approach ignores much of the global structure of a body and instead focuses on the details of the physics occurring in a small patch of a star. For example, Hawley and Balbus (1992), Balbus and Hawley (1994), Balbus (1995), Hawley et al. (1996), Sharma et al. (2006), and Barker et al. (2019) have all exploited the use of local models to understand small scale instabilities that would have been more difficult to capture – or perhaps would be impossible to represent – in global models. While the local approach can offer insights into a specific region, extrapolating these findings to a global scale can be challenging and requires careful consideration.

Since the GSF instability is expected to be the primary instability of interest in our hydrodynamic system, its small scale nature (required for thermal diffusion to become appropriately strong) suggests a local approach is more appropriate. In particular the construction of our local model here follows in the footsteps of previous authors (Barker et al., 2019, 2020) and a small scale Cartesian box model is adopted.

Boussinesq Approximation

In essence the Boussinesq approximation linearises the ideal gas law for small departures from a reference state and ignores density differences in all but the gravity terms of the momentum equation (Spiegel & Veronis, 1960). An approximation valid for most local instabilities in the radiative interior and tachocline of the Sun, which are very subsonic (i.e. with $u \ll u_s$, u being the fluid velocity and u_s the sound speed). The Boussinesq approximation also requires the reference length $d \ll H_p$ and $d \ll H_\rho$, where $H_p = |\frac{1}{p}\frac{dp}{dz_h}|$ is the pressure scale height and $H_\rho = |\frac{1}{\rho}\frac{d\rho}{dz_h}|$ is the density scale height, so that the domain height is much less than the local pressure and density scale heights (and z_h is height locally). Adopting the Boussinesq approximation results in the mass conservation equation taking the form of an incompressibility condition.

2.2 Local Cartesian Box Model and Equations

Our model simulates a localised region of a stably-stratified and differentially-rotating star, akin to the lower segments of the solar tachocline. This region is represented as a Cartesian box with dimensions (L_x, L_y, L_z) and coordinates (x, y, z). Here, y denotes the local azimuthal direction, while x and z define two directions within the meridional plane.

The typical lengthscale d in our problem, following other double-diffusive instabilities, for example see Radko (2013), is taken to be,

$$d = \left(\frac{\nu\kappa}{\mathcal{N}^2}\right)^{\frac{1}{4}}, \tag{2.1}$$

and has been observed to well describe the scale of the dominant hydrodynamic GSF modes (Barker et al., 2020). Recalling the physical values in the tachocline as calculated by Gough (2007) and Caleo et al. (2016) that we stated in Chapter 1, we find $\nu = 2.7 \times 10^1 \text{cm}^2\text{s}^{-1}$, $\kappa = 1.4 \times 10^7 \text{cm}^2\text{s}^{-1}$, hence $\text{Pr} = 2 \times 10^{-6}$ and

$\mathcal{N} = 8 \times 10^{-4}\mathrm{s}^{-1}$. This produces a length scale $d \approx 49.3$m. The linear GSF modes thus have very short length-scales, approximately 10^{-5} times smaller than the tachocline thickness, which we take to be $0.02R_{\odot}$ (Christensen-Dalsgaard & Thompson, 2007).

Since the typical length-scales for GSF modes are so small (much smaller than the density and pressure scale heights) we are justified in adopting the Boussinesq approximation (Spiegel & Veronis, 1960) (see 2.1). This allows us to neglect variations in density except in the direction of gravity and converts our conservation of mass equation into an incompressibility condition.

The local nature of our model means we represent the differential rotation $\boldsymbol{\Omega}(r, \beta) = \Omega(r, \beta)\hat{\boldsymbol{\Omega}}$, where $\hat{\boldsymbol{\Omega}}$ is a unit vector, r is the radius and β is the latitude, using two components, one with a constant value of Ω together with a linear shear flow $\boldsymbol{U}_0 = -\mathcal{S}x\boldsymbol{e}_y$ representing the local differential rotation. The shear strength $\mathcal{S}$ is determined as the locally constant value of $-\varpi|\nabla\Omega(r, \beta)|$, where ϖ denotes the distance from the axis of rotation (cylindrical radius).

For computational convenience when undertaking nonlinear simulations using a shearing box method, we align the x-axis with the variation of the shear flow $\boldsymbol{U}_0$, despite its misalignment with respect to the local effective gravity vector $\boldsymbol{e}_g = (\cos\phi, 0, \sin\phi)$. The effective gravity is the sum of the ‘actual’ gravitational effects along with the effects of centrifugal acceleration. Since the Sun is a slow rotator $\boldsymbol{e}_g$ is assumed to be approximately along the spherical radial direction. This approximation breaks down for rapidly rotating stars in which centrifugal deformations of equipotential surfaces/isobars are much stronger, though our model is still valid for these with an appropriate interpretation of e_g.

The angle Λ is defined such that $\hat{\boldsymbol{\Omega}} = (\sin\Lambda, 0, \cos\Lambda)$. Since Λ characterizes the angle from the equator (perpendicular to $\hat{\boldsymbol{\Omega}}$) to the x-axis, and considering the misalignment of the x-axis from the spherical radial direction is ϕ, the latitude is characterised by $\beta = \Lambda + \phi$.

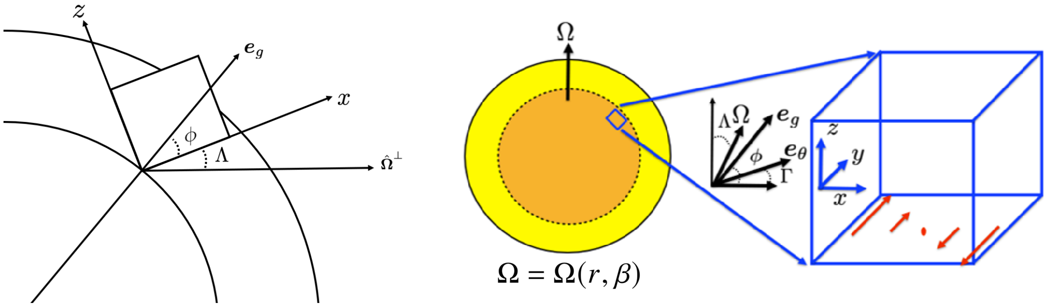

Figure 2.1: Two panels indicating the local Cartesian model with arbitrarily oriented local effective gravity $\boldsymbol{e}_g$ describing local differential rotation depending on both spherical radius and latitude in general (note, we refer to rotation profiles as $\Omega(r, \beta)$, where β is the latitude). For illustration, the dark orange region may represent a radiation zone and the yellow region an overlying convection zone, if we consider applications to the solar tachocline. We consider a general location in a differentially-rotating star at a latitude $\Lambda + \phi$, with local shear along x, and normal to the stratification surfaces (i.e. along the temperature gradient) $\boldsymbol{e}_\theta$, which is inclined relative to the local radial direction (approximately along $\boldsymbol{e}_g$) by an angle $\phi - \Gamma$ that is determined by the thermal wind equation.

The model is illustrated in Fig. 2.1, where the left panel shows the orientation of the box with respect to the local effective gravity $\boldsymbol{e}_g$, and the right panel illustrates the various angles and the shear flow considered in this thesis.

BJT1 and BJT2 (Barker et al., 2019, Barker et al., 2020) employed a similar model but with purely radial shear (i.e., co-linear with the effective gravity), so that $\phi = 0$ and $\boldsymbol{e}_g$ is aligned along x. This configuration corresponds to a "shellular" rotation profile in which the differential rotation only depends on spherical radius, i.e. $\Omega(r, \beta) = \Omega(r)$. However rotation profiles can be much more general than this in stellar interiors. The Sun, for example, exhibits both latitudinal and radial differential rotation, at least in the vicinity of the convection zone as we saw from Fig. 1.5 in Chapter 1. These are known to have different stability properties to the purely radial shear (Knobloch & Spruit, 1982), and so it's a natural extension for us to investigate these properties in-depth and begin to quantify the associated transport properties of arbitrary local differential rotations.

The governing equations describing fluid flows in our local model are:

$$\begin{aligned}
\frac{D\boldsymbol{U}}{Dt} + 2\boldsymbol{\Omega}\times\boldsymbol{U} &= -\frac{1}{\rho}\nabla p + \theta\boldsymbol{e}_g + \nu\nabla^2\boldsymbol{U}, \\
\frac{D\theta}{Dt} &= \mathcal{N}^2 e_\theta + \kappa\nabla^2\theta, \\
\nabla\cdot\boldsymbol{U} &= 0, \\
D &\equiv \partial_t + \boldsymbol{U}\cdot\nabla,
\end{aligned}$$

which represent the conservation of momentum and mass and transport of heat, respectively for our velocity field $\boldsymbol{U} = \boldsymbol{U}_0 + \boldsymbol{u}$ (where $\boldsymbol{U}_0 = -\mathcal{S}x\boldsymbol{e}_y$ is the background shear flow and $\boldsymbol{u}$ the velocity perturbation). Here $\theta = g\alpha\tilde{T}$ is a scaled temperature perturbation, $T + \tilde{T}$ being the full temperature, with g being the gravitational acceleration and α the coefficient of thermal expansion. We have adopted a background temperature (entropy) profile $T(x, z)$, with uniform gradient $\alpha g\nabla T = \mathcal{N}^2\boldsymbol{e}_\theta$, where $\boldsymbol{e}_\theta = (\cos\Gamma, 0, \sin\Gamma)$, whilst noting that our buoyancy frequency $\mathcal{N}^2 = g\left(\frac{1}{\Gamma_1}\frac{\partial\ln p_0}{\partial r} - \frac{\partial\ln\rho_0}{\partial r}\right) > 0$ where $\Gamma_1 = \left(\frac{\partial\ln p_0}{\partial\ln\rho_0}\right)_{ad}$ in the radiative zone of a star. Throughout our system we also take $\rho = 1$ as the reference density and take constant kinematic viscosity ν and thermal diffusivity κ, both of which are vital ingredients in studying the GSF instability.

Throughout our nonlinear simulations, we adopt Ω^{-1} as our unit of time and define the length scale d accordingly. This choice is motivated by the fact that the fastest-growing GSF modes typically exhibit a wavelength of $O(d)$. With this characteristic length scale, the buoyancy timescale $\mathcal{N}^{-1}$ equals the geometric mean of the product of viscous (d^2/ν) and thermal diffusion (d^2/κ) timescales (see e.g., Radko, 2013, for a discussion of its relevance for similar double-diffusive instabilities). Using this length scale allows us to conveniently select a suitable box size relative to the wavelengths of the fastest-growing linear modes. Our dimensionless shear rate is defined as $S = \mathcal{S}/\Omega$, and our dimensionless buoyancy frequency as $N = \mathcal{N}/\Omega$.

In total, excluding the dimensions of the box (and numerical resolution), our problem features 5 independent parameters: S, Pr, N^2, Λ, and ϕ (since Γ will be constrained by Eq. 2.9, the TWE). Notably, the Prandtl number (mentioned in Chapter 1), is a crucial parameter in our system, defined as

$$\mathrm{Pr} = \frac{\nu}{\kappa}. \tag{2.2}$$

The non-dimensional momentum and heat equations can be expressed as follows:

$$\boldsymbol{D}\boldsymbol{u} + 2\hat{\boldsymbol{\Omega}} \times \boldsymbol{u} - Su_x\boldsymbol{e}_y = -\nabla p + \theta\boldsymbol{e}_g + \mathrm{E}\nabla^2\boldsymbol{u}, \tag{2.3}$$

$$D\theta + N^2\boldsymbol{u}\cdot\boldsymbol{e}_\theta = \frac{\mathrm{E}}{\mathrm{Pr}}\nabla^2\theta, \tag{2.4}$$

subject to the incompressibility condition. Note that we define θ as our "temperature perturbation", which has units of acceleration and is related to T by $\theta = \alpha g T$, where α is the thermal expansion coefficient. Here, we define the local Ekman number $\mathrm{E} = \nu/(\Omega d^2)$, which can be related to other parameters. Note that for simplicity, we omit hats to denote non-dimensional quantities.

It is possible to combine this system with an additional equation, known as the 'Thermal wind equation' (TWE), which allows us to eliminate either the Γ or Λ variable; we choose to eliminate Γ.

2.3 The Thermal Wind Relation

As we've already seen, the surfaces of constant pressure and density need not be aligned in stellar interiors. The level of this misalignment, known as baroclinicity, is determined by the so-called "Thermal Wind Equation" (TWE) [1], which, as we shall see, arises from the vorticity equation. Note that if thermal wind balance were not satisfied then we would expect the system to rapidly adjust, on a dynamical timescale, to satisfy it. Our approach involves selecting values for Ω, $\mathcal{S}$, $\mathcal{N}$, Λ,

---

[1] As discussed by Knobloch and Spruit (1982), for a long time authors failed to realise that thermal wind balance should be satisfied when considering diffusive stability. As a result, the initial studies by Goldreich and Schubert (1967) and Fricke (1968) didn't utilise the TWE and contained a spurious free parameter. Acheson and Gibbons (1978) and Busse (1981) were the first to introduce the TWE in this context.

and ϕ to determine Γ. Alternatively, one could assume thermal wind balance by imposing the temperature field, then make use of the thermal wind equation to determine the corresponding differential rotation, as done in Rashid et al. (2008).

2.3.1 Derivation of TWE

The derivation of the thermal wind equation requires we take a closer look at the momentum equation for $\boldsymbol{U}_0$, namely,

$$\frac{\partial \boldsymbol{U}_0}{\partial t} + \boldsymbol{U}_0 \cdot \nabla \boldsymbol{U}_0 + 2\boldsymbol{\Omega} \times \boldsymbol{U}_0 = -\nabla p + \alpha g T \boldsymbol{e}_g + \nu \nabla^2 \boldsymbol{U}_0. \tag{2.5}$$

Since $\boldsymbol{U}_0$ is steady, $\partial \boldsymbol{U}_0/\partial t = 0$, and being linear in x whilst varying purely in the y-direction implies $\boldsymbol{U}_0 \cdot \nabla \boldsymbol{U}_0 = 0$ and $\nabla^2 \boldsymbol{U}_0 = 0$. Implementing these in 2.5 we obtain,

$$2\boldsymbol{\Omega} \times \boldsymbol{U}_0 = -\nabla p + \alpha g T \boldsymbol{e}_g. \tag{2.6}$$

The vorticity of a particular point in a flow $\boldsymbol{u}$ is given by $\nabla \times \boldsymbol{u}$, hence the equation governing the vorticity at all points within our flow is found by taking the curl of 2.6. Doing so yields,

$$\begin{aligned} 2\Omega \nabla \times (\hat{\boldsymbol{\Omega}} \times \boldsymbol{U}_0) &= -\nabla \times \nabla p + \nabla \times \alpha g T \boldsymbol{e}_g \\ &= \alpha g \nabla T \times \boldsymbol{e}_g. \end{aligned} \tag{2.7}$$

Now writing our temperature profile in terms of the buoyancy frequency, $\mathcal{N}^2$, and focusing on the y-component of 2.7, we have

$$2\Omega \mathcal{S} \sin \Lambda \boldsymbol{e}_y = \mathcal{N}^2 \boldsymbol{e}_\theta \times \boldsymbol{e}_g. \tag{2.8}$$

Written out explicitly, 2.8 becomes,

$$2\Omega \mathcal{S} \sin \Lambda = \mathcal{N}^2 \sin(\Gamma - \phi), \tag{2.9}$$

Λ	ϕ	Differential rotation profile	Baroclinic/barotropic?
0	-	$\Omega(\varpi)$ (cylindrical)	barotropic
$\pm 90°$	-	$\Omega(z)$ (axial variation only)	baroclinic
-	0	$\Omega(r)$ (spherical/shellular)	baroclinic except at $\Lambda = 0$
-	$\pm 90°$	$\Omega(\beta)$ (horizontal/latitudinal)	baroclinic
-	-	$\Omega(r, \beta)$ (arbitrary)	baroclinic in general

Table 2.1: Table of differential rotation profiles as Λ and ϕ are varied, where here β is latitude, z is distance along rotation axis, r is spherical radius and ϖ is cylindrical radius in this table.

our chosen form of the TWE.

The baroclinicity within the system can be conceptualized as the component of differential rotation along $\hat{\mathbf{\Omega}}$. The special case $\Lambda = 0$ locally signifies cylindrical differential rotation. In such a scenario the configuration is referred to as barotropic, implying surfaces of constant density and pressure are aligned, i.e., $\Gamma = \phi$. Conversely, if $\sin\Lambda \neq 0$, in general we have a misalignment between surfaces of constant density and pressure, resulting in Γ and ϕ being distinct, a baroclinic configuration. In the latter the rotation profile varies locally with both spherical radius and latitude. The extreme case $\sin\Lambda = 1$ implies Ω varies solely with distance along its axis, denoted by $\hat{\mathbf{\Omega}}$. When $\phi = 0$, we have a spherical or shellular differential rotation, for which Ω depends solely on the spherical radius. $\phi = \pm 90°$ signifies purely latitudinal differential rotation, where Ω depending solely on the latitude. These cases are summarized in Table 2.1. An illustration of the various angles relevant to our problem is also provided in Fig. 2.2.

2.4 Derivation of hydrodynamic dispersion relation

Determining the linear stability of a system requires we inspect the evolution of infinitesimal perturbations made to the background flow. We consider axisymmetric modes (with azimuthal wavenumbers $k_y = 0$) as these are likely to be the most unstable, and follow closely the methods in BJT2. Knobloch and Spruit (1982) argued that although non-axisymmetric baroclinic modes are unstable whenever surfaces of constant pressure and temperature are misaligned (at least with a rigid

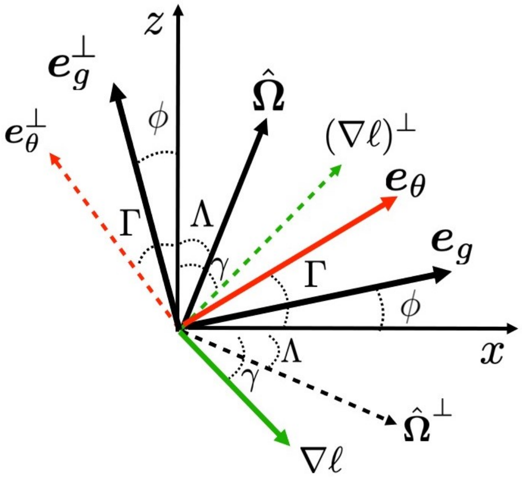

Figure 2.2: Illustration of the various vectors and corresponding angles in the (x, z)-plane as defined in the text. The cylindrical radial direction (along the equator) is along $\hat{\boldsymbol{\Omega}}^\perp$, and the rotation axis is along $\hat{\boldsymbol{\Omega}}$. The local radial direction is (approximately) along the effective gravity direction $\boldsymbol{e}_g$, with is misaligned with respect to the x direction when ϕ is nonzero.

boundary, as also found by Rashid et al., 2008), because the buoyancy frequency greatly exceeds the shear rate in most astrophysical situations, baroclinic modes will only be unstable for wavelengths larger than the stellar radius, which justifies our focus on axisymmetric modes. This section derives the dispersion relation in Knobloch (1982), and generalises that used in BJT1 and BJT2. This dispersion relation will then be used in Chapter 3 to both analytically and numerically explore the effects of varying ϕ on the linear stability of the system and the properties of the unstable modes.

We start by seeking solutions proportional to $\exp(\mathrm{i}k_x x + \mathrm{i}k_z z + st)$, where k_x and k_z are the real wavevector components in the x and z directions in the meridional plane. Recall in our model x is radial if $\phi = 0$, but more generally it is aligned with the angular velocity gradient (shear), rather than in the radial direction. We define the complex growth rate $s = \sigma + \mathrm{i}\omega$, where the growth (decay) rate $\sigma \in \mathbb{R}$ and the oscillation frequency $\omega \in \mathbb{R}$. Substituting this into our governing equations, and retaining only the terms that are linear in perturbation quantities (since higher order terms are very small), it's possible to write our system explicitly as,

$$su_x - 2\Omega u_y \cos\Lambda = -\mathrm{i}k_x p + \theta\cos\phi - \nu k^2 u_x, \tag{2.10}$$

$$su_y + 2\Omega\left(u_x\cos\Lambda - u_z\sin\Lambda\right) - \mathcal{S}u_x = -\nu k^2 u_y, \tag{2.11}$$

$$su_z + 2\Omega u_y \sin\Lambda = -\mathrm{i}k_z p + \theta\sin\phi - \nu k^2 u_z, \tag{2.12}$$

$$s\theta + \mathcal{N}^2\left(u_x\cos\Gamma + u_z\sin\Gamma\right) = -\kappa k^2\theta, \tag{2.13}$$

$$\mathrm{i}k_x u_x + \mathrm{i}k_z u_z = 0, \tag{2.14}$$

where $u_x = \Re[\hat{u}_x \exp(\mathrm{i}\boldsymbol{k}\cdot\boldsymbol{x})]$, and similarly for the other variables. We have dropped the hats for convenience so that all variables in Eqs. (2.10)–(2.14) represent the Fourier coefficients of each quantity. Introducing $s_\nu = s + \nu k^2$ and $s_\kappa = s + \kappa k^2$ into Eqs. (2.10)–(2.14) gives,

$$s_\nu u_x - 2\Omega u_y\cos\Lambda = -\mathrm{i}k_x p + \theta\cos\phi, \tag{2.15}$$

$$s_\nu u_y + 2\Omega\left(u_x\cos\Lambda - u_z\sin\Lambda\right) - \mathcal{S}u_x = 0, \tag{2.16}$$

$$s_\nu u_z + 2\Omega u_y\sin\Lambda = \theta\sin\phi - \mathrm{i}k_z p, \tag{2.17}$$

$$s_\kappa\theta + \mathcal{N}^2\left(u_x\cos\Gamma + u_z\sin\Gamma\right) = 0, \tag{2.18}$$

$$\mathrm{i}k_x u_x + \mathrm{i}k_z u_z = 0. \tag{2.19}$$

Solving 2.18 for θ yields,

$$\theta = -\frac{\mathcal{N}^2\left(u_x\cos\Gamma + u_z\sin\Gamma\right)}{s_\kappa}, \tag{2.20}$$

and rearranging 2.19 in terms of u_z, we have,

$$u_z = -\frac{k_x}{k_z}u_x. \tag{2.21}$$

Combining 2.20 with 2.21 allows us to eliminate any u_z-dependence so that,

$$\theta = -\frac{\mathcal{N}^2 \left(\cos\Gamma - \frac{k_x}{k_z}\sin\Gamma\right) u_x}{s_\kappa}. \tag{2.22}$$

We can calculate a succinct expression for p by taking the sum: $k_x\cdot(2.15) + k_z\cdot(2.16)$, so that,

$$\mathrm{i}k^2 p = -\left(k_x u_x + k_z u_z\right) s_\nu + 2\Omega u_y \left(\cos\Lambda k_x - \sin\Lambda k_z\right) + \left(\cos\phi k_x + \sin\phi k_z\right)\theta. \tag{2.23}$$

Then making use of 2.19 to eliminate u_z, it follows,

$$p = \frac{2\Omega u_y \left(\cos\Lambda k_x - \sin\Lambda k_z\right) + \left(\cos\phi k_x + \sin\phi k_z\right)\theta}{\mathrm{i}k^2}. \tag{2.24}$$

We may now use 2.16 in conjunction with 2.19 to obtain,

$$u_y = \frac{\left(\mathcal{S} - 2\Omega\left(\cos\Lambda + \frac{k_x}{k_z}\sin\Lambda\right)\right) u_x}{s_\nu}, \tag{2.25}$$

then combining this with 2.24 yields,

$$p = \frac{\left(2\mathcal{S}\Omega - 4\Omega^2\left(c_\Lambda + \frac{k_x}{k_z}s_\Lambda\right)\right)\left(c_\Lambda k_x - s_\Lambda k_z\right) s_\kappa - \mathcal{N}^2 s_\nu \left(c_\phi k_x + s_\phi k_z\right)\left(c_\Gamma + \frac{k_x}{k_z}s_\Gamma\right)}{\mathrm{i}s_\kappa s_\nu k^2} u_x. \tag{2.26}$$

The final step is to eliminate u_x by combining the expressions for θ, u_y, and p in the x-component of the momentum equation. This gives,

$$s_\nu^2 s_\kappa + a s_\kappa + b s_\nu = 0, \tag{2.27}$$

where

$$a = \frac{2\Omega}{k^2}\left(2\Omega k_x s_\Lambda + \left(2\Omega c_\Lambda - \mathcal{S}\right) k_z\right)\left(c_\Lambda k_x + s_\Lambda k_z\right), \tag{2.28}$$

and

$$b = \frac{\mathcal{N}^2}{k^2}\left(k_z c_\Gamma - k_x s_\Gamma\right)\left(k_z c_\phi - k_x s_\phi\right). \tag{2.29}$$

Note that in the above and throughout we use c_Λ and s_Λ to refer to $\cos\Lambda$ and $\sin\Lambda$ for brevity, and similarly for trigonometric functions with other arguments. We also define the local specific AM gradient

$$\nabla\ell = \nabla\left(\varpi^2\Omega\right) = \varpi\left(2\Omega c_\Lambda - \mathcal{S}, 0, -2\Omega s_\Lambda\right), = |\nabla\ell|\left(c_\gamma, 0, -s_\gamma\right), \tag{2.30}$$

which has magnitude

$$|\nabla\ell|^2 = \varpi^2\left(\mathcal{S}^2 + 4\Omega\left(\Omega - \mathcal{S}c_\Lambda\right)\right). \tag{2.31}$$

The normal to the local angular momentum gradient is then

$$(\nabla\ell)^\perp = \varpi\left(2\Omega s_\Lambda, 0, 2\Omega c_\Lambda - \mathcal{S}\right) = |\nabla\ell|\left(s_\gamma, 0, c_\gamma\right). \tag{2.32}$$

The vector perpendicular to the effective gravity is

$$\boldsymbol{e}_g^\perp = \left(-s_\phi, 0, c_\phi\right), \tag{2.33}$$

and the normal to stratification surfaces

$$\boldsymbol{e}_\theta^\perp = \left(-s_\Gamma, 0, c_\Gamma\right). \tag{2.34}$$

The equatorial direction is defined locally as

$$\hat{\boldsymbol{\Omega}}^\perp = \left(c_\Lambda, 0, -s_\Lambda\right), \tag{2.35}$$

meaning the shear along the rotation axis is

$$\hat{\boldsymbol{\Omega}} \cdot (\nabla\ell) = \varpi\left(\left(2\Omega c_\Lambda - \mathcal{S}\right)s_\Lambda - 2\Omega s_\Lambda c_\Lambda\right) = -\mathcal{S}\varpi s_\Lambda \tag{2.36}$$

$$= |\nabla\ell|(s_\Lambda c_\gamma - s_\gamma c_\Lambda) = -|\nabla\ell| s_{\gamma-\Lambda}. \tag{2.37}$$

Hence, the angle between the rotation axis and local angular momentum gradient is $\cos^{-1}\left(-\frac{\mathcal{S}\varpi s_\Lambda}{|\nabla\ell|}\right)$. It will also be helpful to define a modified Richardson number,

$$\mathrm{R} = \frac{\mathcal{N}^2\varpi}{2\Omega|\nabla\ell|}, \tag{2.38}$$

which can be thought of as a comparison between the stabilising effects of the stratification against the destabilising effects from the angular momentum gradient (Knobloch & Spruit, 1982). We also have

$$\varpi\mathcal{S}s_\Lambda = -|\nabla\ell|s_{\gamma-\Lambda}. \tag{2.39}$$

This means that, with some rearranging, the thermal wind equation (Eq. 2.9) can be written as

$$\frac{2\Omega|\nabla\ell|}{\varpi}s_{\gamma-\Lambda} = \mathcal{N}^2 s_{\Gamma-\phi}, \tag{2.40}$$

or in the form

$$s_{\gamma-\Lambda} = \mathrm{R}s_{\Gamma-\phi}. \tag{2.41}$$

2.5 Summary

This section establishes the theoretical framework within which the research in Chapter 3 is conducted, and which we will build upon through the introduction of a poloidal magnetic field in Chapter 5. We began by discussing both global and local modeling approaches, exploring their respective advantages and limitations, as well as providing examples of problems suitable for each approach. We then introduced a local Cartesian box model for simulating a stably stratified region of a differentially rotating star.

We introduced ϕ, which characterizes the angle between effective gravity and the local angular velocity gradient, allowing for the local study of general differential rotation profiles (as explored to some extent in Knobloch & Spruit, 1982).

The validity and utility of the Boussinesq approximation for local instabilities is then examined. This approximation enables us to linearise the ideal gas law and reduce the mass conservation equation to a simple incompressibility condition.

Following this, we addressed the role of the TWE in governing the misalignment between surfaces of constant pressure and density, and considered how this allows us to eliminate Γ as a variable. We then derived a modified version of the TWE which includes the angle ϕ.

Our focus on axisymmetric modes was justified by the expectation that these modes would be the most unstable in real systems, influenced by the effect of realistic values of $\mathcal{N}^2$ on their wavelengths. A detailed derivation of the hydrodynamic dispersion relation was then presented.

We concluded by defining additional vectors and parameters that would later be key to our research. Overall, Chapter 2 set the stage for the subsequent detailed exploration and analysis of the linear and nonlinear behaviour of the system.

Chapter 3

Local linear stability of arbitrary differential rotation profiles

3.1 Introduction

Next we shall examine in detail the linear stability of generalised differential rotation profiles in stably stratified radiative regions, using the modelling approach discussed in Chapter 2. We begin with the non-diffusive (adiabatic) case, where $\nu = \kappa = 0$, and derive the corresponding stability criteria. A similar analysis is then performed for the $\nu \neq 0, \kappa \neq 0$ case, as well as for the oscillatory case where the real part of the growth rate is nearly zero, leading to weakly growing gravity waves.

The following work builds upon initial studies conducted by Knobloch (1982), who identified many of the same instability criteria for the standard cases. Their choice to work in a cylindrical geometry and their selection of parameters led to visual differences between criteria; however, we have verified that these are equivalent with the correct conversions.

Subsequently, we analyse several asymptotic limits of interest, including infinite thermal diffusivity and strong stratification. This exploration is followed by various numerical visualizations, including a selection of 'lobe' plots in Fourier space demonstrating the strength and orientation of the unstable modes for a range of ϕ at a fixed Λ. The maximum growth rates as a function of ϕ for both the adiabatic and diffusive regimes are also calculated here at various latitudes. Noting that we define a perturbation wavevector $\boldsymbol{k} = k(\cos\theta_k, 0, -\sin\theta_k)$, we present each case alongside a selection of figures characterising k and θ_k against ϕ for the corresponding dominant mode, as well as the critical shear necessary for the onset of instability at each latitude.

3.2 Non-diffusive stability

Physical systems such as stably stratified radiative regions can host several different instabilities depending on the parameter regime. Whilst our primary focus is on the GSF instability, which indeed relies on diffusion, studying the diffusion-free case allows us to identify when the diffusive system is really operating due to diffusion (in which case we refer to these as "secular instabilities") or if instead we are observing a dynamical instability that would operate without the presence of diffusion. In particular we expect to observe a stably stratified variation of the centrifugal instability discussed in Chapter 1.

To inspect the non-diffusive case we take $\nu = \kappa = 0$, reducing 2.27 to

$$s^2 = -\left(a + b\right). \tag{3.1}$$

For stability we require the real component of the growth rate $\sigma \leq 0$. Since a and b are real, this implies the flow is stable whenever

$$a + b > 0, \tag{3.2}$$

$$\implies \frac{2}{\bar{\varpi}}\left(\hat{\boldsymbol{k}} \cdot \boldsymbol{\Omega}\right)\left(\hat{\boldsymbol{k}} \cdot (\nabla\ell)^{\perp}\right) + \mathcal{N}^2\left(\hat{\boldsymbol{k}} \cdot \boldsymbol{e}_{\theta}^{\perp}\right)\left(\hat{\boldsymbol{k}} \cdot \boldsymbol{e}_{g}^{\perp}\right) > 0, \tag{3.3}$$

$$\implies \left(k_x s_\Lambda + k_z c_\Lambda\right)\left(k_x s_\gamma + k_z c_\gamma\right) + \mathrm{R}\left(k_x s_\Gamma - k_z c_\Gamma\right)\left(k_x s_\phi - k_z c_\phi\right) > 0. \tag{3.4}$$

Finding a stability criterion requires us to eliminate any dependence on $\boldsymbol{k}$, which can be done by dividing by k_z and defining a quantity $q = k_x/k_z$, which gives:

$$\left(q s_\Lambda + c_\Lambda\right)\left(q s_\gamma + c_\gamma\right) + \mathrm{R}\left(q s_\Gamma - c_\Gamma\right)\left(q s_\phi - c_\phi\right) > 0. \tag{3.5}$$

Rewriting it in the form of a quadratic equation yields:

$$q^2\left(s_\Lambda s_\gamma + \mathrm{R} s_\Gamma s_\phi\right) + q\left(s_{\Lambda+\gamma} - \mathrm{R} s_{\Gamma+\phi}\right) + \left(c_\Lambda c_\gamma + \mathrm{R} c_\Gamma c_\phi\right) > 0. \tag{3.6}$$

Eq. 3.6 holds when the quadratic on the LHS has no real roots. Via use of the discriminant, this is equivalent to,

$$\left(s_{\Lambda+\gamma} - \mathrm{R} s_{\Gamma+\phi}\right)^2 - 4\left(s_\Lambda s_\gamma + \mathrm{R} s_\Gamma s_\phi\right)\left(c_\Lambda c_\gamma + \mathrm{R} c_\Gamma c_\phi\right) < 0. \tag{3.7}$$

We're now in a position to use the thermal wind equation in the form, $s_{\gamma-\Lambda} = \mathrm{R} s_{\Gamma-\phi}$, to eliminate R. Doing so we obtain:

$$\left(s_{\Lambda+\gamma} - \left(\frac{s_{\gamma-\Lambda}}{s_{\Gamma-\phi}}\right) s_{\Gamma+\phi}\right)^2 - 4\left(s_\Lambda s_\gamma + \left(\frac{s_{\gamma-\Lambda}}{s_{\Gamma-\phi}}\right) s_\Gamma s_\phi\right)\left(c_\Lambda c_\gamma + \left(\frac{s_{\gamma-\Lambda}}{s_{\Gamma-\phi}}\right) c_\Gamma c_\phi\right) < 0, \tag{3.8}$$

subsequently multiplying through by $s^2_{\Gamma-\phi}$ and simplifying leads to

$$s^2_{\Gamma-\phi}\left(2 s_\Lambda c_\gamma\right)^2 - 4\left(s_{\Gamma-\phi} s_\Lambda s_\gamma + s_{\gamma-\Lambda} s_\Gamma s_\phi\right)\left(s_{\Gamma-\phi} c_\Lambda c_\gamma + s_{\gamma-\Lambda} c_\Gamma c_\phi\right) < 0, \tag{3.9}$$

which can then be rewritten to form the criterion

$$-\frac{s_{\gamma+\Gamma} s_{\gamma-\Lambda} s_{\Lambda+\phi}}{s_{\Gamma-\phi}} < 0. \tag{3.10}$$

Using TWE this implies $-R s_{\gamma+\Gamma} s_{\Lambda+\phi} < 0$, or equivalently $\nabla\ell\cdot\boldsymbol{e}_\theta^\perp < 0$ when $\Lambda+\phi > 0$ and $\nabla\ell\cdot\boldsymbol{e}_\theta^\perp > 0$ when $\Lambda+\phi < 0$. Together, these are equivalent to the Solberg-Høiland conditions (or Rayleigh criteria) discussed in Chapter 1.

3.3 Diffusive instabilities

3.3.1 Steady modes

As previously mentioned the effects of viscous and thermal diffusion, $\nu \neq 0$ and $\kappa \neq 0$, can relax the stabilising effects of gravitational buoyancy, allowing the GSF instability to operate under conditions that would otherwise be stable. We start by noting that when the constant term in 2.27 is negative, we will have instability, since this requires a real positive s. The criterion for instability can then be written,

$$\nu^2 \kappa \left(k^2\right)^3 + a\kappa k^2 + b\nu k^2 < 0, \tag{3.11}$$

dividing through by κk^2 (note $\kappa k^2 > 0$) and writing $\mathrm{Pr} = \nu/\kappa$, we have

$$a + \mathrm{Pr} b + \nu^2 k^4 < 0. \tag{3.12}$$

If we seek diffusive instability when there is non-diffusive stability at small Pr, the classic GSF situation, we have to satisfy 3.12 with $a + b > 0$. This requires $b > 0$ and

$$a < 0, \tag{3.13}$$

so this is a necessary condition for instability. To obtain a sufficient condition for stability we follow a similar approach to that used in the non-diffusive case. Expanding a and b results in,

$$\frac{2}{\bar{\omega}} \left(\hat{\boldsymbol{k}} \cdot \boldsymbol{\Omega}\right) \left(\hat{\boldsymbol{k}} \cdot (\nabla \ell)^{\perp}\right) + \mathrm{Pr} \mathcal{N}^2 \left(\hat{\boldsymbol{k}} \cdot \boldsymbol{e}_{\theta}^{\perp}\right) \left(\hat{\boldsymbol{k}} \cdot \boldsymbol{e}_{g}^{\perp}\right) + \nu^2 k^4 < 0, \tag{3.14}$$

$$\implies \left(k_x s_\Lambda + k_z c_\Lambda\right)\left(k_x s_\gamma + k_z c_\gamma\right) + \mathrm{Pr} \mathrm{R} \left(k_x s_\Gamma - k_z c_\Gamma\right)\left(k_x s_\phi - k_z c_\phi\right) + \nu^2 k^4 < 0. \tag{3.15}$$

We divide by k_z and again define $q = k_x/k_z$, noting that $\nu^2 \kappa^4$ is always positive so only ever acts to stabilise the system, and thus may be ignored. This leads to

$$\left(q s_\Lambda + c_\Lambda\right)\left(q s_\gamma + c_\gamma\right) + \mathrm{Pr} \mathrm{R} \left(q s_\Gamma - c_\Gamma\right)\left(q s_\phi - c_\phi\right) < 0, \tag{3.16}$$

or equivalently

$$q^2 \left(s_\Lambda s_\gamma + \mathrm{PrR} s_\Gamma s_\phi \right) + q \left(s_{\Lambda+\gamma} - \mathrm{PrR} s_{\Gamma+\phi} \right) + \left(c_\Lambda c_\gamma + \mathrm{PrR} c_\Gamma c_\phi \right) < 0. \tag{3.17}$$

We are again in a suitable position to use the properties of the discriminant to find a criterion independent of $\boldsymbol{k}$, namely,

$$\left(s_{\Lambda+\gamma} - \mathrm{PrR} s_{\Gamma+\phi} \right)^2 - 4 \left(s_\Lambda s_\gamma + \mathrm{PrR} s_\Gamma s_\phi \right) \left(c_\Lambda c_\gamma + \mathrm{PrR} c_\Gamma c_\phi \right) > 0. \tag{3.18}$$

In the limit of strong stratification, surfaces of constant pressure and density align and Eq. 2.9 implies $\Gamma \to \phi$. This simplifies 3.18 as follows,

$$\begin{aligned} \left(s_{\Lambda+\gamma} - \mathrm{PrR} s_{2\phi} \right)^2 - 4 \left(s_\Lambda s_\gamma + \mathrm{PrR} s_\phi^2 \right) \left(c_\Lambda c_\gamma + \mathrm{PrR} c_\phi^2 \right) > 0, \\ s_{\Lambda-\gamma}^2 - 4 \mathrm{PrR} s_{\phi+\Lambda} s_{\phi+\gamma} > 0, \end{aligned}$$

leading to (cf Eq.2.30 of Knobloch, 1982),

$$\mathrm{RPr} < \frac{s_{\Lambda-\gamma}^2}{4 s_{\phi+\Lambda} s_{\phi+\gamma}}. \tag{3.19}$$

Noting that $\mathrm{R} = \mathrm{Ri}(s_{\gamma-\Lambda}^2/(s_\gamma s_\Lambda))$, 3.19 can be written in terms of the usual Richardson number as,

$$\mathrm{RiPr} < \frac{s_\gamma s_\Lambda}{4 s_{\phi+\Lambda} s_{\phi+\gamma}}, \tag{3.20}$$

which must be satisfied for instability. This criterion reduces to $\mathrm{RiPr} < 1/4$ for onset of instability when $\phi \to 0$ (shellular differential rotation; BJT2). However, 3.20 shows that instability is possible for weaker differential rotation than for $\phi = 0$.

The growth rate in the limit of small Pr where the instability is strongly driven (but adiabatically stable) can be determined by considering the limit $\mathrm{RiPr} \to 0$ as $\mathrm{Pr} \to 0$. In this regime, we find $s = \sqrt{-a}$, and hence both the maximum growth rate and the wedge angle of instability in the (k_x, k_z)-plane are independent of ϕ for fixed Λ. In reality though, we are usually interested in a fixed latitude $\Lambda + \phi$, in which case the growth rate and unstable wedge angles do depend on ϕ, being maximised for mixed radial and horizontal shears rather than purely radial ones. In this regime, the maximum growth rate and wave-vector magnitude can be predicted from Eq.43-44 of BJT2, which we reproduce here:

$$s^2 = \frac{2\Omega|\nabla\ell|}{\varpi}\sin^2\left(\frac{1}{2}(\gamma-\Lambda)\right), \tag{3.21}$$

$$k^4 = \frac{1}{2d^4}\sin^2\left(\frac{\gamma+\Lambda}{2}\right). \tag{3.22}$$

These will be plotted later in Fig. 3.3 for $S = 2$ as a function of ϕ for various latitudes $\Lambda+\phi$. On the other hand, if $\mathrm{RiPr} = O(1)$ as $\mathrm{Pr} \to 0$, the growth rate and unstable wedge may depend on ϕ for a fixed Λ; this case is studied in A.

3.3.2 Oscillatory modes

Our cubic dispersion relation Eq. 2.27 also allows oscillatory instabilities, for which $s = \sigma + \mathrm{i}\omega$ and $\omega \neq 0$ at onset. These are essentially weakly destabilised inertia-gravity waves gaining energy from the differential rotation or baroclinicity. To derive a criterion for onset ($\sigma = 0$) we substitute $s = \mathrm{i}\omega$ into Eq. 2.27, consider the limit of strong stratification for which the TWE implies $\Gamma \to \phi$, neglect terms with higher powers of k (following Knobloch, 1982), and equate real and imaginary parts to obtain:

$$\begin{aligned}-\omega^2(1+2\mathrm{Pr})\left(1+q^2\right)+2\Omega\frac{|\nabla\ell|}{\varpi}(c_\gamma+qs_\gamma)(c_\Lambda+qs_\Lambda)&\\ +\mathcal{N}^2\mathrm{Pr}(c_\phi-qs_\phi)^2=0,&\end{aligned} \tag{3.23}$$

$$\begin{aligned}\omega\Big(-\omega^2\left(1+q^2\right)+2\Omega\frac{|\nabla\ell|}{\varpi}(c_\gamma+qs_\gamma)(c_\Lambda+qs_\Lambda)&\\ +\mathcal{N}^2(c_\phi-qs_\phi)^2\Big)=0.&\end{aligned} \tag{3.24}$$

Since we are looking for oscillatory instabilities, we omit the solution with $\omega = 0$, thus we can combine the above to eliminate ω^2, giving the quadratic

$$\mathrm{Pr}\left(c_\gamma + q s_\gamma\right)\left(c_\Lambda + q s_\Lambda\right) + \mathrm{R}\left(1+\mathrm{Pr}\right)\left(c_\phi - q s_\phi\right)^2 = 0. \tag{3.25}$$

We require a positive discriminant, so that

$$\mathrm{R} < \frac{\mathrm{Pr}}{2\left(1+\mathrm{Pr}\right)} \frac{s^2_{\Lambda-\gamma}}{s_{\phi+\Lambda} s_{\phi+\gamma}}, \tag{3.26}$$

for oscillatory instability to onset (cf Eq.2.32 of Knobloch, 1982). Equivalently,

$$\mathrm{Ri} < \frac{\mathrm{Pr}}{2\left(1+\mathrm{Pr}\right)} \frac{s_\gamma s_\Lambda}{s_{\phi+\Lambda} s_{\phi+\gamma}}. \tag{3.27}$$

This can be contrasted with Eq. 3.20 for direct instability (steady modes with $\omega = 0$). The ratio of the quantity RiPr predicted by Eq. 3.20 to that from Eq. 3.27 is

$$\frac{(1+\mathrm{Pr})}{2\mathrm{Pr}^2} \to \infty \quad \text{as } \mathrm{Pr} \to 0. \tag{3.28}$$

Hence, GSF instability occurs first as a direct instability at onset for small Pr (in agreement with Knobloch, 1982), since oscillatory instability requires a much smaller value of RiPr.

To determine the properties of the modes at onset in the limit Pr $\to$ 0 (and RPr$\to$ 0), we can solve Eqs. 3.23 and 3.24 to obtain a preferred wavevector orientation and squared frequency

$$q = \cot\phi, \tag{3.29}$$

$$\omega^2 = \frac{2\Omega|\nabla\ell|}{\varpi} s_{\gamma+\phi} s_{\Lambda+\phi}. \tag{3.30}$$

The first result implies that the waves have wavevectors $\boldsymbol{k}$ that lie approximately along $\boldsymbol{e}_g$. We will shortly see that we have numerically determined that these modes lie between $\boldsymbol{e}_g$ and $\boldsymbol{e}_\theta$ and that they always have smaller growth rates than the fastest growing direct GSF instability.

3.4 Numerical analysis of the linear theory

In addition to analysing the dispersion relation analytically, here we solve it numerically to illustrate the nature of the instabilities that operate for certain sets of parameters. Throughout this section and the remainder of this thesis, we will take our 'standard' set of parameters to be $S = 2$, $N^2 = 10$, and $\mathrm{Pr} = 10^{-2}$ to allow a direct comparison with BJT1 and BJT2. This choice of values was originally motivated by them being in a regime that is readily computationally accessible using nonlinear simulations (see Chapter 4). Note that in the solar tachocline $S < 2$, $N^2 > 10$ and $\mathrm{Pr} < 10^{-2}$.

To better understand the spatial characteristics of the instability, a selection of 'lobe' figures, as seen in Fig. 3.1, have been made. These illustrate the base 10 logarithm of the growth rate σ obtained by solving Eq.2.27 on the (k_x, k_z)-plane for axisymmetric instabilities. In the majority of our investigations, we fix the latitude $\Lambda + \phi$. We then vary ϕ (and consequently Λ) to probe the effects of shear orientation on the linear instability. Additional cases, including fixing $\Lambda = 60°$ are also presented. In these figures we also plot the vectors $\hat{\boldsymbol{\Omega}}^{\perp}$ and $\nabla\ell$ as the solid red lines. These lines delineate the wedge within which $a < 0$ and GSF-unstable modes are expected. We also plot the vectors $\boldsymbol{e}_g$ and $\boldsymbol{e}_\theta$ as the light blue lines, and the wedge between them is where $b < 0$; this is where oscillatory modes can be found. The angles of the red and blue lines can be found from Table 3.1 and Figure 2.2.

The main feature seen in all of these plots are "primary lobes" corresponding to either the diffusive GSF instability, or to the adiabatic instability when Eq. 3.10 is violated. These lobes contain (directly) unstable modes (with $\omega = 0$) and have a preferred wavevector orientation lying between the AM gradient $\nabla\ell$, and the line perpendicular to the rotation axis $\hat{\boldsymbol{\Omega}}^{\perp}$. Since $\mathcal{S} \sim \Omega$ and given that our unit of time is Ω^{-1}, the fastest growing modes have growth rates $O(1)$ and are observed to lie along the line that is approximately half-way between these two vectors (as predicted by 3.21). Note that this wedge is perpendicular to the physical wedge

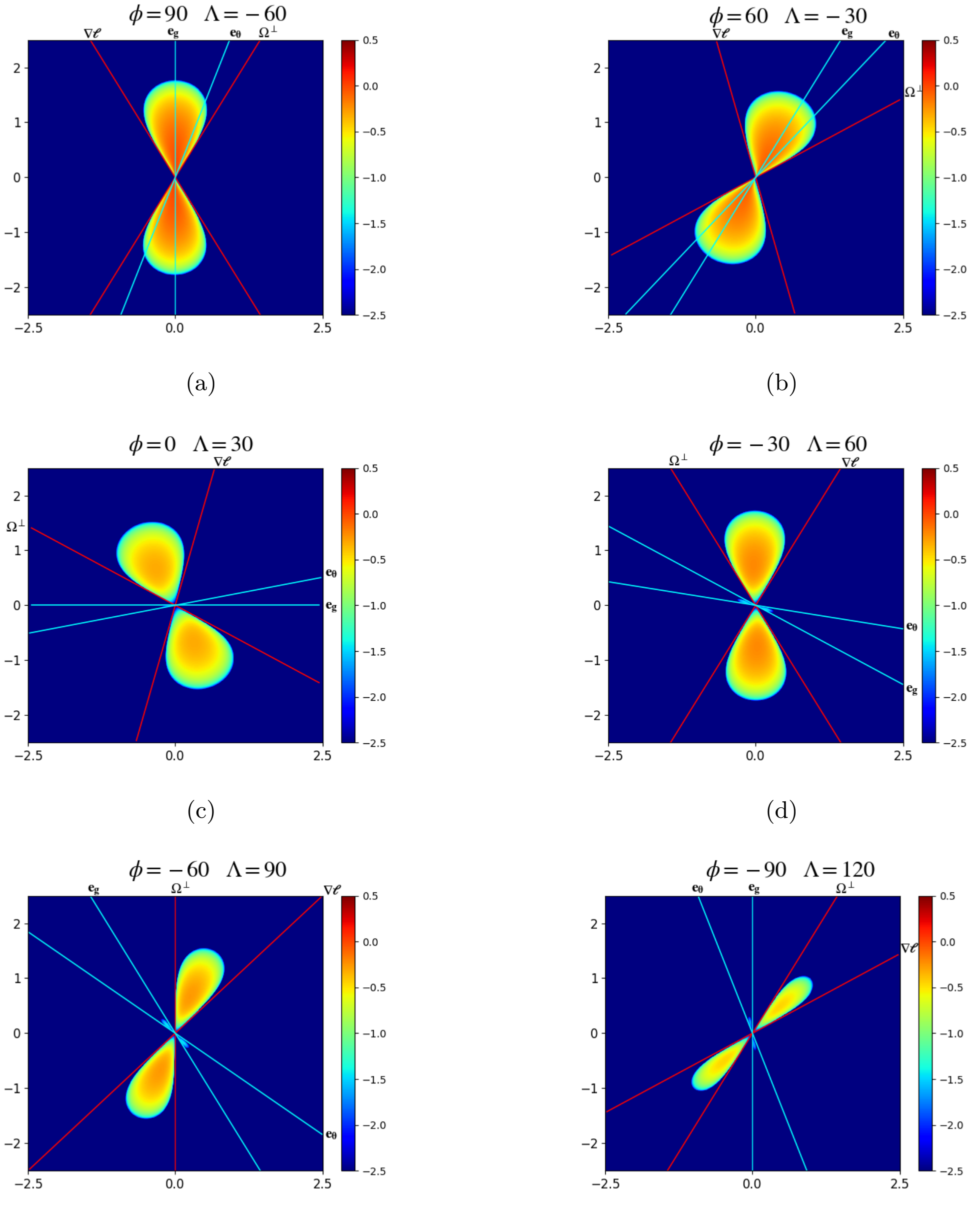

(a) (b) (c) (d) (e) (f)

Figure 3.1: Figures of linear growth rate $\log_{10}(\sigma/\Omega)$ for the axisymmetric GSF (or adiabatic) instability for various ϕ on the (k_x, k_z)-plane for $\mathcal{N}^2/\Omega^2 = 10$, Pr$= 10^{-2}$, $\mathcal{S}/\Omega = 2$, at a fixed latitude $\Lambda + \phi = 30°$. Here we vary ϕ in multiples of 30° from $-90°$ to $90°$. GSF (or adiabatically) unstable modes are contained within the wedge bounded by the two vectors $\hat{\mathbf{\Omega}}^\perp$ and $\nabla\ell$ (red lines). Note that panels (a) and (b) are adiabatically unstable according to Eq. 3.10. We also observe a smaller wedge outside this region in panels (d), (e) and (f) containing weakly growing oscillatory modes which are bounded by the light blue lines. The fastest growing modes (darkest red) in adiabatically unstable cases occur for $k \to 0$ suggesting that the presence of diffusion leads to the preference of the largest possible wavelengths in this regime. This is in comparison to the GSF cases where the darkest areas have a non-zero wavenumber and hence a preferred wavelength in real space.

within which the GSF (or adiabatically) unstable mode displacements (and velocity perturbations) arise due to the incompressibility condition $\boldsymbol{k} \cdot \boldsymbol{u} = 0$. Hence, these modes have flows/displacements lying between the rotation axis and surfaces of constant AM.

We observed in Fig. 3.1 that the orientation of the primary lobes and the maximum growth rates at a fixed latitude $\Lambda + \phi = 30^\circ$ depend strongly on ϕ. In particular, we observe the fastest growth (and the widest primary lobes) at this latitude for $\phi \in [60^\circ, 90^\circ]$, which are adiabatically unstable according to Eq. 3.10 (see also panel (b) in Fig. 3.3 that displays the maximum growth rate vs ϕ). For adiabatically stable but GSF unstable cases, here for $\phi < 30^\circ$, we observe somewhat slower growth (but still $O(1)$) and lobes that narrow as $\phi \to -90^\circ$. The fastest growing modes (darkest red) in adiabatically unstable cases occur for $|\boldsymbol{k}| = k \to 0$, suggesting that with the presence of diffusion the dominant modes grow on the largest possible wavelengths (without diffusion these modes do not have a preferred wavevector magnitude k, only a preferred wavevector orientation). This is in comparison to the GSF cases where the darkest areas have a unique non-zero wavenumber, and hence a preferred wavelength in real space.

On the other hand, we have observed that for a fixed Λ, varying ϕ alone does not change the orientation or sizes of the primary lobes, but it does modify the maximum growth rates, with cases with horizontal shears for $\phi \sim 90^\circ$ exhibiting faster growth than radial shears with $\phi \sim 0^\circ$. This result might be expected because radial motions will be inhibited to a greater extent by the stable stratification than latitudinal displacements. Decreasing Pr to a smaller, more realistic, value substantially increases the size of the primary lobes for a given RiPr. This result holds even in the presence of a more realistic and much larger buoyancy frequency (not shown) as the key parameter for diffusive instability is RiPr.

We additionally note the appearance in Fig. 3.1 (and Fig. 3.2) of two further, but much smaller "secondary lobes", which are barely visible when $\phi = 0$ and were not previously identified by BJT2 owing to the wavenumber resolution and colour-

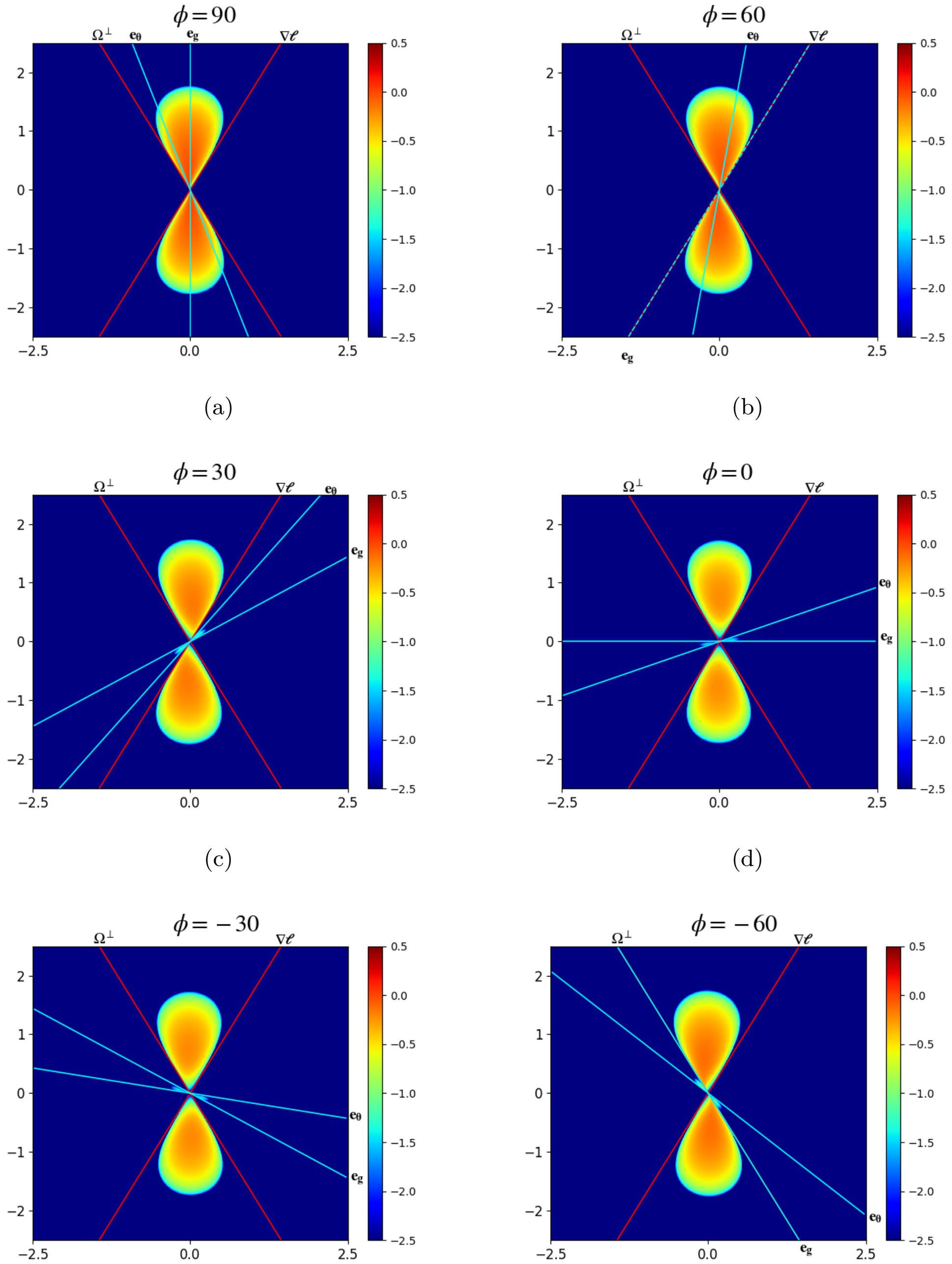

(a) (b)

(c) (d)

(e) (f)

Figure 3.2: Figures of linear growth rate $\log_{10}(\sigma/\Omega)$ for the axisymmetric GSF (or adiabatic) instability for various ϕ on the (k_x, k_z)-plane for $\mathcal{N}^2/\Omega^2 = 10$, Pr$= 10^{-2}$, $\mathcal{S}/\Omega = 2$, with $\Lambda = 60°$ fixed. Here we vary ϕ in multiples of 30° from $-90°$ to $60°$. GSF (or adiabatically) unstable modes are contained within the wedge bounded by the two vectors $\hat{\mathbf{\Omega}}^\perp$ and $\nabla\ell$. We also observe two secondary lobes outside the primary one. While the primary lobe is fixed in orientation, the strength and orientation of secondary modes depends on ϕ and are only present when we are adiabatically stable.

scale adopted for their figures. These lobes are most visible here for $\phi = -30°$ and $\phi = -90°$, and correspond to the oscillatory ($\omega \neq 0$) axisymmetric baroclinic instabilities that can develop in this system (McIntyre, 1970; Knobloch, 1982; Labarbe & Kirillov, 2021; Le Bars, 2021). These are oscillatory modes – noted in section 3.3.2 as essentially weakly excited inertia-gravity waves – in contrast to the usual GSF (or adiabatic) instability that onsets as a direct instability within the primary lobes. The smaller secondary lobes are likely to be overpowered by the GSF instability in stellar interiors (see § 3.3.2), as their maximum growth rates are generally much smaller than the primary lobes for $\mathrm{Pr} \ll 1$, however they could potentially become important in the presence of strong chemical gradients where there are stricter criteria for instability (Knobloch & Spruit, 1982).

3.4.1 Properties of the fastest growing modes

The next set of figures we present are a selection illustrating how the maximum linear growth rates and wavenumber magnitudes vary with ϕ. We show results for both the GSF instability (black) and the adiabatic instability (red) by solving the dispersion relations directly, as well as the growth rate in the asymptotic limits as $\mathrm{RiPr} \to 0$ (green; based on Eq. 3.21) and $\mathrm{RiPr} \sim O(1)$ (blue; based on Appendix A.2, Eqs. A.18 and A.19). In Fig. 3.3, we plot the growth rate of a given instability against ϕ (in the full range between ±180°), whilst keeping the latitude $\Lambda + \phi$ fixed, and setting $S = 2$, $N^2 = 10$, $\mathrm{Pr} = 10^{-2}$.

At the equator (where $\phi + \Lambda = 0$), $\phi = 0$ is marginally stable with $\mathcal{S} = 2$, corresponding to Rayleigh stability (Chandrasekhar, 1961). This is also true for any case where ϕ is such that $\Lambda = 0$, which corresponds with cylindrical differential rotation ($\Omega(\varpi)$ only) which is neutrally stable for $\mathcal{S} = 2$ (constant angular momentum as a function of cylindrical radius ϖ). Interestingly, we see that the effects of varying ϕ are symmetric about zero at the equator, and there is no adiabatic instability in this case. The fastest growing instability occurs for mixed radial/latitudinal shears with $\phi \sim 60°$, rather than purely latitudinal shears with $\phi \sim 90°$, which is intu-

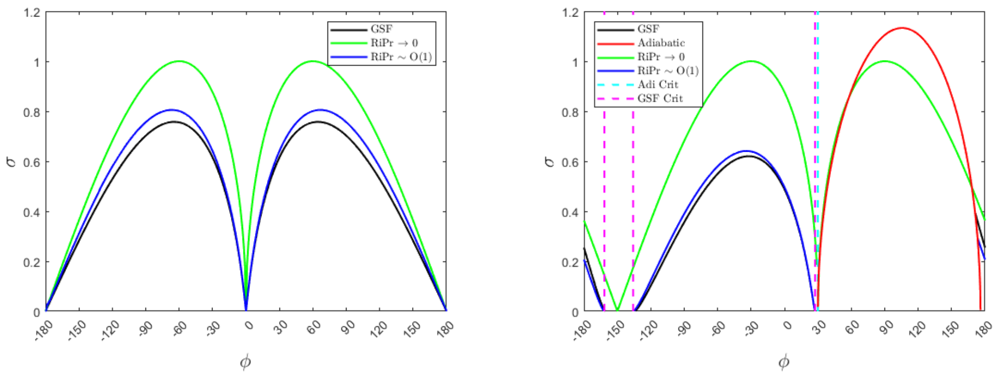

(a) Latitude $\Lambda + \phi = 0°$

(b) Latitude $\Lambda + \phi = 30°$

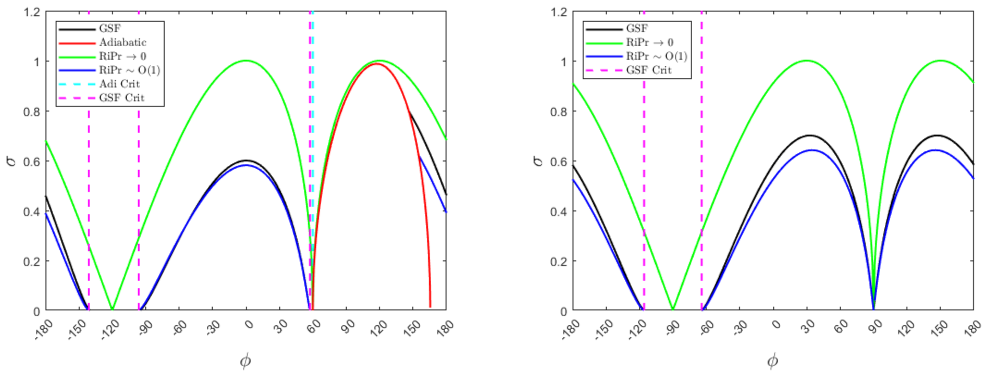

(c) Latitude $\Lambda + \phi = 60°$

(d) Latitude $\Lambda + \phi = 90°$

Figure 3.3: A selection of figures comparing the maximum linear growth rates in both the adiabatic (red) and diffusive (black) regimes for $S = 2, \mathrm{Pr} = 10^{-2}, N^2 = 10$. The light blue dashed line corresponds to the critical ϕ for onset of adiabatic instability predicted by Eq. 3.10. Onset of GSF instability as predicted by Eq. 3.20 is shown as magenta dashed lines. Predictions for the growth rate in the limits assuming $\mathrm{RiPr} \sim O(1)$ and $\mathrm{RiPr} \to 0$ are shown as the blue and green lines, respectively.

itively surprising. We observe the growth rate to be in very good agreement with the prediction from the asymptotic limit as $\mathrm{RiPr} \sim O(1)$, but it is smaller than the "upper bound" predicted by considering its evaluation in the limit as $\mathrm{RiPr} \to 0$.

Moving away from the equator, at $\phi + \Lambda = 30°$ latitude we again see the expected marginal stability when $\phi \sim 30°$, but we also observe onset of adiabatic instability between $\phi = 30°$ and $\phi = 90°$. Only diffusive instability is observed for $\phi < 30°$, but adiabatic instability dominates instead when $\phi > 30°$, which typically has a larger growth rate than GSF unstable modes. The transition between diffusive and adiabatic instability is given by the dashed blue line, which shows the critical value of

ϕ predicted by Eq. 3.10, and the magenta dashed lines indicate the bounds for GSF instability given by Eq. 3.20. These are in excellent agreement with our numerical results. Note that there is a tiny nonzero range of ϕ for which neither instability occurs near $\phi \sim 30^\circ$ between the magenta and light blue dashed lines. This is a finite Pr effect due to viscosity, which is not present in the RiPr $\to 0$ prediction (in green; that matches the light blue dashed line). We observe that the numerically-computed growth rate of the GSF instability from directly solving the cubic (black) is again in very good agreement with the prediction from the asymptotic limit as RiPr $\sim O(1)$, and is somewhat smaller than the prediction valid when RiPr $\to 0$. The latter case also occurs for a wider range of ϕ, namely $-161.6^\circ \lesssim \phi \lesssim -135.8^\circ$ which is stable for the black and blue curves. One subtle feature of this case is the change of dominant mode for $\phi \sim 175^\circ$ where the black, blue, and green lines all dominate over the adiabatic instability.

The 60° latitude case shows similar behaviour to the 30° latitude case, except that marginal stability for adiabatic instability now occurs at $\phi \sim 60^\circ$. However, here the RiPr $\to 0$ curve always produces the largest growth rates, and, in comparison to $\phi + \Lambda = 30^\circ$, there is an extended region $\phi \gtrsim 150^\circ$ where the GSF curve dominates over the adiabatic one. At the pole ($\Lambda + \phi = 90^\circ$), we firstly see that the system is stable to adiabatic instabilities for all ϕ, and onset for GSF occurs at $\phi = -64^\circ$ and lasts until a point of stability $\phi = 90^\circ$ (cylindrical rotation), after which a second curve predicts instability for $90^\circ \lesssim \phi \lesssim 180^\circ$ and $-180^\circ \lesssim \phi \lesssim -116^\circ$. The transition to GSF instability is predicted by Eq. 3.20, plotted as the dashed magenta line, which is in excellent agreement with our numerical results. Like at the equator, but unlike at latitudes 30° and 60°, the pole exhibits instabilities symmetrically with respect to cylindrical rotation ($\phi = 90^\circ$), at which point the solution is singular and therefore is not plotted. Again, we see that the prediction in the asymptotic limit assuming RiPr $\sim O(1)$ is in very good agreement with our results, whereas the RiPr $\to 0$ prediction is an upper bound.

We thus observe from these figures that the maximum growth rates depend strongly

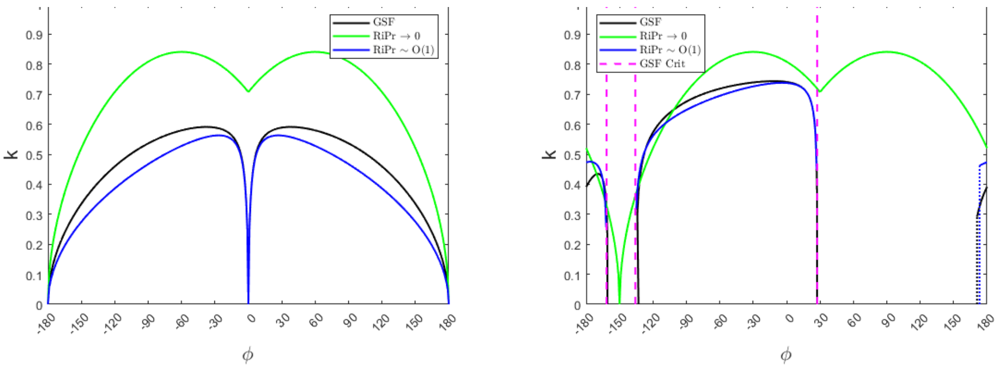

(a) $\Lambda + \phi = 0°$ (b) $\Lambda + \phi = 30°$

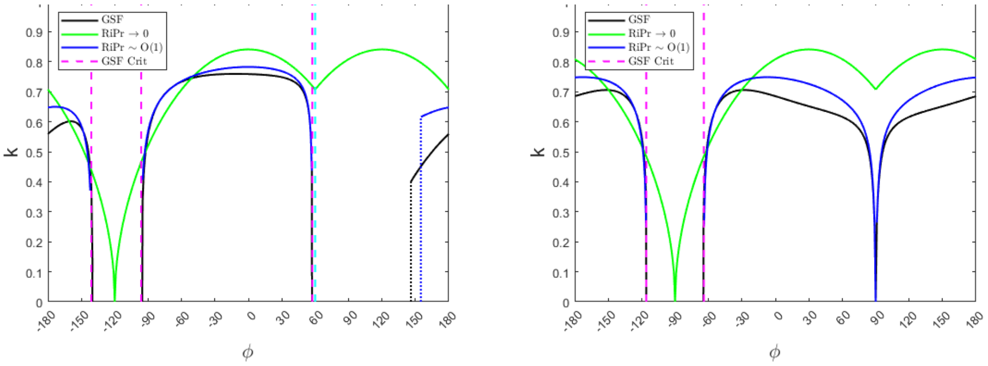

(c) $\Lambda + \phi = 60°$ (d) $\Lambda + \phi = 90°$

Figure 3.4: A selection of figures comparing the fastest growing wavevector magnitudes against ϕ at the latitudes 0°, 30°, 60°, 90° for $S = 2, \mathrm{Pr} = 10^{-2}, N^2 = 10$. Onset of adiabatic instability as predicted by Eq. 3.10 is shown as a blue dashed line. Onset of GSF instability predicted by Eq. 3.20 is shown as the magenta dashed lines, and onset of adiabatic instability predicted by Eq. 3.10 is indicated by the light blue dashed lines. We plot predictions from solving our cubic numerically (black) as well as the corresponding asymptotic predictions assuming RiPr $\sim O(1)$ (blue) and RiPr $\to 0$ (green).

on latitude and on the differential rotation angle ϕ, but typically have similar maximum values $O(1)$ (when $S \sim O(1)$) when (either adiabatic or diffusive) instability occurs. In general, the fastest growing modes typically occur for mixed radial/latitudinal shears rather than purely radial or latitudinal shears, and the most unstable orientation of the shear depends on latitude.

Fig. 3.4 shows the corresponding wavevector magnitudes ($k = |\boldsymbol{k}|$) for the fastest growing modes as a function of ϕ between $\phi = -180°$ and 180° for each panel plotted in Fig. 3.3. We observe that in the adiabatically unstable regime (to the right of

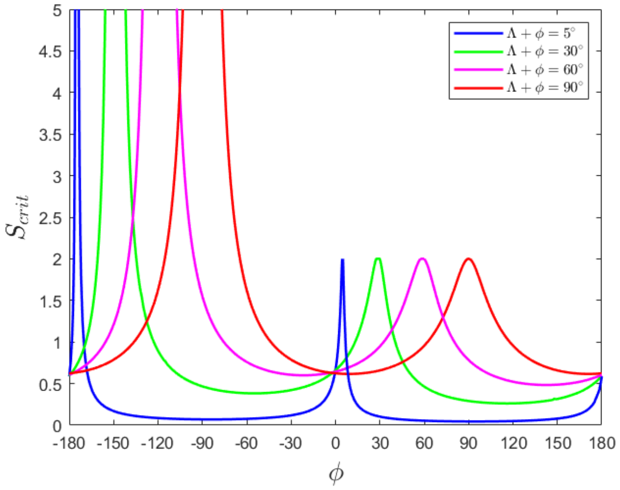

Figure 3.5: Critical shear strength S_{crit} required for onset of GSF instability for $\phi \in [-180^\circ, 180^\circ]$ at the latitudes $\Lambda + \phi = 5^\circ, 30^\circ, 60^\circ$ and 90° (assuming $N^2 = 10, \mathrm{Pr} = 10^{-2}$). Note: we choose 5° to approximate the equatorial region for numerical reasons. For each latitude, $\Lambda \sim 0$, corresponding to an approximately cylindrical rotation profile, is a local maximum in S_{crit} because GSF instability requires Rayleigh's stability criterion to be violated, whereas for other latitudes Eq. 3.20 is usually a less stringent condition except for large negative values of ϕ.

the blue dashed lines showing the predictions of Eq. 3.10) the preferred wavevector magnitude is not plotted. This is because the diffusion-free quadratic dispersion relation exhibits a preferred orientation but no preferred wavevector magnitude in this local model. There is a preference for $k \to 0$ however in this regime when diffusion is present, as we have observed by solving our cubic dispersion relation here, but we omit showing this.

Interestingly, we see that in the three cases that showed the largest growth rates (latitudes $0^\circ, 60^\circ$ and 90°) we also see that all of these cases have similar $|\boldsymbol{k}|$ values on average in the range 0.5-0.7 (in units of d^{-1}). We observe that the asymptotic predictions for k assuming $\mathrm{RiPr} \sim O(1)$ are in very good agreement with the numerical results from solving our cubic (black), whereas the predictions assuming $\mathrm{RiPr} \to 0$ are typically slightly larger (indicating slightly smaller wavelength modes).

The critical shear strength S_{crit} required for onset of GSF instability (i.e. which occurs for $S > S_{crit}$) at a given latitude $\Lambda + \phi$ is highly dependent on ϕ.

The results we found are presented in Fig. 3.5 for various latitudes (assuming $N^2 = 10, \mathrm{Pr} = 10^{-2}$). Note that when $\Lambda = 0$, corresponding with cylindrical rotation, and for values $\Lambda \sim 0$, there is a region with a local maximum constant value in $S_{crit} = 2$. This is because cylindrical rotation profiles are only unstable if Rayleigh's stability criterion is violated, which is typically a more stringent condition than Eq. 3.20.

On the other hand, we show that when ϕ is negative the instability is stabilised for sufficiently large values of ϕ. Such ϕ values (e.g. $\phi \sim -180°$ near the equator) correspond to outwardly varying angular momentum profiles when S is positive, which are thus Rayleigh-stable. Hence for such negative values of ϕ (depending on latitude), large or even infinite values of S_{crit} are required for instability.

Fig. 3.5 shows that a large reduction in S_{crit} is possible when ϕ and Λ are both nonzero, particularly near the equator. For shellular rotation ($\phi = 0$), we note that the most readily destabilised cases are near the poles ($\Lambda + \phi \approx 90°$), as identified in BJT2. On the other hand, the equatorial regions are most readily destabilised for primarily horizontal (or mixed radial/latitudinal) shears. In particular, note that $\Lambda + \phi \approx 5°$ is unstable for very weak horizontal shears, and more generally for those with $|\phi - 5°| \gtrsim 5°$. This figure illustrates the non-trivial behaviour of the GSF instability as a function of latitude and ϕ.

3.5 Conclusions

This chapter focused on analysing the local linear stability of generalised differential rotation profiles in stably stratified radiation zones through the use of our local Cartesian box model.

Initially, we re-derived and built upon results from previous studies by authors such as BJT1, BJT2, and Knobloch (1982), exploring both non-diffusive and diffusive regimes and investigating their linear stability.

We then examined several asymptotic limits of particular interest by exploiting some of the extreme parameter values typical in stellar interiors, specifically small Pr and large Ri. This allowed us to derive simple expressions characterising the growth rates and behaviour of the wave vectors for the unstable modes in each of these limits, as well as to develop a clear understanding of the effects of the various physical processes in the system.

We then presented extensive numerical visualisations, exploring the dynamics of the growth rate and properties of the most unstable modes as a function of ϕ. Our ‘lobe’ plots (Figures 3.1 and 3.2) identified two key instabilities: a set of primary lobes corresponding to dominant direct instability (GSF or adiabatic), along with a set of secondary lobes representing weakly growing inertial gravity waves.

Figures 3.3 and 3.4 reveal how variations in ϕ and ultimately different rotational profiles affect the growth rate of the most unstable mode, highlighting how mixed radial/latitudinal shears can be more unstable than the purely radial ones studied in BJT1 and BJT2. Table 3.1 summarises our results from this numerical analysis.

Finally, Figure 3.5 demonstrates the clear dependence between the minimum shear strength required for the onset of instability and the choice of differential rotation profile at a fixed latitude.

Together, these figures have shown that the linear problem is strongly controlled by the differential rotation profile within our local box model. We have seen that mixed shears lead to the lowest S_{crit} and largest growth rates at all of the latitudes we considered. It is important to now explore how these results translate into the nonlinear evolution and determine for which parameters the GSF instability is most efficient at transporting angular momentum.

S	ϕ	Λ	Γ	γ	RiPr	k_x	k_z	$\lvert\boldsymbol{k}\rvert$	σ	θ_k	Adi stable?
Latitude = 0°											
2	-90°	90°	-66.42°	135°	0.025	-0.17	0.51	0.54	0.70	71.08°	✓
2	-60°	60°	-39.73°	120°	0.025	-0.053	0.58	0.58	0.76	84.81°	✓
2	-30°	30°	-18.46°	105°	0.025	-0.30	0.51	0.59	0.61	59.21°	✓
2	0°	0°	NA	NA	0.025	NA	NA	NA	NA	NA	✓
2	30°	-30°	18.46°	-105°	0.025	-0.30	0.51	0.59	0.61	59.21°	✓
2	60°	-60°	39.73°	-120°	0.025	-0.05	0.58	0.58	0.76	84.81°	✓
2	90°	-90°	66.42°	-135°	0.025	-0.17	0.51	0.54	0.70	71.08°	✓
Latitude = 30°											
2	-90°	120°	-69.73°	150°	0.025	0.47	0.49	0.68	0.36	46.28°	✓
2	-60°	90°	-36.42°	135°	0.025	0.26	0.67	0.72	0.55	69.19°	✓
2	-30°	60°	-9.73°	120°	0.025	-0.03	0.74	0.74	0.62	87.72°	✓
2	0°	30°	11.54°	105°	0.025	0.32	-0.67	0.74	0.49	64.14°	✓
2	30°	-30°	NA	NA	0.025	NA	NA	NA	NA	NA	✓
2	60°	-30°	48.46°	-105°	0.025	-0.01	0.015	0.018	0.88	57.09°	×
2	90°	-60°	69.73°	-120°	0.025	-0.001	0.01	0.01	1.10	81.87°	×
Latitude = 60°											
2	-90°	150°	-78.46°	165°	0.025	0.52	0.22	0.56	0.03	22.77°	✓
2	-60°	120°	-39.73°	150°	0.025	0.52	0.52	0.73	0.29	45.20°	✓
2	-30°	90°	-6.42°	135°	0.025	0.29	0.70	0.76	0.51	67.21°	✓
2	0.0°	60°	20.27°	120°	0.025	0.015	0.76	0.76	0.60	88.86°	✓
2	30°	30°	41.54°	105°	0.025	-0.25	0.70	0.75	0.48	70.19°	✓
2	60°	0°	NA	NA	0.025	NA	NA	NA	NA	NA	✓
2	90°	-30°	78.46°	-105°	0.025	0.001	0.01	0.01	0.85	81.87°	×
Latitude = 90°											
2	-90°	180°	NA	NA	0.025	NA	NA	NA	NA	NA	✓
2	-60°	150°	-48.46°	165°	0.025	0.51	0.21	0.55	0.024	22.30°	✓
2	-30°	120°	-9.73°	150°	0.025	0.51	0.49	0.71	0.32	43.98°	✓
2	0°	90°	23.58°	135°	0.025	0.29	0.62	0.69	0.58	65.20°	✓
2	30°	60°	50.27°	120°	0.025	0.049	0.65	0.65	0.70	85.69°	✓
2	60°	30°	71.54°	105°	0.025	-0.16	0.60	0.62	0.59	75.34°	✓
2	90°	0°	NA	NA	0.025	NA	NA	NA	NA	NA	✓
Variations in shear (GSF instability at $S = 2$ in Fig. 4.7 panels (a) and (b))											
0.5	-30°	60°	-25.037°	73.90°	0.40	0.18	-0.39	0.43	0.013	66.03°	✓
1.0	-30°	60°	-20.035°	90°	0.10	-0.18	0.60	0.63	0.18	72.95°	✓
1.5	-30°	60°	-14.94°	106.1°	0.044	-0.11	0.69	0.70	0.40	80.55°	✓
2.0	-30°	60°	-9.73°	120°	0.025	-0.029	0.74	0.74	0.62	87.72°	✓
2.5	-30°	60°	-4.34°	130.89°	0.016	0.053	0.76	0.76	0.84	86.04°	✓
3.0	-30°	60°	1.31°	139.11°	0.011	-0.12	-0.76	0.77	1.06	-81.12°	✓
Variations in shear (adiabatic instability at $S = 2$ in Fig. 4.7 panels (c) and (d))											
0.5	90°	-60°	-25.03°	-73.90°	0.40	0.18	-0.39	0.43	0.013	66.03°	✓
1.0	90°	-60°	99.97°	-90°	0.10	0	0	0	0.48	NA	×
1.5	90°	-60°	105.06°	-106.1°	0.044	0	0	0	0.85	NA	×
2.0	90°	-60°	110.27°	-120°	0.025	0	0	0	1.10	NA	×
2.5	90°	-60°	115.66°	-130.89°	0.016	0	0	0	1.31	NA	×
3.0	90°	-60°	121.31°	-139.11°	0.011	0	0	0	1.49	NA	×

Table 3.1: Table of linear properties for simulation parameters. For all of these we fix $\mathrm{Pr} = 10^{-2}$ and $N^2 = 10$. k_x and k_z are wavevector components of the fastest growing linear mode, σ is the corresponding growth rate. The cases which investigated variations in shear S were considered at $\Lambda+\phi = 30^\circ$ latitude with $\Lambda = 60^\circ, \phi = -30^\circ$ in the case that was GSF-unstable at $S = 2$, and $\Lambda = -60^\circ, \phi = 90^\circ$ in the case that is adiabatically unstable if $S = 2$. Our simulation units are determined by setting $\Omega = d = 1$.

Chapter 4

Nonlinear hydrodynamical simulations

4.1 Nonlinear hydrodynamical simulations and results

The primary aim of the following chapter is to develop an understanding of how variations in the orientation of the shear, denoted by ϕ, affect the GSF instability for the first time, and to quantify the resultant turbulent transport. Our nonlinear simulations are performed using the pseudo-spectral code SNOOPY, as discussed in Lesur and Longaretti (2005). We start by discussing several key elements of SNOOPY, including the advantages of it being a Fourier code and its utilization of shearing waves.

Following this we present the results from our 3D simulations, for several GSF unstable cases, primarily at the latitudes $\Lambda + \phi = 0^\circ, 30^\circ$ and 90°. We quantify the time evolution of the kinetic energy and relevant Reynolds stress components in Figs. 4.2 and 4.3, which are presented alongside snapshots of the flow at the various key stages throughout its evolution. Non-dimensional parameters are used throughout, and following Fig. 3.3 (and BJT2), are fixed as $S = 2$, $N^2 = 10$, $\mathrm{Pr} = 10^{-2}$, along with box dimensions of $L_x = L_y = L_z = 100$, unless otherwise stated. Note that

$S = 2$ represents the critical value for instability onset for a cylindrical differential rotation profile ($\Lambda = 0$) or at the equator for a shellular profile ($\phi = 0$).

We then turn our focus to cases predicted in Fig. 3.3 to be adiabatically unstable in order to gauge how the lack of a preferred wave vector magnitude, discussed in Chapter 3, translates into the nonlinear regime. Following this we probe the effects of varying shear strength S and box size (L_x, L_y, L_z) in § 4.3.1 and 4.3.2. Table B.1 summarises the majority of our nonlinear hydrodynamical simulations.

Finally, we analyse the angular momentum transport properties of the operating instabilities as a function of ϕ. From this we aim to provide insights into how and why the orientation of the shear, and consequently the local differential rotation profile, affects the angular momentum transport within the system.

4.2 SNOOPY

All simulations presented in this chapter are performed using the pseudo-spectral code SNOOPY. SNOOPY is a 3D incompressible Fourier code, in Cartesian geometry, with the capacity to implement shearing sheet boundary conditions through the use of 'shearing waves'. SNOOPY solves the nonlinear equations of magnetohydrodyamics, and was originally developed by Lesur and Longaretti (2005) to simulate local instabilities in accretion disks. The code is parallelised using Message Passing Interface (MPI) and Open Multi-Processing (OpenMP) to utilise multiple cores on high-performance computing (HPC) facilities (such as ARC at the University of Leeds), enabling simulations that would be otherwise impractical on a single processor.

Being a pseudo-spectral code, SNOOPY does calculations in both Fourier and real space depending on which is more convenient in different stages of the simulation. As a Fourier code, SNOOPY involves expanding solutions in terms of complex exponentials (sines and cosines) of the form:

$$\boldsymbol{u} = \Re[(\hat{u}_x, \hat{u}_y, \hat{u}_z) \exp(\mathrm{i}\boldsymbol{k}(t) \cdot \boldsymbol{x})], \tag{4.1}$$

$$p = \Re[\hat{p} \exp(\mathrm{i}\boldsymbol{k}(t) \cdot \boldsymbol{x})], \tag{4.2}$$

$$\theta = \Re[\hat{\theta} \exp(\mathrm{i}\boldsymbol{k}(t) \cdot \boldsymbol{x})], \tag{4.3}$$

where the coefficients with hats are complex numbers in general, and where the total solution is the sum of all of the allowed Fourier modes of this form within the box. Once we've determined the coefficients of the expanded terms, taking the sum of all Fourier modes gives us the physical velocity, temperature, and pressure fields seen in our simulations.

One interesting feature of SNOOPY is its use of time-dependent wave vectors, also known as 'shearing waves', to deal with the periodic nature of the flow whilst remaining consistent with the background shear flow.

4.2.1 Shearing Waves

Having a background shear flow that varies linearly with x means that the modes in our system are constantly being sheared out in the x-direction. In order to deal with this one can either adopt shear-periodic boundary conditions (e.g. Hawley et al., 1995) or use shearing waves. In the following we choose the latter because, as we shall we, it allows for some simplifications to be made to the equations solved by SNOOPY.

In the shearing wave formalism, Fourier modes don't take the usual form $\exp(\mathrm{i}\boldsymbol{k} \cdot \boldsymbol{x})$ with constant $\boldsymbol{k}$. Instead, in order to account for the continuous deformation of $\boldsymbol{k}$ due to the background shear flow, we use time-dependent wave vectors $\boldsymbol{k}(t)$. This means our basis functions are sheared waves (known as 'shearing waves') which take the form $\exp(\mathrm{i}\boldsymbol{k}(t) \cdot \boldsymbol{x})$. The k_y and k_z wave numbers remain time-independent and are given by those typical in a periodic domain,

$$k_y = 2\pi n_y/L_y, \qquad n_y \in \mathbb{Z}, \tag{4.4}$$

$$k_z = 2\pi n_z/L_z, \qquad n_z \in \mathbb{Z}. \tag{4.5}$$

The main difference comes from the k_x wave vector, which is the one affected by the shear, for which we have:

$$k_x(t) = 2\pi n_x/L_x + Sk_y t, \qquad n_x \in \mathbb{Z}. \tag{4.6}$$

The periodicity of these waves implies that every mode in the system automatically satisfies shear-periodic boundary conditions, and hence our whole system satisfies periodic boundary conditions without the need to impose the boundary conditions further in the code.

To see how the shearing wave formulation benefits SNOOPY, let's consider the advective derivative arising from the background flow $\boldsymbol{U}_0$, before taking the real part,

$$\frac{\partial \boldsymbol{u}}{\partial t} + \boldsymbol{U}_0 \cdot \nabla \boldsymbol{u} = \frac{\partial}{\partial t}\left(\hat{\boldsymbol{u}} \exp\left(\mathrm{i}\boldsymbol{k}(t)\cdot\boldsymbol{x}\right)\right) + \mathrm{i}\left(\dot{\boldsymbol{k}}\cdot\boldsymbol{x}\right)\hat{\boldsymbol{u}}\exp\left(\mathrm{i}\boldsymbol{k}(t)\cdot\boldsymbol{x}\right) - \mathrm{i}k_y S x \hat{\boldsymbol{u}} \exp\left(\mathrm{i}\boldsymbol{k}(t)\cdot\boldsymbol{x}\right). \tag{4.7}$$

Without shearing waves (i.e., if $\dot{\boldsymbol{k}} = \boldsymbol{0}$), the final term creates difficulties due to its linear dependence on x, since it therefore doesn't satisfy typical periodic boundary conditions. However, we can choose to define,

$$\dot{\boldsymbol{k}}(t) = Sk_y \boldsymbol{e}_x, \tag{4.8}$$

so that the final term is exactly balanced by the middle term in 4.7 and thus they both vanish thanks to the use of shearing waves. Using shearing waves is equivalent to using coordinates that follow the background flow $\boldsymbol{U}_0$, which allows us to express any perturbation using Fourier modes as long as they can be assumed to satisfy periodic boundary conditions in such a frame. Since k_x increases linearly with time, we must apply a remapping procedure to be able to resolve flow structures with a given spatial scale for a long time. To do so, we apply a periodic remap on the timescale $t = nL_y/SL_x$ for $n = 1, 2, 3, ...$ This procedure is explained in Umurhan and Regev (2004) and Lesur and Longaretti (2005). It is required because a given wave in the shearing coordinates frame appears as a time-dependent wave in the original steady frame. As time progresses the wavenumbers in the shearing frame describe increasingly higher wavenumbers in the steady frame, and consequently, the original wave will eventually no longer be represented if only a finite number of Fourier modes are employed. Using a periodic remap prevents us from losing energy on the large scales (Rogallo, 1981).

4.3 Nonlinear Evolution of GSF instability

Snapshots of the y component of the velocity field, u_y, (which is the variable that most clearly shows both the linear and nonlinear behaviour) in the $(x, z)-$plane are given in Figs. 4.1-4.5. The upper left image in each of these figures shows how the local model fits into the global picture for each choice of parameters. Panel (c) shows the linear growth phase, which is dominated by the fastest growing mode velocity perturbations ("AM fingers") that are orientated roughly half-way between $\hat{\boldsymbol{\Omega}}$ and $(\nabla\ell)^{\perp}$ (indicated by solid black lines). Here, centrifugally-driven AM fingers develop. Panel (d) shows the initial nonlinear saturation of these fingers and the formation of zonal jets. Panels (e) and (f) show the evolution of the zonal jets, illustrating the potential for them to grow in strength and tilt away from their initial orientation depending on the parameters. Given sufficient time all cases here with nonzero ϕ (and nonzero Λ) achieved a steady layered state, in which the zonal jets contribute to generating sustained AM transport. For additional details on AM transport (and the role of Reynolds stresses), see Aside 4.3.

Reynolds Stress

The role of stresses are not only to ensure a timely submission of this thesis but also to describe how the forces internal to a fluid affect its evolution.

The particular stress tensor of interest in quantifying angular momentum transport is the Reynolds stress (and additionally when magnetic fields are present, the Maxwell stresses).

We wish to understand the interaction between some perturbation and the surrounding flow. One way of gaining additional insights would be to calculate the kinetic energy equation and see which terms transfer energy between the two.

We calculate the energy equation by taking the dot product of $\boldsymbol{u}$ with our perturbed momentum equation

$$\boldsymbol{u}\cdot(D\mathbf{u}+2\boldsymbol{\Omega}\times\mathbf{u}+\mathbf{u}\cdot\nabla\boldsymbol{U}_0)=\boldsymbol{u}\cdot(-\nabla p+\theta\mathbf{e}_g+\nu\nabla^2\mathbf{u}). \tag{4.9}$$

Simplifying and volume averaging gives

$$\begin{aligned}&\frac{1}{V}\int_V D|\mathbf{u}|^2 dV=-\frac{2}{V}\int_V(\boldsymbol{\Omega}\times\mathbf{u})\cdot\boldsymbol{u}\,dV-\frac{1}{V}\int_V\nabla p\cdot\boldsymbol{u}\,dV\\&+\frac{1}{V}\int_V(\theta\mathbf{e}_g)\cdot\boldsymbol{u}\,dV+\frac{1}{V}\int_V(\nu\nabla^2\mathbf{u})\cdot\boldsymbol{u}\,dV-\frac{1}{V}\int_V(\mathbf{u}\cdot\nabla\boldsymbol{U}_{\mathbf{0}})\cdot\boldsymbol{u}\,dV.\end{aligned} \tag{4.10}$$

An application of the divergence theorem to the pressure and non-linear advection terms leads to (and applying periodic boundary conditions),

$$\int_V\nabla\cdot(p\boldsymbol{u})\,dV=\int_S p\boldsymbol{u}\cdot\boldsymbol{n}\,dS=0, \tag{4.11}$$

and

$$\int_V\boldsymbol{u}\cdot(\boldsymbol{u}\cdot\nabla\boldsymbol{u})dV=\int_V\nabla\cdot(\frac{1}{2}|\boldsymbol{u}|^2\boldsymbol{u})dV=\int_S\frac{1}{2}|\boldsymbol{u}|^2\boldsymbol{u}\cdot dS=0. \tag{4.12}$$

Reynolds Stress

Noting that the term $-\frac{2}{V}\int_V(\boldsymbol{\Omega}\times\mathbf{u})\cdot\boldsymbol{u}\,dV=0$ since $(\boldsymbol{\Omega}\times\mathbf{u})\cdot\boldsymbol{u}=0$, means the only term that determines kinetic energy transfer between the perturbation and the shear flow is the last term,

$$-\frac{1}{V}\int_V(\mathbf{u}\cdot\nabla\boldsymbol{U}_0)\cdot\boldsymbol{u}\,dV=-\frac{1}{V}\int_V Su_xu_ydV=-\frac{S}{V}R_{xy}(t). \tag{4.13}$$

R_{xy} is the Reynolds stress where

$$R_{xy}=\frac{1}{V}\int_V u_xu_ydV. \tag{4.14}$$

The Reynolds stresses (and where applicable Maxwell stresses) are vital quantities indicating the angular momentum and energy transport properties of a fluid. We will go into further detail of the energetics in § 5.5.1.

Panel (b) in each of Figs. 4.1-4.5 shows the kinetic energy spectrum on the (k_x,k_z)-plane (averaged over y) at $t=250$, by which point every simulation we investigated had reached a statistically steady state exhibiting strong zonal jets. This shows the orientations of the modes as a function of their spatial scale, which strongly exhibit a preferred direction at small wavenumbers and become increasingly isotropic for larger wavenumbers. Note that the de-aliasing wavenumber in these simulations has magnitude 5.83, so the decrease in spectral power by then is evidently more than a factor of 10^3 from the peak, suggesting that our simulations are well resolved spatially. We also checked the initial more turbulent phases of our simulations, such as $t=50$, and all were verified to be well resolved spatially by analysing the k_x,k_y and k_z spectra.

The first set of snapshots are presented in Fig. 4.1. These illustrate the y-component of the velocity at various points throughout the evolution of the instability at the equator (at the times $t=10,50,100$ and 250). This is an equatorial ($\Lambda+\phi=0$) case with $\phi=30°$, $\Lambda=-30°$, which we can see from Fig. 3.3 is within the GSF-unstable

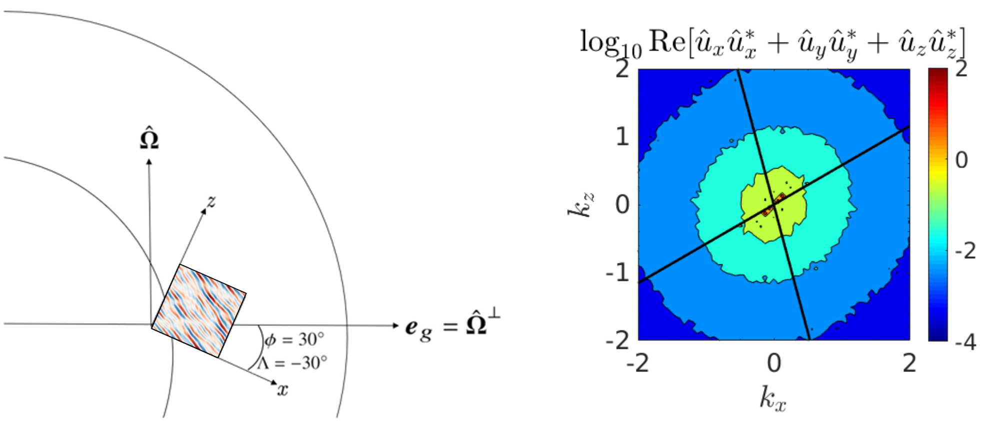

(a) Diagram

(b) KE spectrum at $t = 250$

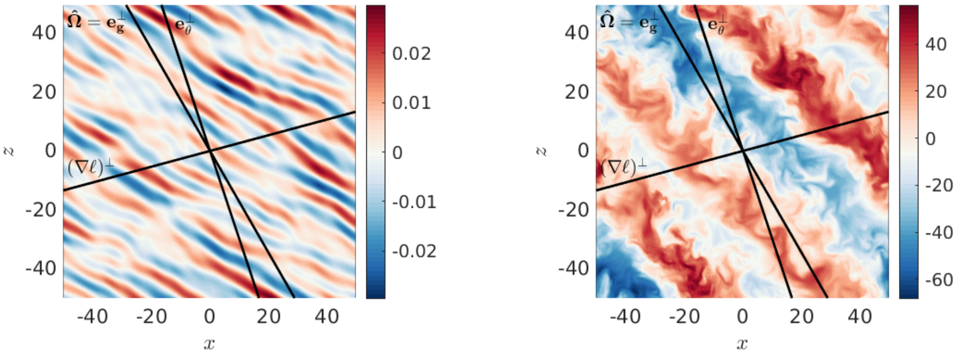

(c) u_y at $t = 10$

(d) u_y at $t = 50$

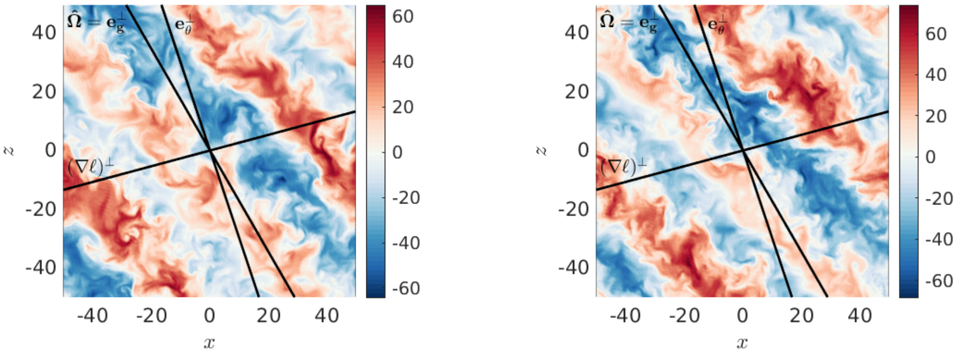

(e) u_y at $t = 100$

(f) u_y at $t = 250$

Figure 4.1: Panel (a) depicts the local configuration of the box, filled with the snapshot of u_y at $t = 10$, within the global picture at the equator with $\phi = 30°, \Lambda = -30°$, $S = 2, \mathrm{Pr} = 10^{-2}$ and $N^2 = 10$. This is coupled with snapshots of the y-component of the velocity in (x, z) slices at $y = 0$ at various points throughout the evolution of the GSF instability. By $t = 10$ AM fingers have developed in the wedge of instability, in between $(\nabla\ell)^{\perp}$, and $\hat{\mathbf{\Omega}}$. By $t = 50$ we already see clear layering, made up of oppositely-directed zonal jets. The jets are fully developed by $t = 100$ and we see from its evolution at $t = 250$, along with Figs. 4.2 and 4.3, that this is a statistically steady state transporting enhanced levels of AM. Panel (b) shows the KE spectrum, $\log_{10}\mathrm{Re}[\hat{u}_x\hat{u}_x^* + \hat{u}_y\hat{u}_y^* + \hat{u}_z\hat{u}_z^*]$, in the (k_x, k_z)-plane at $t = 250$, illustrating how the orientation of the layered state differs from that of the initial fingers.

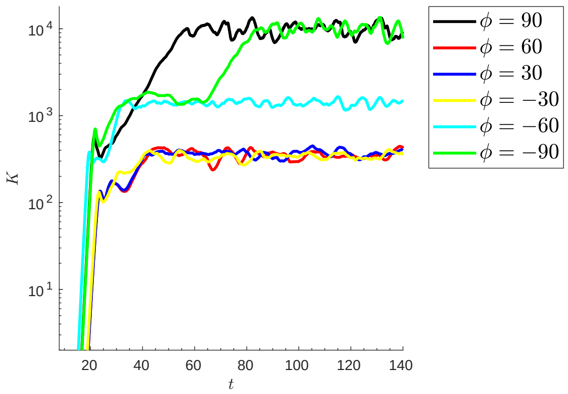

(a) Lat = 0°

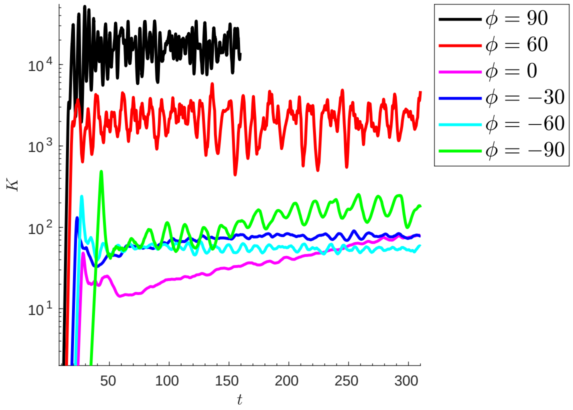

(b) Lat = 30°

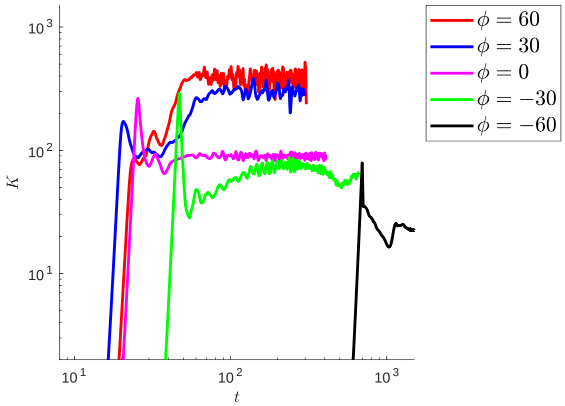

(c) Lat= 90°

Figure 4.2: Evolution of the kinetic energy K ($K = \frac{1}{2}\langle|\boldsymbol{u}|^2\rangle$) for $S = 2$, $N^2 = 10$, $\mathrm{Pr} = 10^{-2}$, with ϕ varied but at a fixed latitude $\Lambda + \phi$. We observe the orientation of the shear to directly affect the final K levels within both the GSF and adiabatically unstable regimes. Panels (a) and (b) are plotted on a semi-log scale which clearly captures the exponential growth phases, whereas the slow evolution for $\phi = -60°$ necessitated the use of a log-log scale for panel (c) which exhibited a lower initial growth rate.

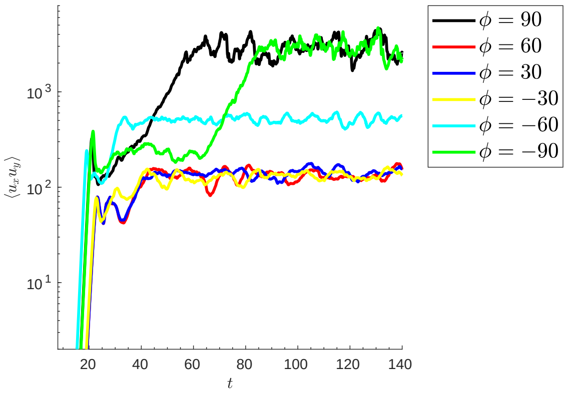

(a) Lat = 0°

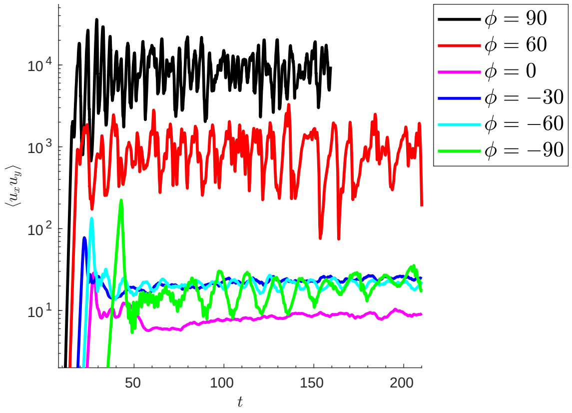

(b) Lat = 30°

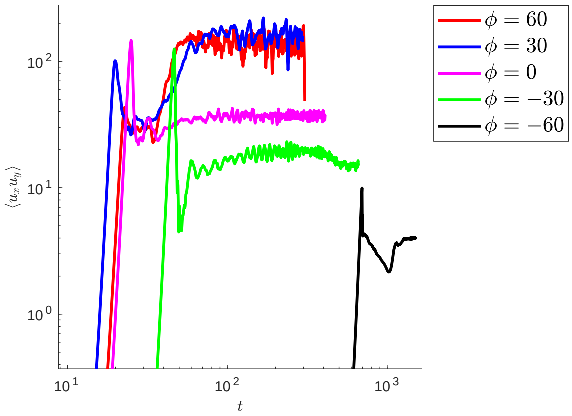

(c) Lat= 90°

Figure 4.3: Reynolds stress component $\langle u_x u_y \rangle$ illustrating angular momentum (AM) transport for the same cases as Fig. 4.2. Variations in ϕ at a fixed latitude $\Lambda + \phi$ can lead to enhanced levels of AM transport, illustrating the influence of shear orientation on the turbulent dynamics. These effects are observed within both the GSF regime and the adiabatic instability. Panels (a) and (b) show the results on a semi-log scale to highlight differences across several orders of magnitude, while panel (c) uses a log-log scale to better capture the slow evolution observed for $\phi = -60°$.

regime. By $t = 10$ centrifugally-driven AM fingers have developed within the wedge of unstable directions. At $t = 50$ the AM fingers have saturated nonlinearly and formed zonal jets or AM layers. Figs. 4.2 and 4.3 show the corresponding volume-averaged kinetic energy ($K = \frac{1}{2}\langle|\boldsymbol{u}|^2\rangle$, where $\langle\cdot\rangle$ denotes a volume average), and AM transport (i.e. Reynolds stress component $\langle u_x u_y\rangle$), respectively. The jets are fully formed by $t = 100$, and we see from the subsequent evolution at $t = 250$, and Figs. 4.2 and 4.3, that this is a statistically steady state, which is transporting enhanced levels of AM.

Figs. 4.2 and 4.3 indicate that the transport properties of the GSF (and adiabatic) instability depend heavily on shear flow orientation ϕ and at a fixed latitude $\Lambda + \phi$. We notice that the magnitudes of turbulent transport in the final states are, on a whole, well ordered with respect to the predictions for the linear growth rates in Fig. 3.3, in that $\langle u_x u_y\rangle$ is generally larger for cases with larger growth rates σ. However exceptions are observed, resulting from undetermined nonlinear factors such as the strengths of zonal jets in each case. We also notice that the case with $\phi = -60°$ at the equator ($\Lambda + \phi = 0$) doesn't behave in the same way as $\phi = 60°$, despite the symmetrical nature (about zero) of the growth rate σ predicted by linear theory in Figs. 3.3 and 3.4. Instead KE and AM transport properties are significantly increased in comparison with $\phi = 60°$, which Fig. 3.3 would suggest to be roughly equal based on the linear growth rates.

Once the initial growth phase becomes nonlinearly saturated, jet migration and mergers dominate the dynamics. A merger can be seen particularly clearly in the equatorial case with $\phi = -90°$ (the green line in Fig. 4.2), between times $t \approx 65$ and $t \approx 85$ the layers in the system merge to form larger scale jets that transport angular momentum more efficiently.

Fig. 4.4 shows snapshots from a simulation at a non-equatorial latitude $\Lambda + \phi = 30°$ (cf. BJT2) within the GSF unstable regime, with $\phi = -30°, \Lambda = 60°$, with otherwise the same parameters. As predicted by 3.1 instability onsets initially between lines $(\nabla \ell)^{\perp}$ and $\hat{\boldsymbol{\Omega}}$, such that the preferred direction is along x. Parasitic instabilities

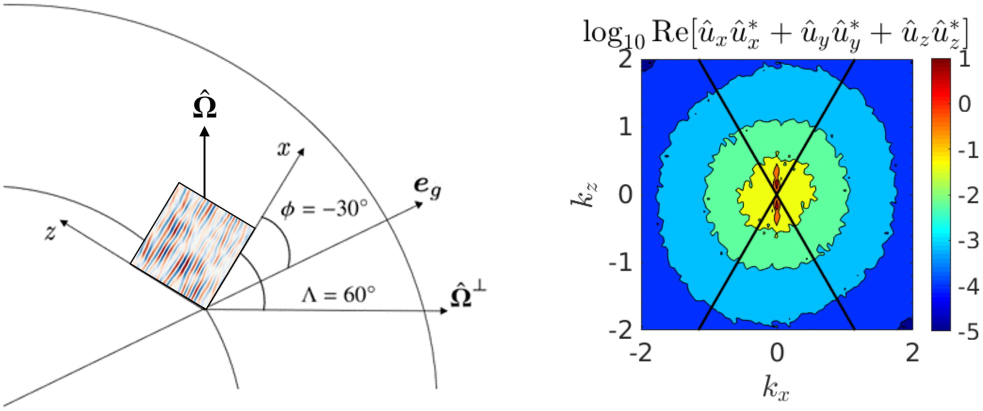

(a) Diagram

(b) KE spectrum at $t = 10$

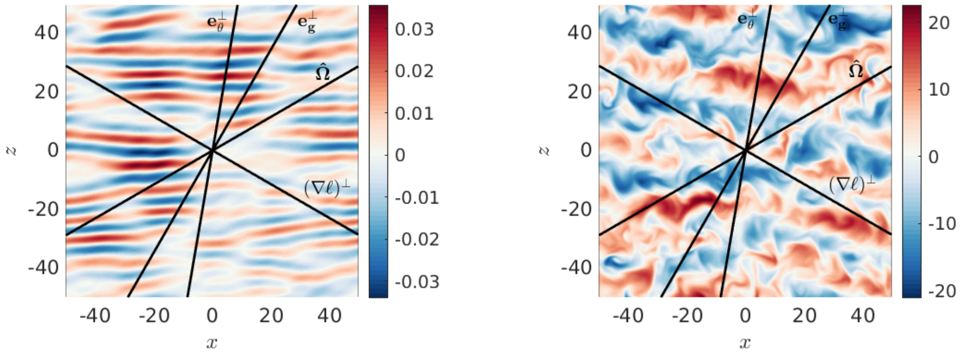

(c) u_y at $t = 10$

(d) u_y at $t = 50$

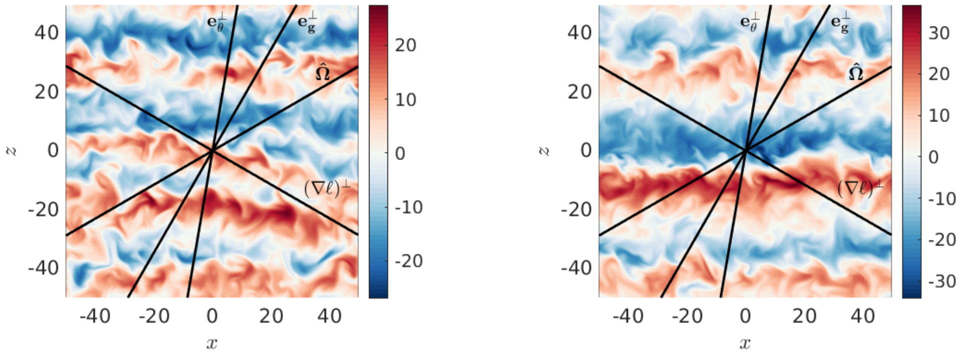

(e) u_y at $t = 100$

(f) u_y at $t = 250$

Figure 4.4: Panel (a) depicts the local configuration of the box, filled with the snapshot of u_y at $t = 10$, within the global picture for a non-equatorial case at latitude $\Lambda + \phi = 30°$ with $\phi = -30°, \Lambda = 60°$, $S = 2, \mathrm{Pr} = 10^{-2}$ and $N^2 = 10$. This is coupled with snapshots of the y-component of the velocity in (x, z) slices at $y = 0$ at various points throughout the evolution (at times $t = 10, 50, 100$ and 250) of the observed GSF instability in panels (c) to (f). At $t = 10$ AM fingers are observed inside the wedge of instability, in between the lines $(\nabla\ell)^\perp$ and $\hat{\boldsymbol{\Omega}}$. By $t = 50$ AM fingers have saturated by parasitic instabilities and are now well within the non-linear regime and the onset of layer formation. The flow at $t = 100$ and $t = 250$ is weaker in magnitude than that in Fig. 4.1, and the layers are less distinct from one another here. Panel (b) shows the kinetic energy spectrum in the (k_x, k_z)-plane at $t = 250$.

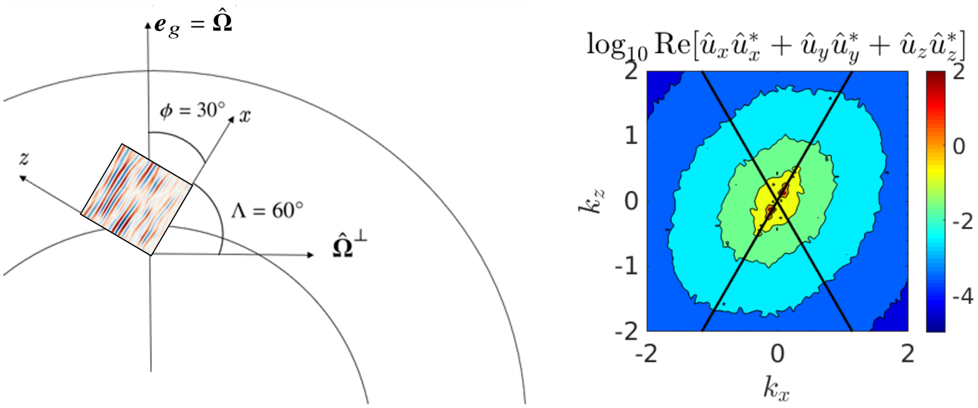

(a) Diagram

(b) KE spectrum at $t = 250$

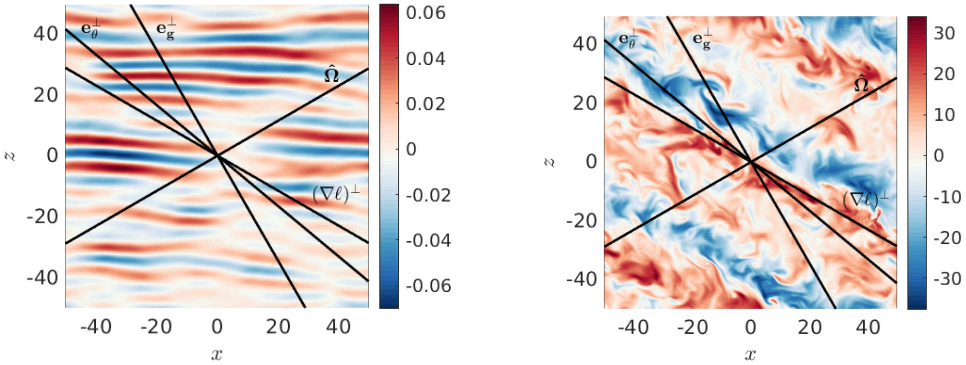

(c) u_y at $t = 10$

(d) u_y at $t = 50$

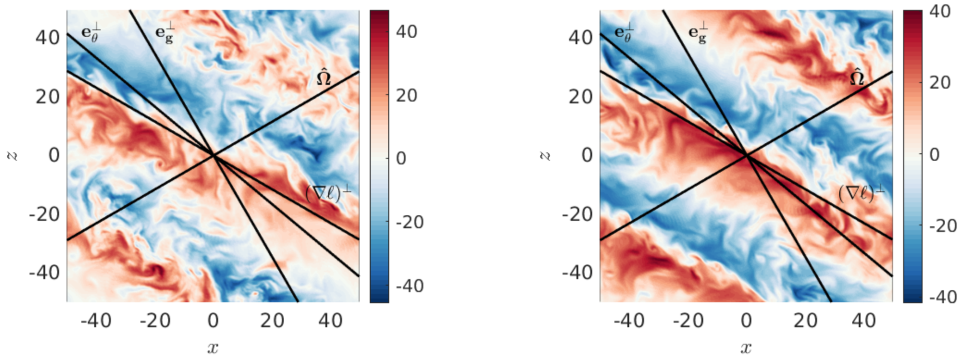

(e) u_y at $t = 100$

(f) u_y at $t = 250$

Figure 4.5: Panel (a) depicts the local configuration of the box, filled with the snapshot of u_y at $t = 10$, within the global picture for a case at the north pole with latitude $\Lambda + \phi = 90°$ with $\phi = 30°, \Lambda = 60°$, $S = 2, \mathrm{Pr} = 10^{-2}$ and $N^2 = 10$. This is coupled with snapshots of the y-component of the velocity in (x, z) slices at $y = 0$ at several points in the evolution (at times $t = 10, 50, 100$ and 250) of the GSF instability in panels (c) to (f). At $t = 10$ AM fingers develop within the unstable wedge, and by $t = 50$ they have saturated and clear AM layers start to appear. Interestingly, we see throughout the $t = 50, 100$ and 250 snapshots that these layers rotate to orientate themselves along lines of constant AM. The lack of changes after $t = 100$ indicates the system has attained a statistically steady state. Panel (b) shows the kinetic energy spectrum in the (k_x, k_z)-plane at $t = 250$.

acting on these fingers then lead into the non-linear regime, which quickly starts forming zonal jets. Comparing these panels with Figs. 4.2 and 4.3 clarifies that at $t \approx 50$ the initial exponential growth has subsided and the following growth in energy and turbulent transport results from strengthening or mergers of the jets. Potentially as a result of similarities in both the wavevector magnitudes and growth rates predicted by Figs. 3.4 and 3.3 for $\phi < 30°$, cases within $-90° < \phi < 30°$ have roughly the same velocities and hence mean kinetic energies. Interestingly a purely radial shear with $\phi = 0°$ produced the least AM transfer of these cases at this latitude.

The final case for which we will show snapshots in the GSF unstable regime in this section is a case at the (north) pole $\Lambda + \phi = 90°$ in Fig. 4.5. Here $\phi = 30°, \Lambda = 60°$, $S = 2, \mathrm{Pr} = 10^{-2}$ and $N^2 = 10$. Early phases of evolution have unstable mode flows excited between $(\nabla \ell)^{\perp}$ and $\hat{\mathbf{\Omega}}$ but the nonlinear evolution orientates the subsequent zonal jets to become approximately parallel to lines of constant AM. This is consistent with what we might expect if the instability saturates by moving the system back towards marginal stability, though it is difficult to understand this quantitatively given the complexity of our shear flow at this time. Again, we conclude from the lack of changes between $t = 100$ and $t = 500$ that these layers have reached a statistically-steady state with enhanced transport properties.

It should be noted that the small initial growth rate for $\phi = -60°$ requires the use of a logarithmic time scale in 4.2 and 4.3 to see that this case does grow in strength and form layers; albeit over a much longer period of time. This case appears to saturate at a very low level, as might be expected based on its linear growth rate being relatively small compared to the other cases plotted.

Adiabatically unstable cases

As we have identified in Chapter 3 and shown in Fig. 3.3, the system can be adiabatically unstable for certain ϕ and latitudes $\Lambda + \phi$. When the adiabatic stability criterion Eq. 3.10 is violated, we expect much more violent instabilities that do not

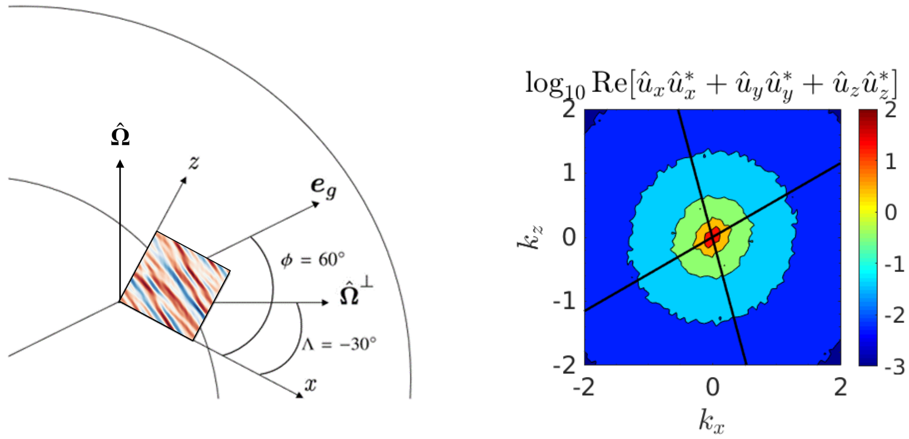

(a) Diagram (b) KE spectrum at $t = 250$

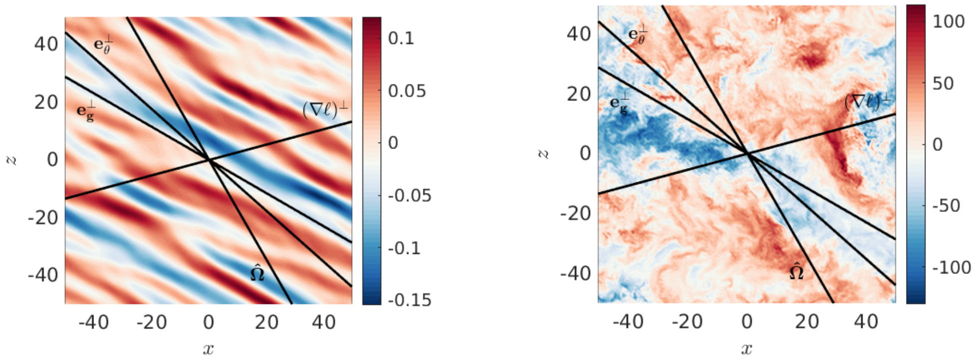

(c) u_y at $t = 10$ (d) u_y at $t = 50$

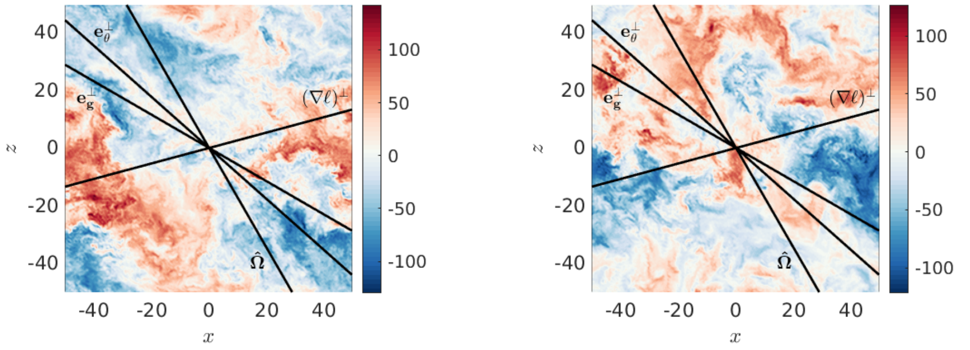

(e) u_y at $t = 100$ (f) u_y at $t = 250$

Figure 4.6: Panel (a) depicts the local configuration of the box, filled with the snapshot of u_y at $t = 10$, within the global picture for a case in the adiabatically-unstable regime at $\Lambda + \phi = 30°$ latitude, with $\phi = 60°, \Lambda = -30°$, $S = 2, \mathrm{Pr} = 10^{-2}$ and $N^2 = 10$. This is coupled with snapshots of the y-component of the velocity in (x, z) slices at $y = 0$ at various points throughout the evolution. This adiabatically unstable case exhibits rapidly growing AM fingers, which saturate shortly after $t = 10$. By $t = 50$, the system is highly turbulent, and $|u_y|$ is far larger here than observed in any of the cases. By $t = 100$ and 250 we see AM layers orientated along the same line as the initial fingers, despite the strong flows that develop. The zonal jets formed are much stronger than any in the GSF-unstable regime, in agreement with Figs. 4.2 and 4.3. Panel (b) shows the kinetic energy spectrum in the (k_x, k_z)-plane at $t = 250$.

require diffusion to operate. These are essentially adiabatic centrifugal instabilities. We have shown in Fig. 3.4 that in this regime the unstable modes do not have a finite preferred wavevector magnitude in the absence of diffusion, with all modes having the same orientation growing at the same rate, but that the presence of diffusion prefers modes to have arbitrarily large length-scales, with $k \to 0$.

We show the flow for one case at latitude $\Lambda + \phi = 30°$ with $\phi = 60°, \Lambda = -30°$ in Fig. 4.6. This is the case in Figs. 4.2 and 4.3 with the highest levels of turbulent transport (and one of the highest for energy, only below the other adiabatically unstable case with $\phi = 90°$) for this latitude. The growth rate in this regime predicted by Fig. 3.3 is only marginally higher than that with $\phi = 0°$ (as shown in BJT2). However, the lack of a finite preferred wavevector magnitude (without diffusion) always permits large wavelength modes on the scale of the box to grow, resulting in a dependence on the size of our Cartesian box we will analyse in §4.3.2. These then saturate leading to flows with much larger amplitudes than any of the GSF unstable cases in Figs. 4.1-4.5. The zonal jets in these cases are correspondingly stronger, and these adiabatically unstable cases lead to the highest values of turbulent transport. Note that Fig. 4.3 shows up to three orders of magnitude stronger AM transport in these adiabatically-unstable cases when compared to the GSF-unstable ones.

Ostensibly the dynamics are similar to the GSF-unstable cases, however the timescales for the different phases to occur, and strengths of the flows, vary largely between these regimes. We notice that the AM fingers at $t = 10$ are larger than those in the GSF regime, and by $t = 50$, the system is in a highly turbulent state, with $|u_y|$ being far larger than observed in any of the adiabatically-stable cases. Whilst fluctuations tend to be large in the adiabatic regime, by $t = 100$ we reach a statistically steady state in which large-scale layers have formed, orientated along the same line as the initial fingers by $t = 250$, despite their large amplitudes.

Adiabatically unstable differential rotation profiles are primarily driven by latitudinal rather than radial shears ($\phi \sim 90°$). Since the orientation of these shears is less impeded by gravitational buoyancy, thermal diffusion is less important. As a result, such instabilities are expected to evolve much more rapidly than the diffusive instability analysed in the previous section.

We note that an increase in angular momentum transport always accompanies an increase in lengthscale of the layered flow. For cases where the initial instability occurs at finite small scale, this increase in lengthscale arises owing to mergers of the zonal jets; these mergers can take significant time to onset and complete. For the adiabatically unstable cases where the initial instability occurs on a large spatial scale, the increase in angular momentum transport is significant even at early times.

4.3.1 Variation of shear strength S

We now examine the effect of varying the shear strength S for two different shear orientations at a latitude $\Lambda + \phi = 30°$. The first has $\Lambda = 60°$ and $\phi = -30°$ ("mixed radial/horizontal shear") and is GSF-unstable (but adiabatically stable) when $S = 2$, and the second has $\Lambda = -60°$ and $\phi = 90°$ ("horizontal shear") which is adiabatically unstable when $S = 2$. However, note that whether these cases are diffusively or adiabatically unstable depends on S. We have observed the qualitative behaviour of the flow in these simulations to be very similar to the cases presented in § 4.1, so we restrict our presentation to the volume-averaged quantities. The mean kinetic energy and AM transport are shown in Fig. 4.7. Cases that are adiabatically unstable in Fig. 4.7 are indicated by dashed lines.

The criterion for diffusive instability given by Eq. 3.20, and for adiabatic instability given by Eq. 3.10, both indicate that the shear strength S directly affects the onset of each type of instability. In addition, larger shears lead to larger growth rates. Interestingly though, whilst larger shears lead to larger initial growth rates, the results of Fig. 4.7 suggest that this doesn't necessarily translate into a higher kinetic energy K in the final steady state. Counter-intuitively, if we look carefully at panel (a) we can see that after the initial growth phase, the energy for $S = 1$ grows to slightly overtake that for $S = 1.5$. This was also observed in some cases in BJT2, and is potentially related to the relatively stronger, larger wavelength, and potentially more stable (to parasitic shear instabilities) zonal jets for lower shears.

However the AM transport, shown via $\langle u_x u_y \rangle$, in the final steady state is in all cases ordered in the way predicted by their initial linear growth rates, with larger S cases providing larger $\langle u_x u_y \rangle$. Adiabatically unstable cases have more energetic flows and provide higher levels of AM transport than GSF unstable cases, indicating that when the Solberg-Høiland stability criteria (i.e. Eq. 3.10) are violated in stars we would expect much more rapid dynamical evolution.

4.3.2 Dependence on box size

In order to verify whether the nonlinear results for our local simulations might be applicable to astrophysical objects we must check whether the nonlinear saturation properties of each instability depend on the box size. To do this, we performed additional simulations with $S = 2$ at a latitude of $\Lambda + \phi = 30°$ with $L_x = L_y = L_z = 200d$ and $300d$, and with appropriate spatial resolutions (as indicated in 4.1), for both a GSF unstable case with $\Lambda = 60°$ and $\phi = -30°$, and an adiabatically unstable case with $\Lambda = -60°$ and $\phi = 90°$. Results are shown in Figs. 4.8 and 4.9 for the mean kinetic energy and AM transport. In order to ensure the smallest scales remain well resolved even in larger boxes, we increase our resolutions as specified in Table 4.1.

Fig. 4.8 demonstrates that AM transport ($\langle u_x u_y \rangle$) in GSF-unstable cases is approximately independent of box size. This is a very promising and important result, since it indicates that the turbulent transport predicted by our simulations is robust, and can potentially be applied to model AM evolution in stars (once other parameters have been adjusted). The smallest L_x case is more bursty than the flow in larger boxes, but the mean values are very similar throughout its evolution. The kinetic energy attained in the final state is also very similar, though this varies slightly more as the box is enlarged. These results are consistent, but not obvious, from the fact that the GSF instability has preferred wave-vector magnitude in linear theory, as predicted by Fig. 3.4. This useful result means that the results from this the-

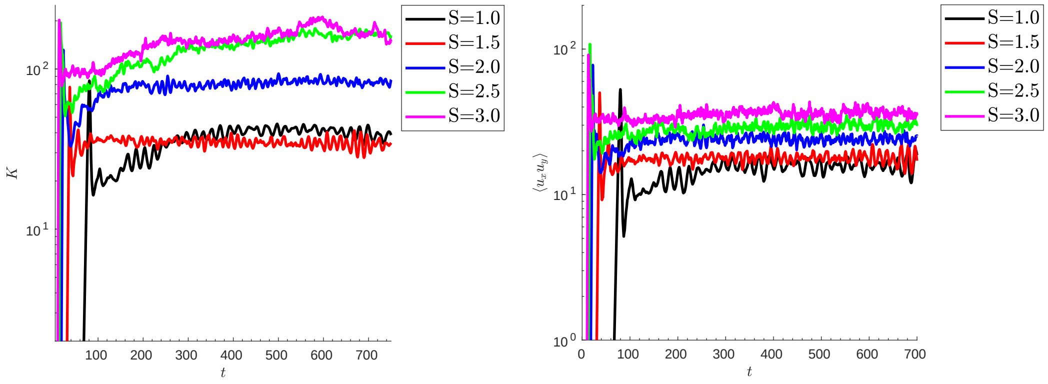

(a) $\Lambda = 60^\circ, \phi = -30^\circ$ (b) $\Lambda = 60^\circ, \phi = -30^\circ$

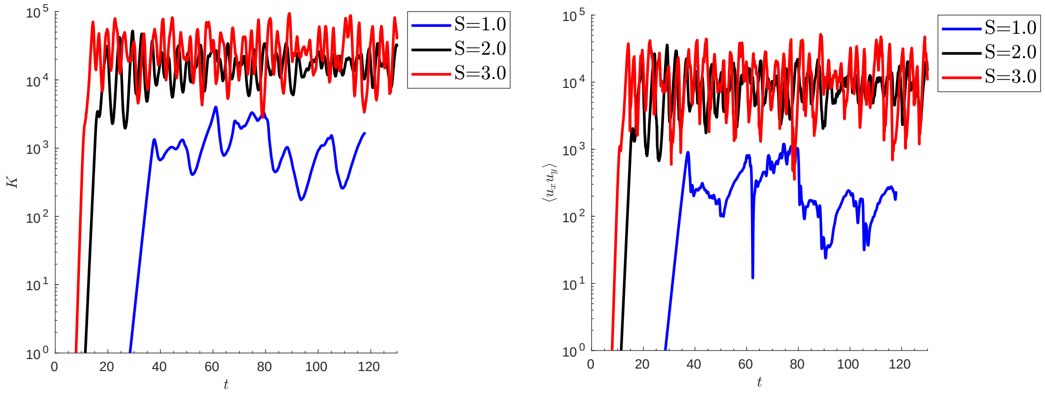

(c) $\Lambda = -60^\circ, \phi = 90^\circ$ (d) $\Lambda = -60^\circ, \phi = 90^\circ$

Figure 4.7: Dependence of mean kinetic energy and AM transport (Reynolds stress) on shear flow strength S for two different shear orientations. Panels (a) and (b) show a case with $\Lambda = 60^\circ$ and $\phi = -30^\circ$ that is GSF-unstable when $S = 2$, and panels (c) and (d) show a case with $\Lambda = -60^\circ$ and $\phi = 90^\circ$ that is an adiabatically unstable when $S = 2$. Both of these are at $\Lambda + \phi = 30^\circ$ latitude with $N^2 = 10$ and $\mathrm{Pr} = 10^{-2}$. AM transport in the final steady states are well ordered with respect to initial linear growth rates. K is not however, perhaps due to the relatively stronger and larger wavelength zonal jets for $S = 1$. Note that every shear strength we tested for $\Lambda = 60^\circ$ and $\phi = -30^\circ$ was GSF unstable and similarly every $\Lambda = -60^\circ$ and $\phi = 90^\circ$ case was adiabatically unstable.

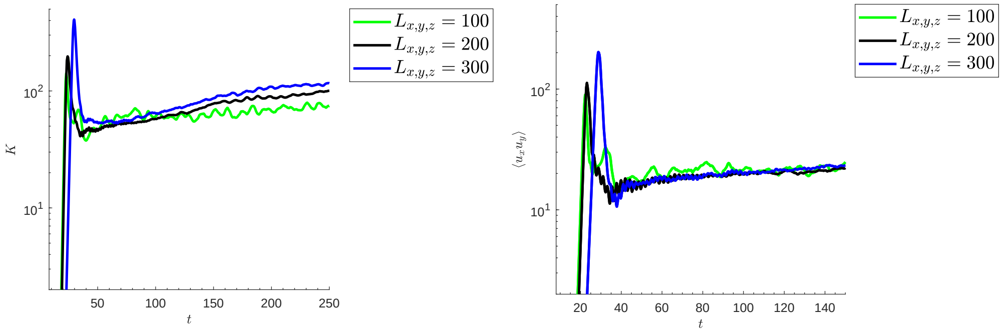

(a) $\Lambda = 60^\circ, \phi = -30^\circ$ (b) $\Lambda = 60^\circ, \phi = -30^\circ$

Figure 4.8: Dependence of K and $\langle u_x u_y \rangle$ on box size for the GSF instability at a latitude $\Lambda + \phi = 30^\circ$, where we vary each of (L_x, L_y, L_z). We fix $S = 2$, $N^2 = 10$, $\mathrm{Pr} = 10^{-2}$, $\Lambda = 60^\circ$ and $\phi = -30^\circ$. The AM transport is approximately independent of box size, and K only depends weakly on it, implying that we can potentially extrapolate results in this GSF-unstable regime to stars.

sis, within the GSF unstable regime, can be applied to astrophysical problems with confidence.

On the other hand, Fig. 4.9 shows that both the kinetic energy and AM transport in adiabatically unstable cases that violate Eq. 3.10 exhibit a strong dependence on box size. This might be predicted from linear theory, because in this regime there is a preferred orientation but not a preferred wavevector magnitude for adiabatic instability, and Fig. 3.4 indicates that in this regime the fastest growing mode in

	N_x	N_y	N_z
GSF unstable $(\phi = -30^\circ\ \Lambda = 60^\circ)$			
$L_{x,y,z} = 100$	256	256	256
$L_{x,y,z} = 200$	512	256	512
$L_{x,y,z} = 300$	512	512	512
Adiabatically unstable $(\phi = 90^\circ\ \Lambda = -60^\circ)$			
$L_{x,y,z} = 100$	256	256	256
$L_{x,y,z} = 200$	512	256	512
$L_{x,y,z} = 300$	512	512	512

Table 4.1: Table of resolutions (number of grid points in each dimension before dealiasing) used when testing the effects of boxsize on the nonlinear properties of both types of instability. Cases with $L_{x,y,z} = 100$ were also re-run with higher resolution but no differences were found over the original resolution.

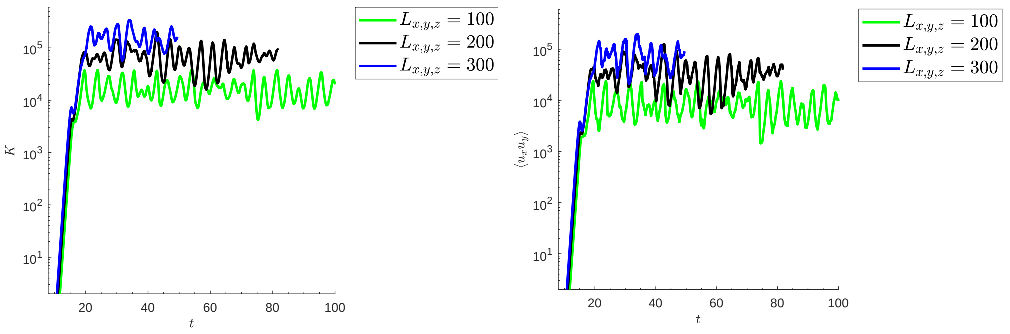

(a) $\Lambda = -60°, \phi = 90°$ (b) $\Lambda = -60°, \phi = 90°$

Figure 4.9: Dependence of K and $\langle u_x u_y \rangle$ on box size for the adiabatic instability at a latitude $\Lambda + \phi = 30°$, where we vary each of (L_x, L_y, L_z). We fix $S = 2$, $N^2 = 10$, $\mathrm{Pr} = 10^{-2}$, $\Lambda = -60°$ and $\phi = 90°$. The strong dependence on box size implies that results obtained in this regime in our local model cannot be reliably extrapolated to stars.

the presence of diffusion has $k \to 0$. As a result, the wavelengths of the fastest growing modes grow without bound to fit within the box. Fig. 4.9 verifies that in this regime, where the mechanism limiting k is the box size, then the nonlinear properties of the instability also depend on it. While this leads to a violent instability that transports AM very efficiently, our results in this regime cannot therefore be reliably extrapolated to stars and planets due to this clear box size dependence. To simulate this regime reliably, we would either need to know a reliable box size for our model in terms of our length scale d, or we would need to use models with non-linear shear profiles, different geometries, or which incorporate other effects that could introduce a preferred scale or limit the wavelengths of the modes (e.g., inclusion of the β effect or compressibility).

4.3.3 Momentum transport as a function of ϕ

In Fig. 4.10, we summarise the mean Reynolds stress components $\langle u_x u_y \rangle$, $\langle u_x u_z \rangle$ and $\langle u_y u_z \rangle$ as a function of ϕ, after performing both spatial and temporal averaging in the final turbulent state (after layer mergers). The angular momentum transport is quantified by $\langle u_x u_y \rangle$, whereas the other two would correspond with turbulent driving of mean flows/circulations in the meridional plane.

Out of all the GSF-unstable (but adiabatically stable) cases studied, we found mixed radial/latitudinal shears ($\phi \neq 0°$) and particularly latitudinal shears ($\phi \sim \pm 90°$) at the equator ($\Lambda + \phi = 0°$) to lead to the most transport. As shown in Fig. 4.10, purely latitudinal shears are the most unstable and produce AM transfer over three orders of magnitude greater than we previously found in BJT2 for the case of radial differential rotation ($\phi = 0°$). The increased transport properties when ($|\phi| \sim 90°$) are at least in part due to the nearly perpendicular directions of the buoyancy and shear, such that buoyancy restoring forces are expected to be weaker. This nonlinear finding is consistent with the linear results shown in Fig. 3.5, which suggests that the configuration is least stable near the equator for $|\phi| \sim 90°$ compared both with $\phi = 0°$ and with other latitudes in the GSF-unstable regime. On the other hand, adiabatically-unstable cases generally have much larger transport than the GSF-unstable ones for a latitude of 30°. It is interesting that in the GSF-unstable regime, $\langle u_x u_y \rangle$ is only weakly dependent on ϕ for latitude 30°.

In summary, we have found that the GSF instability is typically much more efficient at transporting momentum in stars with mixed radial/latitudinal or purely latitudinal differential rotations vs the shellular (radial) case, particularly near the equatorial regions. When adiabatic instability occurs, it also significantly enhances the transport. The most efficient transport is found near the equator for primarily latitudinal differential rotation profiles. A configuration with purely latitudinal shear at the equator would be unusual, but this tendency for predominantly horizontal shears to be more unstable and to transport momentum more efficiently than vertical/radial shears, and for the growth rates and transport rates for primarily horizontal shears to be maximised near the equator are the general trends we have observed. Note that $\langle u_x u_y \rangle$ for a purely latitudinal shear would correspond with latitudinal transport of angular momentum, which we have shown is generally much more efficient than radial transport. When $\phi \neq 0°$, $\langle u_x u_y \rangle$ does not correspond with radial momentum transport, as would be most commonly parameterised in 1D

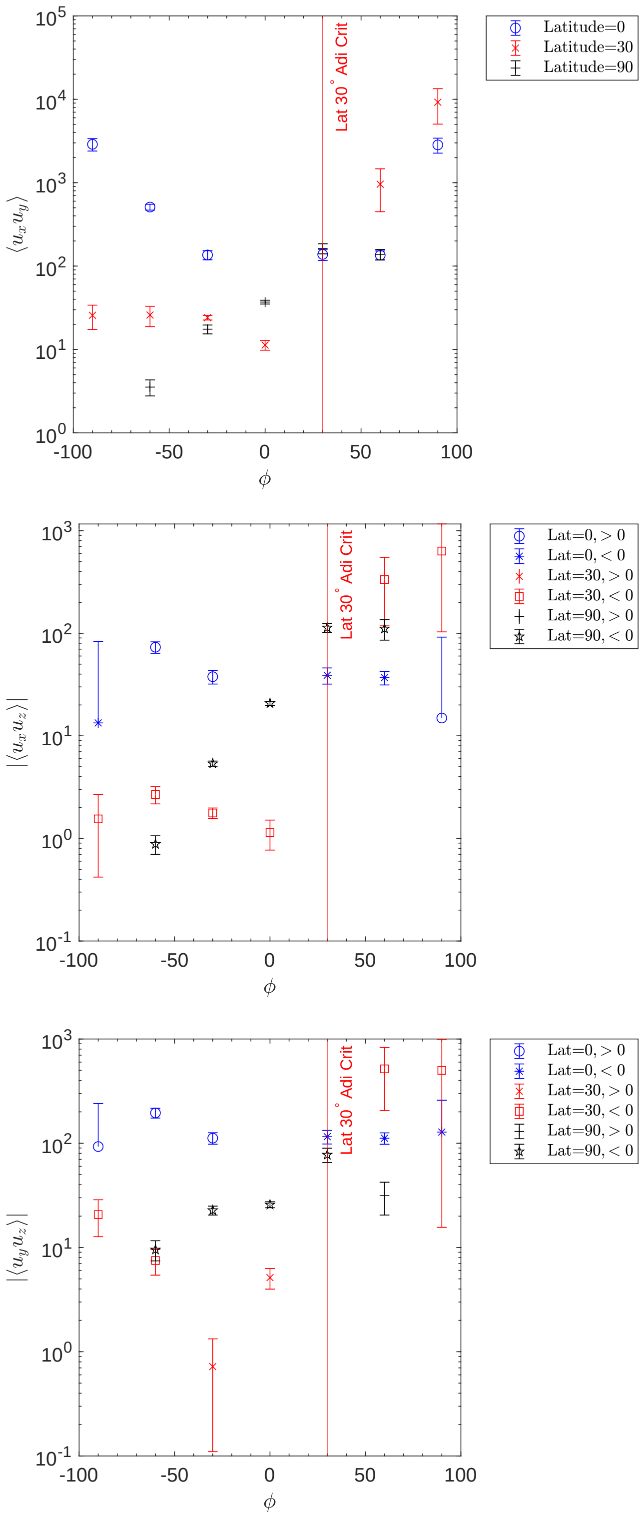

Figure 4.10: Figure showing the Reynolds stresses (and hence momentum transport) as a function of ϕ for various latitudes. The mean value in each case is calculated once the instability has reached its final turbulent/layered state after mergers, and the error bars indicating fluctuations are the standard deviations from the mean. All the latitude $= 0^\circ$ and 90° cases are GSF unstable (adiabatically stable) and adiabatically unstable cases occur for latitude $= 30^\circ$ after the vertical red lines at $\phi = 30^\circ$.

stellar models. Indeed, it is unclear how relevant 1D stellar models with rotation – even with a suitable parameterisation for turbulent transport – would be at capturing the long-term consequences of angular momentum transport due to these (and other) fluid and MHD instabilities.

4.4 Conclusions

The research in this chapter has revolved around understanding the nonlinear effects of varying shear orientation, parameterised by the angle ϕ, on the GSF instability and quantifying the resultant turbulent transport.

Our simulations were performed using the 3D incompressible Fourier code SNOOPY, which was originally developed by Lesur and Longaretti (2005) to simulate local instabilities in accretion disks. We've worked in a Cartesian geometry (following Chapter 2) with shear periodic boundary conditions that are automatically satisfied thanks to the use of time-dependent wave vectors (shearing waves).

Through a combination of figures showing time series of volume-averaged flow quantities and snapshots of the flow (4.1-4.6), we've seen a strong dependence of the dynamics on variations in ϕ. Initially at ($t \approx 10$) we saw the development of AM fingers with an orientation and strength that closely followed the predictions made in Chapter 3. By ($t \approx 50$) parasitic instabilities had started to turn the system turbulent, and by ($t \approx 100$) nearly all simulations had become layered, some of which exhibited merges by our final snapshot ($t \approx 250$). Such mergers led to larger scale jets and correspondingly higher levels of turbulent transport.

Varying S showed that, on a whole, increases in the strength of the background shear generally leads to higher angular momentum transport in the final layered system.

Simulations run with various box dimensions (L_x, L_y, L_z) showed that the preferred $|k|$ for the GSF instability seen in Fig. 3.4 lead to consistent results across boxes of different sizes. This suggests that our simulations capture the transport well in GSF unstable cases, potentially allowing us to extrapolate our results to astrophysical objects. However, the lack of a preferred $|k|$ for cases within the adiabatic regime (also observed in Fig. 3.4) manifested itself as a strong dependence on the dimensions of the box. These results ultimately suggest that it would be difficult to draw astrophysically-relevant conclusions from cases in this regime.

In terms of practical applications the main result of this section has been that the AM transporting properties in a stably stratified, differentially rotating flow, can be significantly enhanced by mixed radial/latitudinal shears over purely radial ones. Since this level of detail is not currently incorporated into stellar evolution modes it may account for some of the discrepancies that are observed between theoretical predictions and helioseismic observations that further work should explore in more detail.

Whilst a rigorous stability analysis has not yet been conducted on the quasi-stably layered state, larger layers were observed to support more angular momentum transport than several smaller layers over the same box size. Note that we saw no indication of the number of layers increasing; rather, layers tended to combine to create larger layers and never split into an increasing number of layers. This suggests that over longer time scales, such as those in a physical system such as the tachocline, the transport properties would either increase or remain steady if this holds there. It could then be speculated that should the GSF instability operate in a physical system such as the solar tachocline, the jets may eventually grow to become large-scale, stable structures that enhance what are currently believed to be the transporting properties in the tachocline. Along with the possible dynamo-generating properties of the jets, these factors make the final system particularly interesting to study.

Whilst the value of S in the solar tachocline is generally thought to be less than 2, the relatively stable nature of the jets suggests the possibility that jets may have formed during the Sun's earlier stages of evolution, when it was more rapidly rotating, with stronger shears. During this period, S may have been significantly larger (and closer to our 'standard' choice $S = 2$) than what is currently observed.

The results from this chapter, in combination with those from BJT1 and BJT2 have explored in detail the linear and nonlinear properties of the hydrodynamical system. However, astrophysical bodies are rarely non-magnetic and are highly likely to exhibit dynamically important magnetic fields. Such fields constrain the system to not only be described by Newtonian laws of motion but also to Maxwell's laws of electromagnetism (supplemented by the Lorentz force). The combination of these sets of equations leads to new, complex interactions, and magnetic fields are known to drastically alter the dynamics of many astrophysical systems. As such it's a natural step to next consider the implications of including such fields in our system.

Chapter 5

Linear stability of magnetised differentially rotating radiative regions

5.1 Introduction

In this thesis chapter, we study the local axisymmetric magnetohydrodynamical instabilities of differential rotation in magnetised and stably-stratified regions of stars and planets. We use a small-scale Cartesian Boussinesq model at an arbitrary latitude and with the most general shear (so as to model radial, latitudinal, or mixed differential rotations) as we have studied hydrodynamically in Chapter 3. We study both non-diffusive instabilities (including magnetorotational, MRI, and adiabatic Solberg-Høiland instabilities) and diffusive ones (including GSF, and double-diffusive MRI). These instabilities could drive turbulent transport and mixing in stellar/planetary radiative regions, including the solar tachocline, but their linear and nonlinear dynamics are incompletely understood. We revisit linear axisymmetric instabilities with and without diffusion and analyse their properties in the presence of magnetic fields, including deriving stability criteria and computing growth rates, wavevectors and energetics, both analytically and numerically. We perform a more general analysis of axisymmetric local instabilities than prior work, exploring arbitrary orientations of the differential rotation and diffusive processes. The presence of a magnetic field leads to stability criteria depending upon angular velocity rather than angular momentum gradients, as has been found previously (Balbus, 1995).

The presence of even a weak magnetic field is known to drastically modify the stability of differentially-rotating flows (e.g. Chandrasekhar, 1961; Acheson & Gibbons, 1978; Balbus & Hawley, 1991). Stability criteria with magnetic fields tend to involve angular velocity gradients – which typically require much weaker differential rotations to ensure instability – rather than the angular momentum gradients without fields, because the field can act as a tether between fluid particles and allow them to exchange angular momentum. The magneto-rotational instability (MRI) is one such manifestation when a weak magnetic field is introduced into a differentially-rotating flow (e.g. Chandrasekhar, 1961; Acheson & Gibbons, 1978; Balbus & Hawley, 1991, 1994; Balbus, 1995; Spruit, 1999; Ogilvie, 2007; Balbus, 2009; Oishi et al., 2020; Vasil et al., 2024). This can operate and drive turbulence even in flows that would be hydrodynamically stable. Its operation in stably-stratified stellar interiors (i.e. radiation zones) in the presence of diffusive processes has been studied in some prior works (Menou et al., 2004; Menou & Le Mer, 2006; Parfrey & Menou, 2007; Guilet & Müller, 2015; Caleo & Balbus, 2016; Caleo et al., 2016), but much remains to be explored of its linear properties, and especially its nonlinear evolution in stars. Guilet and Müller, 2015 performed linear analysis and numerical simulations of the MRI in a local stably-stratified model of a proto-neutron star (with extra neutrino cooling). Our approach is broadly similar to theirs but we will study arbitrary local differential rotations. Global simulations in spherical geometry of the MRI (or Tayler instability that is also present in these) in stellar radiative zones have also been performed (Gaurat et al., 2015; Jouve et al., 2015; Meduri et al., 2019; Jouve et al., 2020), though these kinds of studies may not adequately represent all of the possible local instabilities. As in earlier chapters of this thesis, we choose to adopt a local model here, partly because such models are the simplest ones for studying small-scale MHD instabilities, and also because they can explore more realistic parameter regimes with numerical simulations (particularly with regards to smaller diffusivities) than global models would allow in the nonlinear regime.

Here we introduce magnetic fields to build directly upon Barker et al. (2019, hereafter BJT1), Barker et al. (2020, hereafter BJT2), and Chapters 3-4 that studied hydrodynamical instabilities in a local Cartesian representation of a small patch of a stably-stratified, differentially-rotating stellar or planetary radiation zone. A global "shellular" (radial) differential rotation varying only with spherical radius was considered at the equator in BJT1 (and an axisymmetric turbulence closure model was developed and verified for this case by Tripathi et al., 2024), and at a general latitude in BJT2. In Chapter 3, we generalised the model to consider an arbitrary differential rotation profile, which varies with both radius and latitude. Here we incorporate magnetic fields into this more general model. Following a similar approach, we perform an axisymmetric linear stability analysis here, which we will follow with complementary three-dimensional nonlinear numerical simulations in future work. Our primary goals are to understand the properties of the GSF instability in the magnetic system, the possibility of an additional double-diffusive MRI, and determining their potential roles in angular momentum transport, chemical mixing, and dynamo generation. Our linear study is related to the one undertaken by Latter and Papaloizou (2018) for the Vertical Shear Instability in astrophysical discs (e.g. Urpin & Brandenburg, 1998; Nelson et al., 2013; Barker & Latter, 2015), which is the same as the GSF instability in that context.

The goal of this chapter is to gain insights into how the presence of a locally uniform magnetic field affects the linear properties of local magnetohydrodynamical instabilities of differential rotation in stellar and planetary radiative zones. We determine how the properties of the unstable modes depend on magnetic field strength B_0 and magnetic Prandtl number $\mathrm{Pm} = \nu/\eta$ (the ratio of kinematic viscosity ν to ohmic

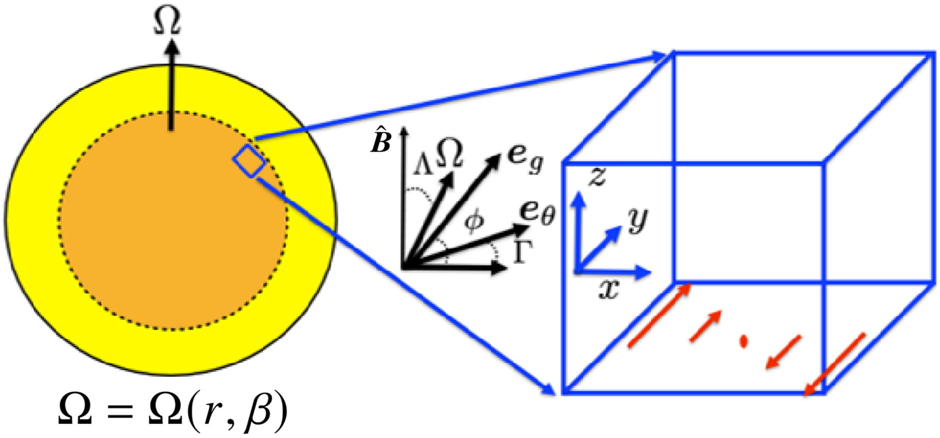

Figure 5.1: Illustration of the various vectors and corresponding angles in the context of our local box model. The cylindrical radial direction (along the equator) is $\hat{\boldsymbol{\Omega}}^{\perp}$, and the rotation axis is $\hat{\boldsymbol{\Omega}}$. The local radial direction is (approximately) along the effective gravity direction $\boldsymbol{e}_g$, which is misaligned with respect to the x-direction when ϕ is nonzero. The magnetic field in linear theory is always along z (therefore perpendicular to the shear in x), which is the only direction in the meridional plane in which a steady equilibrium exists.

diffusivity η). This is accompanied by an analysis of the energetics of the various instabilities in our model and derivations of several new results.

5.2 Local Cartesian model

We follow Chapter 2 by employing a local Cartesian box model to study small-scale magnetohydrodynamical instabilities of differential rotation in a stably-stratified region of a star or planet.

We build upon the hydrodynamical studies of BJT1, BJT2 and the results seen in Chapters 3 and 4 by now introducing a uniform static background poloidal magnetic field $\boldsymbol{B}_0 = B_0\hat{\boldsymbol{B}}$ that is in equilibrium, satisfying the local analogue of Ferraro's law of isorotation (Ferraro, 1937). For this flow to be in equilibrium in the meridional/poloidal (x, z) plane, it must lie along z with $\hat{\boldsymbol{B}} = (0, 0, 1)$, being always perpendicular to variation of the shear flow $\boldsymbol{U}_0$ locally. This permits a well-defined equilibrium state even if it may complicate interpretation of our model because the field is not purely radial or horizontal, depending on the value of ϕ. The field is radial if $\phi = \pm 90^\circ$ and it is latitudinal if $\phi = 0^\circ, \pm 180^\circ$. We do not consider toroidal/azimuthal fields in our linear analysis, which are typically thought to be dominant in the solar tachocline, because they play no role for local linear incompressible axisymmetric perturbations. They can, however, affect global perturbations through hoop stresses (Mamatsashvili et al., 2019), but we will not pursue this here. A toroidal field would affect non-axisymmetric perturbations (e.g. Ogilvie & Pringle, 1996; Hollerbach et al., 2010) but analysing those (and their non-modal growth) is less straightforward, and it is likely that axisymmetric instabilities are the fastest growing ones in any case (e.g. Latter & Papaloizou, 2018). An initially purely toroidal field can play a role nonlinearly even if the linear instability is axisymmetric however, so future nonlinear simulations should explore these fields, also because of their possible role in driving non-axisymmetric instabilities.

The incompressible MHD equations governing perturbations to the shear flow $\boldsymbol{U}_0$ and background stable stratification in the Boussinesq approximation, in the frame rotating at the rate $\boldsymbol{\Omega}$, are

$$D\boldsymbol{u} + 2\boldsymbol{\Omega} \times \boldsymbol{u} + \boldsymbol{u} \cdot \nabla \boldsymbol{U}_0 = -\nabla p + \theta \boldsymbol{e}_g + \boldsymbol{B} \cdot \nabla \boldsymbol{B} + \nu \nabla^2 \boldsymbol{u}, \tag{5.1}$$

$$D\theta + \mathcal{N}^2 \boldsymbol{u} \cdot \boldsymbol{e}_\theta = \kappa \nabla^2 \theta, \tag{5.2}$$

$$D\boldsymbol{B} = \boldsymbol{B} \cdot \nabla \boldsymbol{u} + \boldsymbol{B} \cdot \nabla \boldsymbol{U}_0 + \eta \nabla^2 \boldsymbol{B}, \tag{5.3}$$

$$\nabla \cdot \boldsymbol{B} = 0, \tag{5.4}$$

$$\nabla \cdot \boldsymbol{u} = 0, \tag{5.5}$$

$$D \equiv \partial_t + \boldsymbol{u} \cdot \nabla + \boldsymbol{U}_0 \cdot \nabla. \tag{5.6}$$

Here the temperature perturbation θ is defined as in Chapter 2. We use Alfvén speed units for the magnetic field, such that the dimensional magnetic field is $\boldsymbol{B}/\sqrt{\mu_0 \rho}$, where ρ is the constant reference density that we henceforth set to unity and μ_0 is the vacuum permeability. Magnetic pressure is contained within the total pressure p.

We again expect the star to adjust rapidly to satisfy thermal wind balance, and

Λ	ϕ	Differential rotation	Magnetic field
0	-	$\Omega(\varpi)$ (cylindrical)	arbitrary
$\pm 90°$	-	$\Omega(z)$ (axial variation)	arbitrary
-	0	$\Omega(r)$ (spherical/shellular)	horizontal/latitudinal
-	$\pm 90°$	$\Omega(\beta)$ (horizontal/latitudinal)	radial
-	-	$\Omega(r, \beta)$ (arbitrary)	arbitrary

Table 5.1: Table of differential rotation profiles and magnetic field orientations (in the meridional plane) as Λ and ϕ are varied. Here β is latitude, z is distance along rotation axis, r is spherical radius and ϖ is cylindrical radius.

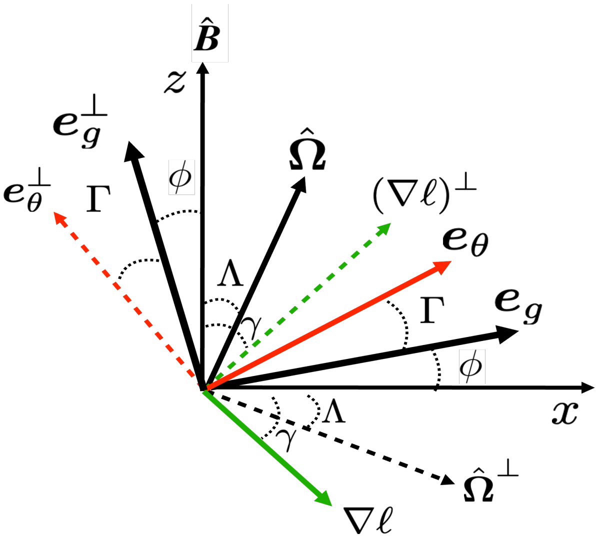

Figure 5.2: Illustration of the key vectors and corresponding angles in the (x, z)-plane. The cylindrical radial direction (along the equator) is along $\hat{\boldsymbol{\Omega}}^\perp$, and the rotation axis is along $\hat{\boldsymbol{\Omega}}$. The local radial direction is (approximately) along the effective gravity direction $\boldsymbol{e}_g$, which is misaligned with respect to the x-direction when ϕ is nonzero. The magnetic field is along z.

enforcing this requirement eliminates the angle Γ as a free parameter as in Chapters 2-4. This means that $\boldsymbol{U}_0$ and its thermal state satisfy the thermal wind equation. This is unaffected by our magnetic field $\boldsymbol{B}_0$. The representation of various global differential rotation profiles and magnetic field orientations in our local model are summarised in Table 5.1. We also illustrate the various angles in our problem in Fig. 5.2. See Chapter 2 for further details of the non-magnetic model. As before we use units defined by the rotational timescale, Ω^{-1}, and lengthscale d since the fastest growing hydrodynamic (GSF) modes typically have wavelengths $O(d)$. Note that with the addition of a magnetic field, it is not clear that unstable modes will necessarily have lengthscales $O(d)$, and in fact, we will show that MRI modes may have much larger scales. However, for comparison with BJT1, BJT2, and earlier chapters, and for comparing GSF and MRI modes, we continue to adopt this choice of non-dimensionalisation here.

5.3 Linear theory

We consider linear perturbations to our flow $\boldsymbol{U}_0$, thermal state, and magnetic field $\boldsymbol{B}_0$. From Eqs. 5.1–5.6, such velocity ($\boldsymbol{u}$), magnetic ($\boldsymbol{B}$), pressure (p) and temperature (θ) perturbations are described by (where we have avoided introducing hats on perturbations)

$$D\boldsymbol{u} + 2\boldsymbol{\Omega} \times \boldsymbol{u} + \boldsymbol{u} \cdot \nabla \boldsymbol{U}_0 = -\nabla p + \theta \boldsymbol{e}_g + \boldsymbol{B}_0 \cdot \nabla \boldsymbol{B} + \nu \nabla^2 \boldsymbol{u}, \tag{5.7}$$

$$D\theta + \mathcal{N}^2 \boldsymbol{u} \cdot \boldsymbol{e}_\theta = \kappa \nabla^2 \theta, \tag{5.8}$$

$$D\boldsymbol{B} = \boldsymbol{B}_0 \cdot \nabla \boldsymbol{u} + \boldsymbol{B} \cdot \nabla \boldsymbol{U}_0 + \eta \nabla^2 \boldsymbol{B}, \tag{5.9}$$

$$\nabla \cdot \boldsymbol{B} = 0, \tag{5.10}$$

$$\nabla \cdot \boldsymbol{u} = 0, \tag{5.11}$$

$$D \equiv \partial_t + \boldsymbol{U}_0 \cdot \nabla. \tag{5.12}$$

Note that we have defined our field and flow to satisfy $\boldsymbol{B}_0 \cdot \nabla \boldsymbol{U}_0 = 0$ so that the basic state is an equilibrium configuration. Note that this restriction was *not* made in many prior works, including Balbus and Hawley, 1994; Menou et al., 2004; Menou and Le Mer, 2006, but it is necessary to have a well-defined static basic state. Having a time-dependent basic state also makes results obtained for any other poloidal field configuration difficult to interpret.

5.3.1 Derivation of the magnetic dispersion relation

To understand the stability in our system, we first need to derive the dispersion relation. We start with the same hydrodynamic equations describing the viscous rotating shear flow with gravity in the $\boldsymbol{e}_g$ direction as before, but this time including a magnetic field $\boldsymbol{B}_0 = (0, 0, B_0)$. Hence, we have the momentum equation with additional magnetic tension and pressure terms. The variables are represented as:

$$\boldsymbol{U} \to \boldsymbol{U}_0 + \boldsymbol{u}, \quad p \to p + \tilde{p}, \quad \rho \to \rho + \tilde{\rho}, \quad T \to T + \tilde{T}, \quad \boldsymbol{B} \to \boldsymbol{B}_0 + \boldsymbol{b}. \tag{5.13}$$

Writing our equations out in component form, we have the momentum equation:

$$\partial_t u_x - 2\Omega c_\Lambda u_y = -\partial_x \tilde{p} + \theta c_\phi + \nu u_{xx} + B_0 \partial_z b_x, \tag{5.14}$$

$$\partial_t u_y - 2\Omega \left(s_\Lambda u_z - c_\Lambda u_x\right) - \mathcal{S} u_x = -\partial_y \tilde{p} + \nu u_{yy} + B_0 \partial_z b_y, \tag{5.15}$$

$$\partial_t u_z + 2\Omega s_\Lambda u_y = -\partial_z \tilde{p} + \theta s_\phi + \nu u_{zz} + B_0 \partial_z b_z. \tag{5.16}$$

The heat equation is:

$$\partial_t \theta - \mathcal{S} x \partial_z \theta + \mathcal{N}^2 \left(u_x c_\Gamma + u_z s_\Gamma\right) = \kappa \left(\theta_{xx} + \theta_{yy} + \theta_{zz}\right). \tag{5.17}$$

The induction equation is:

$$\partial_t b_x = B_0 \partial_y u_x + \eta \partial^2_{xx} b_x, \tag{5.18}$$

$$\partial_t b_y - \mathcal{S} x \partial_y b_y = B_0 \partial_z u_y - b_x \mathcal{S} + \eta \partial^2_{yy} b_y, \tag{5.19}$$

$$\partial_t b_z = B_0 \partial_z u_z + \eta \partial^2_{zz} b_z. \tag{5.20}$$

We consider axisymmetric modes with meridional wavevectors $\boldsymbol{k} = (k_x, 0, k_z) = k\left(\cos\theta_k, 0, -\sin\theta_k\right)$ with magnitudes $k = \sqrt{k_x^2 + k_z^2}$ and angles θ_k, since axisymmetric modes are likely to be the fastest growing (e.g. Latter & Papaloizou, 2018). These permit complex exponential solutions proportional to $\exp\left(\mathrm{i}k_x x + \mathrm{i}k_z z + st\right)$. We define the complex growth rate $s = \sigma + \mathrm{i}\omega$, where the growth (decay) rate $\sigma \in \mathbb{R}$ and the oscillation frequency $\omega \in \mathbb{R}$. Doing so we obtain:

$$\left(s + \nu k^2\right) u_x - 2\Omega c_\Lambda u_y = -\mathrm{i}k_x p + \theta c_\phi + \mathrm{i}\left(\boldsymbol{B}_0 \cdot \boldsymbol{k}\right) b_x, \tag{5.21}$$

$$\left(s+\nu k^2\right) u_y - 2\Omega\left(s_\Lambda u_z - c_\Lambda u_x\right) - \mathcal{S} u_x = \mathrm{i}\left(\boldsymbol{B}_0 \cdot \boldsymbol{k}\right) b_y, \tag{5.22}$$

$$\left(s+\nu k^2\right) u_z + 2\Omega s_\Lambda u_y = -\mathrm{i} k_z p + \theta s_\phi + \mathrm{i}\left(\boldsymbol{B}_0 \cdot \boldsymbol{k}\right) b_z. \tag{5.23}$$

For the heat equation, we have:

$$\left(s+\kappa k^2\right) \theta = -\mathcal{N}^2\left(u_x c_\Gamma + u_z s_\Gamma\right). \tag{5.24}$$

For the induction equation:

$$\left(s+\eta k^2\right) b_x = B_0 \partial_z u_x, \tag{5.25}$$

$$\left(s+\eta k^2\right) b_y = B_0 \partial_z u_y, -b_x \mathcal{S} \tag{5.26}$$

$$\left(s+\eta k^2\right) b_z = B_0 \partial_z u_z, \tag{5.27}$$

alongside the solenoidal and conservation of mass equations:

$$k_x u_x + k_z u_z = 0, \tag{5.28}$$

and

$$k_x b_x + k_z b_z = 0. \tag{5.29}$$

It's helpful to rewrite $s_\nu = s+\nu k^2, s_\kappa = s+\nu k^2, s_\eta = s+\nu k^2$. By rearranging the induction and conservation equations, we may also obtain expressions for u_x and b_x. By doing so, we quickly obtain helpful new forms for some of the variables,

$$u_z = -\frac{k_x}{k_z} u_x, \tag{5.30}$$

$$b_z = -\frac{k_x}{k_z} b_x, \tag{5.31}$$

$$b_x = \frac{\mathrm{i}\boldsymbol{B}_0 \cdot \boldsymbol{k}}{s_\eta} u_x, \tag{5.32}$$

$$b_z = \frac{\mathrm{i}\boldsymbol{B}_0 \cdot \boldsymbol{k}}{s_\eta} u_z, \tag{5.33}$$

and using the above expression for b_x:

$$b_y = -\frac{\mathrm{i}\mathcal{S}\boldsymbol{B}_0 \cdot \boldsymbol{k}}{s_\eta^2} u_x + \frac{\mathrm{i}\boldsymbol{B}_0 \cdot \boldsymbol{k}}{s_\eta} u_y. \tag{5.34}$$

We can now write θ as,

$$\theta = -\frac{\mathcal{N}^2}{s_\kappa}\left(c_\Gamma - \frac{k_x}{k_z} s_\Gamma\right) u_x. \tag{5.35}$$

Using these expressions in the y-component of the momentum equation, we obtain,

$$u_y = \frac{s_\eta}{s_\nu s_\eta + \mathrm{i}\left(\boldsymbol{B}_0 \cdot \boldsymbol{k}\right)^2}\left(\mathcal{S}\left(1 + \frac{\left(\mathrm{i}\boldsymbol{B}_0 \cdot \boldsymbol{k}\right)^2}{s_\eta^2}\right) - 2\Omega\left(c_\Lambda + \frac{k_x}{k_z} s_\Lambda\right)\right) u_x. \tag{5.36}$$

We can then compute the y-component of the vorticity equation to eliminate p giving,

$$s_\nu(k_z u_x - k_x u_z) - 2\Omega(c_\Lambda k_z + s_\Lambda k_x) u_y = (k_z c_\phi - k_x s_\phi)\theta + i(\boldsymbol{B}_0 \cdot \boldsymbol{k})^2 (k_z b_x - k_x b_z), \tag{5.37}$$

which we can combine with the previous information to determine the dispersion relation,

$$\begin{aligned} &\frac{k^2}{k_z}\left(s_\nu + \frac{\mathrm{i}\left(\boldsymbol{B}_0 \cdot \boldsymbol{k}\right)^2}{s_\eta}\right) + \frac{\mathcal{N}^2\left(k_z c_\Gamma - k_x s_\Gamma\right)\left(k_z c_\phi - k_x s_\phi\right)}{s_\kappa} - \\ &\frac{2\Omega s_\eta\left(c_\Lambda k_z + s_\Lambda k_x\right)}{s_\nu s_\eta + \mathrm{i}\left(\boldsymbol{B}_0 \cdot \boldsymbol{k}\right)^2}\left(\mathcal{S}\left(1 + \frac{\left(\mathrm{i}\boldsymbol{B}_0 \cdot \boldsymbol{k}\right)^2}{s_\eta^2}\right) - 2\Omega\left(c_\Lambda + \frac{k_x}{k_z} s_\Lambda\right)\right) = 0. \end{aligned} \tag{5.38}$$

Multiplying by $\frac{k_z}{k^2}\left(s_\nu + \frac{\mathrm{i}(\boldsymbol{B}_0 \cdot \boldsymbol{k})^2}{s_\eta}\right)$ and using our definition of $b = (k_z c_\Gamma - k_x s_\Gamma)(k_z c_\phi - k_x s_\phi)$, defining $\omega_A^2 = (\boldsymbol{B}_0 \cdot \boldsymbol{k})^2$ and rewriting in terms of vectors where possible we obtain:

$$\left(s_\nu + \frac{\omega_A^2}{s_\eta}\right)^2 + b\frac{\mathcal{N}^2}{s_\kappa}\frac{k_z}{k^2}\left(s_\nu + \frac{\omega_A^2}{s_\eta}\right) - 2\Omega\left(c_\Lambda k_z + s_\Lambda k_x\right)\left(\mathcal{S}\left(1 + \frac{\omega_A^2}{s_\eta^2}\right) - 2\Omega\left(c_\Lambda + \frac{k_x}{k_z} s_\Lambda\right)\right) = 0, \tag{5.39}$$

or (multiplying through by $s_\eta^2 s_\kappa$),

$$\begin{aligned} & s_\kappa \left(s_\eta s_\nu + \omega_A^2\right)^2 + s_\eta b \mathcal{N}^2 \frac{k_z}{k^2}\left(s_\nu s_\eta + \omega_A^2\right) \\ & - 2\left(\boldsymbol{\Omega}\cdot\hat{\boldsymbol{k}}\right) s_\kappa \left(\mathcal{S}\left(s_\eta^2 + \omega_A^2\right) - 2\Omega s_\eta^2 (c_\Lambda + \frac{k_x}{k_z} s_\Lambda)\right) = 0. \end{aligned} \tag{5.40}$$

Manipulating the above equation one can obtain the quintic dispersion relation in the form,

$$s_\eta^2 s_\nu^2 s_\kappa + 2 s_\eta s_\nu s_\kappa \omega_A^2 + s_\kappa \omega_A^4 + a s_\eta^2 s_\kappa + s_\kappa \xi + b(s_\eta^2 s_\nu + s_\eta \omega_A^2) = 0, \tag{5.41}$$

where

$$\begin{aligned} a &= \frac{2}{\varpi}\left(\hat{\boldsymbol{k}}\cdot\boldsymbol{\Omega}\right)\left(\hat{\boldsymbol{k}}\cdot(\nabla\ell)^\perp\right), \\ &= \frac{2\Omega}{k^2}\left(s_\Lambda k_x + c_\Lambda k_z\right)\left(2\Omega k_x s_\Lambda + \left(2\Omega c_\Lambda - \mathcal{S}\right)k_z\right), \\ &= \frac{2\Omega|\nabla\ell|}{\varpi} s_{\Lambda-\theta_k} s_{\gamma-\theta_k}, && (5.42) \\ b &= \mathcal{N}^2\left(\hat{\boldsymbol{k}}\cdot\boldsymbol{e}_\theta^\perp\right)\left(\hat{\boldsymbol{k}}\cdot\boldsymbol{e}_g^\perp\right), \\ &= \frac{\mathcal{N}^2}{k^2}(k_z c_\Gamma - k_x s_\Gamma)(k_z c_\phi - k_x s_\phi), \\ &= \mathcal{N}^2 s_{\theta_k+\phi} s_{\theta_k+\Gamma}, && (5.43) \\ \xi &= -2\left(\hat{\boldsymbol{k}}\cdot\boldsymbol{\Omega}\right)\mathcal{S}\omega_A^2 \frac{k_z}{k} = 2S\Omega s_{\Lambda-\theta_k} s_{\theta_k}\omega_A^2, && (5.44) \end{aligned}$$

and

$$\omega_A^2 = (\boldsymbol{B}_0\cdot\boldsymbol{k})^2 = k^2 B_0^2 s_{\theta_k}^2, \tag{5.45}$$

is the squared Alfvén frequency. We remind the reader that we have also defined the local angular momentum gradient

$$\nabla\ell = \varpi\left(2\Omega c_\Lambda - \mathcal{S}, 0, -2\Omega s_\Lambda\right), = |\nabla\ell|\left(c_\gamma, 0, -s_\gamma\right), \tag{5.46}$$

which has magnitude

$$|\nabla\ell|^2 = \varpi^2 \left(\mathcal{S}^2 + 4\Omega\left(\Omega - \mathcal{S}c_\Lambda\right)\right). \tag{5.47}$$

The normal to this is

$$(\nabla\ell)^\perp = \varpi\left(2\Omega s_\Lambda, 0, 2\Omega c_\Lambda - \mathcal{S}\right) = |\nabla\ell|(s_\gamma, 0, c_\gamma). \tag{5.48}$$

We also define the vector perpendicular to the effective gravity,

$$\boldsymbol{e}_g^\perp = (-s_\phi, 0, c_\phi), \tag{5.49}$$

and the normal to stratification surfaces,

$$\boldsymbol{e}_\theta^\perp = (-s_\Gamma, 0, c_\Gamma). \tag{5.50}$$

The baroclinic shear (along the rotation axis) is

$$\hat{\boldsymbol{\Omega}} \cdot (\nabla\ell) = -\mathcal{S}\varpi s_\Lambda = |\nabla\ell| s_{\gamma-\Lambda}. \tag{5.51}$$

The dispersion relation (5.41) can be expanded out as a quintic equation

$$s^5 + c_1 s^4 + c_2 s^3 + c_3 s^2 + c_4 s + c_5 = 0, \tag{5.52}$$

where the coefficients c_1 to c_5 are given by

$$c_1 = k^2(2\eta + 2\nu + \kappa), \tag{5.53}$$

$$c_2 = k^4(\eta^2 + 2\eta\kappa + 4\eta\nu + 2\nu\kappa + \nu^2) + 2\omega_A^2 + a + b, \tag{5.54}$$

$$\begin{aligned} c_3 = {} & k^6(\eta^2\kappa + 2\eta\nu^2 + 2\eta^2\nu + \kappa\nu^2 + 4\eta\kappa\nu) \\ & + 2\omega_A^2 k^2(\eta + \nu + \kappa) + ak^2(2\eta + \kappa) + bk^2(2\eta + \nu), \end{aligned} \tag{5.55}$$

$$c_4 = k^8(2\eta\nu^2\kappa + 2\eta^2\nu\kappa + \eta^2\nu^2) + 2\omega_a^2 k^4(\eta\nu + \eta\kappa + \nu\kappa)$$
$$+ \omega_A^4 + ak^4(2\eta\kappa + \eta^2) + \xi + bk^4(2\eta\nu + \eta^2) + b\omega_A^2, \tag{5.56}$$
$$c_5 = k^{10}\eta^2\nu^2\kappa + 2\omega_A^2 k^6\eta\nu\kappa + \omega_A^4 k^2\kappa + a\eta^2\kappa k^6$$
$$+ \xi k^2\kappa + bk^6\eta^2\nu + b\omega_A^2 k^2\eta. \tag{5.57}$$

5.3.2 Non-diffusive (in)stability

Non-diffusive modes, i.e. those with $\nu = \kappa = \eta = 0$, are described by the reduced dispersion relation

$$s^4 + \left(2\omega_A^2 + a + b\right) s^2 + \left(\omega_A^4 + b\omega_A^2 + \xi\right) = 0, \tag{5.58}$$

ignoring neutral modes with $s = 0$. Note that the only appearance of the magnetic field is through the combination $\boldsymbol{B}_0 \cdot \boldsymbol{k} = B_0 k_z$ in ω_A, therefore the adiabatic growth rate is independent of B_0 if arbitrary k_z are permitted. This can be solved to give

$$s^2 = \frac{-\left(2\omega_A^2 + a + b\right) \pm \sqrt{4a\omega_A^2 - 4\xi + (a+b)^2}}{2}. \tag{5.59}$$

If we take $B_0 = 0$ this reduces to the adiabatic dispersion relation Chapter 3, $s^2 = -(a + b)$. Since s^2 is always negative if $a + b$ is positive, with s being purely imaginary, then the system is Solberg-Høiland stable. The discriminant $\Delta = 4a\omega_A^2 - 4\xi + (a + b)^2$ in (5.58) is always positive (see below), so the roots for s^2 are always real. Hence, non-diffusive oscillatory instabilities cannot occur. To see this, note that from Eqs. 5.42 and 5.48 we have

$$\hat{\boldsymbol{k}} \cdot (\nabla \ell)^{\perp} = \varpi \left(2\left(\hat{\boldsymbol{k}} \cdot \boldsymbol{\Omega}\right) - \mathcal{S}\right), \tag{5.60}$$

and using the definition of ξ (Eq. 5.44),

$$\Delta = 4a\omega_A^2 - 4\xi + (a+b)^2 = (a+b)^2 + 8\omega_A^2 \left(\hat{\boldsymbol{k}} \cdot \boldsymbol{\Omega}\right)^2, \tag{5.61}$$

which being the sum of squares must be non-negative. The criterion for onset of direct instability (real roots) occurs when (for neutral stability $s = 0$)

$$\omega_A^4 + b\omega_A^2 + \xi = 0, \tag{5.62}$$

and instabilities occur when this term is negative. So the only way to destabilise a hydrodynamically Solberg-Høiland stable configuration without diffusion is for the left hand side of Eq. 5.62 to be negative, which corresponds with a direct instability, the MRI. For fixed $|k|$ the MRI works best with a weak field, meaning the stabilising term ω_A^4 is small compared to the others, and when the fluid is neutrally rather than stably stratified ($b = 0$). Then, MRI just requires a mode with a $\boldsymbol{k}$ which makes ξ negative. In the weak field or small wavenumber case, $\omega_A^4 \to 0$ faster than the remaining terms in Eq. 5.62, so for non-zero B_0, instability occurs if

$$b - 2\left(\hat{\boldsymbol{k}} \cdot \boldsymbol{\Omega}\right) \mathcal{S}\frac{k_z}{k} < 0. \tag{5.63}$$

Hence when $\Omega(\varpi)$, we have $N^2 - 2\Omega\mathcal{S} < 0$. If the stabilising effects of buoyancy can be eliminated by fast thermal diffusion when $\mathrm{Pr}/\mathrm{Pm} \to 0$, the stability criterion in the weak field case is $-2\Omega\mathcal{S} < 0$, which involves angular velocity rather than angular momentum gradients (e.g. Balbus & Hawley, 1998). So $\mathcal{S} > 0$ is required for instability (to MRI), which is generally much easier to satisfy than Rayleigh's criterion for centrifugal instability, which requires $\mathcal{S} > 2$ in the hydrodynamic case, implying outwardly decreasing angular momentum.

Marginal stability to stratified non-diffusive MRI

In order to find the non-diffusive unstable modes for weak fields we substitute $\boldsymbol{k} = k(\cos\theta_k, 0, -\sin\theta_k)$ into Eq. 5.63 and solve for the marginal stability lines, giving

$$\mathcal{N}^2 \sin(\theta_k + \Gamma)\sin(\theta_k + \phi) + 2\Omega\mathcal{S}\sin(\Lambda - \theta_k)\sin\theta_k = 0. \tag{5.64}$$

In the strongly stratified limit, $N^2 \gg |\Omega S|$ and $\Gamma \sim \phi$ (from Eq. 2.9),

$$\mathcal{N}^2 \sin^2(\theta_k + \phi) - 2\Omega\mathcal{S}\sin(\theta_k - \Lambda)\sin\theta_k = 0. \tag{5.65}$$

This can only be satisfied if $N^2 \gg 2|\Omega S|$ when $\sin^2(\theta_k + \phi) \sim 0$, hence $\theta_k + \phi \approx n\pi$ where $n \in \mathbb{N}$. Note that θ_k is defined below the x-axis so $-\theta_k$ is the angle above it. This means that $-\theta_k = \phi = \Gamma$ when $n = 0$, indicating that $\boldsymbol{k}$ lies along $\boldsymbol{e}_\theta$ or $\boldsymbol{e}_g$, so that fluid motions are along stratification (or constant pressure) surfaces, i.e. parallel to $\boldsymbol{e}_\theta^\perp \sim \boldsymbol{e}_g^\perp$. Hence instability is possible for a wedge of wavevector angles around $\boldsymbol{e}_\theta$ (e.g. Balbus, 1995).

Fastest growing non-diffusive modes

We now find the wavevector magnitude k and orientation θ_k corresponding to the maximum growth rate, and in turn identify the dominant mode. To find the fastest growing mode we first maximise over k^2, and then maximise over the angle θ_k. Note a and b only depend on θ_k and not on the magnitude k, so $\partial a/\partial k^2$ and $\partial b/\partial k^2$ are both zero. We also have

$$\frac{\partial \omega_A^2}{\partial k^2} = \frac{\omega_A^2}{k^2}, \quad \text{and} \quad \frac{\partial \xi}{\partial k^2} = \frac{\xi}{k^2}. \tag{5.66}$$

We now examine the adiabatic quartic dispersion relation

$$s^4 + \left(2\omega_A^2 + a + b\right)s^2 + \left(\omega_A^4 + b\omega_A^2 + \xi\right) = 0. \tag{5.67}$$

To obtain the fastest growing mode properties, we differentiate with respect to both k^2 and θ_k and require $\partial_{k^2} s = \partial_{\theta_k} s = 0$. Setting the k^2 derivative of Eq. 5.67 to zero gives:

$$s^2 = -\frac{\mathcal{N}^2}{2} s_{\phi+\theta_k} s_{\Gamma+\theta_k} - \Omega S s_{\theta_k} s_{\Lambda-\theta_k} - k^2 B_0^2 s_{\theta_k}^2. \tag{5.68}$$

This is clearly maximised for weak fields or for modes with $k \to 0$ where the last term vanishes, since that provides a stabilising effect, though we must have nonzero B_0 to obtain this result. Now we can maximise over θ_k to obtain

$$0 = -\frac{\mathcal{N}^2}{2} s_{\Gamma+\phi+2\theta_k} - \Omega S s_{\Lambda-2\theta_k} - k^2 B_0^2 s_{2\theta_k}. \tag{5.69}$$

In the strongly stratified limit the dominant term is usually the first one involving $\mathcal{N}^2$, which is stabilising, unless we choose a specific range of θ_k. This means that in order to maximise the growth rate we need to minimise this term. Indeed the magnitude of this term is smallest when $\theta_k \approx -\frac{\Gamma+\phi}{2}$ i.e. when the wavevector is approximately halfway between $\boldsymbol{e}_g$ and $\boldsymbol{e}_\theta$. Note that in the strongly stratified limit the TWE implies that $\phi \approx \Gamma$ and hence this term approximately vanishes for $\theta_k \approx -\phi \approx -\Gamma$. For such wavevectors that minimise the stabilising effects of buoyancy,

$$s^2 = \Omega S s_\phi s_{\Lambda+\phi} - B_0^2 \omega_A^2 s_\phi^2. \tag{5.70}$$

Note that the magnetic term that only occurs in the non-weak field limit is always positive, meaning that in the adiabatic regime a stronger magnetic field should increase the maximum growth rate of the instability. In the weak field case we can ignore the second term and are just left with

$$s^2 = 2\Omega S s_\phi s_{\Lambda+\phi}. \tag{5.71}$$

Hence, we require both ϕ and $\Lambda + \phi$ to have the same sign, either both in the northern or southern hemisphere for onset of instability.

Note that Eq. 5.68 is an expression for s^2 in terms of θ_k. From this we can show (also using TWE) that $\partial_{\theta_k} s^2 = 0$ (max growth rate) implies $s_{\Gamma+\phi+2\theta_k} s_\Lambda + s_{\Lambda+2\theta_k} s_{\Gamma-\phi} = 0$. Hence when strongly stratified $\Gamma \approx \phi$, this predicts the fastest growing direction to be along $\boldsymbol{e}_\theta$ since it requires $s_{\Gamma+\phi+2\theta_k} \approx 0$, hence $-\theta_k \approx \phi$, consistent with marginal stability results above.

5.3.3 Diffusive instabilities

Small Pr/Pm **limit: efficient thermal diffusion**

In the limit of very efficient thermal diffusion relative to viscous and ohmic diffusivities, we would expect Eq. 5.58 to approximately apply for sufficiently large wavelength instabilities (with smallish k, for which viscous and ohmic diffusion are relatively unimportant) but with $b = 0$. To show that this is indeed the case, if we consider Eq. 5.52, set $\nu = \eta = 0$ and then consider the limit $\kappa \to \infty$ (this is like considering the joint limits $\mathrm{Pr}/\mathrm{Pm} \to 0$ and $\mathrm{Pr} \to 0$) with all other quantities $O(1)$, we obtain the dispersion relation

$$s^4 + \left(2\omega_A^2 + a\right) s^2 + \left(\omega_A^4 + \xi\right) = 0. \tag{5.72}$$

This is the same as Eq. 5.58 with $b = 0$ and describes MRI modes satisfying the unstratified ($b = 0$) non-diffusive dispersion relation with nonzero field[1]. The fastest growing modes (maximising over k^2, i.e. setting $\partial_{k^2} s = 0$) in the limit of weak fields or small k (for which ω_A^4 can be ignored relative to the other terms) satisfy

$$s^2 = -\frac{\xi}{2\omega_A^2} = \left(\hat{\boldsymbol{k}} \cdot \boldsymbol{\Omega}\right) S \frac{k_z}{k} \tag{5.73}$$

$$= S\Omega s_{\Lambda-\theta_k} s_{\theta_k}. \tag{5.74}$$

In this limit instability occurs for any $\mathcal{S} > 0$ (though strictly the approximations for which this limit applies are then no longer valid). The growth rate is maximised over θ_k when $\partial_{\theta_k} s^2 = 0$, giving

$$s_{\Lambda-2\theta_k} = 0 \quad \Rightarrow \quad \theta_k = \frac{\Lambda}{2} - n\frac{\pi}{2}, \tag{5.75}$$

---

[1] This is analogous to what we found for the hydrodynamic case in the limit $\mathrm{Pr} \to 0$ and $\mathrm{RiPr} \to 0$, where the fastest growing mode growth rates were described by $s^2 = -a$, the adiabatic unstratified dispersion relation, see Chapter 3 or A.2.3. However, the dispersion relation here requires the presence of non-vanishing magnetic field.

for $n \in \mathbb{N}$, i.e. for modes with orientations halfway between the rotation axis (along $\hat{\mathbf{\Omega}}$) and the angular velocity gradient (along x) when $n = 1$. For cylindrical differential rotation ($\Lambda = 0$), this implies $\theta_k = \pm\frac{\pi}{2}$, and hence wavevectors are along z, as expected (e.g. Balbus & Hawley, 1991). On the other hand, when $\Lambda = -30°$, $\theta_k = -105°$ (indicating 105° *above* the x axis), and when $\Lambda = 60°$, $\theta_k = -60°$ (indicating 60° *above* the x axis). This will be found to be consistent with our later Figures 5.3–5.5 for the largest Pm considered, and is most evident for the strongest magnetic fields plotted there.

These results are consistent with the discussion of (e.g. Menou & Le Mer, 2006) that postulate the relevance of the parameter

$$\frac{\mathrm{Pr}}{\mathrm{Pm}} = \frac{\eta}{\kappa} \lesssim \frac{\mathcal{S}\Omega}{\mathcal{N}^2}. \tag{5.76}$$

For even stronger fields or larger wavenumbers, there is a stabilising effect of magnetic tension through the ω_A^4 term in the dispersion relation. Fields are sufficiently strong when $\omega_A^2 = B_0^2 k^2 s_{\theta_k}^2 \sim 2\Omega S s_{\theta_k - \Lambda} s_{\theta_k}$, and hence typically for $k^2 \sim \frac{2\Omega S}{B_0^2}$. In addition, larger k modes will be increasingly affected by ohmic diffusion and viscosity.

Diffusive modes in the small shear (small $\mathcal{S}$) limit

In Chapter 3, we computed the curves showing the lowest value of the shear S for which instability is possible as a function of the angle ϕ, the angle between the shear and gravity directions (see figure 3.3, Chapter 3). Apart from the exceptional case at the equator, there is a finite minimum S below which no instability occurs. This is no longer the case when a magnetic field is added. There is then a whole range of ϕ for which the system is unstable for arbitrarily small S. This is quite surprising, as the shear drives both GSF and MRI instability, so one might imagine that reducing the shear towards zero would eliminate the instability. What happens is that the growth rate does tend to zero as S is reduced, but it can always remain positive, so the critical value of S for instability can be zero. To establish this, we consider the case $\phi > 0$. Since S is small, the thermal wind equation Eq. 2.9 means that Γ is very close to ϕ, so both are positive if $\phi > 0$. We then look for modes with wavenumber $\boldsymbol{k} = k(c_{\theta_k}, 0, -s_{\theta_k})$ with $\theta_k = \pi - (\Gamma + \phi)/2$ so that $\boldsymbol{k}$ is nearly antiparallel to both $\boldsymbol{e}_\theta$ and $\boldsymbol{e}_g$. Since $b = \mathcal{N}^2 \sin(\theta_k + \Gamma)\sin(\theta_k + \phi)$, this makes b very small, $O(S^2)$. For these disturbances, fluid flows along the stratified surfaces, doing negligible work against gravity. We also choose the magnitude of k such that $k^2 \sim O(S)$, so since S is small, k is also small. We now put these scalings into the diffusive quintic equation Eq. 5.52-5.55 noting that the growth rate $s \sim O(S) \sim O(k^2)$, to obtain at leading order

$$\omega_A^2 = B_0^2 k^2 \sin^2\phi,\ a = 4\Omega^2 \sin^2\beta,\ \xi = -2k^2 S B_0^2 \sin\beta \sin^3\phi, \tag{5.77}$$

where β is the (positive) latitude,

$$\begin{aligned} &as^3 + ak^2\left(2\eta + \kappa\right)s^2 + \left(\omega_A^4 + ak^4\left(2\eta\kappa + \eta^2\right) + \xi\right)s \\ &\quad + \omega_A^4 k^2 \kappa + ak^6\eta^2\kappa + \xi k^2 \kappa = 0. \end{aligned} \tag{5.78}$$

Since $\phi > 0$, ξ is negative and a and ω_a^2 are positive, so we can choose k^2 relative to S so that the constant term in this cubic is very slightly negative, say $-\epsilon\kappa k^2$, where $\epsilon > 0$ is very small. Then s is $O(\epsilon)$ so the quadratic and cubic terms in Eq. 5.78 can be ignored. The linear term can now be written

$$\left(\omega_A^4 + ak^4\left(2\eta\kappa + \eta^2\right) + \xi\right)s = \left(-\epsilon + 2ak^4\eta\kappa\right)s, \tag{5.79}$$

so provided $\epsilon < 2ak^4\eta\kappa$ (this requires non-zero latitude) the linear term has a positive coefficient, so the growth rate s is positive. This establishes that for any latitude $\beta > 0$ and $\phi > 0$ there is always instability for any shear. Note, however, that the growth rate predicted is only $O(SB_0^2)$, i.e. small, and it does require a small k, so that the bounding box has to be large, despite the box being local, so there are clearly limits on how small S can be in practice.

5.4 Numerical linear results

In this section we numerically solve the dispersion relation to graphically analyse the properties of the possible instabilities in our system. In Figures 5.3–5.5 we probe effects of varying the magnetic field strength B_0 and magnetic Prandtl number Pm for three different configurations with different latitudes $\beta = \Lambda + \phi$ and orientations of the shear with respect to gravity ϕ. We fix $\mathrm{Pr} = 0.01$, small, but motivated by parameters accessible with nonlinear numerical simulations, and $S = 2$ (following Barker et al., 2020; Dymott et al., 2023) and Chapters 3 & 4, since the latter choice would be marginally stable according to Rayleigh's criterion for cylindrical differential rotation. We present pseudocolour plots of the base 10 logarithm of the growth rate of an axisymmetric perturbation in Fourier space (k_x, k_z) in these figures. Over-plotted in red are the lines $\hat{\boldsymbol{\Omega}}^{\perp}$ and $\nabla\ell$, within which the direct GSF instability occurs, and in light blue are the directions of buoyancy (more specifically, the normal to stratification surfaces) and gravity, $\boldsymbol{e_\theta}$ and $\boldsymbol{e_g}$, respectively. For comparison the hydrodynamic cases with $B_0 = 0$ are shown in the top row of each figure. The magnetic field strength B_0 is increased within the set $[0, 1, 2.5, 5]$ with each successive row, and Pm is increased within $[0.01, 0.1, 1]$ with each successive column.

We identify two sets of 'lobes' of instability operating in the system. The dominant set are bounded by $\nabla\ell$ and $\hat{\boldsymbol{\Omega}}^{\perp}$ in the hydrodynamic case, and they correspond to the dominant direct instability. This is either the double-diffusive GSF or the adiabatic Solberg-Høiland instability. The fastest growing modes typically have growth rates $O(1)$, which we note is comparable to Ω^{-1}, given our unit of time, and are initially (in the hydrodynamic case) observed to lie along the line that is approximately half-way between $\nabla\ell$ and $\hat{\boldsymbol{\Omega}}^{\perp}$. This wedge – in Fourier space – is perpendicular to the physical wedge within which the unstable mode displacements and velocity perturbations arise, since the incompressibility condition implies $\hat{\boldsymbol{k}} \cdot \boldsymbol{u} = 0$. The second set of smaller lobes, when present, contains oscillatory modes, which are weakly growing internal magneto-inertia-gravity waves that propagate and are destabilised within

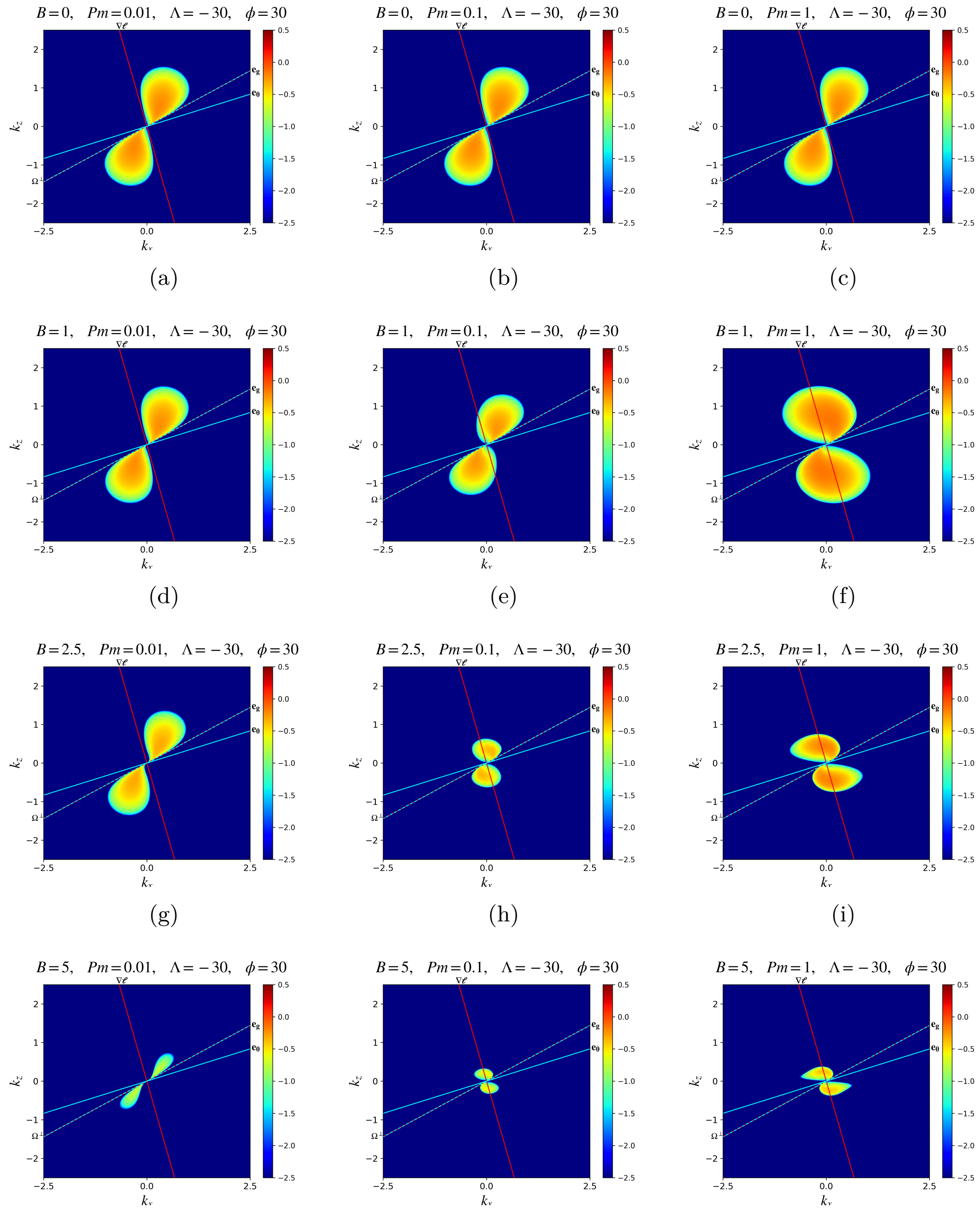

(a) (b) (c)

(d) (e) (f)

(g) (h) (i)

(j) (k) (l)

Figure 5.3: Logarithm of the growth rate $\log_{10}(\sigma/\Omega)$ of axisymmetric perturbations plotted on the (k_x, k_z)-plane according to Eq. 5.41, for various B_0 and Pm, with $\phi = 30°, \Lambda = -30°$. Parameters are $\mathcal{N}^2/\Omega^2 = 10$, Pr$= 10^{-2}$, $\mathcal{S}/\Omega = 2$. We vary the strength of the magnetic field from $B_0 = 0$ to $B_0 = 5$ down each column, and vary Pm from Pm $= 0.01$ to Pm $= 1$ along each row. GSF modes are primarily confined within the wedge bounded by $\hat{\boldsymbol{\Omega}}^\perp$ and $\nabla\ell$ (red lines). However as the field strength increases (downwards) the wavevector orientation is shifted to correspond more with the double-diffusive MRI. Increasing B at fixed Pm decreases both the maximum growth rate and the size of the unstable region on the (k_x, k_z)-plane. Reducing magnetic diffusivity by increasing Pm on the other hand seems to have the opposite effect and enhances the destabilising effects of the field, leading to a larger region of instability as well as a stronger destabilisation of the dominant mode.

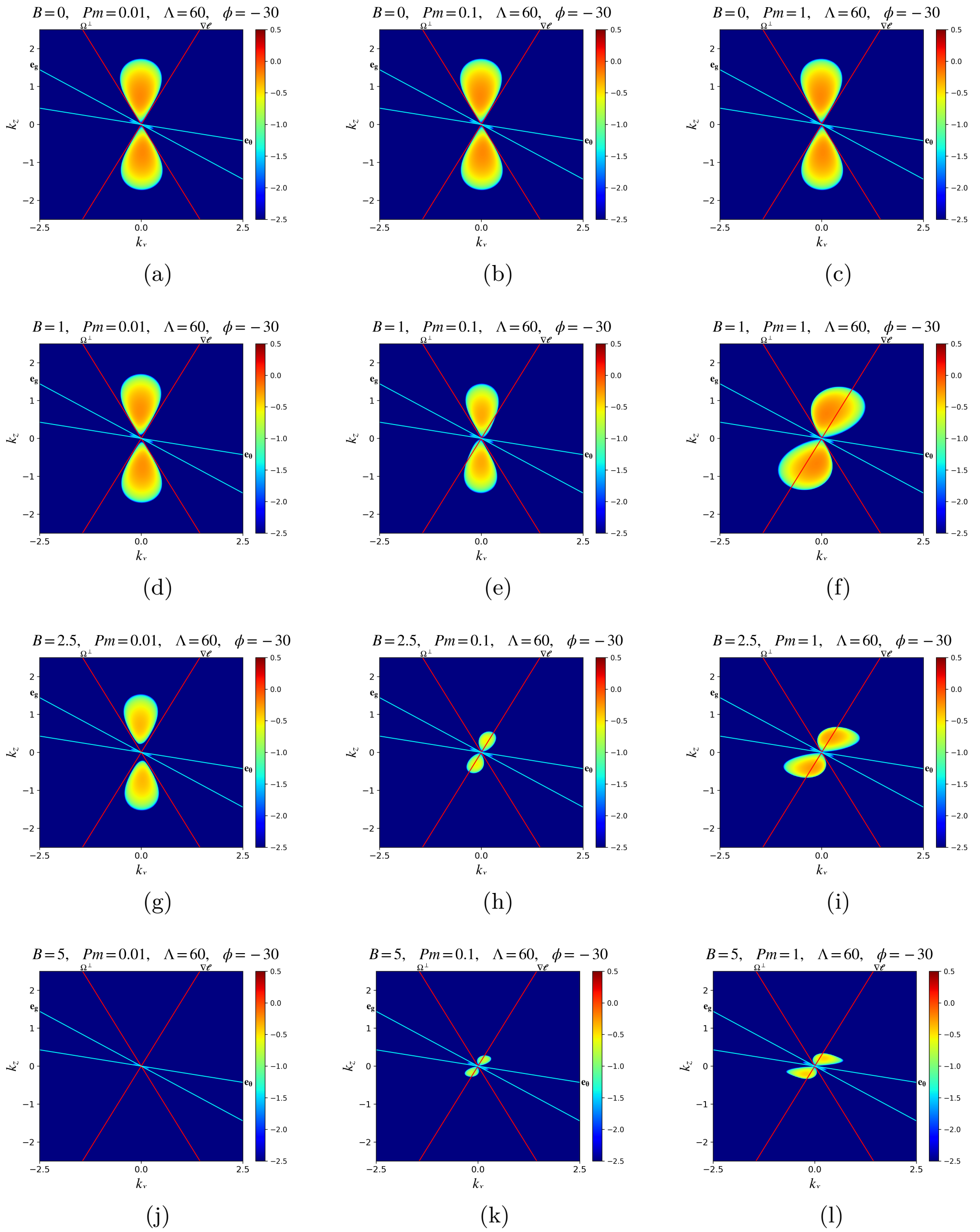

(a) (b) (c)

(d) (e) (f)

(g) (h) (i)

(j) (k) (l)

Figure 5.4: Logarithm of the growth rate $\log_{10}(\sigma/\Omega)$ of axisymmetric perturbations plotted on the (k_x, k_z)-plane according to Eq. 5.41, for various B_0 and Pm, with $\phi = -30°, \Lambda = 60°$, i.e. a mixed radial/latitudinal shear at latitude $\Lambda + \phi = 30°$. Parameters are $\mathcal{N}^2/\Omega^2 = 10$, Pr$= 10^{-2}$, $\mathcal{S}/\Omega = 2$. We vary the strength of the magnetic field from $B_0 = 0$ to $B_0 = 5$ down each column, and vary Pm from Pm $= 0.01$ to Pm $= 1$ along each row. GSF unstable modes are primarily confined to within the wedge bounded by $\hat{\mathbf{\Omega}}^{\perp}$ and $\nabla\ell$ (red lines) for weak fields, but this direction is modified when the double-diffusive MRI takes over. We observe a secondary set of unstable oscillatory modes, consisting of weakly destabilised magneto-inertial-gravity waves. These grow more weakly than the primary lobes but they are less affected by the stabilising effects of the magnetic field.

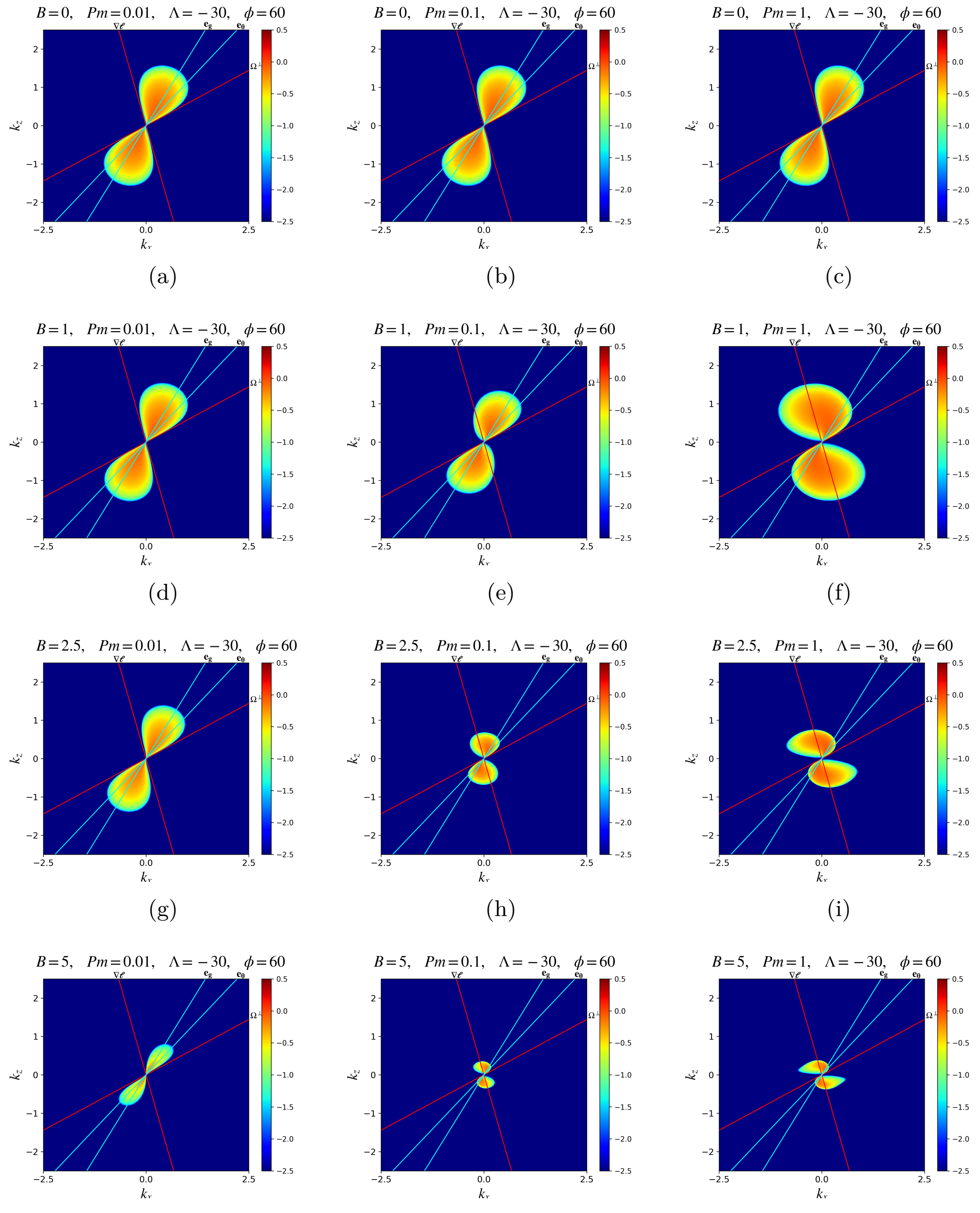

(a) (b) (c)

(d) (e) (f)

(g) (h) (i)

(j) (k) (l)

Figure 5.5: Logarithm of the growth rate $\log_{10}(\sigma/\Omega)$ of axisymmetric perturbations plotted on the (k_x, k_z)-plane according to Eq. 5.41, for various B_0 and Pm, with $\phi = 60°, \Lambda = -30°$, i.e. a mixed radial/latitudinal shear at latitude $\Lambda + \phi = 30°$. Parameters are $\mathcal{N}^2/\Omega^2 = 10$, Pr$= 10^{-2}$, $\mathcal{S}/\Omega = 2$. We vary the strength of the magnetic field from $B_0 = 0$ to $B_0 = 5$ down each column, and vary Pm from Pm $= 0.01$ to Pm $= 1$ along each row. When $B = 0$ the system is adiabatically unstable since it violates the Solberg-Høiland criterion. This is visually characterised by a tendency for the fastest growing modes to occur even as $k \to 0$, suggesting that the presence of diffusion leads to the preference of the largest possible wavelengths in this regime. This is in comparison to the GSF and double-diffusive MRI modes cases where the fastest growing modes here have a unique non-zero wavenumber and hence a preferred wavelength in real space.

the wedges bounded by $\boldsymbol{e}_g$ and $\boldsymbol{e}_\theta$.

The introduction of non-zero $\boldsymbol{B}_0$ has observable effects on the orientation, strength and structure of the unstable region in parameter space. Increasing the strength of the field for a fixed Pm has a tendency to force the modes into alignment with the preferred direction for double-diffusive MRI modes, as predicted by the analysis in § 5.3.3, and to shift them to larger scales (smaller k magnitudes). Note that we do not observe the adiabatic MRI to dominate here, which would be identifiable by modes aligned with $\boldsymbol{e}_\theta$ as explained in § 5.3.2. This is likely due to the effects of thermal diffusion in eliminating the stabilising effects of buoyancy forces on MRI modes when $\mathrm{Pr}/\mathrm{Pm} = \eta/\kappa$ is small, which is the case here when $\mathrm{Pm} \geq 0.01$ as $\mathrm{Pr} = 0.01$ remains fixed. The addition of a field seems to impose a stabilising effect on the hydrodynamically-unstable GSF modes, ultimately resulting from the stabilising effects of magnetic tension (see also Latter & Papaloizou, 2018), and so the majority of cases exhibit a smaller growth rate for the dominant instability as B_0 is increased.

Magnetic diffusivity counteracts the effects of magnetic fields, and this is clearest for small Pm in the left panels of Figures 5.3–5.5. Cases with $\mathrm{Pm} = 1$ have the weakest ohmic diffusion, and cases with $\mathrm{Pm} = 0.01$ have much more efficient ohmic than viscous diffusion. Small Pm allows magnetic cases to return to the hydrodynamic limit and larger Pm closer to unity therefore exhibit the strongest magnetic effects for a given B_0. When $\mathrm{Pm} = 1$, instability is possible outside the hydrodynamic region contained within the lines $\hat{\boldsymbol{\Omega}}^{\perp}$ and $\nabla\ell$. This can be seen most clearly in the right-most bottom panel of these figures, where magnetic effects are strongest (and magnetic diffusion is weakest). The direction of the preferred modes in that case are better described by the unstratified (due to rapid thermal diffusion) MRI in § 5.3.3.

The oscillatory modes seem to be only very marginally modified by the magnetic field, as is seen most clearly in Fig. 5.4. This suggests that the internal inertia-gravity waves (IGWs) observed to be destabilised in Chapter 3, within the wedge between $\boldsymbol{e}_g$ and $\boldsymbol{e}_\theta$ continue to be weakly destabilised magneto-inertial-gravity waves.

5.4.1 Parameter dependence of fastest growing mode

After displaying the properties of all unstable axisymmetric modes on the (k_x, k_z)-plane in our system as B_0 and Pm are varied, we now turn to explore the variation in the fastest growing mode optimised over k_x and k_z as the parameters are varied. We primarily consider $S = 2$, $N^2 = 10$ at 4 latitudes ($\beta = \phi + \Lambda = 0°, 30°, 60°$ and $90°$).

Non-diffusive instabilities

We first explore non-diffusive (stratified) instabilities by solving the quartic dispersion relation in Eq. 5.67 numerically (using `fminsearch` on $-\Re[s]$ in Matlab), to determine the properties of the fastest growing mode, which we present in Figs. 5.6-5.8 as a function of the direction of the differential rotation ϕ for all possible values, for three different latitudes $\beta = 30°$, $60°$ and $90°$. The left panels show the growth rate σ of the fastest growing mode, the middle panels the corresponding wavenumber magnitude k, and the right panels the wavevector orientation $\theta_k = \tan^{-1}(-k_z/k_x)$. Note that the magnetic field only appears in Eq. 5.67 through powers of ω_A, therefore the results in the left and right panels of Fig. 5.6 are independent of the magnetic field, whereas the middle panels show results for $B_0 = 1$ but k can be straightforwardly scaled to consider any B_0 since the y-axis can be interpreted as $B_0 k$ (and k_z can be obtained using the corresponding θ_k). This means that for strong fields, instability prefers small k.

Fig. 5.6-5.8 shows results at a latitude of $30°$. Red lines indicate where the non-diffusive hydrodynamic Solberg-Høiland instability operates, and blue lines where the magnetic field modifies the instability over the hydrodynamic case (shown in Fig. 4(b) in Dymott et al., 2023). When the non-diffusive hydrodynamic Solberg-Høiland modes are unstable in red, between approximately $\phi \in [60°, 150°]$, there is no preferred k, only a preferred wavevector orientation. In this limit, the blue lines suggest the wavevector $k \to 0$ for this range of ϕ, corresponding to large-scale modes. The magnetic field widens the unstable region to below $\phi = 0°$ from $\phi \approx 30°$.

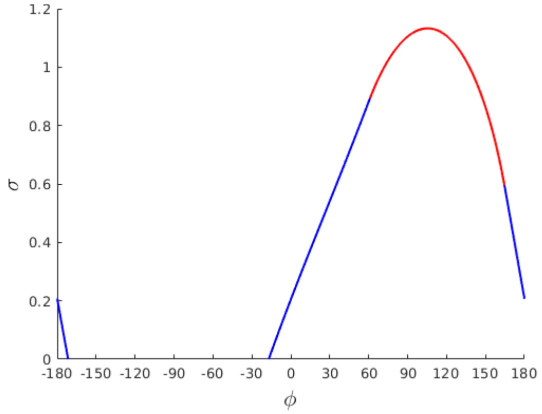

(a) σ at latitude 30 ($B = 1$)

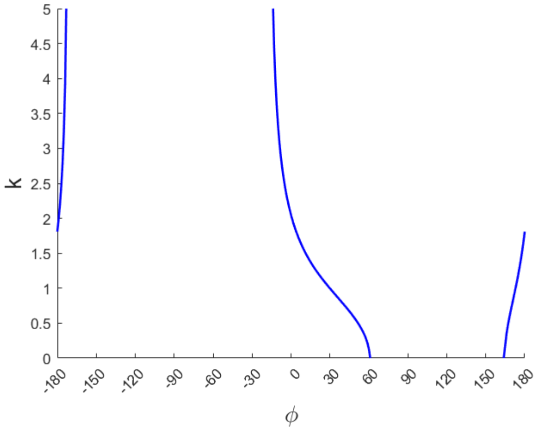

(b) k at latitude 30 ($B = 1$)

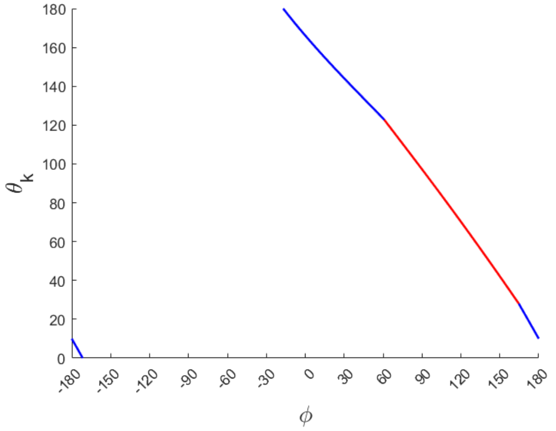

(c) θ_k at latitude 30 ($B = 1$)

Figure 5.6: A selection of figures illustrating the properties of the fastest growing non-diffusive ($\nu = \kappa = \eta = 0$) modes with an imposed magnetic field for $S = 2$ and $N^2 = 10$ for latitude 30°. Top panel: maximum growth rate σ as a function of ϕ. The red curve is where the fastest growing mode is hydrodynamic and the magnetic field plays no role, which prefers modes with $k \to 0$. The blue curves are where the corresponding k is non-zero and magnetic field affects the growth rate. Middle: k when it is finite and there is instability. Bottom: corresponding wavevector orientation θ_k, which is well-defined for all growing modes.

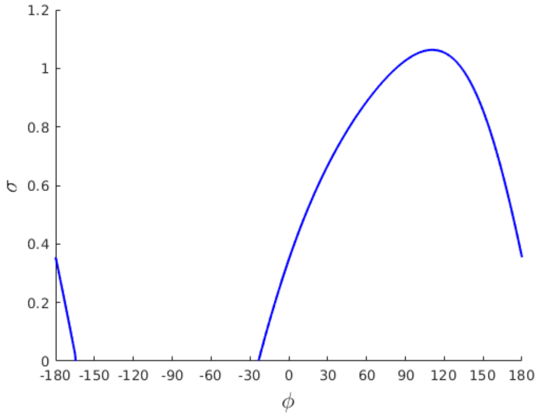

(a) σ at latitude 60 ($B = 1$)

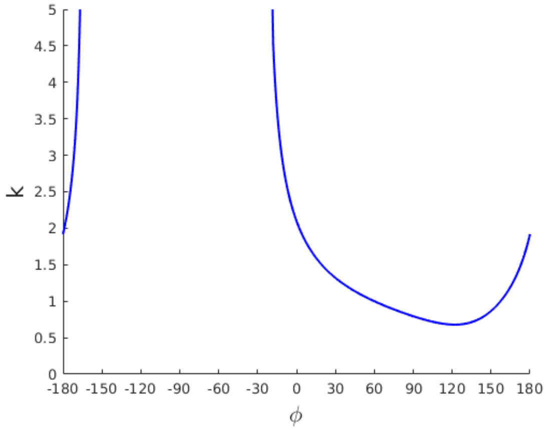

(b) k at latitude 60 ($B = 1$)

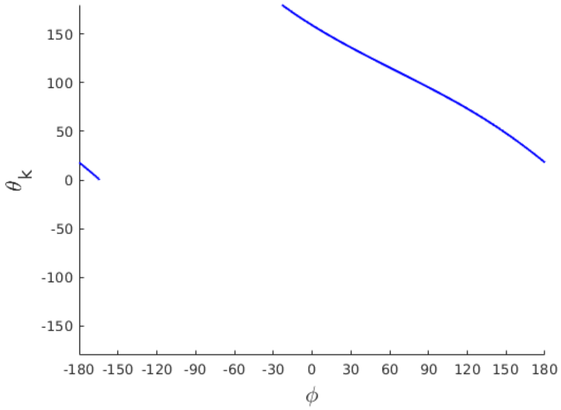

(c) θ_k at latitude 60 ($B = 1$)

Figure 5.7: A selection of figures comparing the properties of the fastest growing non-diffusive ($\nu = \kappa = \eta = 0$) modes with an imposed magnetic field for $S = 2$ and $N^2 = 10$ for $\phi + \Lambda = 60^\circ$. Top panel: maximum growth rate σ as a function of ϕ. Middle: k when it is finite and there is instability. Bottom: corresponding wavevector orientation θ_k, which is well-defined for all growing modes.

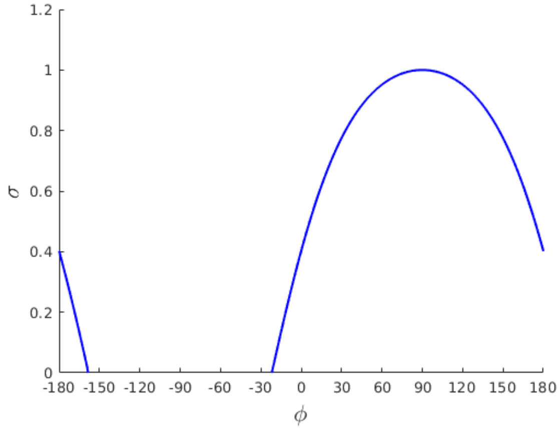

(a) σ at latitude 90 ($B = 1$)

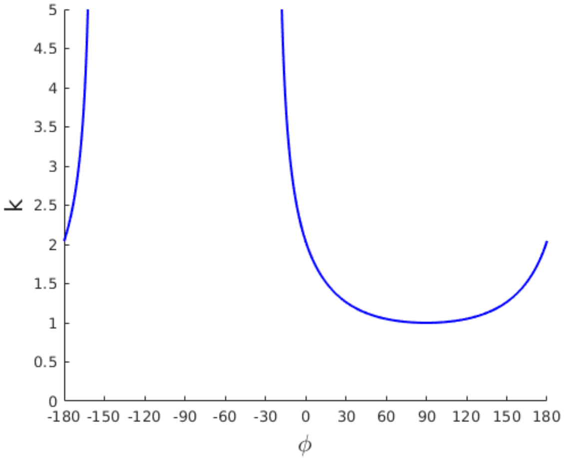

(b) k at latitude 90 ($B = 1$)

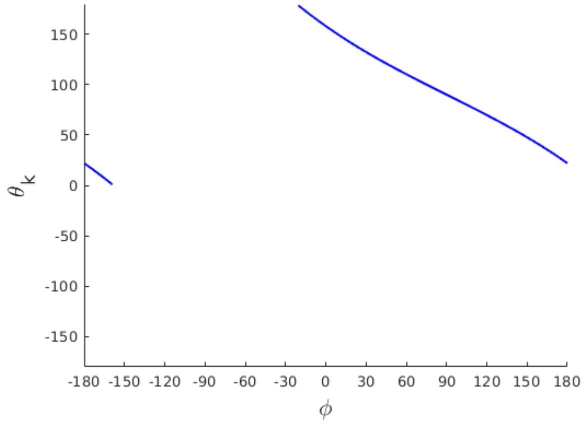

(c) θ_k at latitude 90 ($B = 1$)

Figure 5.8: A selection of figures illustrating the properties of the fastest growing non-diffusive ($\nu = \kappa = \eta = 0$) modes with an imposed magnetic field for $S = 2$ and $N^2 = 10$ for $\phi + \Lambda = 90°$. Top panel: maximum growth rate σ as a function of ϕ. Middle: k when it is finite and there is instability. Bottom: corresponding wavevector orientation θ_k, which is well-defined for all growing modes.

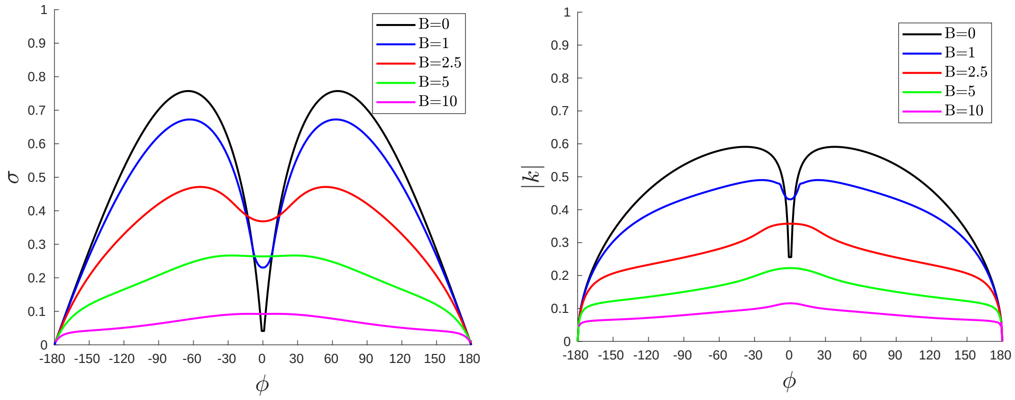

(a) σ at $\Lambda + \phi = 0$

(b) $|k|$ at $\Lambda + \phi = 0$

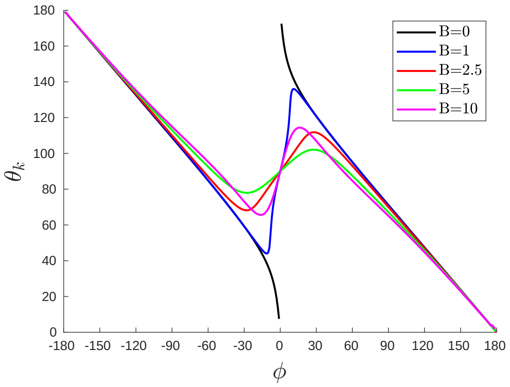

(c) θ_k at $\Lambda + \phi = 0$

Figure 5.9: Properties of the fastest growing modes for various values of the magnetic field B_0 with $S = 2, \mathrm{Pr} = 10^{-2}, N^2 = 10$, $\mathrm{Pm} = 0.1$, for different rotation profiles (values of ϕ) at the equator. The hydrodynamically stable case of $\phi = 0^\circ$, corresponding to cylindrical rotation, is destabilised by the magnetic field. Within close proximity of cylindrical rotation ($-15^\circ \lesssim \phi \lesssim 15^\circ$) increases in field strength of up to roughly $B_0 = 2.5$ increase the growth rate. This is paired with a decrease in the wavelength of this mode and deviation in orientation from the hydrodynamic case, where θ_k tends to align itself more so with the orientation of the field. For other ϕ, the field tends to stabilise the instability over the hydrodynamic case, reducing its maximum growth rate and wavenumber k.

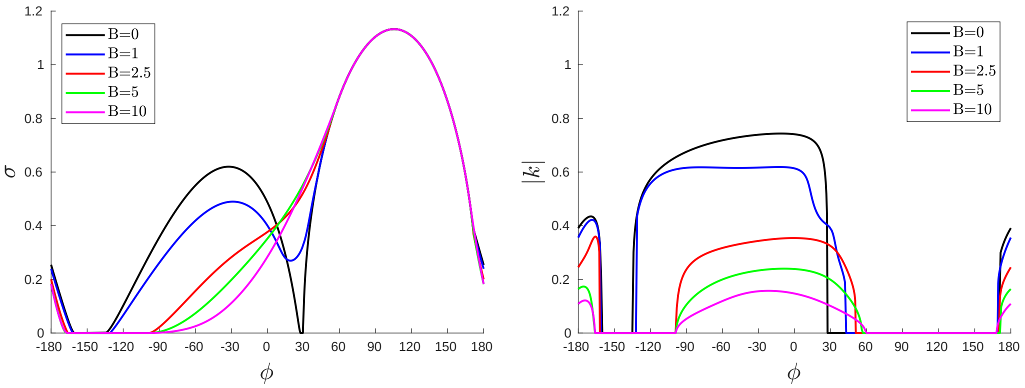

(a) σ at $\Lambda + \phi = 30$

(b) $|k|$ at $\Lambda + \phi = 30$

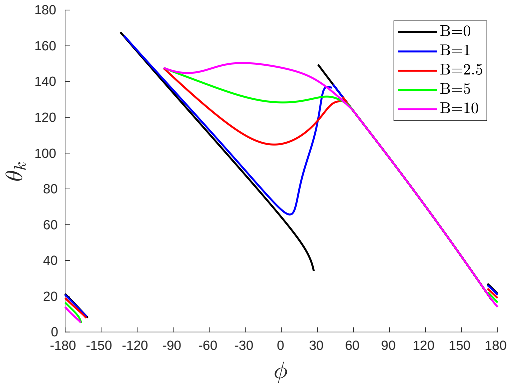

(c) θ_k at $\Lambda + \phi = 30$

Figure 5.10: Properties of the fastest growing modes for various values of the magnetic field B_0 with $S = 2, \mathrm{Pr} = 10^{-2}, N^2 = 10$, $\mathrm{Pm} = 0.1$, for different rotation profiles (values of ϕ) at a latitude $\beta = \Lambda + \phi = 30^\circ$. The addition of a magnetic field significantly alters the linear growth rate of the diffusive modes, and typically acts to reduce both the growth rate σ and wavenumber k, but it does not affect the adiabatically unstable region for $\phi \in [60^\circ, 170^\circ]$. The effect of the magnetic field depends on both field strength (B_0) and differential rotation profile (ϕ). Nearly cylindrical differential rotations $\phi \approx 30^\circ$ ($\Lambda = 0$) that are hydrodynamically stable are heavily destabilised by the addition of a magnetic field, which corresponds to onset of the MRI.

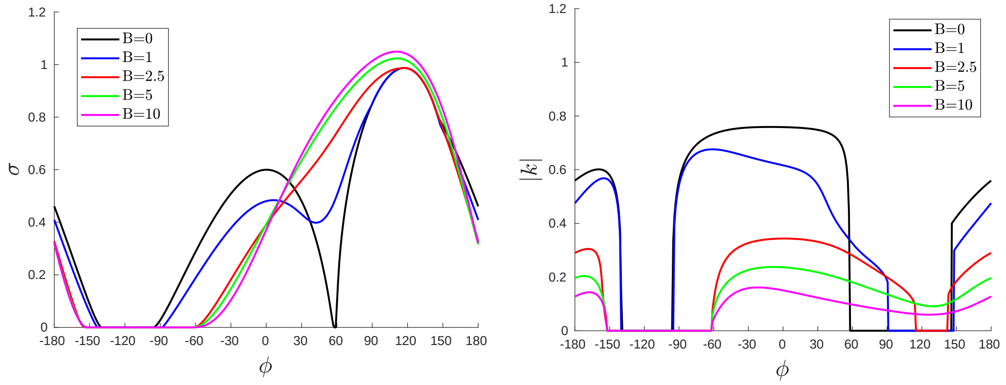

(a) σ at $\Lambda + \phi = 60$

(b) $|k|$ at $\Lambda + \phi = 60$

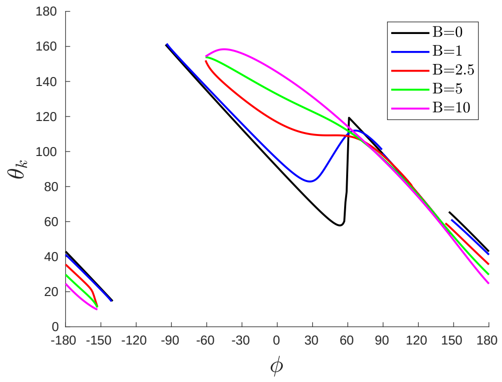

(c) θ_k at $\Lambda + \phi = 60$

Figure 5.11: Properties of the fastest growing modes for various values of the magnetic field B_0 with $S = 2, \mathrm{Pr} = 10^{-2}, N^2 = 10$, $\mathrm{Pm} = 0.1$, for different rotation profiles (values of ϕ) at a latitude $\beta = \Lambda + \phi = 60°$. The addition of a magnetic field significantly alters the linear growth rate of the diffusive modes, and typically acts to reduce both the growth rate σ and wavenumber k for $\phi \in [-180°, 30°]$, but instead increases the growth rate for $\phi \in [30°, 170°]$. The effect of the magnetic field depends on both field strength (B_0) and differential rotation profile (ϕ). Nearly cylindrical differential rotations $\phi \approx 60°$ ($\Lambda = 0$) that were hydrodynamically stable have become heavily destabilised by the addition of a magnetic field, which corresponds to onset of the MRI.

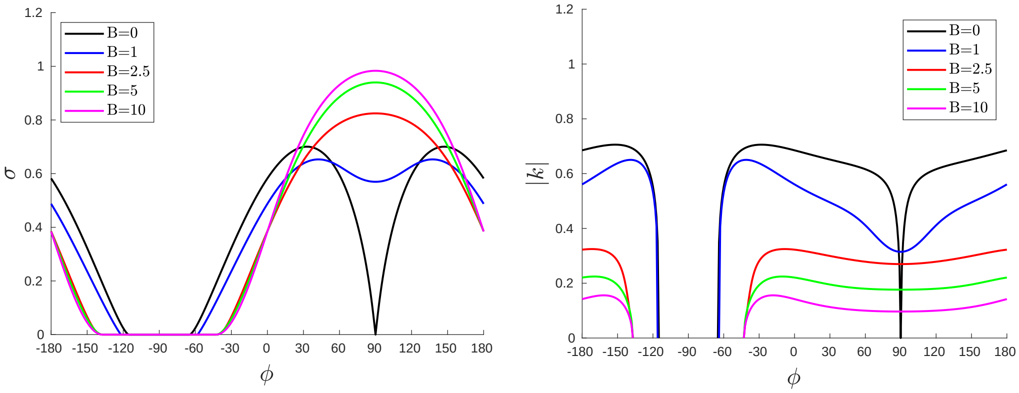

(a) σ at $\Lambda + \phi = 90$

(b) $|k|$ at $\Lambda + \phi = 90$

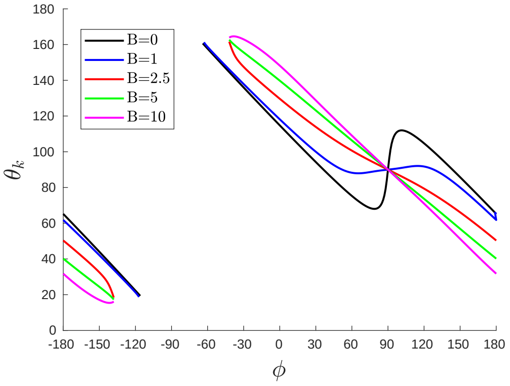

(c) θ_k at $\Lambda + \phi = 90$

Figure 5.12: Properties of the fastest growing modes for various values of the magnetic field B_0 with $S = 2, \mathrm{Pr} = 10^{-2}, N^2 = 10$, $\mathrm{Pm} = 0.1$, for different rotation profiles (values of ϕ) at a latitude $\beta = \Lambda + \phi = 90°$. The magnetic field significantly alters the linear growth rate of the diffusive modes, and in the range $\phi \in [-180°, 30°]$ typically acts to reduce both the growth rate σ and wavenumber k. However for nearly cylindrical differential rotation profiles with $\phi \approx 90°$ ($\Lambda = 0$) we see a significant destabilisation of the previously hydrodynamically stable modes, which corresponds to onset of the MRI which are the most unstable of cases at this latitude.

For latitudes 60° and 90°, there are no purely hydrodynamically unstable non-diffusive modes, but it can be seen by comparison with Fig. 3.4 in Chapter 3 that the field widens the unstable range of ϕ. The growth rate has a similar maximum value to the hydrodynamic case, with $\sigma \sim 1$ for the maximal ϕ. $\phi \approx -30^\circ$ to 180° are typically the most unstable configurations, and they also have the largest wavelength (smallest k) instabilities, whereas ϕ approximately between -150° and -30° are typically non-diffusively stable.

Diffusive instabilities

In stellar radiation zones, rapid thermal diffusion means that $\mathrm{Pr} \ll 1$ and $\mathrm{Pm} \ll 1$ but $\mathrm{Pr}/\mathrm{Pm} = \eta/\kappa \ll 1$. Hence, the stratified non-diffusive instability we have just analysed is likely to be substantially modified by thermal diffusion. As a result, we turn to solve the full triply-diffusive dispersion relation Eq. 5.41 with $\mathrm{Pr} = 10^{-2}$ and $\mathrm{Pm} = 0.1$, for which $\mathrm{Pr}/\mathrm{Pm} = 0.1$ and is therefore small. We show the growth rate (left panels), wavevector magnitudes (middle panels) and orientations θ_k (right panels) as a function of ϕ for various field strengths strengths $B \in [0, 1, 2.5, 5, 10]$ in Figs 5.9, 5.10, 5.11, 5.12 for latitudes $0^\circ, 30^\circ, 60^\circ$ and 90°, respectively. These demonstrate the effect of a magnetic field on the linear growth rate over the complete range of differential rotation configurations (value of ϕ) with $S = 2$.

The equatorial case in Fig 5.9 is symmetric about $\phi = 0$ and is adiabatically (non-diffusively) stable for $S = 2$ for any ϕ and B_0. The hydrodynamic $B_0 = 0$ case is stable when $\phi = 0$, corresponding to cylindrical rotation at the equator, but it becomes destabilised by even a weak magnetic field. This destabilisation is seen at all latitudes and is a result of a change in the stability criteria governing instability here. In the hydrodynamic case we require a violation of Rayleigh's criterion, which requires angular momentum to decrease outwards on isobars for instability, whereas in the magnetic case this criteria can – for certain field strengths – correspond to an MRI mode that requires angular velocity to decrease along isobars without diffusion instead, which is a condition that is much easier to satisfy. Within close proximity to the cylindrically-rotating profile ($-15^\circ \lesssim \phi \lesssim 15^\circ$), the magnetic instability operating is significantly more unstable than the hydrodynamic case. Increases in field strength of up to roughly $B_0 = 2.5$ lead to larger linear growth rates for the corresponding dominant mode, which is paired with a decrease in the wavelength (increase in $|k|$) and a significant deviation in orientation from the hydrodynamic case there, where θ_k tends to align itself more closely with the orientation of the field ($\theta_k \sim 90^\circ$, implying $\boldsymbol{k}$ is along z). Outside of this region (and particularly so for ϕ outside of $-60^\circ \lesssim \phi \lesssim 60^\circ$), the field acts to inhibit the growth rate of the hydrodynamic GSF instability and to increase its wavelength (reduce its k). For these parameters it is clear that the magnetic field typically has a stabilising effect on the growth rate except close to cylindrical rotation.

Fig. 5.10 shows the same results for the latitude $\Lambda+\phi = 30^\circ$ case. Here the symmetry about $\phi = 0^\circ$ seen at the equator is broken and varying ϕ has more complex effects. Cylindrical differential rotation corresponds here to $\phi = 30^\circ$ (since then $\Lambda = 0^\circ$), and we observe that it is stable when $B_0 = 0$ but is destabilised by the addition of a magnetic field, with more magnetised cases becoming more unstable until the growth rate becomes independent of B_0 for $B_0 \geq 2.5$. After $\phi \approx 60^\circ$ there is very good agreement between all cases. This is when the non-diffusive hydrodynamic Solberg-Høiland instability operates (as seen in Fig. 5.6), which prefers $k \to 0$, and magnetic fields have no effect on it.

There is a notable change in the range of non-zero $|k|$, which goes from $|k| \neq 0$ for $169^\circ \lesssim \phi \lesssim -157^\circ \cup -135^\circ \lesssim \phi \lesssim 28^\circ$ in the hydrodynamic case (note that the boundary between 180° and -180° is continuous due to symmetry) to $168^\circ \lesssim \phi \lesssim -160^\circ \cup -100^\circ \lesssim \phi \lesssim 60^\circ$ in the strongest $B = 10$ case. Note however that in any region where more than one B has defined $|k|$ values the smaller B_0 always has the shorter wavelength. In regions where the magnetic instability is operational the field again acts to force θ_k into alignment with the preferred direction for unstratified MRI modes discussed in § 5.3.3. Regions where the dominant mode switches from one form of instability to another can also be seen by a discontinuity in θ_k, as seen in panel (c).

At latitude $\Lambda + \phi = 60°$, shown in Fig. 5.11, the effects of the field are in many ways similar to Fig. 5.10. The range of unstable ϕ values does however decrease with increasing B_0, with the smallest range of instability being $-145° \lesssim \phi \lesssim -100°$ in the hydrodynamic case up to $-155° \lesssim \phi \lesssim -59°$ at $B_0 = 10$. However, the field is destabilising, leading to larger growth rates between $15° \lesssim \phi \lesssim 160°$, where the largest B_0 is the most unstable.

Similar results are found at latitude $\Lambda + \phi = 90°$ in Fig. 5.12. Modes with $20° \lesssim \phi \lesssim 150°$ are destabilised by the field, with nearly cylindrical rotation profiles ($\Lambda \sim 0$) being most strongly destabilised by the field. Cylindrical rotation is marginally stable in the hydrodynamic case but is the most unstable configuration for any $B_0 > 1$ plotted here, and grows faster than any hydrodynamic case in this figure. Finally, we determine numerically the critical value of S for instability (S_{crit}), once again by optimising over k_x and k_z. We show results in Fig 5.13 for S_{crit} as a function of ϕ for $B_0 = 0.1$ (solid lines) and $B_0 = 1$ (dashed lines) at a latitude 30°, along with the corresponding wavevector magnitude k and orientation θ_k. Our numerical results confirm the arguments presented in § 5.3.3. In complete contrast to the hydrodynamic case, we find double-diffusive MRI occurs for any $S > 0$ for $\phi > 0°$, such that $S_{\mathrm{crit}} = 0$ for such differential rotations. The corresponding wavenumber k also becomes arbitrarily small, implying arbitrarily large wavelength instabilities according to our local model. When $\phi < 0°$, the dominant instability is primarily the hydrodynamic GSF instability, weakly modified by magnetic fields. This has a preferred $k = O(1)$ (in units of d^{-1}) when it operates, and it is weakly inhibited by the presence of the magnetic field. We expect to find similar results – in terms of the modification of the hydrodynamic results shown in Chapter 3 – for different latitudes and field strengths. Stronger fields would widen the operation of the diffusive MRI and inhibit the GSF modes further. However, GSF modes may still be the dominant instability for differential rotations with $\phi < 0°$.

Overall, the addition of a magnetic field tends to inhibit diffusive rotational insta-

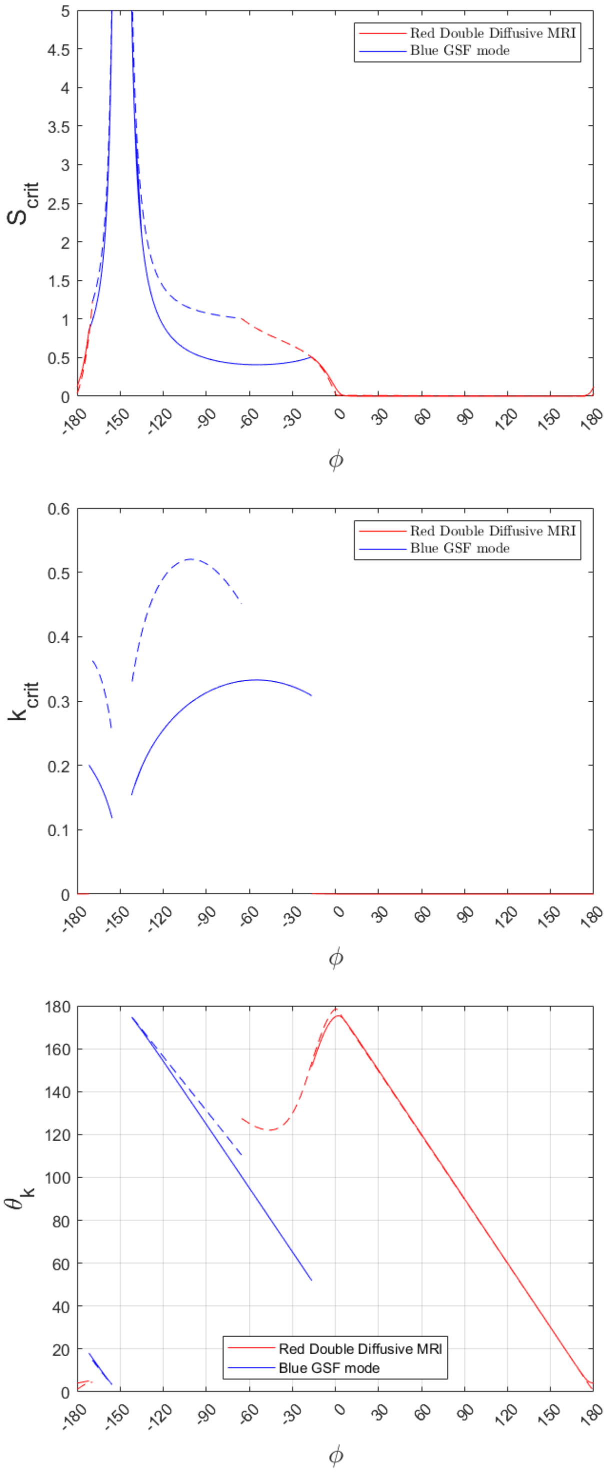

Figure 5.13: Critical value of S for instability (top), and the corresponding wavevector magnitude (middle) and orientation (bottom), for $B_0 = 0.1$ and 1, with $S = 2, \mathrm{Pr} = 10^{-2}, N^2 = 10$, $\mathrm{Pm} = 0.1$, for different rotation profiles (values of ϕ) at latitude $\Lambda + \phi = 30°$. For $\phi > 0°$ there is instability for any $S > 0$ for $B_0 \neq 0$, consistent with results obtained in § 5.3, due to the operation of the double-diffusive MRI (shown in red). For $\phi < 0°$, the instability is similar to the hydrodynamic GSF instability (shown in blue; cf. 3.3 in Chapter 3), and exhibits a preferred $k \sim d$. The magnetic field slightly weakens operation of the GSF instability for $\phi < 0°$.

bilities by reducing σ for $\phi \lesssim 0°$, and to promote (increase σ) instability for $\phi \gtrsim 0°$, particularly for nearly cylindrical differential rotations ($\Lambda \sim 0°$, where ϕ equals the latitude). The wavelength of the dominant instability is typically affected by the strength of the field, with stronger fields generally exciting larger wavelengths (smaller k's). The orientation of the mode also differs from the hydrodynamic prediction for strong enough fields. The effects of magnetic fields on diffusive rotational instabilities are therefore complex, but in nearly all cases the field strongly modifies the growth rate or wavenumber of the dominant mode. We may thus expect magnetic fields to substantially modify turbulent transport in stellar radiative regions.

5.5 Energetics of the instabilities

5.5.1 Derivation of the energy equations and evaluation for linear modes

In this section we analyse the energetics of the instabilities in our model, which is helpful to explore in more detail the physical mechanisms and energy sources that drive the various instabilities and to further quantify the role of magnetic fields. In order to derive the total energy equation we must first calculate equations that govern the different types of energy in our system, namely, kinetic, thermal/potential and magnetic. We start with the equations governing the evolution of perturbations given by Eqs. 5.7–5.12. To obtain volume-averaged energy equations we take the scalar product of Eq. 5.7 with $\boldsymbol{u}$ and 5.9 with $\boldsymbol{B}$ for the kinetic and magnetic energies, and multiply 5.8 by θ for thermal energy, and then volume average. We denote volume averages by $\langle \cdot \rangle$ where $\langle \cdot \rangle = \frac{1}{V} \iiint \cdot \, \mathrm{d}V$, where V is the volume of our box, which for linear modes is taken to be a single wavelength of the dominant mode. We define the kinetic, magnetic and thermal energies of our perturbations according to

$$\mathcal{K} = \frac{1}{2}\langle |\boldsymbol{u}|^2 \rangle, \qquad \mathcal{M} = \frac{1}{2}\langle |\boldsymbol{B}|^2 \rangle, \qquad \mathcal{P} = \frac{1}{2}\langle \frac{|\theta|^2}{\mathcal{N}^2} \rangle. \tag{5.80}$$

For the kinetic energy equation we obtain

$$\begin{aligned}\partial_t \mathcal{K} = -\langle \boldsymbol{u} \cdot (\boldsymbol{u} \cdot \nabla)\boldsymbol{U}_0 \rangle + \langle \theta \boldsymbol{u} \cdot \boldsymbol{e}_g \rangle + \nu \langle \boldsymbol{u} \cdot \nabla^2 \boldsymbol{u} \rangle \\ + \langle \boldsymbol{u} \cdot (\boldsymbol{B}_0 \cdot \nabla)\boldsymbol{B} \rangle.\end{aligned} \tag{5.81}$$

Note that $\langle \boldsymbol{u} \cdot (\boldsymbol{u} \cdot \nabla)\boldsymbol{u} \rangle = \langle \boldsymbol{u} \cdot (\boldsymbol{U}_0 \cdot \nabla)\boldsymbol{u} \rangle = \langle \boldsymbol{u} \cdot \nabla p \rangle = 0$ using the chain rule, incompressibility and the divergence theorem (applying periodic boundary conditions), and noting that the Coriolis force does no work ($\boldsymbol{u} \cdot (2\boldsymbol{\Omega} \times \boldsymbol{u}) = 0$). Alternatively, we can substitute $\boldsymbol{U}_0 = -\mathcal{S} x \boldsymbol{e}_y$ and this becomes

$$\partial_t \mathcal{K} = \mathcal{S} \langle u_x u_y \rangle + \langle \theta \boldsymbol{u} \cdot \boldsymbol{e}_g \rangle + \langle \boldsymbol{u} \cdot (\boldsymbol{B}_0 \cdot \nabla)\boldsymbol{B} \rangle + \nu \langle \boldsymbol{u} \cdot \nabla^2 \boldsymbol{u} \rangle. \tag{5.82}$$

This indicates that the kinetic energy of perturbations can grow by extracting kinetic energy from the shear flow/differential rotation (first term), from conversions of thermal to kinetic energy (second term), from conversions of magnetic to kinetic energy (third term), and that it is dissipated by viscosity (fourth term, which can be shown to be negative definite through integration by parts).

Similarly we can obtain the magnetic energy equation, noting that $\langle \boldsymbol{B} \cdot (\boldsymbol{u} \cdot \nabla)\boldsymbol{B} \rangle = \langle \boldsymbol{B} \cdot (\boldsymbol{U}_0 \cdot \nabla)\boldsymbol{B} \rangle = 0$, giving

$$\partial_t \mathcal{M} = \langle \boldsymbol{B} \cdot (\boldsymbol{B}_0 \cdot \nabla)\boldsymbol{u} \rangle - \mathcal{S} \langle B_x B_y \rangle + \eta \langle \boldsymbol{B} \cdot \nabla^2 \boldsymbol{B} \rangle. \tag{5.83}$$

This indicates that magnetic energy of perturbations can grow from conversion of kinetic to magnetic energy (first term), from extracting kinetic energy from the background shear flow/differential rotation (second term), and that it is dissipated ohmically (fourth term). Note that the term $\langle \boldsymbol{B} \cdot (\boldsymbol{B}_0 \cdot \nabla)\boldsymbol{u} \rangle$ in Eq. 5.83 can be shown to be equivalent with $-\langle \boldsymbol{u} \cdot (\boldsymbol{B}_0 \cdot \nabla)\boldsymbol{B} \rangle$ in Eq. 5.82 using integration by parts, which indicates that these just convert kinetic to magnetic energy and vice versa, and do not inject total energy into the system.

The final energy equation that we need to consider is the one governing the thermal energy in the system. For this, we obtain

$$\partial_t \mathcal{P} = -\langle \theta \boldsymbol{u} \cdot \boldsymbol{e}_\theta \rangle + \kappa \langle \frac{\theta \nabla^2 \theta}{\mathcal{N}^2} \rangle, \tag{5.84}$$

using the results $\langle \theta(\boldsymbol{u} \cdot \boldsymbol{\nabla})\theta \rangle = \langle \theta(\boldsymbol{U}_0 \cdot \nabla)\theta \rangle = 0$. This shows that thermal energy grows through conversion from kinetic to thermal energy (first term) and that it is dissipated by thermal diffusion (second term). Hence, the equation for the total energy $\mathcal{E} = \mathcal{K} + \mathcal{M} + \mathcal{P}$, is

$$\begin{aligned} \partial_t \mathcal{E} =& \mathcal{S}(\langle u_x u_y \rangle - \langle B_x B_y \rangle) + \langle \theta \boldsymbol{u} \cdot (\boldsymbol{e}_g - \boldsymbol{e}_\theta) \rangle \\ &+ \nu \langle \boldsymbol{u} \cdot \nabla^2 \boldsymbol{u} \rangle + \eta \langle \boldsymbol{B} \cdot \nabla^2 \boldsymbol{B} \rangle + \kappa \langle \frac{\theta \nabla^2 \theta}{\mathcal{N}^2} \rangle. \end{aligned} \tag{5.85}$$

This indicates that the total energy of perturbations can grow only via extraction of kinetic energy from the shear flow/differential rotation into perturbation kinetic or magnetic energies (first two terms), or via the baroclinic term that extracts potential energy from the basic state into kinetic and thermal energies (last term on first the line), if and only if these contributions exceed the sum of the viscous, ohmic and thermal dissipations (terms on the bottom line).

We can use these results to analyse the energy sources contributing to the instabilities described by Eq. 5.41. To do this, we calculate each of the terms in these energy equations for a single axisymmetric Fourier mode with a wavevector $\boldsymbol{k} = (k_x, 0, k_z)$. This can be used to understand better both the driving forces of the instability and the momentum transporting properties of the instability. We first express $\langle u_x u_y \rangle$ for a single mode with $u_x = \Re\left[\hat{u}_x \exp\left(\mathrm{i}\boldsymbol{k} \cdot \boldsymbol{x} + st\right)\right]$ and $u_y = \Re\left[\hat{u}_y \exp\left(\mathrm{i}\boldsymbol{k} \cdot \boldsymbol{x} + st\right)\right]$. Using the properties of complex numbers, $\Re(A)\Re(B) = \frac{1}{2}\Re(AB + AB^*)$, where $*$ denotes the complex conjugate, this can be written

$$\begin{aligned} \langle u_x u_y \rangle &= \frac{1}{2} \langle \Re(\hat{u}_x \hat{u}_y \exp\left(2st + 2\mathrm{i}\boldsymbol{k} \cdot \boldsymbol{x}\right) + \exp(2\Re[s]t)\hat{u}_x \hat{u}_y^*) \rangle \\ &= \frac{1}{2} \exp(2\Re[s]t)\Re(\hat{u}_x \hat{u}_y^*), \end{aligned} \tag{5.86}$$

upon applying the periodic boundary conditions (thereby eliminating the first term on the top line).

For a single linear mode we can use Eqs. 5.7–5.12 to relate $\hat{u}_y$ to $\hat{u}_x$ (and similarly for all other variables) to obtain

$$\hat{u}_y = \frac{s_\eta}{s_\nu s_\eta + \omega_A^2}\left(\mathcal{S}\left(1 + \frac{\omega_A^2}{s_\eta^2}\right) - 2\Omega\left(c_\Lambda + \frac{k_x}{k_z}s_\Lambda\right)\right)\hat{u}_x, \tag{5.87}$$

and we also note that $\hat{u}_z = -(k_x/k_z)\hat{u}_x$. Substituting this into Eq. 5.86, and using $\Re[\hat{u}_x\hat{u}_y^*] = \Re[\hat{u}_x^*\hat{u}_y]$, gives the concise form for the xy-component of the Reynolds stress

$$\langle u_x u_y\rangle = \frac{|\hat{u}_x|^2}{2}\Re\left[\frac{s_\eta\left(\mathcal{S}\left(1 + \frac{\omega_A^2}{s_\eta^2}\right) - 2\Omega\left(c_\Lambda + \frac{k_x}{k_z}s_\Lambda\right)\right)}{s_\nu s_\eta + \omega_A^2}\right]. \tag{5.88}$$

We also have

$$\begin{aligned}\hat{B}_y &= \frac{\mathrm{i}\omega_A}{s_\eta}\left[\hat{u}_y - \frac{\mathcal{S}}{s_\eta}\hat{u}_x\right]\\ &= \frac{\mathrm{i}\omega_A\hat{u}_x}{s_\eta}\left[-\frac{\mathcal{S}}{s_\eta} + \frac{\mathcal{S}\left(1 + \frac{\omega_A^2}{s_\eta^2}\right) - 2\Omega\left(c_\Lambda + s_\Lambda\frac{k_x}{k_z}\right)}{s_\nu + \frac{\omega_A^2}{s_\eta}}\right],\end{aligned} \tag{5.89}$$

along with $\hat{B}_z = -(k_x/k_z)\hat{B}_x$, which allows the xy-component of the Maxwell stress for a single mode to be written

$$\begin{aligned}\langle B_x B_y\rangle &= \frac{1}{2}\Re[\hat{B}_x\hat{B}_y^*]\exp(2\Re[s]t)\\ &= \Re\left[\frac{\omega_A^2|\hat{u}_x|^2}{2s_\eta^2}\left(-\frac{\mathcal{S}}{s_\eta} + \frac{\mathcal{S}\left(1 + \frac{\omega_A^2}{s_\eta^2}\right) - 2\Omega\left(c_\Lambda + s_\Lambda\frac{k_x}{k_z}\right)}{s_\nu + \frac{\omega_A^2}{s_\eta}}\right)\right].\end{aligned} \tag{5.90}$$

The third and final term that can inject energy into the system is

$$\langle\theta\boldsymbol{u}\cdot(\boldsymbol{e}_g - \boldsymbol{e}_\theta)\rangle = \langle\theta[u_x\left(c_\phi - c_\Gamma\right) + u_z\left(s_\phi - s_\Gamma\right)]\rangle, \tag{5.91}$$

which is essentially a measure of the extent that baroclinicity (i.e. non-coincidence of constant density and pressure surfaces) drives the instability. We use

$$\hat{\theta} = -\frac{\mathcal{N}^2}{s_\kappa}\left(c_\Gamma - \frac{k_x}{k_z}s_\Gamma\right)\hat{u}_x, \tag{5.92}$$

along with incompressibility to write:

$$\langle \theta \boldsymbol{u} \cdot (\boldsymbol{e}_g - \boldsymbol{e}_\theta)\rangle = \frac{1}{2}\Re\left[\frac{\mathcal{N}^2}{s_\kappa}\left(\frac{k_x}{k_z}s_\Gamma - c_\Gamma\right)\left((c_\phi - c_\Gamma) - \frac{k_x}{k_z}\left(s_\phi - s_\Gamma\right)\right)\right]|\hat{u}_x|^2. \tag{5.93}$$

Note that this term vanishes entirely when $\boldsymbol{e}_g = \boldsymbol{e}_\theta$, and is thus unimportant when $s_\Lambda = 0$ (no differential rotation along the rotation axis), and it is small in the strongly stratified limit when $\mathcal{N}^2 \gg 2\Omega\mathcal{S}s_\Lambda$.

The kinetic energy is

$$\mathcal{K} = \frac{1}{2}\langle|\boldsymbol{u}|^2\rangle = \frac{1}{4}[|\hat{u}_x|^2 + |\hat{u}_y|^2 + |\hat{u}_z|^2]\exp(2\Re[s]t), \tag{5.94}$$

which can be expressed in terms of $|\hat{u}_x|^2$ using our equations for $\hat{u}_y$ (5.87) and $\hat{u}_z$ (conservation of mass). The magnetic energy is

$$\mathcal{M} = \frac{1}{2}\langle|\boldsymbol{B}|^2\rangle = \frac{1}{4}\left[|\hat{B}_x|^2 + |\hat{B}_y|^2 + |\hat{B}_z|^2\right]\exp 2\Re[s]t, \tag{5.95}$$

which can also be expressed in terms of $|\hat{u}_x|^2$ using the following expressions:

$$|\hat{B}_x|^2 = \frac{\omega_A^2}{|s_\eta|^2}|\hat{u}_x|^2, \tag{5.96}$$

$$|\hat{B}_y|^2 = -\frac{\omega_A^2}{|s_\eta|^2}\left|-\frac{\mathcal{S}}{s_\eta} + \frac{\mathcal{S}\left(1 + \frac{\omega_A^2}{s_\eta^2}\right) - 2\Omega\left(c_\Lambda + s_\Lambda\frac{k_x}{k_z}\right)}{s_\nu + \frac{\omega_A^2}{s_\eta}}\right|^2|\hat{u}_x|^2, \tag{5.97}$$

$$|\hat{B}_z|^2 = \frac{\omega_A^2}{|s_\eta|^2}\left(\frac{k_x}{k_z}\right)^2|\hat{u}_x|^2. \tag{5.98}$$

The thermal energy for a single mode can be expressed as

$$\langle\frac{|\theta|^2}{2\mathcal{N}^2}\rangle = \frac{\mathcal{N}^2}{4|s_\kappa|^2}(c_\Gamma - \frac{k_x}{k_z}s_\Gamma)^2|\hat{u}_x|^2. \tag{5.99}$$

Using these expressions we can determine the energetic contributions to the growth rate for a single Fourier mode by noting that

$$2\Re[s] = \partial_t \ln \mathcal{E} = \frac{1}{\mathcal{E}} \partial_t \mathcal{E}, \tag{5.100}$$

where the right hand side contains all six terms in Eq. 5.85 and is independent of the mode amplitude since $|\hat{u}_x|^2$ cancels in both numerator and denominator. This can also be used as a check of our codes by ensuring that the growth rate $\Re[s]$ is predicted to machine precision by using the linear relations between the components that we have just derived. Once this has been confirmed we can compute the contribution of each of the first three possible driving terms on the right hand side of Eq. 5.85 to the growth rate to determine whether a given instability is driven by Reynolds stress, Maxwell stress or baroclinic term.

5.5.2 Numerical analysis of linear mode energetics

Unstable modes energetics: variation with B_0

We present results from computing the contributions to the growth rate from the three source terms on the right hand side of Eq. 5.85. In particular, we determine the contributions to the growth rate from the Reynolds stress, Maxwell stress, and baroclinic driving terms in Eqs. 5.88, 5.90 and 5.93 as a visual tool to better understand the mechanisms driving the various instabilities, as well as the role of the magnetic field. Each of these are divided by $2\mathcal{E}$ in order to compute their contribution to σ for the reason explained in Eq. 5.100. All of the figures in this section use our standard choice of parameters, $\mathrm{Pr} = 10^{-2}$, $\mathcal{N}^2 = 10$ and $\mathcal{S} = 2$ unless stated otherwise.

Figs. 5.14 and show pseudocolour plots for various Λ and ϕ of the growth rate (first row) along with the contributions to it from Reynolds stresses (second row), Maxwell stresses (third row) and baroclinic source terms (fourth row) on the (k_x, k_z)-plane, for various magnetic field strengths $B_0 = 1, 2.5$ and 5. Rows two to four represent the

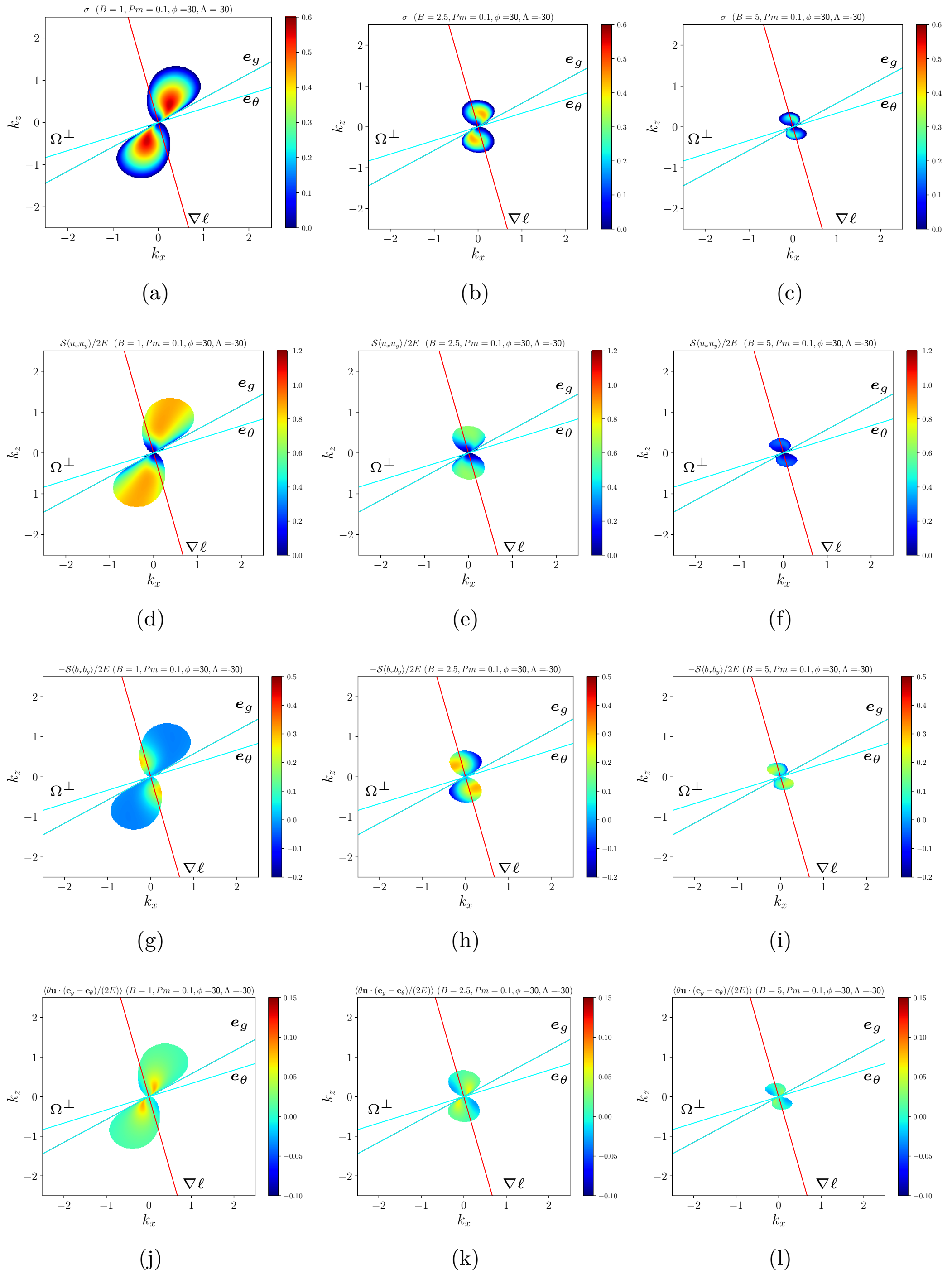

(a) (b) (c)

(d) (e) (f)

(g) (h) (i)

(j) (k) (l)

Figure 5.14: Energetic contributions to instability on the (k_x, k_z)-plane for $\Lambda = -30°$ and $\phi = 30°$, $B_0 = 1, 2.5$ and 5 (increasing in columns as we go from left to right) all with $S = 2$, $N^2 = 10$, $\mathrm{Pr} = 0.01$ and $\mathrm{Pm} = 0.1$. Top row: growth rate. Second row: Reynolds stress contribution. Third row: Maxwell stress contribution. Fourth row: baroclinic contribution. Stable modes with $\Re[s] \leq 0$ are indicated in white for clarity.

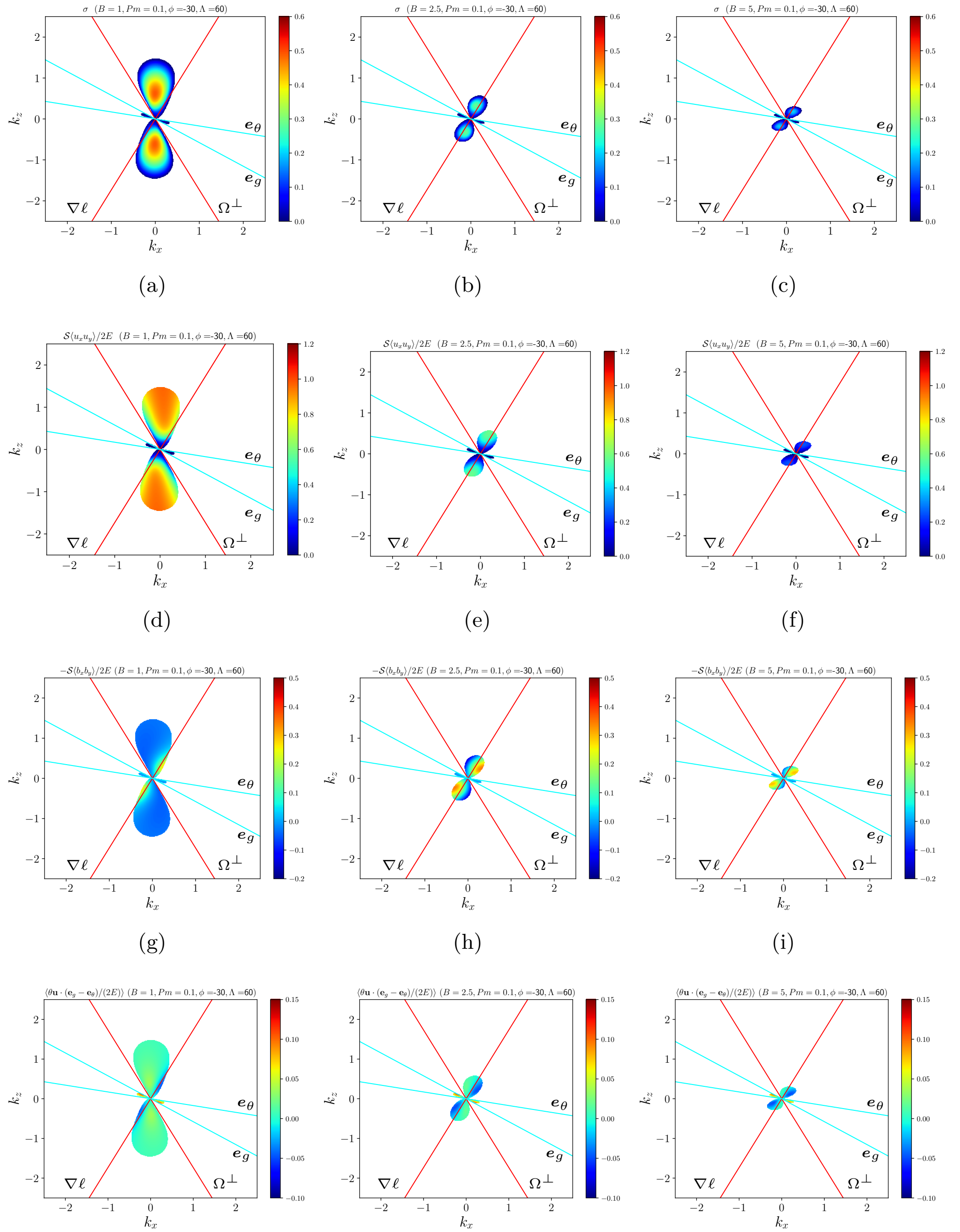

(a) (b) (c)

(d) (e) (f)

(g) (h) (i)

(j) (k) (l)

Figure 5.15: Energetic contributions to instability on the (k_x, k_z)-plane for $\Lambda = 60°$ and $\phi = -30°$, $B_0 = 1, 2.5$ and 5 (increasing in columns as we go from left to right) all with $S = 2$, $N^2 = 10$, Pr $= 0.01$ and Pm $= 0.1$. Top row: growth rate. Second row: Reynolds stress contribution. Third row: Maxwell stress contribution. Fourth row: baroclinic contribution. Stable modes with $\Re[s] \leq 0$ are indicated in white for clarity.

first three terms in Eq. 5.85, the sum of these, together with the three diffusive terms (not plotted) in Eq. 5.85 has been verified to match the growth rate σ to machine precision. In contrast to Figs. 5.3–5.5 they use a linear colour scale since the various contributions plotted can take either sign, as we observe in these figures. Overall, these figures allow us to explore how variations in field strength for ($B_0 = 1, 2.5, 5$) and rotation profile (through Λ and ϕ) alter the instabilities whilst simultaneously probing which energy source terms are responsible.

In Figs. 5.14 we first analyse the configuration at the equator with mixed shear ($\Lambda = -30^\circ$, $\phi = 30^\circ$) explored earlier in Fig. 5.3. This configuration is GSF unstable in the hydrodynamic case and remains unstable for weak fields. Strong fields tend to inhibit instability for $k \sim 1$ and to shrink the unstable lobes, in addition to changing their orientation. For $B_0 \leq 2.5$, Reynolds stresses are the primary drivers of instability for most (k_x, k_z), indicating that unstable modes are primarily driven by extracting kinetic energy from the differential rotation. As B_0 is increased further, Maxwell stresses play an increasingly important role, until they dominate for $B_0 = 5$, indicating that shear flow kinetic energy is extracted in the form of perturbation magnetic energy. The different locations of the peaks in Reynolds and Maxwell stresses – and the increasingly stabilising effects (negative values shown) of Maxwell stresses where the Reynolds stresses are maximal – are consistent with the changes in orientations of the unstable lobes as B_0 is increased, from initially being between $\hat{\boldsymbol{\Omega}}^{\perp}$ and $\nabla \ell$ to become closer to $\nabla \ell$ for the strongest fields. For this latitude and flow baroclinic driving terms are typically subdominant, but they still contribute non-negligibly to driving instabilities for weaker fields. The effect of the field in reducing the maximum growth rate observed in Fig. 5.9 is also confirmed here.

We next look at a case with latitude 30° with mixed shear ($\Lambda = 60^\circ, \phi = -30^\circ$) in Fig. 5.15 as first studied in Fig. 5.4. This configuration is GSF unstable hydrodynamically and remains unstable for weak fields. We saw from Fig. 5.10 that the field acts to monotonically stabilise the system with increasing B_0, which is consistent with Fig. 5.15. We again observe that the primary lobes of instability are driven primarily by Reynolds stresses for $B_0 \leq 2.5$, but become increasingly driven by Maxwell stresses for stronger fields. We also observe the positive Reynolds stress contributions are mainly confined to within the hydrodynamically unstable wedge delineated by the lines $\hat{\boldsymbol{\Omega}}^{\perp}$ and $\nabla\ell$, and are maximal approximately halfway between these. The increasing importance of Maxwell stresses and the shift in orientation of the lobes indicates the transition in the dominant instability from GSF to double-diffusive MRI. Notice that the Maxwell stress generally has a preferred wavevector magnitude, evident by the darkest red (most unstable) modes being located in the centre of the lobes. We also observe the unstable region shrinking as the double-diffusive MRI enables instability for smaller and smaller k for appropriately oriented modes. The baroclinic term is unimportant for the primary lobes, as is indicated by the bottom panels.

The secondary lobes evident in Fig. 5.15 are hydrodynamically unstable oscillatory modes within the wedge defined by $\boldsymbol{e}_g$ and $\boldsymbol{e}_\theta$. The bottom panels of this figure confirm that these modes are baroclinically driven since σ approximately equals its baroclinic contribution, with Reynolds and Maxwell stresses playing negligible roles in driving them. The growth rates and unstable mode wavevectors are mostly unaffected by the magnetic field, except that these become weakly destabilised magneto-inertial-gravity waves rather than inertia-gravity waves when the field is sufficiently strong.

Similar trends as B_0 is varied are found for Λ and ϕ that are adiabatically Solberg-Høiland unstable in the hydrodynamic case, and for cases at the poles that are hydrodynamically adiabatically stable.

Fastest growing mode energetics: variation with B_0

We next turn to analyse how the energetic contributions vary with B_0 for the fastest growing modes, obtained by optimising over k_x and k_z for each case. Results are shown in Fig. 5.16 for various latitudes and differential rotations. We study both

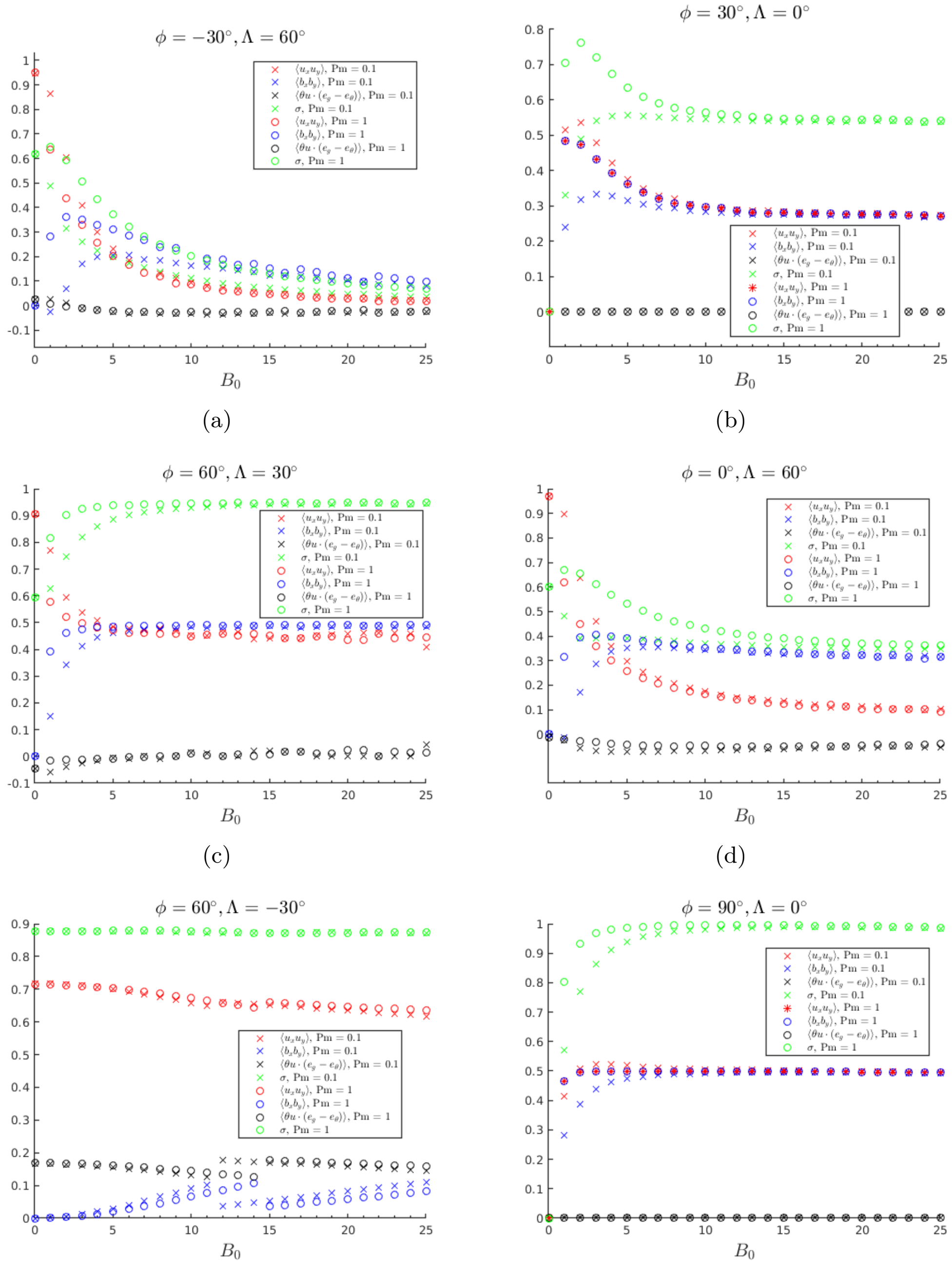

(a) (b) (c) (d) (e) (f)

Figure 5.16: Energetic contributions to instability for the fastest growing mode (optimised over k_x and k_z) as a function of the magnetic field strength B_0 for various Λ and ϕ cases. These show the growth rate, and the contributions to it from Reynolds stresses ($\langle u_x u_y \rangle$), Maxwell stresses ($\langle b_x b_y \rangle$) and baroclinic source terms ($\langle \theta \boldsymbol{u} \cdot (\boldsymbol{e}_g - \boldsymbol{e}_\theta) \rangle$) against field strength B_0. All panels show Pm = 0.1 and Pm = 1, and the other parameters are $\mathrm{Pr} = 10^{-2}$, $\mathcal{N}^2 = 10$ and $\mathcal{S} = 2$.

$\mathrm{Pm} = 1$ and $\mathrm{Pm} = 0.1$ in order to investigate the role magnetic diffusivity plays in these results.

Panel (a) of Fig. 5.16 analyses a case with $\phi = 60°$, $\Lambda = -30°$ that is adiabatically Solberg-Høiland unstable in the hydrodynamic case. We find the growth rate in this case is essentially independent of B_0, as predicted from Figs. 5.6 and 5.10. The primary result of changing B_0 is to decrease the range of unstable k_x and k_z as we have confirmed in Fig. 5.5. This case is driven by the Reynolds stress for all B_0 considered, since the red symbols provide a larger contribution to the total growth rate, for both Pm plotted. Magnetic diffusion does not play an important role here, confirmed by the negligible role of Pm. The baroclinic driving term is the secondary contributor to instability for the smaller B_0, but it appears that it may be superseded for $B_0 \gtrsim 25$ by Maxwell stresses. There is a jump from one unstable mode to another around $B_0 = 12$ where baroclinic and Maxwell stress terms approximately balance, where the k and θ_k values instantly switch.

Panel (b) of Fig. 5.16 analyses a case with cylindrical differential rotation ($\Lambda = 0$, which is neutrally hydrodynamically GSF stable for all latitudes with $S = 2$. This case is significantly destabilised by even weak magnetic fields as we have seen in Figs. 5.10, 5.11 and 5.12, and this instability is the double-diffusive MRI. This instability is driven by an approximately equal combination of Reynolds and Maxwell stresses, which perfectly coincide for large B_0. This can be termed "Alfvénisation" of the instability for fields for sufficiently strong fields. The complete lack of any baroclinic driving is evident in this figure, and is also observed in panel (f) which also has $\Lambda = 0$, as is expected for any cylindrical rotation profile.

Panel (c) probes instabilities at the poles by considering $\phi = 60°$ and $\Lambda = 30°$. Figs. 5.8 and 5.12 indicated that this latitude is widely unstable to adiabatic magnetic instabilities, in stark contrast to the hydrodynamic results (Dymott et al., 2023), which found no adiabatic instability there. This instability is again the MRI, and it is driven by an approximately equal balance of Reynolds and Maxwell stresses indicating "Alfvénisation" once again. The growth rate increases by around 35%

between $B_0 = 0$ and $B_0 = 5$, after which increases in B_0 lead to only marginal increases in σ.

Panel (d) explores a shellular rotation profile with $\phi = 0°$ and $\Lambda = 60°$. These cases were explored hydrodynamically in BJT2. This figure indicates that the instability is initially driven almost entirely by Reynolds stresses when $B_0 \sim 0$, but Maxwell stresses dominate for $B_0 \gtrsim 5$. The introduction of magnetic fields weakens the instability and reduces σ (after a small rise for $B_0 \sim 1$) over the $B_0 = 0$ case. A plateau is reached for σ by $B_0 \gtrsim 15$, where the instability is primarily driven by Maxwell stresses. Once again, the baroclinic driving term is very weak in this case for any B_0.

Panel (e) shows the behaviour of the fastest growing mode from the parameters of Fig. 5.15 with $\phi = -30°$ and $\Lambda = 60°$. As B_0 is increased σ is drastically reduced. Up to $B_0 \approx 5$ for $\mathrm{Pm} = 0.1$ and $B = 3$ for $\mathrm{Pm} = 1$ Reynolds stresses are the dominant contributor to the growth rate, but as the growth rate decreases with increasing field strength Maxwell stresses become the dominant contributor with these lines converging towards each other. We may achieve "Alfvénisation" again for sufficiently large B_0, but this is not observed by $B_0 = 25$. As was observed in Fig. 5.4 the $\mathrm{Pm} = 1$ case is consistently more unstable than the $\mathrm{Pm} = 0.1$ case, however as the growth rate tends to zero this difference becomes marginal.

In this section we have analysed the unstable mode energetics as B_0, Pm and the properties of the differential rotation were varied. We have found that the fastest growing modes are always driven predominantly by a combination of Reynolds and Maxwell stresses for non-zero B_0 and that baroclinic driving is negligible except for the subdominant secondary lobes. For strong enough magnetic fields, in many cases in which the double-diffusive MRI operates, the contributions of Reynolds and Maxwell stresses equalise. Overall, these results confirm that even a weak magnetic field can drastically alter the stability of differentially rotating flows in stellar radiation zones.

5.6 Applications to the Sun and red giant stars

We now turn to estimate parameter values for the solar tachocline as a potential application of this work. Recall that we defined our lengthscale d as

$$d = \left(\frac{\nu\kappa}{\mathcal{N}^2}\right)^{\frac{1}{4}}, \tag{5.101}$$

since this describes the scales of the dominant hydrodynamic GSF modes. In the solar tachocline (e.g. Gough, 2007; Caleo et al., 2016), we find $\nu = 2.7 \times 10^1 \mathrm{cm}^2\mathrm{s}^{-1}$, $\kappa = 1.4 \times 10^7 \mathrm{cm}^2\mathrm{s}^{-1}$, hence $\mathrm{Pr} = 2 \times 10^{-6}$ and $\mathcal{N} = 8 \times 10^{-4}\mathrm{s}^{-1}$. This produces a length scale[2] $d \approx 49.3$m. The linear GSF modes thus have very short length-scales approx 10^{-5} of the tachocline thickness. The dimensional wavenumber $k_{dim} = k/d$, using our dimensionless wavenumber k.

The magnetic field strength and structure in the tachocline is highly uncertain. Nevertheless, any poloidal magnetic field is probably in the range 0.5G to 5kG (e.g. Mestel & Weiss, 1987, and we are not aware of substantially stronger subsequent constraints). The field there is likely to be mostly toroidal, but only poloidal fields enter our stability analysis for axisymmetric modes. The arguments of Gough and McIntyre (1998) for the maintenance of the tachocline also suggest a minimum poloidal field of 1 G is required there.

Our dimensionless magnetic field $\boldsymbol{B}$ is written in Alfvén speed units; therefore it has units $d\,\Omega$ where $\Omega = 2\pi/P_{\mathrm{rot}}$, and $P_{\mathrm{rot}} = 27$ days is the Sun's mean rotation period. The corresponding physical magnetic field magnitude B_{dim} from the dimensional Alfvén speed $V_A = B_{dim}/\sqrt{\mu_0\rho}$

$$B_{dim} = B_0 d\Omega\sqrt{\mu_0\rho}, \tag{5.102}$$

$$\Rightarrow B_{dim} \approx 2.1 \times 10^{-6} B_0\,\mathrm{T} \approx 0.021 B_0\,\mathrm{G}, \tag{5.103}$$

---

[2] Please note the unfortunate typo in BJT1, where this was written as km instead! No other values in BJT1 need modifying and slightly different numbers were used from stellar models for the various parameters there than the ones we quote here.

using $\Omega = 2.7 \times 10^{-6}\mathrm{s}^{-1}$ (implying $\mathcal{N}^2/\Omega^2 \approx 8.7 \times 10^4$), $\rho = 210\,\mathrm{kgm}^{-3}$ and $\mu_0 = 4\pi \times 10^{-7}$ in SI units. This means that a field of 1 G corresponds to a dimensionless $B_0 \approx 46$ in our units if d is the relevant length-scale. Note that d was defined based on the diffusive hydrodynamic GSF modes, and we have found the double-diffusive MRI to potentially have much larger wavelengths.

On the other hand if we want to consider a field of 1 kG, this requires $B_0 = 4.6 \times 10^4$ in dimensionless units, which is much larger than we have considered here. The fields we have primarily explored in this work are at the weaker end, with $B_0 \lesssim 25$, corresponding to fields weaker than approximately 0.5 G in the tachocline. This choice was partly made to permit us to explore the modification of hydrodynamic diffusive rotational instabilities by a weak field, and was partly made because we found that for larger B_0 the GSF mode is primarily stabilised and the dominant instability by far is the double-diffusive MRI. This agrees with several of the conclusions from Caleo and Balbus (2016) and Caleo et al. (2016).

Note that $\eta = 4.1 \times 10^2\mathrm{cm}^2\mathrm{s}^{-1}$ in the tachocline, so $\mathrm{Pm} = 0.065$ and $\mathrm{Pr}/\mathrm{Pm} = 3 \times 10^{-5}$ there. Hence, we are in the regime of rapid thermal diffusion relative to viscous and ohmic diffusion in the tachocline, as discussed in § 5.3.3.

In the core of red giant stars, whose core-envelope differential rotations remain poorly explored, as considered in BJT1 and using the numbers there, $d \sim 100\mathrm{m}$, $\Omega \sim 10^{-7}\mathrm{s}^{-1}$. This produces $B_{dim} \sim 1.12 B_0 \sqrt{\rho/10^5\mathrm{gcm}^{-3}}$ G. Hence in that problem $B_{dim} \sim B_0$ G in the cores of red giant stars. Since there have been constraints on fields in these from asteroseismology of order 40 to 610 kG (Deheuvels et al., 2023), this suggest we should consider $B_0 \gtrsim 10^3$ in red giant stars also. Hence double-diffusive MRI is expected to be more important than GSF, depending on the rotation profile, and perhaps not for $\phi < 0^\circ$.

5.7 Conclusions

We have presented a theoretical analysis of local triply-diffusive instabilities of differential rotation in magnetised radiation zones of stars and planets, building upon the hydrodynamical studies of Barker et al. (2019, 2020) and Dymott et al. (2023) and Chapters 2 & 3. Understanding the properties of these instabilities, and ultimately their nonlinear behaviour, is essential because they have been proposed to play important roles in angular momentum transport and chemical mixing in stars (e.g. Caleo et al., 2016; Aerts et al., 2019), and they may even play a role in the solar dynamo (Parfrey & Menou, 2007; Vasil et al., 2024), but many aspects of them are currently very poorly understood. Our focus has been on the effects of a poloidal magnetic field on the properties of linear axisymmetric instabilities of differential rotation, which are governed by a quintic dispersion relation first derived by Menou et al. (2004). We have performed a detailed analysis of the dispersion relation, firstly for non-diffusive instabilities, reproducing prior work on the stratified MRI (e.g. Balbus, 1995), before analysing diffusive instabilities in various limits analytically and numerically.

In strongly stably stratified regions of stars, adiabatic theories would predict the fastest growing mode displacements to be along stratification (i.e. approximately spherical) surfaces. However, rapid thermal diffusion can eliminate the stabilising effects of buoyancy if Pr/Pm and Pr are sufficiently small, which is very much the case in stars. In this limit double-diffusive[3] MRI operates and can change the properties of the unstable modes depending on the differential rotation. We have obtained new analytical and numerical results on the various instabilities in this triply-diffusive system as a function of the differential rotation profile and magnetic field strength.

Our analytical and numerical results have highlighted that even a weak magnetic field can considerably modify the local instabilities of differentially rotating flows

---

[3] Referred to as such because the relevant diffusing quantities are magnetic field and entropy; molecular viscosity is typically even weaker.

(e.g. Balbus & Hawley, 1998, and many prior works). We have found that for differential rotations with (angle between effective gravity and local angular velocity gradient) $\phi > 0^\circ$, MRI may dominate over the magnetic modification of hydrodynamic GSF instabilities. However, for $\phi < 0^\circ$, hydrodynamic GSF modes could still be important even if they are weakened by magnetic tension for moderately strong fields. We found that even weak fields destabilise hydrodynamically stable regions in parameter space, particularly for nearly cylindrical differential rotation profiles.

We have analysed in detail the properties of axisymmetric modes, including how the growth rates and wavevectors depend on the strength of the magnetic field, magnetic Prandtl number Pm, and local differential rotation profile. We have analysed in detail the energetics of the various instabilities in our system, first by deriving the energy equation and then by evaluating the various source terms for linear axisymmetric modes. These consist of Reynolds stresses, Maxwell stresses and baroclinic driving terms. We find that the MRI is typically driven by Reynolds and Maxwell stresses in approximately equal proportions (so-called Alfvénisation) in a wide range of cases.

We believe that it is important to set up a meaningful time-independent magnetic equilibrium to properly analyse MHD instabilities. We take a different viewpoint to many prior works that attempted to model arbitrary field configurations without ensuring Ferraro's law of isorotation was satisfied (e.g. Balbus & Hawley, 1994; Menou et al., 2004; Menou & Le Mer, 2006; Parfrey & Menou, 2007; Caleo et al., 2016). In our model we ensured our basic state was an equilibrium state and verified the local analogue of Ferraro's law of isorotation. This is analogous to the original works of Goldreich and Schubert (1967) and Fricke (1968) having an additional degree of freedom because they ignored the constraint of thermal wind balance. Similar issues have also plagued studies of the effects of magnetic fields on the vertical shear instability in astrophysical discs (e.g. Urpin & Brandenburg, 1998; Latter & Papaloizou, 2018, in which the latter authors take the same viewpoint as us).

Depending upon the differential rotation, we find that MRI can occur for much weaker shears than the hydrodynamic GSF instability, and that it can occur on much larger scales. We anticipate that when it operates, MRI is likely to be more efficient at transporting angular momentum than the GSF instability, though the latter could still be important for configurations in which the MRI is not excited.

Chapter 6

Nonlinear Magnetohydrodynamical Simulations

6.1 Introduction

The following chapter builds on Chapters 4 and 5 to quantify how the addition of a magnetic field affects the evolution of local instabilities in a stably stratified differentially rotating region of a stellar radiative zone.

Following Chapter 4 we again use the pseudo-spectral code Snoopy to run nonlinear simulations for 4 sets of Λ and ϕ values at the latitudes $\Lambda+\phi = 0^\circ, 30^\circ$ and 90°. Our intention is to quantify the evolution of the energetic and transport properties of the system over time, for which our findings will be presented in Figs. 6.1, 6.4, 6.7 and 6.10. At each of the key stages throughout its evolution we also present snapshots of the flow (see Figs. 6.2, 6.5, 6.8 and 6.11) as a visual guide to the evolution. We fix our non-dimensional parameters throughout to be $S = 2$, $N^2 = 10$, $\mathrm{Pr} = 10^{-2}$, $\mathrm{Pm} = 10^{-1}$ with a typical box size $L_x = L_y = L_z = 100$, and a resolution of $N_x = N_y = N_z = 256$ unless otherwise stated. These choices have been made to allow a direct comparison to some of the cases explored hydrodynamically in Chapter 4 and in Barker et al. (2020). We impose an initial uniform vertical magnetic field $\boldsymbol{B}(t=0) = B_0 \boldsymbol{e}_z$ in our simulations – rather than an imposed background field as in Chapter 5 – so our $\boldsymbol{B}$ here represents the total magnetic field in our simulations.

Depending on the strength of the magnetic field we found in Chapter 5 that the system is unstable to either a magnetically modified version of the operating hydrodynamic axisymmetric instability – either an adiabatically-unstable centrifugal (Solberg-Høiland) instability or the GSF instability depending on the parameter regime – or an axisymmetric MRI-type instability. We analyse simulations exploring the evolution of the various instabilities in our system in the presence of a magnetic field. We also explore the box size dependence of the various instabilities. Fully 3-dimensional box figures are also presented of the flow in the strong $B_0 = 10$ field cases once they've reached their final dynamical regime. These figures are presented alongside corresponding energy spectra that demonstrate these simulations to be well resolved, reinforcing our trust in these results.

6.2 Nonlinear analysis

We first present a selection of figures (Figs. 6.1, 6.4, 6.7 and 6.10) characterizing the time evolution of various properties of interest, including the Reynolds stress component $\langle u_x u_y \rangle$, the Maxwell stress component $\langle B_x B_y \rangle$, the total stress (y-momentum transport rate) given by $\mathcal{S}\langle u_x u_y - B_x B_y \rangle$, as well as the kinetic energy $KE = \frac{1}{2}\langle u_x^2 + u_y^2 + u_z^2 \rangle$, and magnetic energy $ME = \frac{1}{2}\langle B_x^2 + B_y^2 + B_z^2 \rangle$. We explore various field strengths $B_0 \in [0, 1, 2.5, 5, 10]$ with the other parameters defined as stated above. Note that any regions corresponding to negative values of the Reynolds or Maxwell stress in Figs. 6.1 or 6.4 are left blank due to our use of a logarithmic scale, which explains the breaks in the lines for the larger B_0 values after initial saturation of instability.

We present these alongside complementary snapshots (slices through our box in the

(x, z)-plane at $y = 0$) at key stages in the evolution for the field strengths $B_0 = 1, 5$, and 10 in Figs. 6.2, 6.5, 6.8 and 6.11. Following Chapter 4, we consider a set of four values of Λ and ϕ at the three latitudes $0^\circ, 30^\circ, 90^\circ$. These cases include a hydrodynamically GSF-unstable case at each latitude and a hydrodynamically adiabatically-unstable case at latitude 30° so that we can analyse how the addition of a magnetic field modifies these.

Across all cases the system's behaviour depends heavily on the strength of the imposed magnetic field, either showing a magnetically-modified version of the existing hydrodynamic instability, or transitioning to the MRI for strong enough fields. For all cases that are hydrodynamically-unstable to the GSF instability, a change of regime occurs when $B_0 \gtrsim 2.5$ for the parameters (N^2, S, Pr and Pm) we have simulated. In contrast, adiabatically unstable cases appear more resistant to the effects of the magnetic field, presumably because the adiabatic Solberg-Høiland instability is much more strongly driven, typically with larger growth rates and unstable mode length-scales. Only the strongest fields we considered, with $B_0 = 10$, were sufficient to substantially alter the nonlinear evolution in these cases.

6.2.1 Equatorial case ($\phi = 30^\circ, \Lambda = -30^\circ$)

At the equator, we consider $\phi = 30^\circ$ and $\Lambda = -30^\circ$, a case with mixed but primarily radial shear. This case is GSF unstable with diffusion but is adiabatically stable when $B_0 = 0$. Initially the lower linear growth rates caused by the magnetic field predicted in Chapter 5 (see Fig. 5.9) manifests as a prolonged linear growth phase in these cases with $B_0 \neq 0$. After this, cases with stronger fields generally exhibited more energetic flows which typically took longer to settle into a final state. These final states seem to be made up of modes which have saturated close to the box scale as opposed to the layers seen in the hydrodynamic regime; this can be seen in Figs. 6.2 and 6.3. For the lower field strengths $B_0 = 1$ and $B_0 = 2.5$ the layered states have an ostensibly similar nature to the hydrodynamic regime seen in Fig. 4.1; however, the resultant flows with stronger fields seem much less stable and generate far larger fluctuations. Other than having stronger fluctuations, the layered system at the equator only leads to significantly different properties in $\langle B_x B_y \rangle$, whereas $\langle u_x u_y \rangle$ and total stress $\langle u_x u_y \rangle - \langle B_x B_y \rangle$ seem to attain roughly similar levels.

The magnetic field does not appear to substantially modify the magnitude of the total stress, i.e. total angular momentum transport rate, in the final turbulent state, only its relative contributions from Reynolds and Maxwell stresses, which become increasingly dominated by the latter to a greater extent for stronger fields. Due to computational constraints, it is difficult to tell whether the larger B_0 cases (particularly $B_0 = 10$) have converged fully to their final state in Fig. 6.1, however, we do not expect significant subsequent deviations from their final values since the linear instability appears to have saturated by then.

The kinetic energy (KE) and magnetic energy (ME) are also presented in Figs. 6.1. In a similar manner to what was seen for the stresses, the addition of the magnetic field acts to increase the duration of the linear phase of the simulation for these parameters, at the end of which we see an extremely large peak in energy before nonlinearly saturating and evolving into a turbulent flow. The smaller linear growth rates are predicted in the GSF-unstable regime in Chapter 5 (see Fig. 5.9) and arise from magnetic tension partially stabilising GSF modes. Higher field strengths, particularly after the change in regime around $B_0 = 2.5$, lead to layers that are much less stable and fluctuate much more aggressively than the hydrodynamic or low B_0 cases. This is likely to be related to the effects of the magnetic field in increasing the length-scale of the linearly-unstable modes as observed in Fig. 5.9, where there is a change from $k \sim 0.6$ when $B_0 = 0$ (black line) to $k \sim 0.1$ when $B_0 = 10$ (green line) in panel (c). This change in the linear mode wavelength is consistent with the snapshots in the linear growth phase in Fig. 6.2. We might expect then the possible parasitic instabilities of the linear modes to be more severely constrained by the box size, thereby allowing them to attain larger amplitudes. Spatial averaging will also be over a smaller number of unstable mode wavelengths, so we would expect to observe more variability in the temporal dynamics.

After the initial growth phase, the turbulent and layered regimes appear to act as dynamos[1] in generating a significantly enhanced and sustained magnetic field strength throughout the subsequent evolution, as observed in the bottom right panel. Interestingly, despite their differing initial fields, all cases with ($B_0 \geq 2.5$) lead to a similar order of magnitude of magnetic energy in the final turbulent state. The field is enhanced most efficiently for $B_0 = 2.5$ over its initial value and these results indicate the operation of a GSF-induced dynamo for these parameters.

Snapshots are plotted in Fig. 6.2 in the $y = 0$ plane, which verifies that higher field strengths, and their associated lower initial growth rates, lead to a prolonged duration for the unstable modes to grow in the linear regime. For $B_0 = 1$ the initial linearly-unstable fingers are no longer visible by $t = 50$, whereas for the $B_0 = 5$ case, this happens later at nearly $t = 100$, and for $B_0 = 10$ it happens even later at approximately $t = 200$. After these times cases with stronger fields display extended temporal variability before a final statistically-steady state is attained. The addition of a magnetic field also clearly influences the orientation of the flow at all stages throughout its evolution, from the linearly growing modes early on to the final turbulent or layered state. The orientation of the linear fingers aligns with the results in Chapter 5, which predicted $\theta_k \sim 125°$ at $B_0 = 1$, $\theta_k \sim 100°$ at $B_0 = 5$, and $\theta_k \sim 110°$ at $B_0 = 10$. However, the orientation of the modes seems to evolve depending on several factors, including ϕ (as seen in Chapter 4) and the strength of the magnetic field. Unlike the hydrodynamic and weak field cases, the unstable modes grow in the form of "elevator modes", which develop preferentially along x for sufficiently strong fields. They subsequently tilt slightly but evolve over time to become roughly perpendicular to the orientation of the jets observed in the hydrodynamic cases in Fig. 4.1. The jets that form in the presence of a weak $B_0 = 1$ field closely follow the dynamics of the hydrodynamic case, with the jets ending up

---

[1] Note that the usage of the term 'dynamo' does not refer to a true dynamo since we are imposing an initial uniform background magnetic field. Hence, the magnetic energy will not diffuse to zero. Strictly speaking, the flow is acting as an amplifier of the background field we impose. Additional simulations would be required to investigate whether or not these instabilities could act as true dynamos, but we will continue to refer to them as dynamos in the text.

tilted at approximately the same angle. This is well predicted by the linear theory in Chapter 5, as panel (c) of Figure 5.9 suggests that $\theta_k \sim 125^\circ$ for both cases.

We analyse the kinetic energy spectrum on the (k_x, k_z)-plane in the bottom panel of Fig. 6.3 for the case with $B_0 = 10$. This shows the alignment of the mode energy in spectral space to be broadly similar to the initial linear orientation in the hydrodynamic case, being oriented approximately halfway between $\hat{\boldsymbol{\Omega}}^{\perp}$ and $\nabla \ell$, even once the flow has nonlinearly saturated and for $B_0 = 10$. The decay in energy from the peak of the spectrum of approximately 10^2 at the smallest k to 10^{-5} by $k \sim 2$ (comfortably below the de-aliasing wavenumber) indicates that these simulations are spatially well resolved. The top panel of Fig. 6.3 shows the u_y flow in 3D using a pseudo-colour plot. We observe the flow to be predominantly y-invariant. Hence the flow remains essentially axisymmetric even in the nonlinear regime, therefore the flow shown in slices at $y = 0$ in Fig. 4.1, even at the largest B_0, do indeed represent zonal jets. A key aspect of the nonlinear saturation of all instabilities is thus the formation of zonal jets.

6.2.2 Hydrodynamically GSF unstable case at latitude 30° ($\phi = -30^\circ, \Lambda = 60^\circ$)

Moving away from the equator we next consider $\phi = -30^\circ$ and $\Lambda = 60^\circ$, corresponding to the hydrodynamically GSF unstable case at latitude 30° seen in Fig. 4.4. We saw in Fig. 5.10 that magnetic fields of higher strengths again suppress the linear growth rate of the most unstable mode, here resulting in an extended initial growth phase in simulations. We can see from Fig. 6.5 that whilst for $B_0 = 1$ the fingers have become turbulent by $t = 50$, $B_0 = 5$ is still well within the linear growth phase at this time. From Fig. 6.4 we see that the linear phase ends for the $B_0 = 5$ case around $t = 80$. The $B_0 = 10$ case takes longer still, with fingers observed in Fig. 6.5 until $t = 100$, and 6.4 suggesting turbulence onsets at around $t = 200$. The prolonged stability of the linear mode fingers for $B_0 = 2.5, 5$ and 10 is suggested by their linear growth rates (see Fig. 5.10) of $\sigma \sim 0.3, 0.2$ and 0.1 respectively,

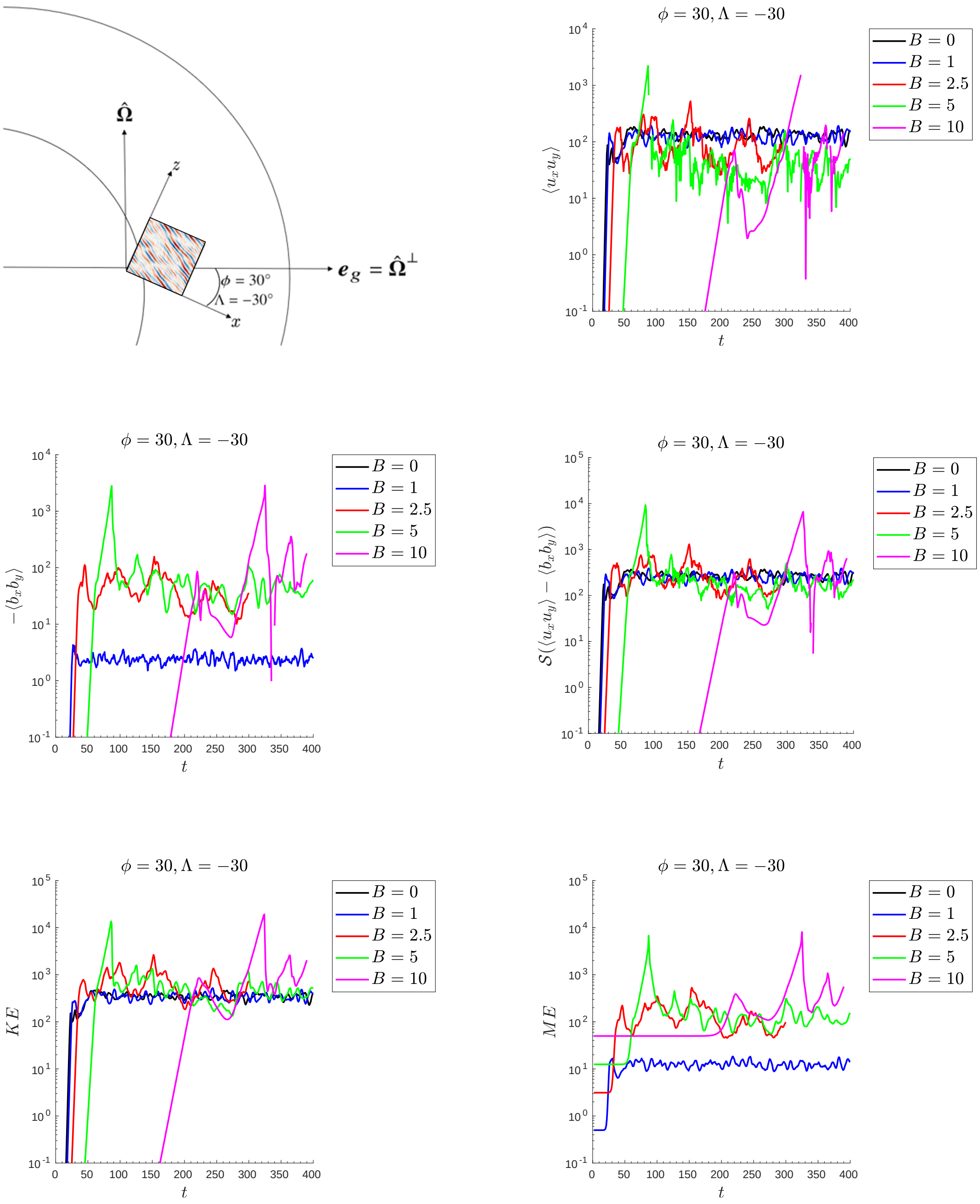

Figure 6.1: Illustrating the nonlinear evolution of $\langle u_x u_y \rangle$, $\langle B_x B_y \rangle$, and the angular momentum transport (total stress) $\mathcal{S}(\langle u_x u_y \rangle - \langle B_x B_y \rangle)$, alongside the kinetic energy (KE) and magnetic energy (ME), for $B_0 = 0, 1, 2.5, 5, 10$, at the equator. These are accompanied by a visual representation of our local box (for $B_0 = 0$ at $t = 10$) in a global context.

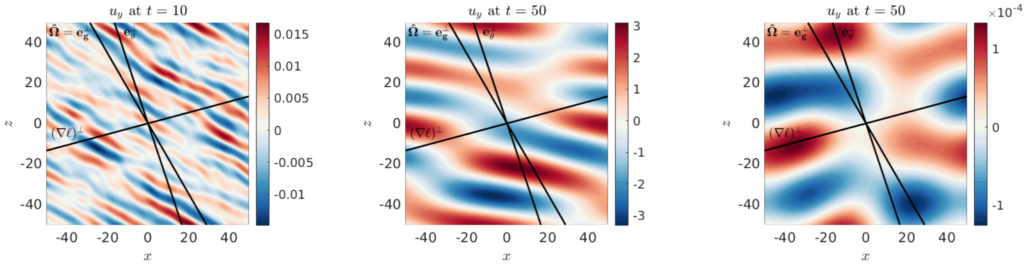

(a) $(B_0 = 1)$ u_y at $t = 10$ (b) $(B_0 = 5)$ u_y at $t = 50$ (c) $(B_0 = 10)$ u_y at $t = 50$

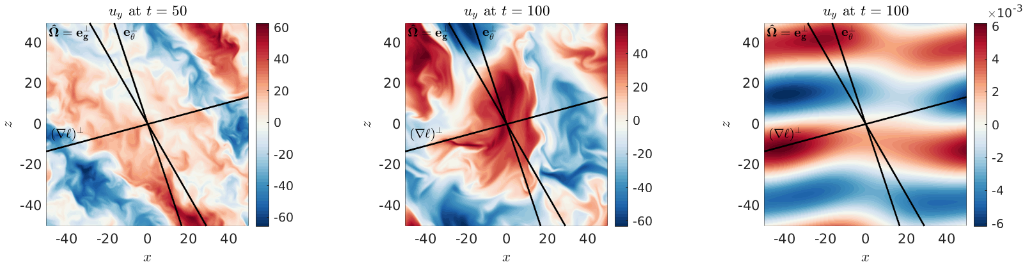

(d) $(B_0 = 1)$ u_y at $t = 50$ (e) $(B_0 = 5)$ u_y at $t = 100$ (f) $(B_0 = 10)$ u_y at $t = 100$

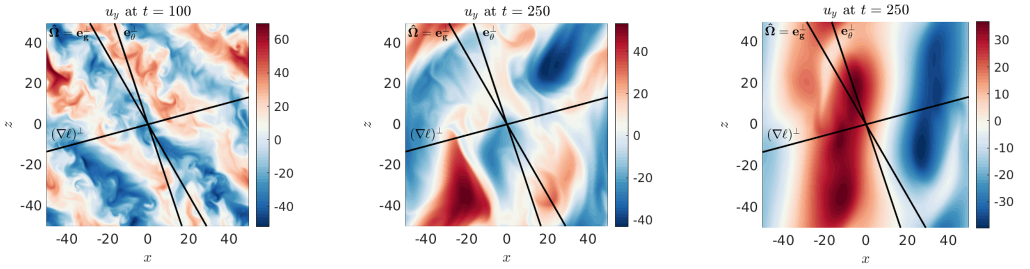

(g) $(B_0 = 1)$ u_y at $t = 100$ (h) $(B_0 = 5)$ u_y at $t = 250$ (i) $(B_0 = 10)$ u_y at $t = 250$

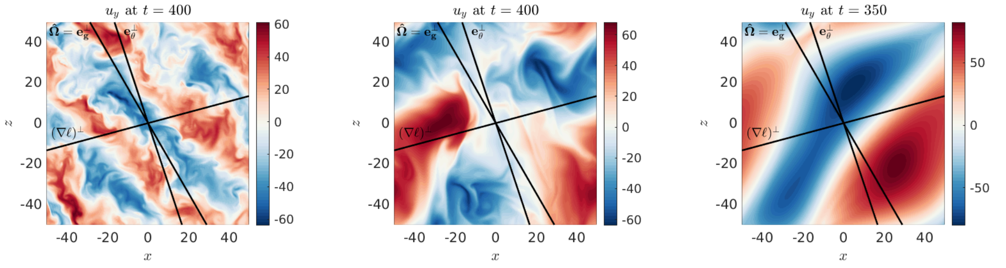

(j) $(B_0 = 1)$ u_y at $t = 400$ (k) $(B_0 = 5)$ u_y at $t = 400$ (l) $(B_0 = 10)$ u_y at $t = 350$

Figure 6.2: Snapshots of the flow component u_y at various times for different magnetic field strengths ($B_0 = 1, 5, 10$) with $\phi = 30°$ and $\Lambda = -30°$. Each row corresponds to a different time: $t = 10$ (top row), $t = 50$ (second row), $t = 100$ (third row), $t = 250$ (fourth row), and $t = 400$ – or $t = 350$ for $B_0 = 10$ – (bottom row). These illustrate the evolution and development of instabilities in the flow, showing how the presence and strength of the magnetic field influence the structure and dynamics over time. Notably, higher magnetic field strengths result in prolonged linear phases and more significant fluctuations before reaching a quasi-stable state. The snapshots highlight the transition from initial linear instabilities to turbulent and layered regimes, emphasizing the role of magnetic fields in altering jet formation and orientation.

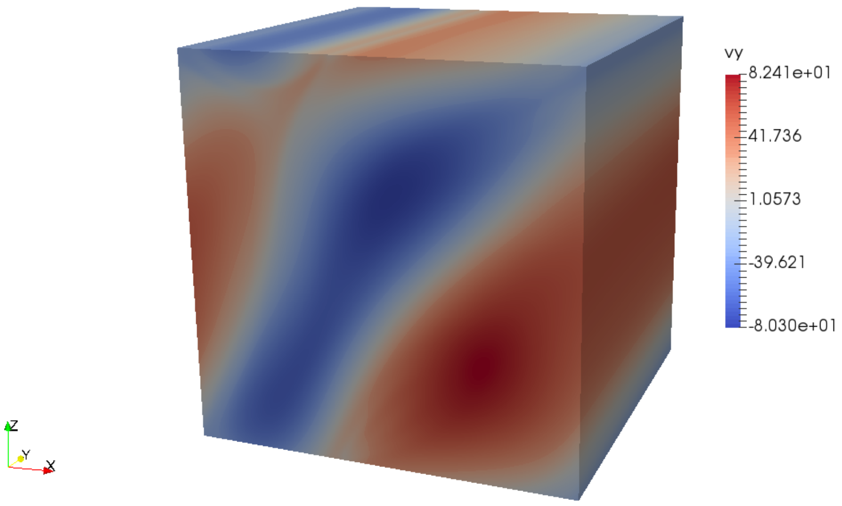

(a) $(B_0 = 10)$ u_y at $t = 350$

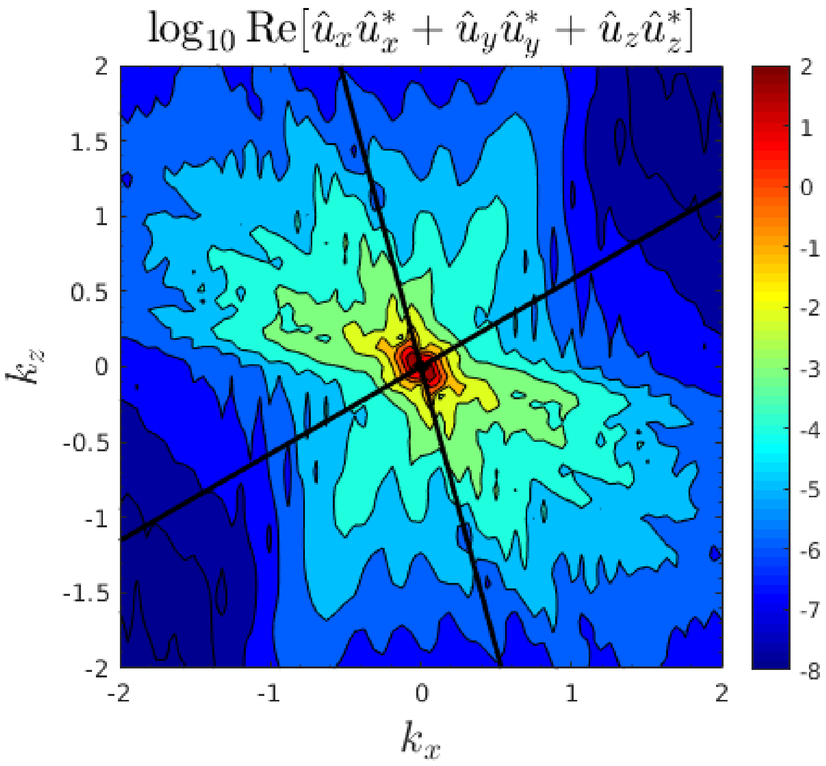

(b) $(B_0 = 10)$ KE spectra at $t = 350$

Figure 6.3: Figures illustrating, in the equatorial case with $B_0 = 10$ with $\phi = 30°$ and $\Lambda = -30°$, (a) the u_y component of the velocity throughout our 3D box of dimensions $L_{x,y,z} = 100$ at $t = 350$ (b) the kinetic energy spectrum on the (k_x, k_z)-plane, which shows these simulations to be well resolved. The two solid lines represent $\hat{\boldsymbol{\Omega}}^{\perp}$ and $\nabla \ell$ within which hydrodynamic GSF modes are unstable.

in comparison to $\sigma \sim 0.5$ and 0.65 for $B_0 = 0$ and 1. However, the increase in wavelength of the modes for these higher field strengths, with $|k| = 0.35, 0.25$ and 0.15 for $B_0 = 2.5, 5$ and 10 compared to $|k| = 0.75$ and 0.6 for $B_0 = 0$ and 1, not only makes the linear modes more resilient to parasitic instabilities, leading to much larger energy levels required for the linear modes to become unstable, but also ultimately results in larger structures once the flow has settled. This is seen in Figures 6.5 and 6.6, which tend to lead to enhanced nonlinear properties, including angular momentum transport.

The magnetic field in our system seems to stabilise the fingers in the linear regime, making them more robust to parasitic instabilities and hence we see these fingers building in strength to extremely large values (several orders of magnitude higher than the hydrodynamic peak) before they become unstable, after which the release of this energy produces very turbulent flows. This could partially be related to the field increasing the length-scale of the dominant unstable mode to be closer to the box-scale, thereby constraining the possible parasitic instabilities of these modes.

Potentially as a result of the larger peak at the end of its linear phase, the $B_0 = 5$ case onsets into a more turbulent flow with larger fluctuations than for $B_0 = 1, 2.5$. However, once this stored energy has been released the three cases $B_0 = 1, 2.5$ and 5 all exhibit dynamics similar to the GSF-unstable cases, albeit with mode and jet orientations and length-scales modified by the magnetic field (see Fig. 6.5). However the flow for $\phi = -30°, \Lambda = 60°$ at $B_0 = 10$ develops in a quite different manner to the $B_0 = 0$ simulation. In particular, in Fig. 6.5 we observe weaker jets that have slightly reduced levels of transport than in the $B_0 = 2.5$ and $B_0 = 5$ cases, with the field impeding the Reynolds stresses, with the value of $\langle u_x u_y \rangle$ settling to the lowest of all the field strengths considered here. Whilst the transport properties seen in Fig. 6.4 are the highest for the mid-strength fields, $B_0 = 2.5$ and 5, the increases in $\langle b_x b_y \rangle$ over the hydrodynamic and weak field cases mean that even with its restrictions on $\langle u_x u_y \rangle$, a field of strength $B_0 = 10$ still generates a flow which transports roughly equivalent rates of angular momentum as $B_0 = 0$ and 1. Since the

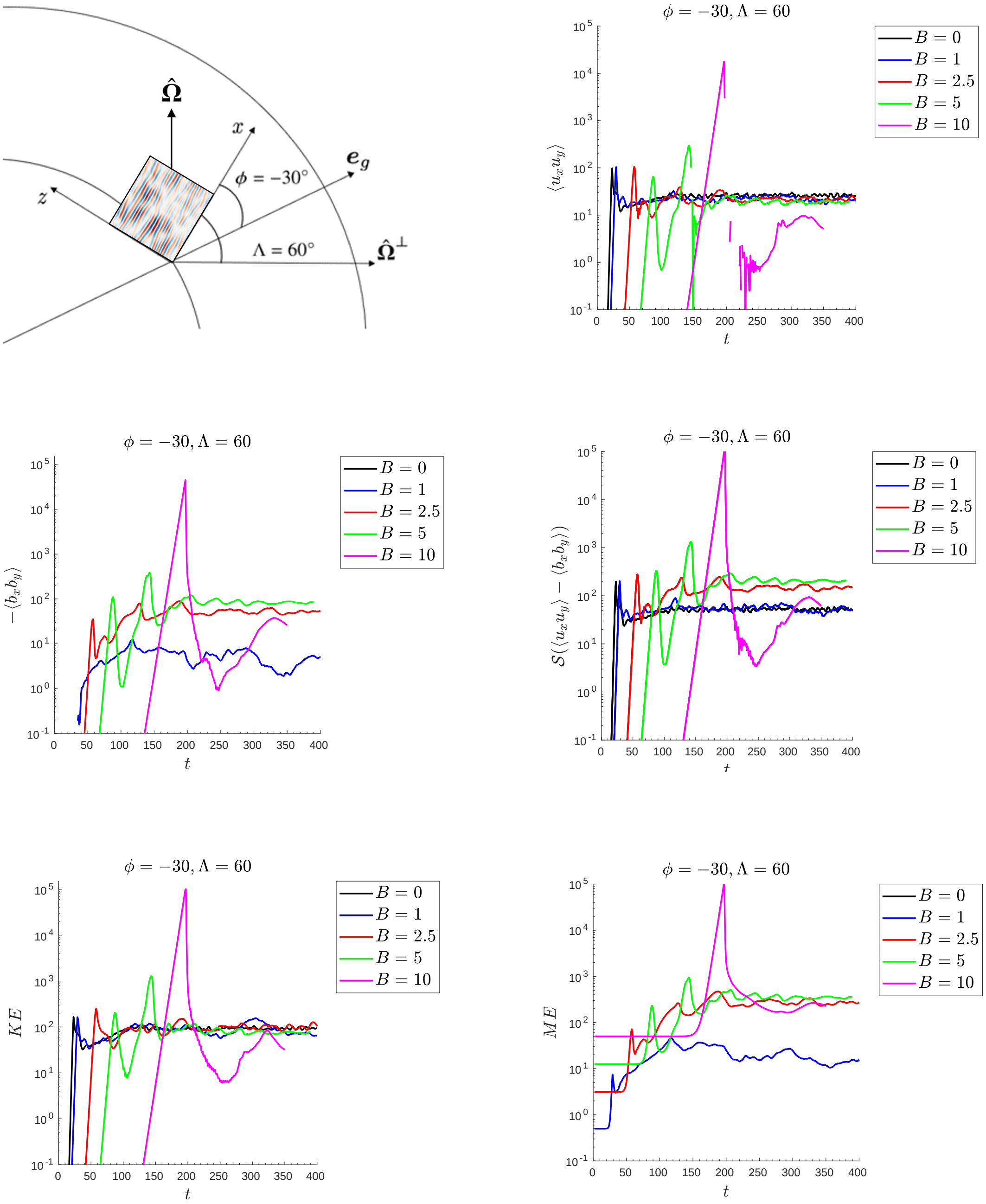

(f) Lat = 0°

Figure 6.4: Illustrating the nonlinear evolution of $\langle u_x u_y \rangle$, $\langle B_x B_y \rangle$, and the angular momentum transport $\mathcal{S}(\langle u_x u_y \rangle - \langle B_x B_y \rangle)$, alongside the kinetic energy (KE) and magnetic energy (ME), for $B_0 = 0, 1, 2.5, 5, 10$, at latitude 30°. These are accompanied by a visual representation of our local box (for $B_0 = 0$ at $t = 10$) in a global context.

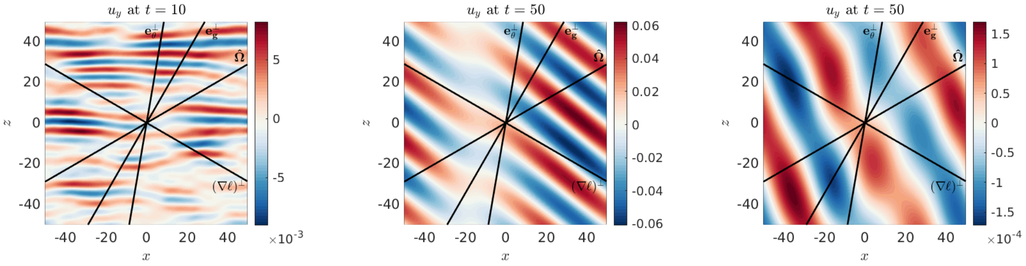

(a) $(B_0 = 1)$ u_y at $t = 10$ (b) $(B_0 = 5)$ u_y at $t = 50$ (c) $(B_0 = 10)$ u_y at $t = 50$

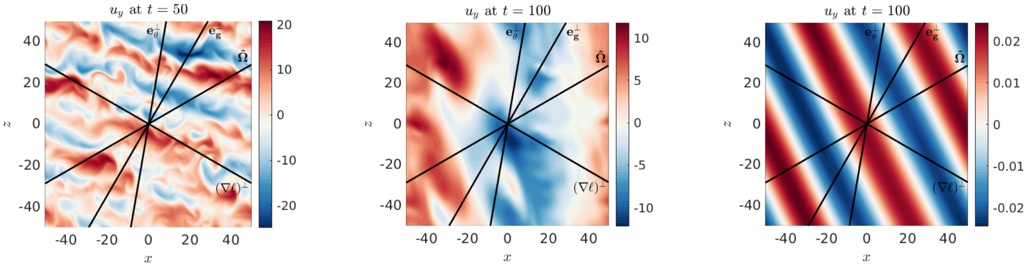

(d) $(B_0 = 1)$ u_y at $t = 50$ (e) $(B_0 = 5)$ u_y at $t = 100$ (f) $(B_0 = 10)$ u_y at $t = 100$

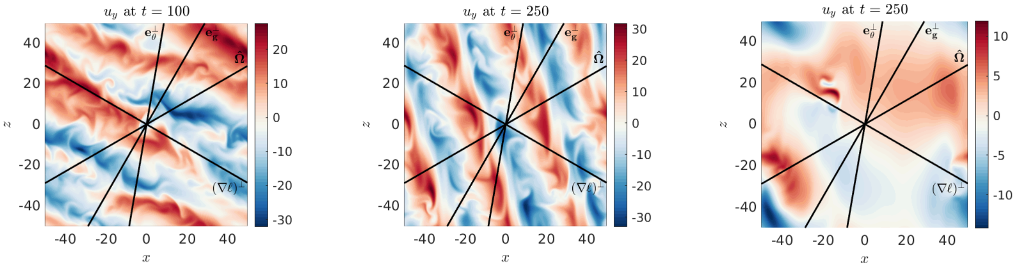

(g) $(B_0 = 1)$ u_y at $t = 100$ (h) $(B_0 = 5)$ u_y at $t = 250$ (i) $(B_0 = 10)$ u_y at $t = 250$

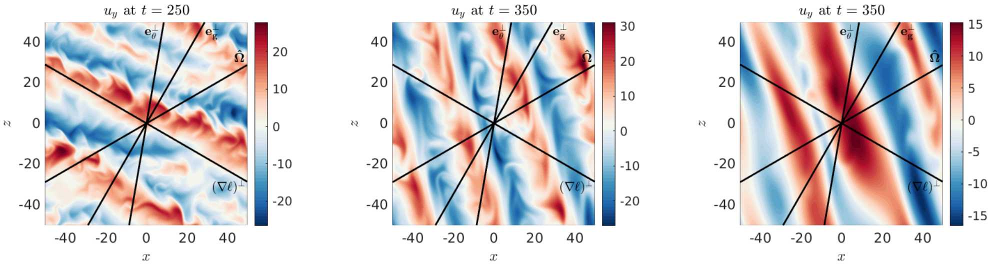

(j) $(B_0 = 1)$ u_y at $t = 250$ (k) $(B_0 = 5)$ u_y at $t = 400$ (l) $(B_0 = 10)$ u_y at $t = 350$

Figure 6.5: Evolution of u_y in snapshots at various times for the case $\phi = -30°, \Lambda = 60°$. Panels (a)-(c) show u_y during the linear growth phase (at $t = 10$ or 50) for magnetic field strengths $B_0 = 1, 5$, and 10 respectively, while (d)-(f) depict u_y at $t = 50$ or 100. Panels (g)-(i) present u_y at $t = 100$, followed by (j)-(l) at $t = 100$ or 250, and (m)-(o) at $t = 250$ or 350 for $B_0 = 1, 5$, and 10 respectively. The plots illustrate the evolution of flow patterns over time, revealing distinct behaviours influenced by varying magnetic field strengths.

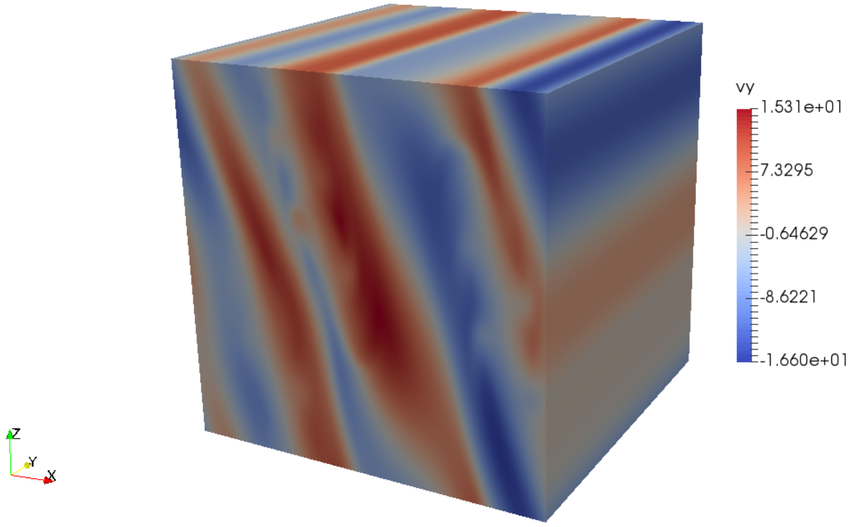

(a) $(B_0 = 10)$ u_y at $t = 350$

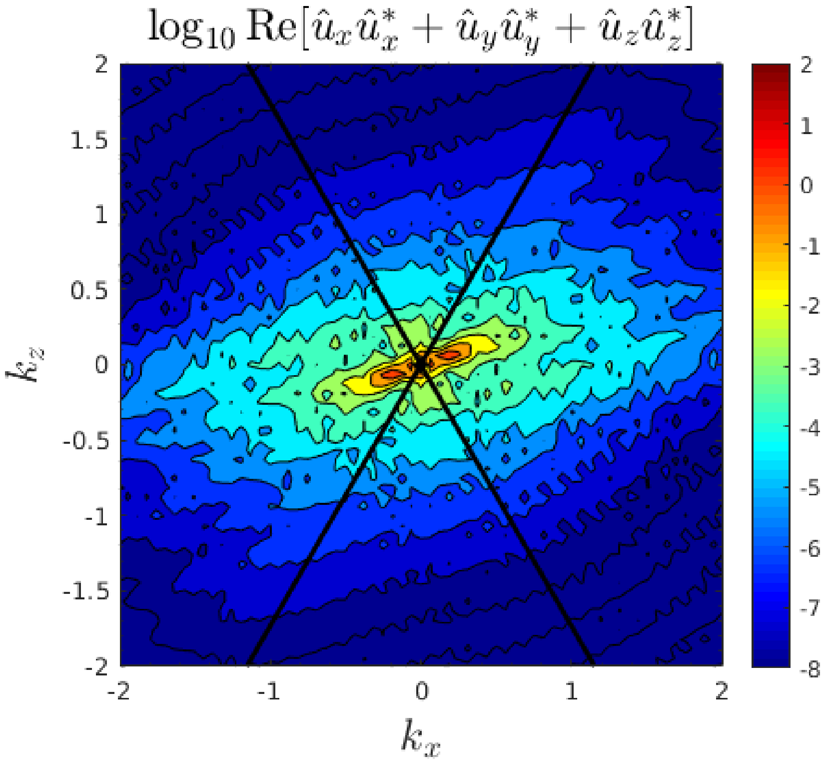

(b) $(B_0 = 10)$ KE spectra at $t = 350$

Figure 6.6: Figures illustrating, in the case $B_0 = 10$ with $\phi = -30°$ and $\Lambda = 60°$, (a) the u_y component of the velocity throughout our 3D box of dimensions $L_{x,y,z} = 100$ at $t = 350$ (b) the kinetic energy spectrum on the (k_x, k_z)-plane, which shows these simulations to be well resolved. The two solid lines represent $\hat{\mathbf{\Omega}}^{\perp}$ and $\nabla\ell$ within which hydrodynamic GSF modes are unstable.

Maxwell stress ($\langle b_x b_y \rangle$) generated by the field seems to have reached a maximum by $B_0 = 5$ we suspect that any further increases in field strength would lead to a reduction in the levels of angular momentum transport occurring for the same parameters otherwise. From Fig. 6.4, we see that outside of the strong temporal fluctuations, the magnetic field has little influence on the mean levels of kinetic energy in the system, with perhaps only a small reduction coming from the field with $B_0 = 10$, but further investigations would be required to confirm this trend. A difference is, however, observed in the magnetic energy of the system. As was seen at the equator, all $B_0 \neq 0$ cases act as dynamos, with the magnetic energy of the system saturating at a similar value for all $B_0 \geq 2.5$. The $B_0 = 1$ case generated a weaker field amplification, about an order of magnitude lower magnetic energy than the cases with larger fields.

We show a 3D snapshot of u_y in the top panel of Fig. 6.6 for $B_0 = 10$ in the final stages of the simulation at $t = 350$. This shows that the flow remains close to axisymmetric, just like for the equatorial case with $B_0 = 10$ shown in the previous section, and that the flows shown in the slices in Fig. 6.5 are zonal jets. The kinetic energy spectrum indicates that the orientation of the modes in the (k_x, k_z)-plane in this case is drastically different from the hydrodynamical modes excited when $B_0 = 0$. The latter are contained within the wedge between the black lines showing $\hat{\boldsymbol{\Omega}}^{\perp}$ and $\nabla \ell$ close to the $k_x = 0$ axis, whereas the unstable modes for $B_0 = 10$ are nearly perpendicular to this, as we have also observed in Fig. 6.5. This is predicted by linear theory in Fig. 5.10 which predicts $\theta_k \sim 90^\circ$ for $B_0 = 0$ whereas $\theta_k \sim 155^\circ$ for $B_0 = 10$. The $B_0 = 10$ case has a similar jet orientation and wavelength in the final stages to the linear modes, whereas the $B_0 \leq 5$ cases exhibit changes in both the direction and wavelengths of the zonal jets, which tend to coarsen with time for smaller B_0. These figures also indicate this simulation to be spatially well resolved.

Our simulations suggest that while the flow is still GSF unstable for latitude 30° (not including $B_0 = 10$), stronger magnetic fields, and in turn larger $|\langle B_x B_y \rangle|$, translate into higher levels of angular momentum transport. Intriguingly, the dynamo amplifying the imposed magnetic field in cases with $B_0 \neq 0$ generates similar levels of magnetic energy in the final states of all cases with $B_0 \geq 2.5$.

6.2.3 Hydrodynamically adiabatically unstable case at latitude $30°$ $(\phi = 60°, \Lambda = -30°)$

Next, we examine a differential rotation profile with $\phi = 60°$ and $\Lambda = -30°$, a scenario previously identified in Fig. 4.6 as hydrodynamically adiabatically unstable. This case was analysed linearly in Fig. 5.10 where we found $\sigma \sim 0.92$ and $\theta_k = 130°$ with a preferred wavenumber $k \to 0$ independently of B_0. Here the evolution of the instability initially seems more resilient to the addition of a magnetic field, until $B_0 = 10$. Fig. 6.7 illustrates that, after a marginally extended linear duration, cases within the adiabatically unstable regime with $(B_0 \leq 5)$ exhibit very similar transport behaviour. The transport $(\mathcal{S}(\langle u_x u_y \rangle - \langle B_x B_y \rangle))$ in these cases is dominated by the Reynolds stress, until the Maxwell stress dominates for $B_0 = 10$. In these simulations the linear growth rate and orientations are not affected by B_0, hence any changes in the wavelength or orientations in the final stages of our simulations must result from nonlinear effects.

The slower linear growth for the $B_0 = 10$ strong field case is surprising given that Fig. 5.10 predicts $\sigma \sim 0.9$ for all field strengths, which is consistent with the growth rates we observe for $B_0 = 0, 1, 2.5$ and 5 in Fig. 6.7. From panels (a) and (b) in Fig. 5.6 we can see that $\phi = 60°$ is the start of adiabatically unstable rotation profiles as ϕ is varied at latitude $= 30°$ and so, regardless of field strength we see a preference for arbitrarily small wave vectors $|k| \to 0$. In this $B_0 = 10$ case the addition of the field generates substantially higher turbulent stresses and final transport properties within the system. This may result from the single, very strong zonal jet that develops in this case (see panels (i) and (l) of Fig. 6.8) that leads to by far the highest velocity flows seen in any of our simulations analysed here. The flow in the final stages is six times faster flowing than the weak field $B_0 = 1$ case (in panel (j) of Fig. 6.8).

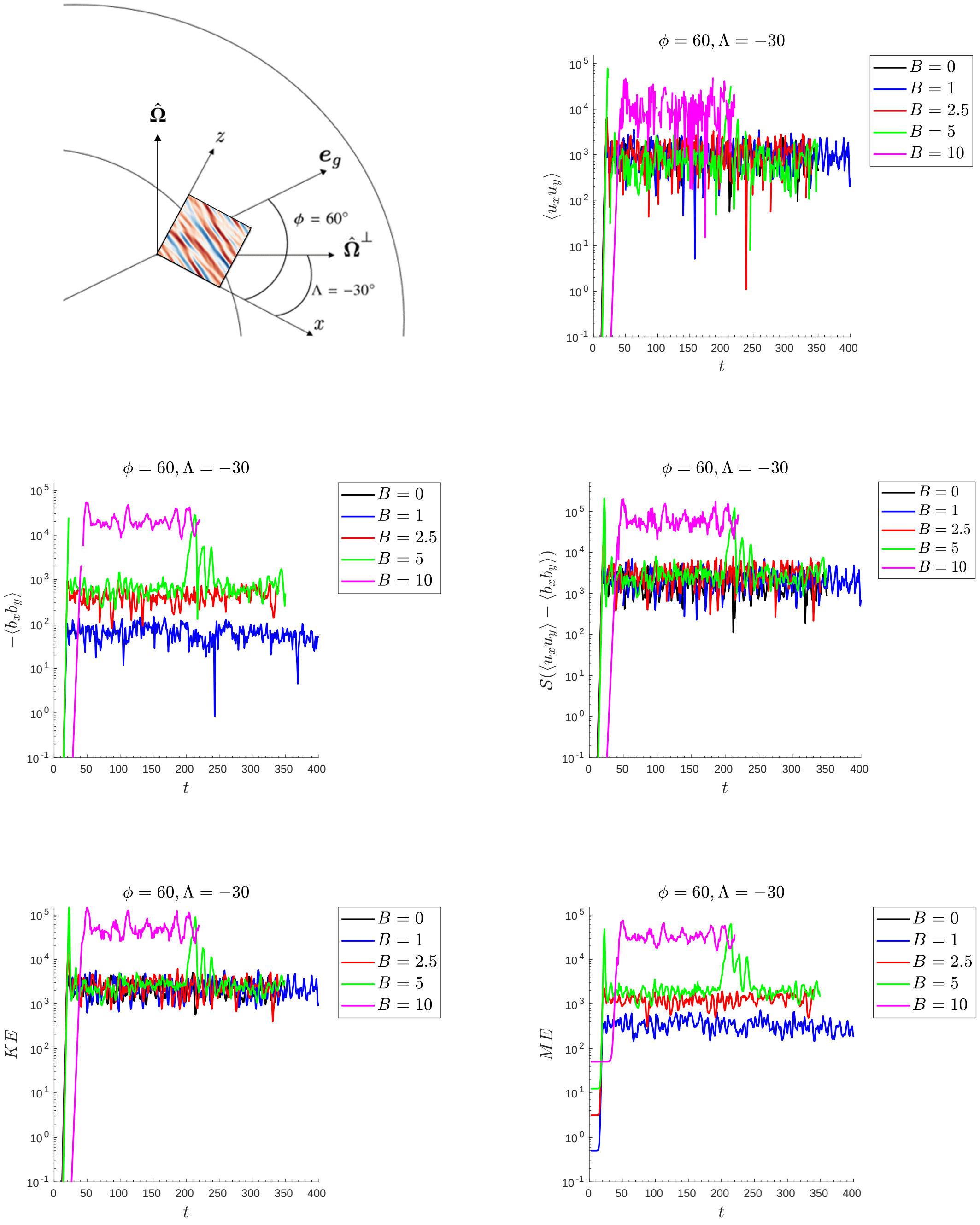

Figure 6.7: A figure illustrating the nonlinear evolution of $\langle u_x u_y \rangle$, $\langle B_x B_y \rangle$, the angular momentum transport $\mathcal{S}(\langle u_x u_y \rangle - \langle B_x B_y \rangle)$, alongside the kinetic energy (KE) and magnetic energy (ME), for $B_0 = 0, 1, 2.5, 5, 10$, in the hydrodynamically adiabatically unstable regime ($\phi = 60°$, $\Lambda = -30°$) at latitude 30°. These are accompanied by a visual representation of our local box (for $B_0 = 0$ at $t = 10$) in a global context.

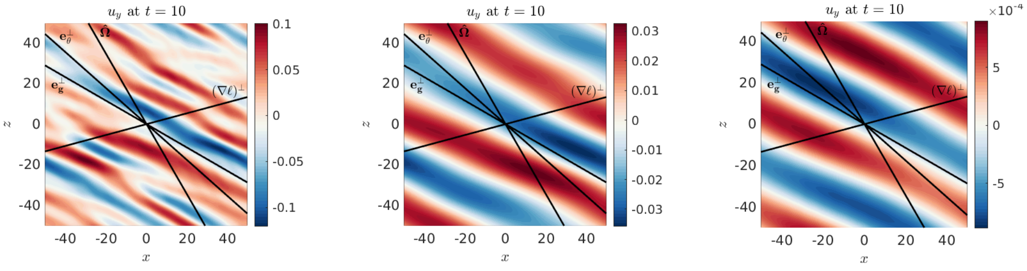

(a) ($B_0 = 1$) u_y at $t = 10$ (b) ($B_0 = 5$) u_y at $t = 10$ (c) ($B_0 = 10$) u_y at $t = 10$

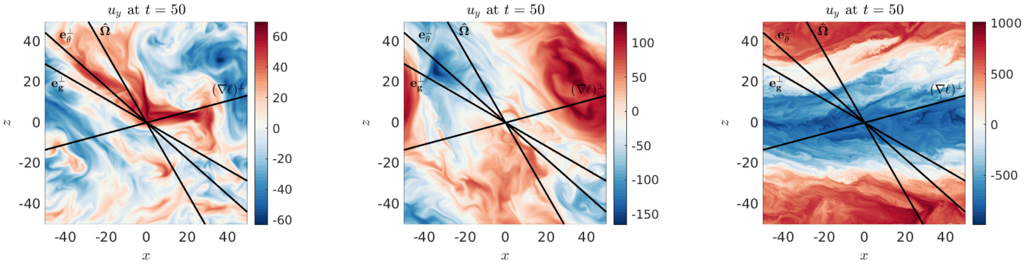

(d) ($B_0 = 1$) u_y at $t = 50$ (e) ($B_0 = 5$) u_y at $t = 50$ (f) ($B_0 = 10$) u_y at $t = 50$

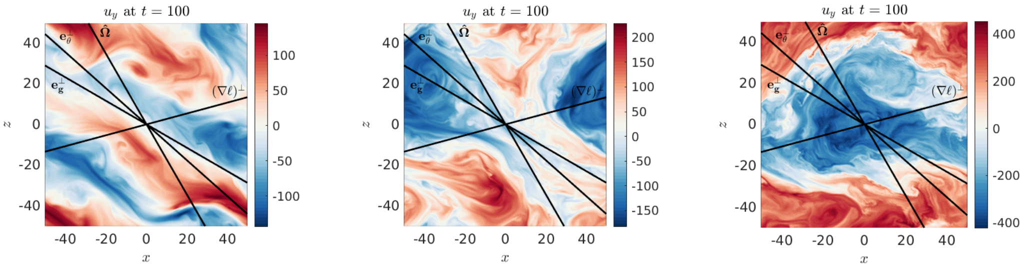

(g) ($B_0 = 1$) u_y at $t = 100$ (h) ($B_0 = 5$) u_y at $t = 100$ (i) ($B_0 = 10$) u_y at $t = 100$

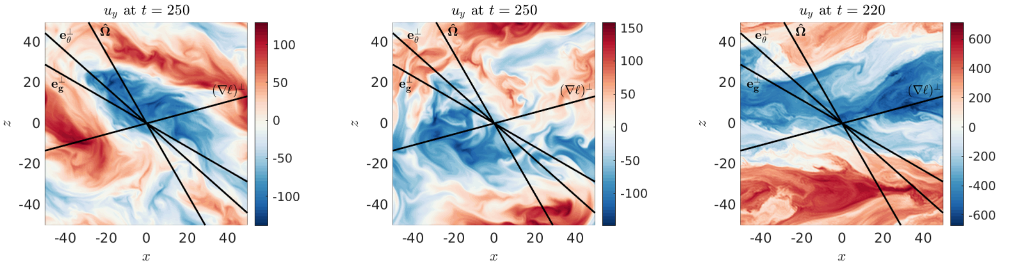

(j) ($B_0 = 1$) u_y at $t = 250$ (k) ($B_0 = 5$) u_y at $t = 250$ (l) ($B_0 = 10$) u_y at $t = 220$

Figure 6.8: Snapshots of the flow evolution for the case with parameters $\phi = 60°$ and $\Lambda = -30°$, illustrating the adiabatically unstable regime throughout the various stages of its evolution. Initially we see the development of fingers of angular momentum, which take longer to develop for higher values of B_0, after which there is a phase of nonlinear saturation due to parasitic instabilities that leads to turbulence which ultimately gives way to layering in the angular momentum. Notably, the figure showcases the development of strong layers filling the box, with smaller scale instabilities suspected to be Kelvin-Helmholtz instabilities observed on the boundaries between the layers. Panel (l) at the bottom highlights these smaller scale instabilities, generating noticeable vortices that may impact the mean flow dynamics, though probably only weakly as they do not significantly alter the layered structures subsequently.

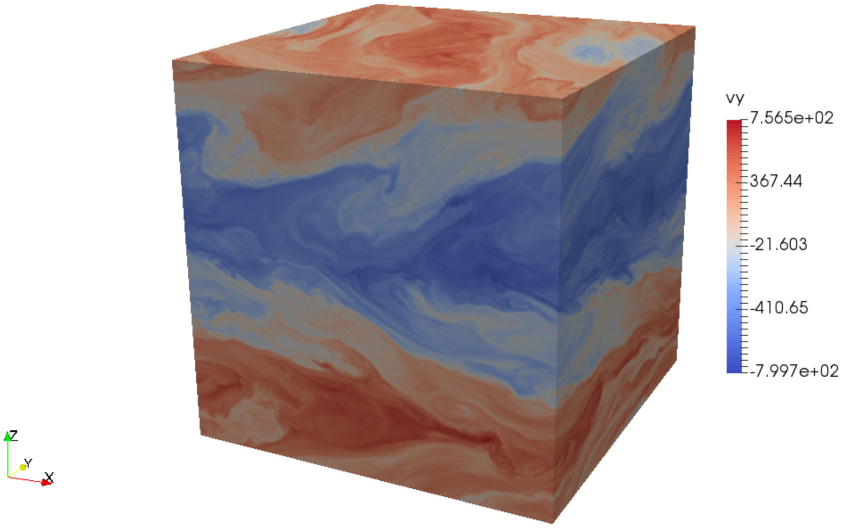

(a) $(B_0 = 10)$ u_y at $t = 220$

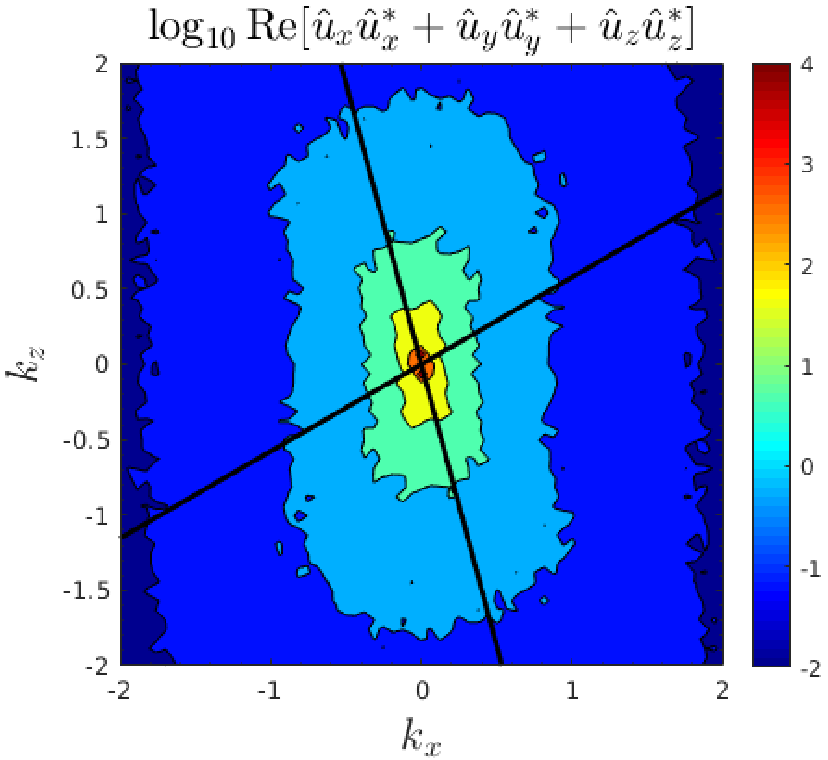

(b) $(B_0 = 10)$ KE spectra at $t = 220$

Figure 6.9: Figures illustrating, in the case $B_0 = 10$ with $\phi = 60°$ and $\Lambda = -30°$, (a) the u_y component of the velocity throughout our 3D box of dimensions $L_{x,y,z} = 100$ at $t = 220$ (b) the kinetic energy spectrum on the (k_x, k_z)-plane, which shows these simulations to be well resolved. The two solid lines represent $\hat{\mathbf{\Omega}}^{\perp}$ and $\nabla\ell$ within which hydrodynamic GSF modes are unstable.

One interesting feature of the $B_0 = 5$ case is the presence of a strong spike in its properties around $t = 220$, occurring well after the initial nonlinear saturation. However, it is not clear whether this is a magnetic phenomenon or just a nonlinear effect.

From Fig. 6.7 and our snapshots in Fig. 6.8 it is clear that the adiabatically unstable regime quickly becomes very turbulent, in line with our expectations from their large growth rates ($\sigma \sim 0.9$) in Fig. 5.10. After the initial elevator modes nonlinearly saturate, layers quickly form throughout the domain, becoming exceedingly strong and box-filling. By $t = 50$ the velocities are an order of magnitude above any another other simulation at this point in time. Nevertheless, the 3D snapshot of the $B_0 = 10$ case in the top panel of Fig. 6.9 is dominated by an axisymmetric zonal flow but with many visible strong smaller-scale vortices. We also observe from the energy spectrum in Fig. 6.9 that the flow appears well resolved despite the very turbulent flows being driven.

On average the zonal jets that form are clear and maintain a consistent orientation in the nonlinear regime in our simulations. However, they do seem to experience relatively strong intermittent turbulence between the layers. Seen clearly in (a) of Fig. 6.9, where the zonal jets here can be seen to have a similar appearance to the other layered states seen in the modified GSF regimes. Not only do these jets have enhanced velocities here but interestingly the strong shear between the layers seems to be an ideal environment to host smaller-scale instabilities, likely similar to Kelvin-Helmholtz instabilities. These instabilities generate discernible vortices that may impact flow properties, however their net influence appears minor on the mean flow as they do not significantly alter the layered flow structures.

All $B_0 \neq 0$ cases again exhibit dynamos, amplifying the initial field substantially, with by far the most efficient dynamo coming from the $B_0 = 10$ case, which amplifies the magnetic energy by a factor of 10^3.

To summarise, this adiabatically unstable case is not strongly affected by the magnetic field linearly or nonlinearly until the strongest field with $B_0 = 10$ is applied. Then, the transport and energetic properties of the flow are substantially enhanced by the field. It would be interesting to explore whether this behaviour would be expected to persist for even larger B_0. We shall study the dependence of box size on the transport properties of this case later in Section 6.3.

6.2.4 Polar case ($\phi = 30°, \Lambda = 60°$)

The final examples we will consider here are hydrodynamically GSF unstable cases at the pole, with $\phi = 30°, \Lambda = 60°$. Much like for the other hydrodynamically GSF unstable cases we see that the cases seem to be split into two sets: $B_0 = 0, 1$, which demonstrate typical GSF-type behavior, and $B_0 = 2.5, 5$, and 10, which seem to be more aggressively unstable, with higher turbulent stresses, energetic, and transport properties seen in Fig. 6.10. We suspect this could be associated with a double-diffusive MRI instability. The more modest properties associated with weak field cases correspond to the smaller wave length modes predicted from Fig. 5.12 in Chapter 5, with $|k| \sim 0.65$ and $|k| \sim 0.5$ at $B_0 = 0$ and $B_0 = 1$ respectively, in comparison to $|k| \sim 0.3, 0.2$ and 0.1 for $B_0 = 2.5, 5$ and 10.

Fig. 5.12 suggests that the larger growth rates $\sigma \sim 0.55, 0.65$ and 0.65 for $B_0 = 2.5, 5$ and 10 would lead to faster growth compared to the value $\sigma \sim 0.45$ for both $B_0 = 0$ and 1. However, our kinetic energy plots in Fig. 6.10 shows that in our nonlinear simulations, after onset, the unstable modes grow in strength slightly slower than the angular momentum fingers in the modified GSF unstable cases. We speculate that this could be related to the initial conditions that might have preferentially excited a smaller-scale mode. The unstable modes also seem more resistant to parasitic instabilities for larger B_0 and grow to much larger energies before becoming unstable and generating turbulence. Strongly magnetised cases lead to higher levels of transport in comparison to the weak field or hydrodynamic cases. Although much lower than the initial peak at the end of their linear growth phases, the higher field strength cases with $B_0 \geq 2.5$ tend to saturate at between one and two orders of magnitude larger transport levels than seen in the weak field regime.

The formation of AM layers is observed to be much weaker in Fig. 6.11 than the other GSF unstable cases, with all fields stronger than $B_0 = 1$ producing box-filling turbulent flows with large-scale eddies rather than coherent zonal jets. Even a weak $B_0 = 1$ field seems to significantly destabilise the formation of AM layers over the hydrodynamic simulations seen in Fig. 4.6. The flow in these magnetic simulations with stronger fields also exhibits stronger non-axisymmetric components in the flow than the weaker field cases, as shown in the top panel of Fig. 6.12 for $B_0 = 10$. For the stronger field cases, the formation of box-scale eddies and zonal flows seems to correspond to the significant, rapid fluctuations in Fig. 6.10, with over an order of magnitude variation between the upper and lower limits of the levels of transport between fluctuations. The fluctuations are less pronounced in the $B_0 \leq 1$ cases, where the zonal jets and associated turbulent flows occur on a length-scale that is a smaller fraction of the box size.

Whilst all $B_0 \neq 0$ cases enhance the level of magnetic energy within the system, the more turbulent flows observed in Fig. 6.11 corresponding to $B_0 = 2.5, 5, 10$, were found to be far more efficient dynamos. The magnetic energy is relatively insensitive to B_0 for $B_0 > 1$ for the cases we explored.

6.3 Dependence on box size

Given that we have found the magnetic field changes the wavevector of the fastest growing linear modes in Chapter 5, it is important to see how these translate into the nonlinear regime, and in particular to determine whether or not these changes lead to changes in the dependence on, or lack thereof, on the dimensions of the box L_x, L_y and L_z. To explore the effects of varying the box size dimensions on our magnetised simulations, we have performed simulations similar to those in Chapter 4. We study cases with $L_{x,y,z} = 200, 300$ and a adopt a higher resolution for these larger boxes, with $N_{x,y,z} = 512$, a resolution which we found in Chapter 4 to be

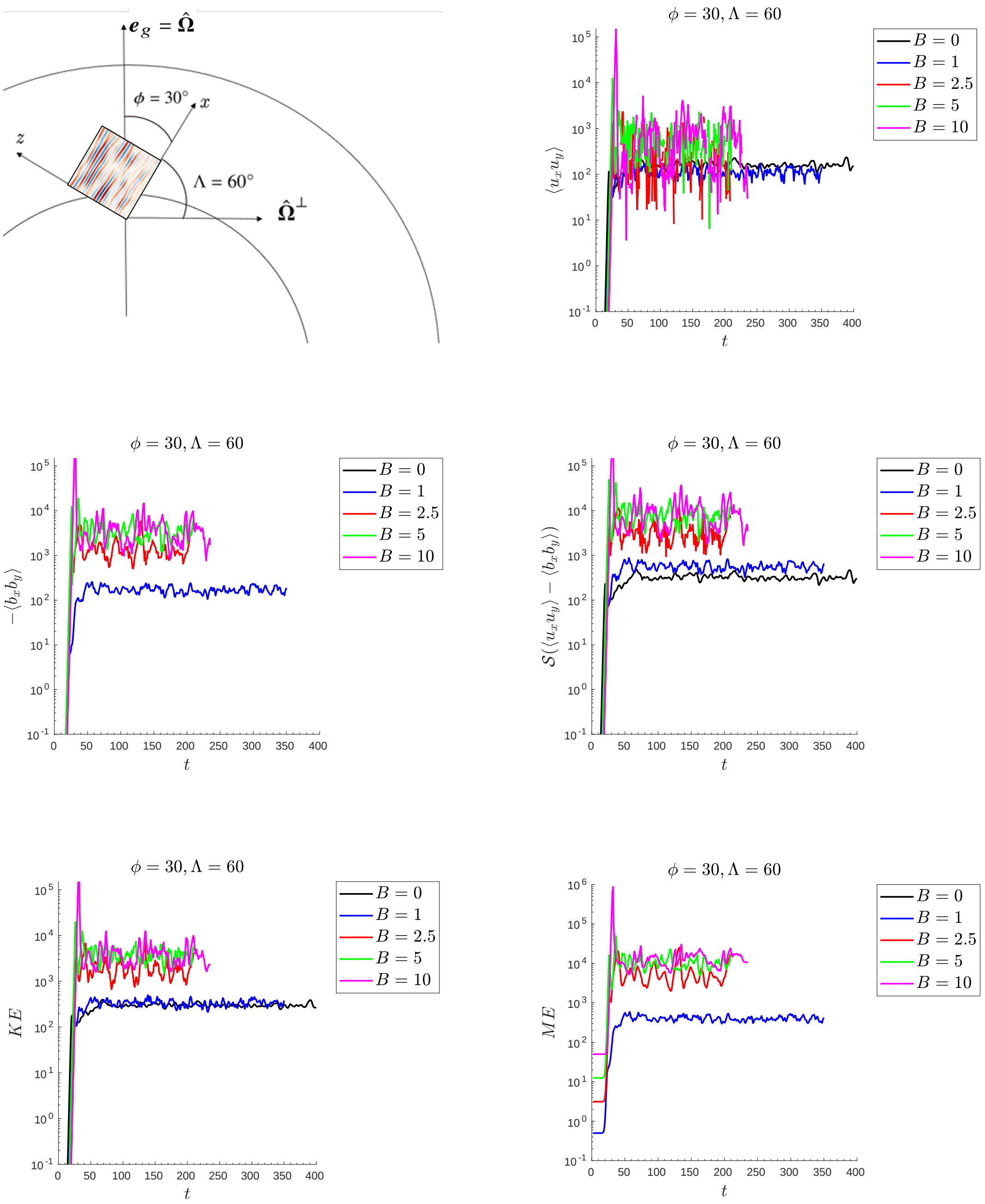

Figure 6.10: A figure illustrating the nonlinear evolution of $\langle u_x u_y \rangle$, $\langle B_x B_y \rangle$, the angular momentum transport $\mathcal{S}(\langle u_x u_y \rangle - \langle B_x B_y \rangle)$, alongside the kinetic energy (KE) and magnetic energy (ME), for $B_0 = 0, 1, 2.5, 5, 10$, at the pole $(\phi = 30°, \Lambda = 60°)$. These are accompanied by a visual representation of our local box (for $B_0 = 0$ at $t = 10$) in a global context.

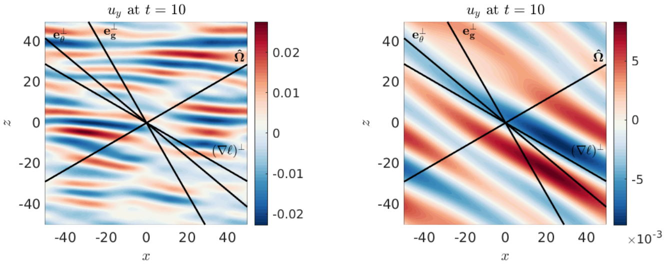

(a) $(B_0 = 1)$ u_y at $t = 10$ (b) $(B_0 = 5) u_y$ at $t = 10$ (c) $(B_0 = 10) u_y$ at $t = 10$

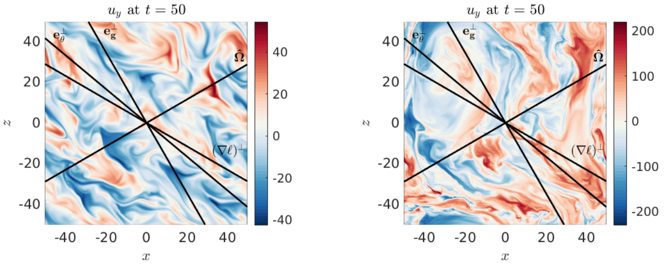

(d) $(B_0 = 1)$ u_y at $t = 50$ (e) $(B_0 = 5)$ u_y at $t = 50$ (f) $(B_0 = 10)$ u_y at $t = 50$

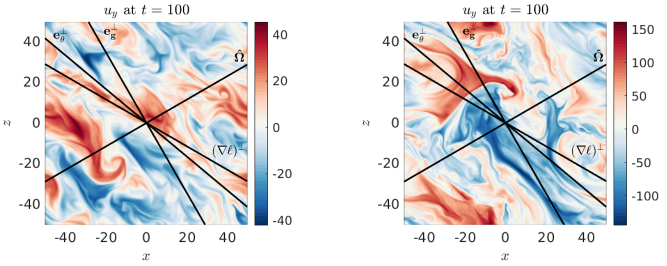

(g) $(B_0 = 1)$ u_y at $t = 100$ (h) $(B_0 = 5)$ u_y at $t = 100$ (i) $(B_0 = 10)$ u_y at $t = 100$

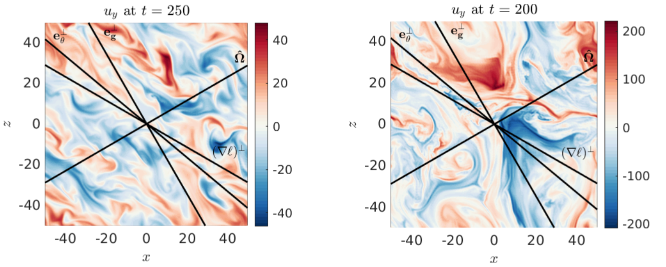

(j) $(B_0 = 1)$ u_y at $t = 250$ (k) $(B_0 = 5)$ u_y at $t = 200$ (l) $(B_0 = 10)$ u_y at $t = 220$

Figure 6.11: Snapshots of the velocity component u_y at various times for different magnetic field strengths $(B_0 = 1, 5, 10)$ with $\phi = 30°$ and $\Lambda = 60°$. These snapshots illustrate the evolution through the various stages of the instability. They demonstrate how the presence and strength of the magnetic field influence the structure and dynamics over time. Notably, higher magnetic field strengths result in prolonged linear phases and more significant fluctuations before reaching a quasi-stable state. The snapshots highlight the transition from initial linear instabilities to turbulent and layered regimes, emphasising the role of magnetic fields in altering jet formation and orientation.

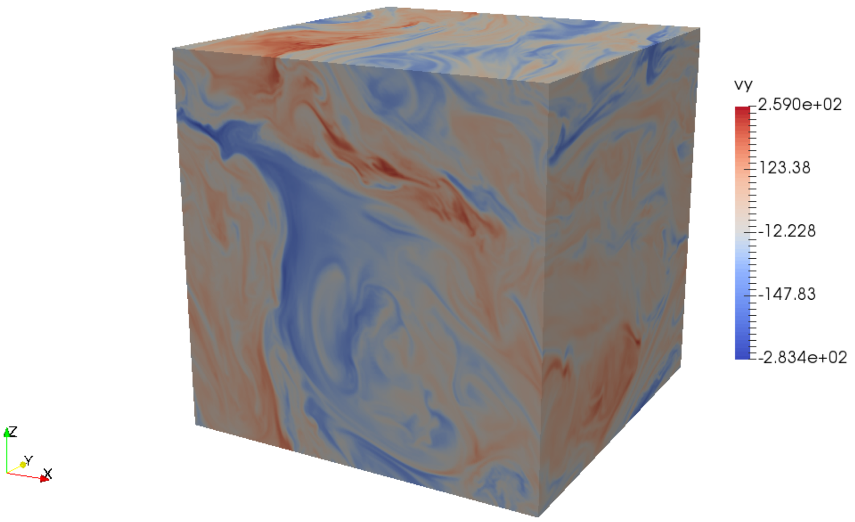

(a) $(B_0 = 10)$ u_y at $t = 220$

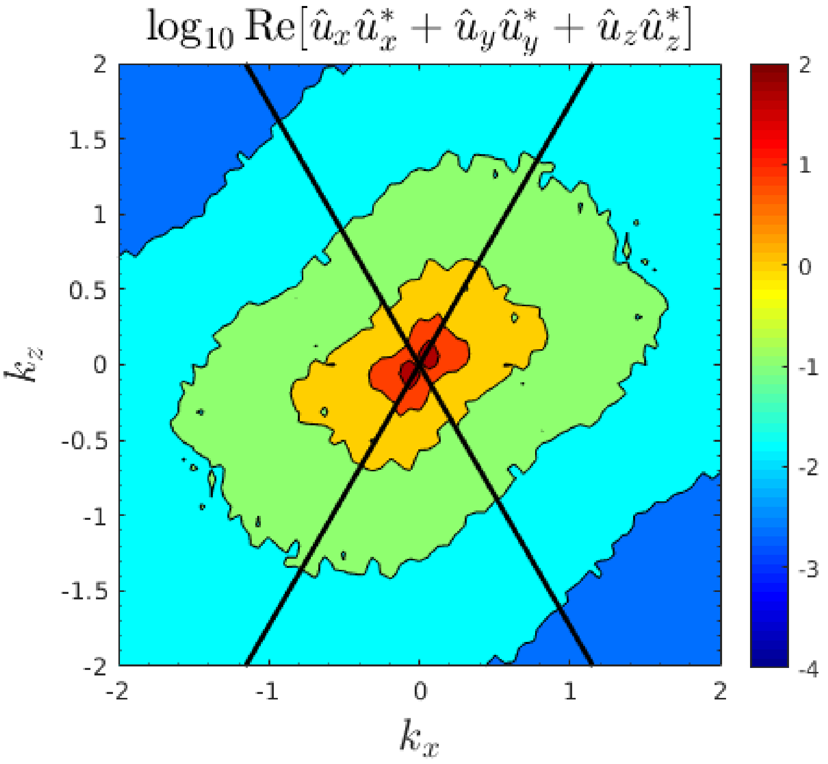

(b) $(B_0 = 10)$ KE spectra at $t = 220$

Figure 6.12: Figures illustrating, in the case $B_0 = 10$ with $\phi = 30°$ and $\Lambda = 60°$, (a) the u_y component of the velocity throughout our 3D box of dimensions $L_{x,y,z} = 100$ at $t = 220$ (b) the kinetic energy spectrum on the (k_x, k_z)-plane, which shows these simulations to be well resolved. The two solid lines represent $\hat{\boldsymbol{\Omega}}^{\perp}$ and $\nabla\ell$ within which hydrodynamic GSF modes are unstable.

sufficiently high for the simulations to be well resolved. Given that our ‘standard’ simulations are run in boxes of dimensions 100^3, a mode must have a wavelength of less than 100 to fit in the box, i.e. $k \leq 2\pi/100 \approx 0.063$. This means we expect modes close to $k = 0.063$, would likely have their evolution strongly affected by the scale of the box in some manner.

In Chapter 4, we saw that having a well-defined wave vector magnitude $|k|$ meant that, regardless of the dimensions of our box, the GSF instability had the same typical scales in the nonlinear evolution and led to approximately the same angular momentum transport rates. This is an important result highlighting the possibility for astrophysically relevant extrapolations to be made from these results. At $\phi = -30°$, Fig. 5.10 shows that the linear effect of the magnetic field is to lower $|k|$, thus increasing the wavelength of the instability. However, unlike in the adiabatically unstable regime, the wavelength of the modes remained (largely) well-defined, suggesting that as long as our box is large enough to capture the unstable modes, there should be no significant dependence on box size, that is, as long as the wavelength associated with that $|k|$ fits in the box. This suggestion is from linear theory but also appeared to hold in our hydrodynamic cases in Chapter 4, so we explore it here for magnetised cases.

We have therefore performed simulations with $B_0 = 1$ and $B_0 = 2.5$ with $\phi = -30°, \Lambda = 60°$ (latitude 30°) at $L_{x,y,z} = 100, 200$ and 300. This case is hydrodynamically GSF-unstable and has a preferred wavenumber for the fastest growing linear mode. We show the evolution of time-averaged quantities for these in Fig. 6.13. This shows that the turbulent transport – both via Reynolds and Maxwell stresses – and the kinetic and magnetic energies are insensitive to the dimensions of the box. Indeed, there is a remarkable convergence in the averaged quantities in the turbulent state towards the end of these simulations between all of these cases. This indicates that the magnetically-modified GSF regime is also insensitive to the box size, hence our simulations can more reliably be used to probe the astrophysical regime than if this was not the case.

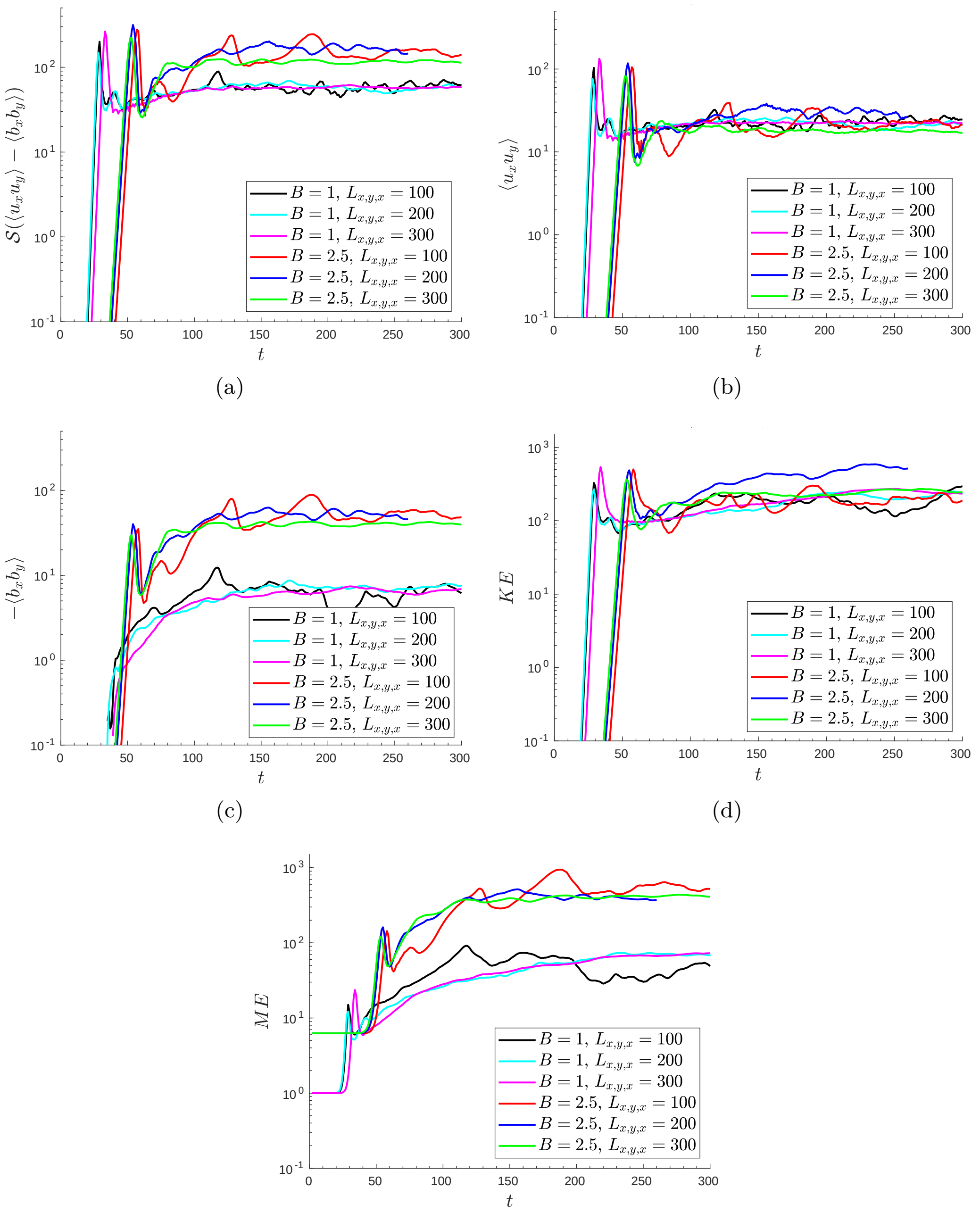

(a) (b) (c) (d) (e)

Figure 6.13: Analysis of nonlinear dynamics for magnetic fields $B_0 = 1$ and $B_0 = 2.5$ with $\phi = -30°$ and $\Lambda = 60°$, examining the dependencies on box dimensions L_x, L_y, and L_z. Panels (a)–(c) show the evolution of the total stress, $\langle u_x u_y\rangle$ and $\langle -B_x B_y\rangle$, indicating the magnetic field's effects on angular momentum transport. Panels (d) and (e) display the variations in kinetic and magnetic energy. Increased box sizes reduce flow fluctuations, suggesting boundary conditions may influence stability. Box size does not significantly affect dynamics, supporting possible extrapolation of our model to larger astrophysical scales.

The second cases we explore are a box size comparison for what is a hydrodynamically unstable case $\phi = 60°, \Lambda = -30°$, this time with the addition of a magnetic field of strength $B_0 = 2.5$. In both the hydrodynamic and magnetohydrodynamic regimes the $\phi = 60°, \Lambda = -30°$ case was found to be adiabatically unstable with linear growth rates and wavevectors independent of B_0. Throughout our simulations in Chapter 4 (which included diffusion) the most unstable modes had a preference for arbitrarily small length scales, resulting in wavelengths that tended to fill the box regardless of its size. The increased wavelengths of the unstable modes and zonal jets that were generated for larger box sizes led to a strong dependence on box size, implying that these findings could not be extrapolated to the astrophysical context reliably without additional information. Our results presented here in Fig. 6.14 show that the addition of a magnetic field does not change this behaviour and the turbulent properties continue to depend on $L_{x,y,z}$. It would be of interest to investigate the $B_0 = 10$ case, as we saw in Fig. 6.10 that the dynamics of the flow was quite different in this case. However, such simulations are very computationally expensive so have not been investigated here, and this topic is left for future studies. Note Fig. 5.6 suggests that $\phi = 60°, \Lambda = -30°$ will continue to have a dependence on box size for any value of B_0.

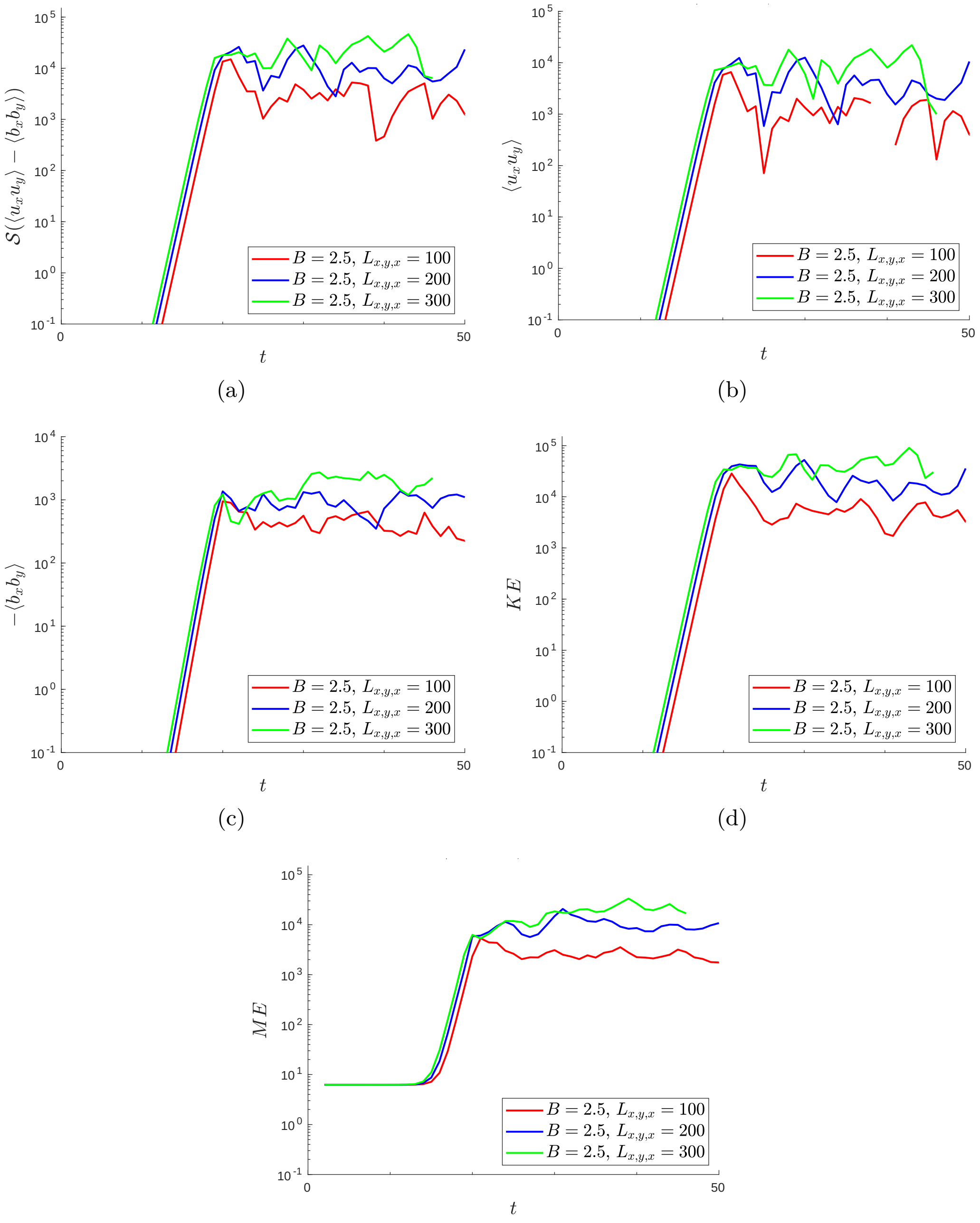

(a) (b)

(c) (d)

(e)

Figure 6.14: Analysis of nonlinear dynamics for magnetic field strength $B_0 = 2.5$ with $\phi = 60°$ and $\Lambda = -30°$, examining the dependencies on box dimensions L_x, L_y, and L_z. Panels (a)–(c) show the evolution of the total stress as well as $\langle u_x u_y\rangle$ and $\langle -B_x B_y\rangle$, indicating the magnetic field's effects on angular momentum transport. Panels (d) and (e) show the evolution of kinetic and magnetic energy. These results suggest a strong dependence on box size, with larger boxes capturing longer wavelength modes and potentially more stable jets.

One noticeable feature of increasing the box size was the notable decrease in fluctuations in the flow over Fig. 6.4, particularly in GSF-unstable cases. This suggests that our boundary conditions may be responsible for some of these fluctuations but we observe that the mean properties of the flow converge as we increase the box size. Larger boxes allow larger wavelength parasitic modes to act on the zonal jets and other large-scale flows. In addition, larger boxes contain more turbulent eddies, so the averaging procedure will tend to smooth out some of the fluctuations seen in smaller boxes.

6.4 Conclusions

This chapter has expanded on our hydrodynamic exploration of the nonlinear evolution presented in Chapter 4 into the magnetohydrodynamic regime. We have presented results obtained using the pseudo-spectral code SNOOPY (discussed in Chapter 4) to perform a number of nonlinear simulations of a stably-stratified, differentially-rotating shear flow in the presence of a magnetic field, and in turn, developed a deeper understanding of the nonlinear evolution of the various instabilities in such flows and their abilities at transporting angular momentum.

Following Chapter 4, we investigated four cases: three GSF (hydrodynamically) unstable cases at the latitudes 0°, 30°, and 90°, and one (hydrodynamically) adiabatically unstable case at latitude 30°. Running these simulations has allowed us to quantify the evolution of the various energetic and turbulent stress-related properties, as well as the associated angular momentum transporting properties of the operating instabilities. To identify the visual properties of each of the operating instabilities and to see the effect that imposing a magnetic field in the z-direction has on the dynamics of the flow (particularly any modifications made to the orientation of the zonal jets), we presented all of our time evolution plots in conjunction with snapshots of the flow at carefully chosen points that highlight various key stages in the flow's evolution.

Throughout our simulations, we observed that the lower linear growth rate generated by the addition of a magnetic field in many cases led to an extended linear growth phase of the instability but ultimately did not impede the instability's consequent angular momentum transport properties. In fact, the highest field strengths generally corresponded to the most energetic flows with the highest turbulent transport levels. The magnetic field thus typically acts to enhance turbulent transport in our system for the cases we have explored.

In cases where the instability was driven primarily the magnetic field, instead of the fingers of AM observed in Chapter 4 we instead initially saw the occurrence of MRI modes on larger scales similar to "channel flows", which seemed more resilient to parasitic instabilities and required much higher energies before becoming themselves unstable.

The hydrodynamically adiabatic instability (with $\phi = 60°, \Lambda = -30°$) seemed initially to be more resilient to the effects of the field, largely showing the field to not strongly affect the mean transport properties until a field as large as $B_0 = 10$ is considered. On the other hand, due to the instability preferring the smallest possible $|k|$ (predicted in Chapter 3 and Chapter 5), we saw in Fig. 6.14 that the instabilities tend to increase their size to fill the box regardless of its dimensions. This leads to transport properties that depend strongly upon (L_x, L_y, L_z), making it difficult to extrapolate these hydrodynamically adiabatically unstable cases to an astrophysical context.

A promising result is however that our simulations of the magnetically-modified GSF instability for both $B_0 = 1$ and $B_0 = 2.5$ (one in either of the instability regimes), the stress, energy, and transport properties remained consistent across different box sizes suggesting a box of $L_{x,y,z} = 100$ is adequate to capture a realistic representation of the both instabilities.

All $B_0 \neq 0$ cases we explored exhibit flows that act as dynamos with varying levels of efficiency. The flows in all simulations significantly enhance the level of magnetic energy in the system over the initial imposed field. We have not explored dynamos starting from a very small seed magnetic field, but that would be interesting in future work. We have therefore found that instabilities of differential rotation in stellar radiation zones can act as dynamos.

Chapter 7

Conclusions

In this thesis we have systematically explored the physics of local (magneto-)hydrodynamical instabilities operating in stably-stratified, differentially-rotating regions of stars, with a particular emphasis on applications to the solar tachocline. Such instabilities are thought to be crucial for developing accurate models of solar and stellar dynamos, transport of chemical elements, and the evolution of solar and stellar rotation profiles. This research has built upon prior works, particularly Knobloch and Spruit (1982) and Barker et al. (2019, 2020), to develop a more comprehensive understanding of the local stability and nonlinear dynamics in these regions.

We described the local Cartesian box model introduced by Barker et al. (2019, 2020) in Chapter 2, including our addition of the angle ϕ, which represents the angle between the local 'effective' gravity, $\boldsymbol{e}_g$, and the orientation of the shear. This addition allowed us to study radial ($\phi = 0^\circ$), latitudinal/horizontal ($\phi = \pm 90^\circ$) and mixed radial and latitudinal shears, which in combination with the uniform background rotation, $\hat{\boldsymbol{\Omega}}$, allowed us to study more general differential rotation profiles than studied by Barker et al. (2019, 2020).

We also discussed how the local nature of the GSF instability (which requires length scales small enough for thermal diffusion to become sufficiently efficient) allows us to adopt the Bousinessq approximation in Chapter 2.1. This simplifies the equations such that the density needs only to be taken into account when it is combined with gravitational terms. We also re-derived both the thermal wind equation (2.9), the equation governing the angle between the surfaces of constant density and pressure in the system, as well as the hydrodynamic cubic dispersion relation 2.27 describing the growth of local axisymmetric instabilities, which is equivalent, albeit using slightly different notation, to that presented in Knobloch and Spruit (1982).

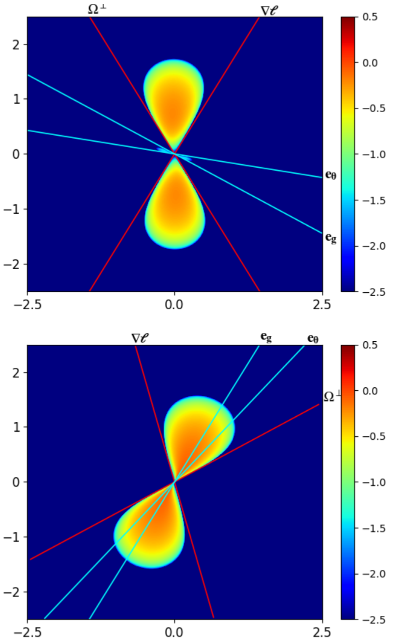

Figure 7.1: A summary of the modal structures of the various instabilities in Fourier space at 30° latitude. The top panel shows both the GSF instabilities (primary lobes) along with additional weakly unstable baroclinic modes (secondary lobes) that operate at $\phi = -30°$ and $\Lambda = 60°$. The bottom panel shows the adiabatic instability that occurs for $\phi = 60°$ and $\Lambda = -30°$. The key result is that unlike for the adiabatic modes the largest growth rates (darkest red) for the GSF instability occur for well-defined (k_x, k_z).

Chapters 3 & 4 present a detailed study into the local hydrodynamic instabilities of differentially-rotating stably-stratified flows in stellar and planetary interiors. The primary focus was on the GSF instability, a double-diffusive axisymmetric instability in differentially-rotating flows that requires thermal diffusion to relax the stabilising effects of buoyancy to operate, but we also analysed the adiabatic instability present when the Solberg-Høiland stability criteria are violated, which can be seen clearly in Fig. 7.1. Chapter 3 revisited the linear stability problem (building upon Knobloch, 1982; Knobloch & Spruit, 1982; Barker et al., 2019, 2020), discussed its properties in detail and derived several new results. An in-depth linear analysis of the most important asymptotic regimes is also presented in Appendix A.2.3. In particular, we derived a criterion Eq. 3.20 for the critical value of

RiPr for onset of (diffusive) axisymmetric instability, where Ri is the local gradient Richardson number and Pr is the Prandtl number. We also solved the cubic linear dispersion relation numerically in the (k_x,k_z) plane for axisymmetric modes and discovered lobes of oscillatory instability previously predicted by Knobloch (1982) but previously never analysed in detail, see Fig. 7.1. These were found to grow more weakly in stellar interiors than the directly growing GSF modes however.

We then solved for the linear growth rates and wavevectors in both the diffusive GSF and adiabatically-unstable regimes (see Fig. 7.2). The GSF instability was found to have broadly similar linear properties for radial, horizontal and mixed radial/horizontal shears, though there are important dependencies on the local orientation of the shear as a function of latitude for both the growth rate and dominant wavevector. On the other hand, we found the adiabatic instability excited when the Solberg-Høiland stability criteria are violated typically has a larger growth rate than the diffusive GSF instability. More importantly though, it has a preferred orientation but no preferred wavevector magnitude in our local model in the absence of diffusion. With diffusion, we find there is a preference for arbitrarily long length-scales.

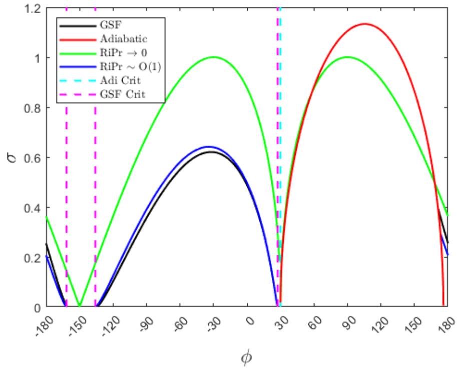

(a) Latitude $\Lambda + \phi = 30°$

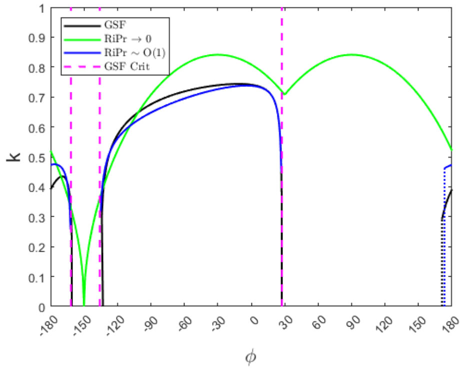

(b) Latitude $\Lambda + \phi = 30°$

Figure 7.2: A figure illustrating the linear growth rate of the fastest growing mode and its corresponding wave vector magnitude across all possible ϕ values for various instabilities and limits at latitude 30°.

In Chapter 4 we used a modified version of the pseudo-spectral code Snoopy, first in-

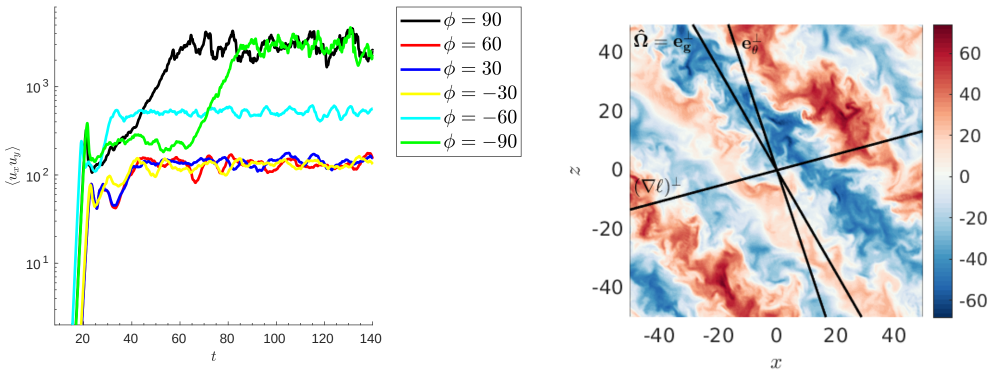

(a)

(b) u_y at $t = 250$

Figure 7.3: A figure summarizing key results from our hydrodynamic nonlinear simulations. The panel on the left shows the strong dependence of angular momentum transport in our system on the angle ϕ, illustrating how more general differential rotation profiles can have enhanced transport properties. These increases typically coincide with the formation and merging of layered structures, as shown in the panel on the right, which displays the final quasi-stable steady state at the end of a simulation with parameters $\phi = 30°$, $\Lambda = -30°$, $S = 2$, $\mathrm{Pr} = 10^{-2}$, and $N^2 = 10$. The merging of layers, particularly evident for the green line at $t \approx 70$, leads to an increase in transport.

troduced by Lesur and Longaretti (2005), to performed a suite of non-linear simulations exploring how more general differential rotation profiles (than purely radial ones) affected the evolution and transport properties of both types of instabilities. Our simulations largely confirmed the linear predictions made in Chapter 3, and identified two distinct regimes (as ϕ is varied) in the nonlinear evolution, corresponding to the GSF-unstable and adiabatically-unstable regimes. GSF-unstable cases typically exhibited the formation of strong zonal jets which often merged over time to form stronger jets with enhanced transport properties, see Fig. 7.3. Such jets had a preferred orientation at first consistent with the fastest-growing linear modes, but later evolved depending on the parameters of the simulation. The mean AM transport and turbulent kinetic energy in the GSF regime also demonstrated convergence as the box size is increased. This is consistent with what might have been predicted based on the linear modes possessing a preferred length-scale. This is a key result meaning our local simulations of the GSF instability could potentially be used to practically study the turbulent transport and its relevance for stellar interiors after suitable extrapolation to astrophysical parameter values.

The adiabatically-unstable cases, on the other hand, resulted in much more efficient AM transport and energetically stronger flows, in some cases leading to sustained AM transfer that is several orders of magnitude larger than the GSF-unstable cases. However, consistent with the linear modes in this regime seeking the largest lengthscales, we found the AM transport continues to increase and does not converge as our box size is increased. This suggests that turbulent transport in stars within the adiabatically-unstable regime cannot be reliably studied using similar local Boussinesq models with linear shear.

In the hydrodynamic regime we also conducted a linear analysis and nonlinear simulations probing the effect of the shear strength S, which suggested that instability is more likely to occur in earlier stages in the life of a star where it rotates more rapidly and potentially has stronger differential rotation. These stages in the life of a star have much more efficient AM transport. However, this instability could potentially operate (e.g. at mid-latitudes) in the solar tachocline, for example (e.g. Barker et al., 2020). We also noted that this instability may operate on the equatorial atmospheric jets of hot Jupiters that advect heat from day-side to night-side (e.g. Goodman, 2009; Li & Goodman, 2010; Barker et al., 2020). It would be difficult or impossible to resolve in existing global simulations (e.g. Showman et al., 2009; Mayne et al., 2017) but could potentially significantly modify their atmospheric flows and should be studied further.

Chapter 5 presented an in-depth theoretical analysis of local triply-diffusive instabilities of differential rotation in magnetised radiation zones of stars and planets, by building upon the hydrodynamical studies of Barker et al. (2019, 2020) and Dymott et al. (2023) and work done in Chapters 3 & 4. Here our focus was regarding the effects of a poloidal magnetic field on the properties of linear axisymmetric instabilities of differential rotation, which are governed by a quintic dispersion relation first derived by Menou et al. (2004) and re-derived here. We have performed a detailed analysis of the dispersion relation, firstly for non-diffusive instabilities, reproducing prior work on the stratified MRI (e.g. Balbus, 1995), before analysing diffusive instabilities in various limits analytically and numerically. Previous adiabatic theories have predicted that in the presence of strong stable stratification, the fastest growing mode displacements are along stratification (i.e. approximately spherical) surfaces. However, we have found that rapid thermal diffusion can eliminate the stabilising effects of buoyancy when Pr/Pm and Pr are sufficiently small, a very appropriate assumption for stellar interiors. In this limit double-diffusive MRI can operate and alters the properties of the unstable modes in a manner dependent on the differential rotation. In addition we obtained new analytical and numerical results on the various instabilities in this triply-diffusive system as a function of the differential rotation profile and magnetic field strength.

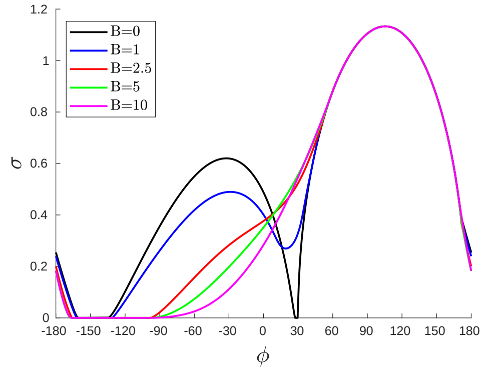

(a) σ at $\Lambda + \phi = 30$

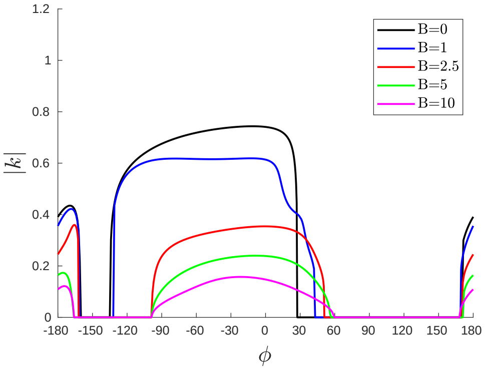

(b) $|k|$ at $\Lambda + \phi = 30$

Figure 7.4: A figure illustrating the linear growth rate of the fastest growing mode and its corresponding wave vector magnitude against ϕ values for various magnetic field strengths at latitude 30°. Whilst the magnetic field generally tended to dampen the growth rate and decrease $|k|$ in all cases hydrodynamically unstable, it destabilizes the special case of cylindrical differential rotation, which is always stable at $S = 2$ in the hydrodynamic regime.

Our analytical and numerical results have highlighted that even a weak magnetic field can considerably modify the local instabilities of differentially rotating flows (e.g. Balbus & Hawley, 1998, and many prior works). We also found that for differential rotation profiles with (angle between effective gravity and local angular velocity gradient) $\phi > 0$, double-diffusive MRI may dominate over

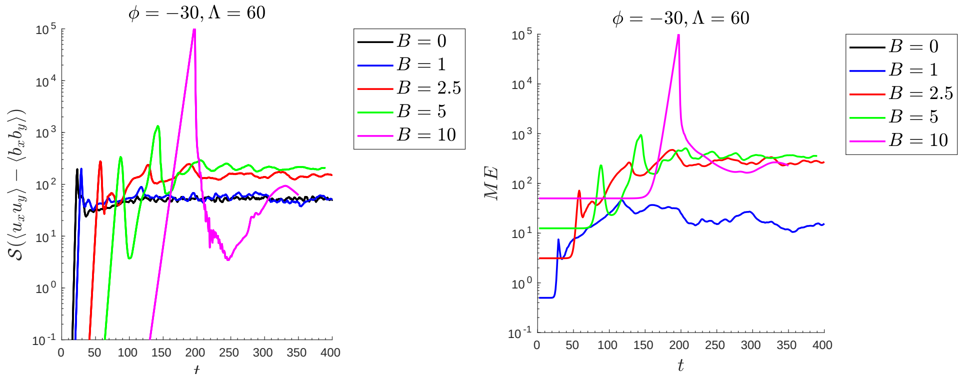

(b) Lat = 0°

Figure 7.5: A figure showing how the nonlinear evolution of the angular momentum transport $\mathcal{S}(\langle u_x u_y \rangle - \langle B_x B_y \rangle)$ and magnetic energy (ME), changes with magnetic field strength ($B_0 = 0, 1, 2.5, 5, 10$), at latitude 30°.

the magnetic modification of hydrodynamic GSF instabilities. However, when $\phi < 0$, hydrodynamic GSF modes could still be important even if their linear growth is weakened by magnetic tension for moderately strong fields. We observed even weak fields to destabilise hydrodynamically stable regions in parameter space, particularly for nearly cylindrical differential rotation profiles, as seen for example in Fig. 7.4.

We have analysed in detail the properties of axisymmetric modes, including how the growth rates and wavevectors depend on the strength of the magnetic field, magnetic Prandtl number Pm, and local differential rotation profile. We have analysed in detail the energetics of the various instabilities in our system, first by deriving the energy equation and then by evaluating the various source terms for linear axisymmetric modes. These consist of Reynolds stresses, Maxwell stresses and baroclinic driving terms. We found that the double-diffusive MRI was driven by Reynolds and Maxwell stresses in approximately equal proportions (so-called Alfvénisation) for a wide range of cases.

Finally, in Chapter 6, we presented simulations of the nonlinear evolution of the stably-stratified, differentially-rotating system in the presence of a purely poloidal field as an initial condition. We focused on the same four Λ and ϕ values presented in Chapter 4 in the hydrodynamical case, three GSF-unstable cases which cover the latitudes 0°, 30°, and 90°, and one hydrodynamically adiabatically-unstable case at latitude 30°.

In general, the reductions in the linear growth rate due to magnetic tension, as discussed in Chapter 5, resulted in an extended linear growth phase for the GSF instability at higher field strengths (see Fig. 7.5). The greatest variations both visually and in the dynamical properties occurred between cases in either magnetically-modified hydrodynamic, or MRI-type regimes. The strength of the field governed which instability operated, for hydrodynamically GSF-unstable cases it was either a magnetically-modified GSF instability or the MRI that operated, whereas for the adiabatic case it was either the modified adiabatic hydrodynamic instability or MRI. Magnetically-modified GSF cases generally exhibited more modest dependence on the field strength, with some increase in the transport properties coming from the increases in the Maxwell stress ($-\langle B_x B_y \rangle$) contribution, but largely this was compensated by a similar decrease in Reynolds stresses ($\langle u_x u_y \rangle$). On the other hand, instabilities significantly modified by the magnetic field lead to far more turbulent and energetic flows, generating both greater levels of transport and more extreme fluctuations once the systems had nonlinearly saturated.

An important feature of our magnetic simulations is that all flows acted as dynamos, in the sense that they significantly enhanced (and subsequently sustained) the level of magnetic energy in the system see for example Fig. 7.5. It would be of interest in future work to study cases with a very weak imposed field to analyse the kinematic stages of the dynamo in more detail.

Our simulations with various box sizes have revealed that the effects of a magnetic field on the wavevector properties, as observed in Chapter 5, extend into the non-linear regime, similarly to our hydrodynamical results in Chapter 4. Specifically, the magnetic field alters the wave vector magnitude $|k|$, influencing the wavelengths of the most unstable modes and the resulting zonal jets. However, cases predicted by Fig. 5.10 to have a well-defined $|k|$ maintain this characteristic for larger field strengths. For $\phi = -30°$ and $\Lambda = 60°$, our results show that as long as the simulation box is large enough to capture the unstable modes, there is no significant dependence of transport properties or averaged quantities on box size.

At both $B_0 = 1$ and $B_0 = 2.5$, the stress, energy, and transport properties remain consistent across different box sizes, suggesting a box of $L_{x,y,z} = 100$ is adequate to capture a realistic representation of both instabilities. This is a promising result.

For our choice of hydrodynamically unstable parameters ($\phi = 60°$ and $\Lambda = -30°$), the presence of a $B_0 = 2.5$ field was not strong enough to hinder the adiabatic instability's preference for larger length scales. The instability filled the box regardless of its size, suggesting that, unlike the hydrodynamically GSF-unstable cases in Fig. 6.13, these simulations cannot be reliably extrapolated to astrophysical contexts.

7.1 Future Work

The study of local magnetohydrodynamic instabilities is a vast topic and their possible applications to astrophysics is no less so. Even without any major deviations from our linear Boussinesq model, such as the inclusion of sound waves or density variation through the anelastic approximation or nonlinear shear profiles (such as $\tanh x$), the possible avenues for further research are seemingly endless.

A good place to start would certainly include a thorough numerical investigation of the linear problem in the context of parameters relevant to the solar tachocline.

A deeper understanding of the quasi-stable zonal jets formed in the nonlinear phases of the GSF instability would be particularly desirable. A numerical linear stability analysis of these jets, with a particular focus on parameter regimes relevant to the tachocline could deepen our knowledge of their transportation and dynamo generation properties.

A more complete suite of nonlinear simulations, particularly in the magnetic case, would also be very illuminating. This could include a broader and a more in-depth analysis into the interaction of general differential rotation profiles with a poloidal magnetic field at a wider range of latitudes. In particular cylindrical rotation profiles have also been overlooked in this thesis, which given the strong effect of even weak magnetic fields in these cases observed in Chapter 5 would be a promising region of parameter space to explore further the stratified MRI. The addition of a magnetic field, in many cases, significantly lowers the critical shear required for onset of instability, so simulations with much lower shears, more applicable to the solar tachocline, would be very interesting to find out if given sufficient time these too formed strong zonal jets with enhanced momentum transporting properties.

More general mixed toroidal/poloidal field configurations would be difficult to study analytically, as the background shear would stretch the magnetic field, making it time-dependent or would require a non-axisymmetric (non-modal) analysis. However, varying the orientation of the magnetic field is straightforward in nonlinear simulations using Snoopy. Since toroidal fields are expected to be most prevalent in the tachocline, their effects on the evolution of the various instabilities discussed here would be particularly interesting to study. It would also be valuable to explore how changes in the field orientation affect the orientation of the zonal jets observed in the later stages of our simulations and how this impacts the levels of angular momentum transport.

A comprehensive nonlinear analysis could be conducted for a range of simulations probing the effects of varying $L_{x,y,z}$ for all of the possible instabilities in the system. It would be particularly interesting to look at the effects of box size on the dynamically unstable MRI, e.g. $\phi = 60°, \Lambda = -30°$ for $B_0 = 10$, as the transport properties here were the highest observed in our simulations presented in Chapter 6.

Whilst direct nonlinear simulations in more realistic parameter regimes (such as Pr or Ri) are currently too computationally expensive, we might imagine that the rapid progress on cutting-edge machine learning techniques may soon offer an opportunity to probe these regimes using our simulation data at more accessible parameters.

Investigating the role of compositional gradients on both the linear (Knobloch & Spruit, 1983) and nonlinear properties of this problem is another promising direction. Chemical gradients are known to significantly influence the stability and evolution of fluid flows in stellar interiors, potentially affecting the mixing and transport properties within these regions. Understanding these effects could provide insights into the chemical evolution and overall dynamics of stars.

Finally, our local simulations are a good approach for understanding the physics of these instabilities, conducting global simulations specifically tailored to studying these instabilities would help bridge the gap between our local models and global stellar dynamics. This approach could lead to a more accurate incorporation of the effects of these instabilities into stellar evolution models, enhancing our understanding of their role in stellar and planetary interiors.

Appendix A

Asymptotic analysis of hydrodynamic model

A.1 Asymptotic limits of interest

Stellar interiors are subject to extreme conditions and correspond to interesting parameter regimes for this problem. For example, Gough (2007) calculates in the tachocline $\nu = 2.7 \times 10^1 \mathrm{cm}^2\mathrm{s}^{-1}$, $\kappa = 1.4 \times 10^7 \mathrm{cm}^2\mathrm{s}^{-1}$ so that $\mathrm{Pr} = 2 \times 10^{-6}$ along with a buoyancy frequency of $\mathcal{N} = 8 \times 10^{-4}\mathrm{s}^{-1}$. The rotation rate is approximately $\Omega = 2.7 \times 10^{-6}\mathrm{s}^{-1}$ corresponding to a mean solar rotation period of 27 days, hence the ratio of $\Omega/\mathcal{N} = 3.4 \times 10^{-3}$.

Asymptotics exploit the largeness or smallness of some parameters to simplify the problem and can also be a method for focusing on particularly dominant properties of the system, such as fast rotation or strong stratification, and to understand what happens in these limits. From a computational perspective, studying simplified systems can enable otherwise intractable simulations to be performed by omitting inessential dynamics (e.g. sound waves in the Boussinesq approximation).

A.2 Instability in the asymptotic limit of small Prandtl number

Given that $\mathrm{Pr} = 2 \times 10^{-6}$ in stellar interiors the first obvious limit to explore is $\mathrm{Pr} \ll 1$.

Expanding our dispersion relation Eq. 2.27, it follows

$$s^3 + s^2(2\nu k^2 + \kappa k^2) + s(a + b + \nu^2 k^4 + 2\nu\kappa k^4) + \nu^2 \kappa k^6 + a\kappa k^2 + b\nu k^2 = 0. \quad \text{(A.1)}$$

Considering the orders of the terms in A.1, when $\mathrm{Pr} \ll 1$ (implying $\nu \ll \kappa$) we have (for $S \sim \Omega$)

$$a \sim O(\Omega^2), \;\; b \sim O(\Omega^2/\mathrm{Pr}), \;\; s \sim O(\Omega), \;\; k^2 \sim O(\Omega/\nu). \quad \text{(A.2)}$$

Since νk^2 is small compared to κk^2 it can thus be neglected, reducing Eq. A.1 to

$$s^3 + s^2 \kappa k^2 + (a + b + 2\nu\kappa k^4)s + \nu^2 \kappa k^6 + a\kappa k^2 + b\nu k^2 = 0. \quad \text{(A.3)}$$

We have $s^3 = O(\Omega^3)$ and $s^2 \kappa k^2 = O(\Omega^3 \kappa/\nu)$, therefore since $\kappa \gg \nu$ this second term is much larger than the first, so we may ignore the s^3 term. Similarly $as = \Omega^3$ but $bs = O(\Omega^3 \kappa/\nu)$, which is much larger, so we may also neglect as by comparison with bs. This means that we can reduce Eq. A.3 to

$$s^2 \kappa k^2 + 2s\nu\kappa k^4 + \nu^2 \kappa k^6 + bs + a\kappa k^2 + b\nu k^2 = 0, \quad \text{(A.4)}$$

where all terms in Eq. A.4 are $O(\Omega^3 \kappa/\nu)$. Note both Ri and R are $O(1/\mathrm{Pr})$ in this scaling, and since Pr is small, Ri and R are large and Ri Pr (and R Pr) are assumed to be $O(1)$. We express

$$a = \frac{2\Omega|\nabla \ell|}{\varpi} \sin(\Lambda - \theta_k) \sin(\gamma - \theta_k), \quad b = \mathcal{N}^2 \sin^2(\theta_k + \phi), \quad \text{(A.5)}$$

by defining the wavevector as $\boldsymbol{k} = k(\cos\theta_k, 0, -\sin\theta_k) = (k_x, 0, k_z)$. In order to maximise s over all possible wavenumbers k_x and k_z, we first maximise over all magnitudes k^2, and then over all possible orientations θ_k. Note a and b only depend on θ_k and not on the magnitude k, so $\partial a/\partial k^2$ and $\partial b/\partial k^2$ are both zero. Differentiating Eq. A.4 with respect to k^2 and setting $\partial s/\partial k^2 = 0$, it follows that

$$\kappa s^2 + 4s\nu\kappa k^2 + 3\nu^2\kappa k^4 + a\kappa + b\nu = 0. \tag{A.6}$$

Multiplying by k^2 and subtracting Eq. A.4 from this equation (to eliminate the s^2 term), gives

$$2s\nu\kappa k^4 + 2\nu^2\kappa k^6 - bs = 0. \tag{A.7}$$

The difference between the non-zero ϕ case investigated here and the case analysed in BJT2 is that our expression for b is more general. If we define

$$\lambda = \frac{\kappa\nu k^4}{b}, \tag{A.8}$$

we obtain

$$s = \frac{2\nu k^2\lambda}{1-2\lambda}. \tag{A.9}$$

To get positive s, i.e. growing modes, we require $0 < \lambda < 1/2$ in Eq. A.9. Now we eliminate s and k^4 from Eq. A.4 and divide by κk^2 to get

$$s^2 + 2s\nu k^2 + \nu^2 k^4 + \frac{bs}{\kappa k^2} + a + b\mathrm{Pr} = 0. \tag{A.10}$$

Eliminating s through the use of Eq. A.9 we get

$$\frac{4\nu^2k^4\lambda^2}{(1-2\lambda)^2} + \frac{4\nu^2k^4\lambda}{(1-2\lambda)} + \nu^2k^4 + \frac{2\nu k^2\lambda b}{(1-2\lambda)\kappa k^2} + a + b\mathrm{Pr} = 0. \tag{A.11}$$

Now we use Eq. A.8 to eliminate k^4 and multiply through by $(1-2\lambda)^2$ to get

$$(1-2\lambda)^2 a = (\lambda - 1)\mathrm{Pr}b. \tag{A.12}$$

We now have the two key equations,A.9 which gives s in terms of λ, and A.12, which relates λ to a and b. Maximising s over θ_k requires us to differentiate A.9 with respect to θ_k and set $\partial s/\partial\theta_k = 0$ to obtain the maximum growth rate. First we eliminate k between A.8 and A.9 to get

$$(1-2\lambda)s = 2\mathrm{Pr}^{1/2}\lambda^{3/2}b^{1/2}. \tag{A.13}$$

Now we differentiate A.13 and A.12 partially with respect to θ_k. Since we require s to be a maximum, we set $\partial s/\partial\theta_k = 0$. These two equations allow us to eliminate $\partial\lambda/\partial\theta_k$, giving an equation between $\partial a/\theta_k$ and $\partial b/\theta_k$. Since we have both a and b in terms of θ_k in A.5, this is the equation that determines the critical value of θ_k that corresponds to $\partial s/\partial\theta_k = 0$, i.e. the maximum growth rate. Differentiating A.13 with respect to θ_k and then multiplying by $2\lambda(1-2\lambda)$ gives

$$(2\lambda-3)b\frac{\partial\lambda}{\partial\theta_k} = \lambda(1-2\lambda)\frac{\partial b}{\partial\theta_k}. \tag{A.14}$$

Differentiating A.12 with respect to θ_k and then multiplying by $(1-2\lambda)(\lambda-1)$ gives

$$\frac{(1-2\lambda)(\lambda-1)}{a}\frac{\partial a}{\partial\theta_k} = (2\lambda-3)\frac{\partial\lambda}{\partial\theta_k} + \frac{(1-2\lambda)(\lambda-1)}{b}\frac{\partial b}{\partial\theta_k}. \tag{A.15}$$

Now A.14 can be used to eliminate $(2\lambda-3)\partial\lambda/\partial\theta_k$ and A.12 can be used to eliminate a/b, to obtain

$$(2\lambda-1)\frac{\partial a}{\partial\theta_k} = \mathrm{Pr}\frac{\partial b}{\partial\theta_k}. \tag{A.16}$$

Differentiating our expressions for a and b in A.5 and substituting them into A.16, we obtain

$$(1-2\lambda)\frac{2\Omega|\nabla\ell|}{\varpi}\sin(\Lambda+\gamma-2\theta_k) = \mathrm{Pr}\mathcal{N}^2\sin 2(\theta_k+\phi), \tag{A.17}$$

or using the definition of R,

$$(1-2\lambda)\sin(\Lambda+\gamma-2\theta_k) = \mathrm{R}\mathrm{Pr}\sin 2(\theta_k+\phi). \tag{A.18}$$

If the parameters RPr, Λ, γ and ϕ are given, A.12 is

$$(1-2\lambda)^2\sin(\Lambda-\theta_k)\sin(\gamma-\theta_k)=(\lambda-1)\mathrm{RPr}\sin^2(\theta_k+\phi). \tag{A.19}$$

A.18 and A.19 form a pair of simultaneous equations for λ and θ_k which can be solved numerically (see Figs. 3.3 and 3.4). Note that once θ_k is found, b can be found from A.5, then A.8 determines k^4 from λ, such that knowing λ determines the magnitude of the critical k for maximum growth rate, and θ_k gives the direction of the vector $\boldsymbol{k}$. Once θ_k is found, a and b can be constructed, and so s, the maximum growth rate, can be found from A.9.

A.2.1 RiPr$= O(1)$ as Pr$\to 0$ ($\lambda \to 0$)

The limit $\lambda \to 1/2$ (in which RiPr$\to 0$ as Pr$\to 0$) is not affected by ϕ because only a, and not b (see 3.21), matters in this limit, and a is independent of ϕ. However in the limit $\lambda \to 0$ (in which RiPr$= O(1)$ as Pr$\to 0$), ϕ does matter, and A.12 becomes

$$a+\mathrm{Pr}b=0, \tag{A.20}$$

and A.18 becomes

$$\sin(\Lambda+\gamma-2\theta_k)=\mathrm{RPr}\sin 2(\theta_k+\phi). \tag{A.21}$$

Putting in the expressions A.5 for a and b into A.20, which are valid in the Pr $\to 0$ limit, it follows that

$$\sin(\Lambda-\theta_k)\sin(\gamma-\theta_k)+\mathrm{RPr}\sin^2(\theta_k+\phi)=0. \tag{A.22}$$

Eliminating RPr between A.21 and A.22 we obtain an equation for the optimum θ_k. To do this, we let

$$\tilde{\theta}_k=\theta_k+\phi, \quad \tilde{\Lambda}=\Lambda+\phi, \quad \tilde{\gamma}=\gamma+\phi. \tag{A.23}$$

Then A.21 and A.22 become

$$\sin(\tilde{\Lambda} + \tilde{\gamma} - 2\tilde{\theta}_k) = \mathrm{RPr}\sin 2\tilde{\theta}_k \tag{A.24}$$

and

$$\sin(\tilde{\Lambda} - \tilde{\theta}_k)\sin(\tilde{\gamma} - \tilde{\theta}_k) + \mathrm{RPr}\sin^2\tilde{\theta}_k = 0. \tag{A.25}$$

We expand the sines in A.25 and divide by $\sin^2\tilde{\theta}_k$, giving

$$\sin\tilde{\Lambda}\sin\tilde{\gamma}\cot^2\tilde{\theta}_k - \sin(\tilde{\Lambda} + \tilde{\gamma})\cot\tilde{\theta}_k + \cos\tilde{\Lambda}\cos\tilde{\gamma} = -\mathrm{RPr}. \tag{A.26}$$

Expanding A.24 using

$$\sin(\tilde{\Lambda} + \tilde{\gamma} - 2\tilde{\theta}_k) = \sin(\tilde{\Lambda} + \tilde{\gamma})\cos 2\tilde{\theta}_k - \cos(\tilde{\Lambda} + \tilde{\gamma})\sin 2\tilde{\theta}_k \tag{A.27}$$

and dividing by $\sin 2\tilde{\theta}_k$ we obtain

$$\sin(\tilde{\Lambda} + \tilde{\gamma})\frac{\cos^2\tilde{\theta}_k - \sin^2\tilde{\theta}_k}{\sin 2\tilde{\theta}_k} - \cos(\tilde{\Lambda} + \tilde{\gamma}) = RPr, \tag{A.28}$$

or noting that $\sin 2\tilde{\theta}_k = 2\sin\tilde{\theta}_k\cos\tilde{\theta}_k$

$$\frac{1}{2}\sin(\tilde{\Lambda} + \tilde{\gamma})\cot\tilde{\theta}_k - \frac{1}{2}\sin(\tilde{\Lambda} + \tilde{\gamma})\tan\tilde{\theta}_k - \cos\tilde{\Lambda}\cos\tilde{\gamma} + \sin\tilde{\Lambda}\sin\tilde{\gamma} = \mathrm{RPr}. \tag{A.29}$$

Adding A.26 and A.29 in order to eliminate R Pr along with some helpful cancellations,

$$\begin{aligned}\sin\tilde{\Lambda}\sin\tilde{\gamma}\cot^2\tilde{\theta}_k - \frac{1}{2}\sin(\tilde{\Lambda} + \tilde{\gamma})\cot\tilde{\theta}_k&\\ - \frac{1}{2}\sin(\tilde{\Lambda} + \tilde{\gamma})\tan\tilde{\theta}_k + \sin\tilde{\Lambda}\sin\tilde{\gamma} &= 0,\end{aligned} \tag{A.30}$$

which can be written as

$$\sin\tilde{\Lambda}\sin\tilde{\gamma}(\cot^2\tilde{\theta}_k + 1) - \frac{1}{2}\sin(\tilde{\Lambda} + \tilde{\gamma})\frac{(\cot^2\tilde{\theta}_k + 1)}{\cot\tilde{\theta}_k} = 0. \tag{A.31}$$

Here a factor $\cot^2\tilde{\theta}_k + 1$, which must be nonzero, cancels out, and expanding $\sin(\tilde{\Lambda} + \tilde{\gamma})$ gives

$$\cot\tilde{\theta}_k = \frac{1}{2}(\cot\tilde{\gamma} + \cot\tilde{\Lambda}), \tag{A.32}$$

which may be rewritten as

$$\cot(\theta_k + \phi) = \frac{1}{2}[\cot(\gamma + \phi) + \cot(\Lambda + \phi)], \tag{A.33}$$

in the original variables. In the $\lambda \to 0$ limit, this simple equation gives θ_k, the angle of $\boldsymbol{k}$ for the fastest growing mode.

A.2.2 Shellular $\phi = 0$ case

This case corresponds to a shelluar differential rotation profile as seen in Barker et al. (2020). If we take Λ as positive, $\nabla\ell$ has z-component $-2\varpi\Omega\sin\Lambda$, so γ must also be positive. Similarly if Λ is negative, γ is also negative. Hence whatever the sign of Λ, in the $\phi = 0$ case there is always just one root θ_k of A.33 and it lies between Λ and γ. The wedge of instability between Λ and γ is the range of angles for θ_k where a is negative. At large $\mathcal{N}^2$, which means large R and Ri, b is large and positive (from $O(\Omega^2/\mathrm{Pr})$ where Pr is small). Inside the wedge, a is negative, but it has smaller magnitude than b, only $O(\Omega^2)$. This means that $a + b$ is positive, which corresponds to being adiabatically stable, but $a + b\mathrm{Pr}$ can be negative, implying GSF/diffusive instability. Diffusion at low Pr reduces the stabilising effects of the b term, allowing the shear instability corresponding to a to overcome it, leading to the GSF instability.

There also exists a smaller wedge in which b is negative for $0 < \theta_k < \Gamma$, since $b = \mathcal{N}^2\sin\theta_k\sin(\Gamma + \theta_k)$. However, for large R and small Pr the thermal wind equation implies Γ is small, only $O(\Omega^2/\mathcal{N}^2)$, so although b is negative it has a very small magnitude, which will normally be wiped out by a in this tiny wedge of b instability. It may be possible for the angles Λ and γ to be very small also, so that both a and b are both very small, and negative b might be bigger than positive a, but this unusual limit has yet not been explored.

A.2.3 The non-shellular $\phi \neq 0$ case

Since ϕ is unrestricted, we have more possibilities than in the shellular case with $\phi = 0$. If $\Lambda + \phi$ and $\gamma + \phi$ both have the same sign, and both lie between 0 and π, then the previous argument for the shellular case still holds, and $\theta_k + \phi$ lies in the wedge between $\Lambda + \phi$ and $\gamma + \phi$, meaning θ_k lies between Λ and γ, i.e. in the unstable wedge of negative a. Example: for $\Lambda = 30°$, $\gamma = 60°$, $\phi = 15°$ the solution of A.33 is $\theta_k = 42.626°$, in the required wedge giving negative a, positive b and positive s, so it's a local maximum of s. This case is very similar to the shellular case, and we complete the analysis of this case below in subsection A.2.3.

However, we could ask, what happens if the vector $\boldsymbol{e}_g$ lies between $\boldsymbol{\Omega}^\perp$ and $\nabla \ell$? If Λ and γ are both positive, this would mean ϕ is negative, and $\Lambda < -\phi < \gamma$. Now $\Lambda + \phi$ is negative and $\gamma + \phi$ is positive. This means that $\cot x$ is no longer continuous as x increases from $\Lambda + \phi$ to $\gamma + \phi$ because it goes to infinity at $x = 0$. Example: $\Lambda = 30°$, $\gamma = 60°$, $\phi = -45°$. Looking at A.33, $\cot(\theta_k + \phi) = 0.5(\cot 15° - \cot 15°) = 0$, so $\theta_k + \phi = 90°$, so $\theta_k = 135°$ which is not in the unstable wedge. We have a solution for A.33 here, but it has both a and b positive, so from A.25 RPr is negative. This is not what we want physically in the radiation zone, because we want the stratification to be stable, with $R > 0$ as it is in the tachocline. If $\boldsymbol{e}_g$ lies between $\boldsymbol{\Omega}^\perp$ and $\nabla \ell$, then there is a value of $\theta_k = -\phi$ which lies in the unstable wedge and has b zero. If b is zero, our original scaling breaks down, because b is no longer $O(\Omega^2/\mathrm{Pr})$. For these modes, with $\boldsymbol{k}$ lined up with gravity, and a negative, the fastest growing modes will be small k^2 adiabatic modes with $\sigma = \sqrt{-a}$, i.e. on the fast rotational timescale.

$\phi \neq 0$ case when $\boldsymbol{e}_g$ lies outside the wedge between $\boldsymbol{\Omega}^\perp$ and $\nabla \ell$

This is the case where A.33 gives a physically satisfactory maximum growth rate with $\boldsymbol{k}$ in the unstable wedge. Expanding the expression for A.5a using sine and cosine rules for sums, and using A.32, the condition for s to be a local maximum, we may obtain, after some simplifications,

$$a = -\frac{\Omega|\nabla\ell|}{2\varpi}\sin^2\tilde{\theta}_k\frac{\sin^2(\tilde{\gamma}-\tilde{\Lambda})}{\sin\tilde{\Lambda}\sin\tilde{\gamma}}. \tag{A.34}$$

Now we have an expression for R/Ri in order to express b in terms of Ri rather than R. To do this we use the definition of $\nabla\ell$, to deduce

$$\frac{2\Omega\varpi}{|\nabla\ell|} = \frac{\sin\gamma}{\sin\Lambda}, \quad \frac{\varpi\mathcal{S}}{|\nabla\ell|} = \frac{\cos\Lambda\sin\gamma}{\sin\Lambda} - \cos\gamma. \tag{A.35}$$

Now $\mathrm{R} = \mathcal{N}^2\varpi/2\Omega|\nabla\ell|$ and $\mathrm{Ri} = \mathcal{N}^2/\mathcal{S}^2$ by definition, hence $\mathrm{R}/\mathrm{Ri} = \mathcal{S}^2\varpi/2\Omega|\nabla\ell|$. So the square of A.35b divided by A.35a gives

$$\frac{\mathrm{R}}{\mathrm{Ri}} = \left(\frac{\cos\Lambda\sin\gamma}{\sin\Lambda} - \cos\gamma\right)^2\frac{\sin\Lambda}{\sin\gamma} = \frac{\sin^2(\gamma-\Lambda)}{\sin\gamma\sin\Lambda}. \tag{A.36}$$

Now from A.5b

$$b = \mathcal{N}^2\sin^2\tilde{\theta}_k = \mathrm{R}\frac{2\Omega|\nabla\ell|}{\varpi}\sin^2\tilde{\theta}_k = \mathrm{Ri}\frac{2\Omega|\nabla\ell|}{\varpi}\sin^2\tilde{\theta}_k\frac{\sin^2(\gamma-\Lambda)}{\sin\gamma\sin\Lambda}. \tag{A.37}$$

Now in the $\lambda \to 0$ limit, A.20 tells us that $a = -\mathrm{Pr}b$. Putting together our expressions for a and b,

$$\begin{aligned} \mathrm{Pr}b &= \mathrm{RiPr}\frac{2\Omega|\nabla\ell|}{\varpi}\sin^2\tilde{\theta}_k\frac{\sin^2(\gamma-\Lambda)}{\sin\gamma\sin\Lambda} \\ &= -a = \frac{\Omega|\nabla\ell|}{2\varpi}\sin^2\tilde{\theta}_k\frac{\sin^2(\tilde{\gamma}-\tilde{\Lambda})}{\sin\tilde{\Lambda}\sin\tilde{\gamma}}. \end{aligned} \tag{A.38}$$

Looking at these expressions, $\sin^2(\gamma-\Lambda) = \sin^2(\tilde{\gamma}-\tilde{\Lambda})$, so these terms cancel. We thus end up with

$$\mathrm{RiPr} = \frac{\sin\gamma\sin\Lambda}{4\sin(\gamma+\phi)\sin(\Lambda+\phi)}, \tag{A.39}$$

which is different from the shellular $\phi = 0$ case where the limit $\lambda \to 0$ corresponded to the simpler $\mathrm{RiPr} = 1/4$.

If Λ and γ are both positive (they must have the same sign) and ϕ is positive, then the limit is $\mathrm{RiPr} < 1/4$. This is stabilising, because it means that Ri has to be smaller for instability, and since $\mathrm{Ri} = \mathcal{N}^2/\mathcal{S}^2$ this means the shear $\mathcal{S}$ has to be larger for instability. Example: $\Lambda = 30°$, $\gamma = 60°$, $\phi = 30°$ gives the limit as $\mathrm{RiPr} = 1/8$, so the range of instability is reduced from $0 < \mathrm{RiPr} < 0.25$ down to $0 < \mathrm{RiPr} < 0.125$ confirming positive ϕ is stabilising if γ and Λ are positive.

However, if ϕ is negative when γ and Λ are positive, ϕ is destabilising. Example: $\Lambda = 30°$, $\gamma = 60°$, $\phi = -15°$, then the upper limit of RiPr is increased to 0.5915 so a smaller shear $\mathcal{S}$ will still be unstable.

If ϕ is negative and $|\phi|$ approaches the smaller of Λ or γ then $\sin(\Lambda+\phi)$ or $\sin(\gamma+\phi)$ will become small so that A.39 will diverge to infinity. This is correct, because as ϕ approaches the wedge of instability, we expect the system to become adiabatically unstable, i.e. unstable whatever Ri is. If $\boldsymbol{e}_g$ is inside the wedge, fluid motion perpendicular to gravity cannot be stabilised by the stratification, and since it is inside the wedge it is driven by the shear, so it is very unstable.

The non-shellular case close to $\lambda = 0$

Now suppose that λ is small but not quite zero (i.e. the limit $\mathrm{RiPr} = O(1)$ as $\mathrm{Pr} \to 0$), so that squares and higher powers of λ can be neglected. Then A.12 gives

$$\lambda = \frac{a + \mathrm{Pr}b}{3a}. \tag{A.40}$$

Now $a + \mathrm{Pr}b$ is small and negative, but not quite zero. If we put in the expressions A.34 for a and A.38 for b, A.40 becomes

$$\lambda = \frac{1}{3}\left(1 - 4\mathrm{RiPr}\frac{\sin\tilde{\gamma}\sin\tilde{\Lambda}}{\sin\gamma\sin\Lambda}\right) = \frac{\kappa\nu k^4}{b}, \tag{A.41}$$

so

$$k^4 = \frac{\mathcal{N}^2\sin^2\tilde{\theta}_k}{3}\left(1 - 4\mathrm{RiPr}\frac{\sin\tilde{\gamma}\sin\tilde{\Lambda}}{\sin\gamma\sin\Lambda}\right). \tag{A.42}$$

This means that if RiPr is just a little less than the limiting value given by A.39 there is an unstable solution with a long wavelength, because k is small from A.42, and the growth rate is also small from A.9, giving

$$s = \frac{2\sqrt{\mathrm{Pr}}\mathcal{N}\sin\tilde{\theta}_k}{\sqrt{3}}\left(1 - 4\mathrm{RiPr}\frac{\sin\tilde{\gamma}\sin\tilde{\Lambda}}{\sin\gamma\sin\Lambda}\right)^{1/2}. \tag{A.43}$$

This result has been confirmed numerically, and describes the slow growth which occurs when the strength of the differential rotation is only just above the minimum value required for instability.

Appendix B

Nonlinear simulation results

S	ϕ	Λ	$\langle u_x u_y \rangle$	$\langle u_x u_z \rangle$	$\langle u_y u_z \rangle$	$\sqrt{\langle u_x^2 \rangle}$	$\sqrt{\langle u_y^2 \rangle}$	$\sqrt{\langle u_z^2 \rangle}$
			Latitude = 0°					
2	−90°	90°	2883.0 ± 490.5	-13.4 ± 69.9	92.9 ± 147.4	34.1 ± 260.7	32.2 ± 89.3	27.2 ± 260.7
2	−60°	60°	510.0 ± 41.5	73.1 ± 9.3	195.4 ± 20.8	15.1 ± 0.6	31.6 ± 1.3	13.0 ± 0.6
2	−30°	30°	135.8 ± 16.8	37.7 ± 5.7	112.0 ± 14.0	7.8 ± 0.4	15.2 ± 0.9	7.7 ± 0.4
2	0°	0°	NA	NA	NA	NA	NA	NA
2	30°	−30°	138.8 ± 20.6	-38.9 ± 7.0	-115.6 ± 17.2	7.9 ± 0.5	15.4 ± 1.1	8.0 ± 0.5
2	60°	−60°	134.8 ± 16.5	-36.9 ± 5.6	-111.8 ± 14.0	7.8 ± 0.4	15.1 ± 0.8	8.0 ± 0.4
2	90°	−90°	2838.2 ± 578.9	14.9 ± 76.8	-128.3 ± 130.6	34.6 ± 4.0	88.3 ± 7.0	28.1 ± 3.8
			Latitude = 30°					
2	−90°	120°	25.7 ± 8.3	-1.6 ± 1.1	-20.7 ± 8.0	2.9 ± 0.6	13.8 ± 2.3	3.2 ± 0.7
2	−60°	90°	25.9 ± 7.1	-2.7 ± 0.5	-7.5 ± 2.1	3.3 ± 0.3	8.1 ± 2.7	3.5 ± 0.3
2	−30°	60°	24.1 ± 1.6	-1.8 ± 0.2	0.7 ± 0.6	3.2 ± 0.1	7.9 ± 0.3	3.3 ± 0.1
2	0°	30°	11.3 ± 1.5	-1.1 ± 0.4	5.2 ± 1.2	2.4 ± 0.2	8.1 ± 1.5	2.6 ± 0.2
2	30°	0°	0	0	0	NA	NA	NA
2	60°	−30°	958.5 ± 509.5	-334.2 ± 216.2	-516.6 ± 311.6	28.4 ± 6.3	29.9 ± 6.6	23.8 ± 5.1
2	90°	−60°	9219.3 ± 4186.1	-633.0 ± 529.9	-499.5 ± 483.9	83.8 ± 15.4	86.7 ± 16.7	53.1 ± 11.2
			Latitude = 90°					
2	−90°	180°	0	0	0	NA	NA	NA
2	−60°	150°	3.5 ± 0.8	-0.9 ± 0.2	-9.5 ± 2.1	0.5 ± 0.1	4.6 ± 0.3	1.2 ± 0.1
2	−30°	120°	17.5 ± 2.1	-5.4 ± 0.3	-22.9 ± 2.2	2.2 ± 0.2	7.1 ± 0.5	3.2 ± 0.2
2	0°	90°	37.0 ± 2.0	-20.7 ± 1.0	-25.6 ± 1.7	4.5 ± 0.1	6.6 ± 0.1	5.1 ± 0.1
2	30°	60°	162.8 ± 22.5	-113.4 ± 11.6	-77.3 ± 12.2	10.6 ± 0.5	11.1 ± 0.7	8.0 ± 0.5
2	60°	30°	138.4 ± 19.8	-110.8 ± 25.1	-31.5 ± 10.9	15.7 ± 1.3	8.2 ± 0.5	8.4 ± 0.6
2	90°	0°	0	0	0	NA	NA	NA
			Variations in shear (GSF instability at $S = 2$ in Fig. 4.7 panels (a) and (b))					
1	−30°	60°	15.5 ± 1.3	1.0 ± 0.1	2.9 ± 0.3	2.2 ± 0.1	5.7 ± 0.5	1.2 ± 0.1
1.5	−30°	60°	17.8 ± 1.5	-0.7 ± 0.2	1.0 ± 0.3	2.6 ± 0.1	4.7 ± 0.2	2.1 ± 0.1
2	−30°	60°	24.1 ± 1.4	-1.8 ± 0.2	0.8 ± 0.6	3.2 ± 0.1	7.8 ± 0.3	3.3 ± 0.1
2.5	−30°	60°	29.5 ± 2.1	-3.7 ± 0.4	-0.1 ± 1.0	4.0 ± 0.1	11.0 ± 1.2	4.2 ± 0.1
			Variations in shear (adiabatic instability at $S = 2$ in Fig. 4.7 panels (c) and (d))					
1	90°	−60°	161.0 ± 69.6	-64.2 ± 71.3	-18.6 ± 24.8	24.5 ± 7.6	11.1 ± 3.3	12.6 ± 6.1
1.5	90°	−30°	646.7 ± 306.2	-790.2 ± 531.5	-365.7 ± 313.6	76.2 ± 14.9	65.9 ± 12.7	42.9 ± 10.0
2	90°	−60°	916.8 ± 459.9	-639.1 ± 563.4	-493.2 ± 481.9	83.5 ± 17.1	86.3 ± 18.4	52.9 ± 12.5
2.5	90°	30°	1082.4 ± 758.1	-567.9 ± 768.2	-580.3 ± 842.6	88.0 ± 24.9	99.8 ± 29.9	61.0 ± 19.6

Table B.1: Table of hydrodynamic simulation parameters and nonlinear outcomes. All simulations have $\mathrm{Pr} = 10^{-2}$, $N^2 = 10$ and $L_{x,y,z} = 100$. Time-averages are based on the entire simulation after the initial linear growth phase. Simulation parameters not listed in this table are given in § 4. Our simulation units are determined by setting $\Omega = d = 1$.

References

Acheson, D. J., & Gibbons, M. P. (1978). On the instability of toroidal magnetic fields and differential rotation in stars. *Philosophical Transactions of the Royal Society of London Series A*, *289*(1363), 459–500. https://doi.org/10.1098/rsta.1978.0066

Aerts, C., Mathis, S., & Rogers, T. M. (2019). Angular momentum transport in stellar interiors. *Annual Review of Astronomy & Astrophysics*, *57*, 35–78.

Alfvén, H. (1942). Existence of electromagnetic-hydrodynamic waves. *Nature*, *150*(3805), 405–406.

Astoul, A., & Barker, A. J. (2023). Tidally excited inertial waves in stars and planets: Exploring the frequency-dependent and averaged dissipation with nonlinear simulations. *The Astrophysical Journal Letters*, *955*(1), L23.

Astoul, A., Park, J., Mathis, S., Baruteau, C., & Gallet, F. (2021). The complex interplay between tidal inertial waves and zonal flows in differentially rotating stellar and planetary convective regions-i. free waves. *Astronomy & Astrophysics*, *647*, A144.

Balbus, S. A. (1995). General local stability criteria for stratified, weakly magnetized rotating systems. *The Astrophysical Journal*, *453*, 380.

Balbus, S. A. (2009). A simple model for solar isorotational contours. *Monthly Notices of the Royal Astronomical Society*, *395*(4), 2056–2064.

Balbus, S. A., Bonart, J., Latter, H. N., & Weiss, N. O. (2009). Differential rotation and convection in the sun. *Monthly Notices of the Royal Astronomical Society*, *400*(1), 176–182.

Balbus, S. A., & Hawley, J. F. (1991). A powerful local shear instability in weakly magnetized disks. I. Linear Analysis. *The Astrophysical Journal*, *376*, 214.

Balbus, S. A., & Hawley, J. F. (1994). The stability of differentially rotating, weakly magnetized stellar radiative zones. *Monthly Notices of the Royal Astronomical Society*, *266*(4), 769–774.

Balbus, S. A., & Hawley, J. F. (1998). Instability, turbulence, and enhanced transport in accretion disks. *Reviews of Modern Physics*, *70*(1), 1–53.

Van Ballegooijen, A. A., & Martens, P. (1989). Formation and eruption of solar prominences. *The Astrophysical Journal, 343*, 971–984.

Barker, A. J., & Latter, H. N. (2015). On the vertical-shear instability in astrophysical discs. *Monthly Notices of the Royal Astronomical Society*, *450*(1), 21–37.

Barker, A. J., Jones, C. A., & Tobias, S. M. (2019). Angular momentum transport by the gsf instability: Non-linear simulations at the equator. *Monthly Notices of the Royal Astronomical Society*, *487*(2), 1777–1794.

Barker, A. J., Jones, C. A., & Tobias, S. M. (2020). Angular momentum transport, layering, and zonal jet formation by the gsf instability: Non-linear simulations at a general latitude. *Monthly Notices of the Royal Astronomical Society*, *495*(1), 1468–1490.

Barker, A. J., & Ogilvie, G. I. (2010). On internal wave breaking and tidal dissipation near the centre of a solar-type star. *Monthly Notices of the Royal Astronomical Society*, *404*(4), 1849–1868.

Barker, A. J., & Ogilvie, G. I. (2011). Stability analysis of a tidally excited internal gravity wave near the centre of a solar-type star. *Monthly Notices of the Royal Astronomical Society*, *417*(1), 745–761.

BBC. (2022). Sunspots [Accessed: 2024-02-04]. https://www.skyatnightmagazine.com/advice/skills/how-observe-track-sunspots/

Brüggen, M., & Hillebrandt, W. (2001). Mixing through shear instabilities. *Monthly Notices of the Royal Astronomical Society*, *320*(1), 73–82.

Brummell, N. H., Clune, T. L., & Toomre, J. (2002). Penetration and overshooting in turbulent compressible convection. *The Astrophysical Journal*, *570*(2), 825.

Bühler, O. (2014). *Waves and mean flows*. Cambridge University Press.

Buldgen, G. (2019a). Global helioseismology. *arXiv preprint:1912.02003*.

Buldgen, G. (2019b). Current problems in stellar evolution. *arXiv preprint:1902.10399*.

Busse, F. H. (1981). Do Eddington–Sweet circulations exist? *Geophysical & Astrophysical Fluid Dynamics*, *17*(1), 215–235.

Caleo, A., & Balbus, S. A. (2016). The radiative zone of the Sun and the tachocline: stability of baroclinic patterns of differential rotation. *Monthly Notices of the Royal Astronomical Society*, *457*(2), 1711–1721.

Caleo, A., Balbus, S. A., & Tognelli, E. (2016). The Goldreich-Schubert-Fricke instability in stellar radiative zones. *Monthly Notices of the Royal Astronomical Society*, *460*(1), 338–344.

Cantiello, M., Mankovich, C., Bildsten, L., Christensen-Dalsgaard, J., & Paxton, B. (2014). Angular momentum transport within evolved low-mass stars. *The Astrophysical Journal*, *788*(1), 93.

Carrington, R. C. (1863). *Observations of the spots on the Sun: from November 9, 1853, to March 24, 1861, made at Redhill.* Williams and Norgate.

Chandrasekhar, S. (1961). *Hydrodynamic and hydromagnetic stability.* Courier Corporation.

Chang, E., & Garaud, P. (2021). Modelling coexisting GSF and shear instabilities in rotating stars. *Monthly Notices of the Royal Astronomical Society*, *506*(4), 4914–4932.

Charbonneau, P. (2020). Dynamo models of the solar cycle. *Living Reviews in Solar Physics*, *17*, 1–104.

Charbonneau, P., Christensen-Dalsgaard, J., Henning, R., Larsen, R., Schou, J., Thompson, M., & Tomczyk, S. (1999). Helioseismic constraints on the structure of the solar tachocline. *The Astrophysical Journal*, *527*(1), 445.

Chiosi, C., & Maeder, A. (1986). The evolution of massive stars with mass loss. *Annual Review of Astronomy & Astrophysics*, *24*(1), 329–375.

Christensen-Dalsgaard, J., & Thompson, M. J. (2007). *Observational results and issues concerning the tachocline* (Vol. 53). Cambridge University Press Cambridge.

Cope, L., Garaud, P., & Caulfield, C. P. (2020). The dynamics of stratified horizontal shear flows at low Péclet number. *Journal of Fluid Mechanics*, *903*.

Corbard, T., Blanc-Féraud, L., Berthomieu, G., & Provost, J. (1999). Non linear regularization for helioseismic inversions. application for the study of the solar tachocline. *arXiv preprint astro-ph/9901112*.

Decressin, T., Mathis, S., Palacios, A., Siess, L., Talon, S., Charbonnel, C., & Zahn, J.-P. (2009). Diagnoses to unravel secular hydrodynamical processes in rotating main sequence stars. *Astronomy & Astrophysics*, *495*(1), 271–286.

Deheuvels, S., Li, G., Ballot, J., & Lignières, F. (2023). Strong magnetic fields detected in the cores of 11 red giant stars using gravity-mode period spacings. *Astronomy & Astrophysics*, *670*.

Deubner, F.-L. (1975). Observations of low wavenumber nonradial eigenmodes of the sun. *Astronomy & Astrophysics, 44*, 371–375.

Dicke, R. H., & Goldenberg, H. M. (1974). The oblateness of the sun. *Astrophysical Journal Supplement, 27*, 131.

Dikpati, M., & Gilman, P. A. (2008). Global solar dynamo models: Simulations and predictions. *Journal of Astrophysics and Astronomy*, *29*, 29–39.

Donati, J.-F., & Landstreet, J. (2009). Magnetic fields of nondegenerate stars. *Annual Review of Astronomy & Astrophysics*, *47*, 333–370.

Dymott, R. W., Barker, A. J., Jones, C. A., & Tobias, S. M. (2023). Linear and non-linear properties of the Goldreich-Schubert-Fricke instability in stellar interiors with arbitrary local radial and latitudinal differential rotation. *Monthly Notices of the Royal Astronomical Society*, *524*(2), 2857–2882.

Dzanic, T., & Witherden, F. D. (2022). Positivity-preserving entropy-based adaptive filtering for discontinuous spectral element methods. *Journal of Computational Physics*, *468*, 111501.

Eddy, J. A., Stephenson, F. R., & Yau, K. K. (1989). On pre-telescopic sunspot records. *Royal Astronomical Society, Quarterly Journal, 30*, 65–73.

Eff-Darwich, A., & Hernández, F. P. (1997). A new strategy for helioseismic inversions. *Astronomy & Astrophysics Supplement Series*, *125*(2), 391–398.

Eggenberger, P., Meynet, G., Maeder, A., Hirschi, R., Charbonnel, C., Talon, S., & Ekström, S. (2008). The geneva stellar evolution code. *Astrophysics and Space Science*, *316*, 43–54.

Engvold, O., Vial, J.-C., & Skumanich, A. (2018). *The sun as a guide to stellar physics*. Elsevier.

Essick, R., Vitale, S., & Weinberg, N. N. (2016). Impact of the tidal p- g instability on the gravitational wave signal from coalescing binary neutron stars. *Physical Review D*, *94*(10), 103012.

Ferraro, V. C. A. (1937). The non-uniform rotation of the Sun and its magnetic field. *Monthly Notices of the Royal Astronomical Society*, *97*, 458.

Fielding, S. (2020). Centrifugally unstable flows [Accessed: 2023-12-12]. http://suzannefielding.webspace.durham.ac.uk

Frazier, E. N. (1968). A spatio-temporal analysis of velocity fields in the solar photosphere. *Zeitschrift für Astrophysik, 68*, 345.

Fricke, K. (1968). Instabilität stationärer Rotation in Sternen. *Zeitschrift für Astrophysik*, *68*, 317.

Gagnier, D., & Garaud, P. (2018). Turbulent transport by diffusive stratified shear flows: from local to global models. II. Limitations of local models. *The Astrophysical Journal*, *862*(1), Article 36.

Garaud, P. (2020a). Horizontal Shear Instabilities at Low Prandtl Number. *The Astrophysical Journal*, *901*(2).

Garaud, P. (2013). Double-diffusive convection. *EAS Publications Series*, *63*, 285–295.

Garaud, P. (2018). Double-diffusive convection at low prandtl number. *Annual Review of Fluid Mechanics*, *50*, 275–298.

Garaud, P. (2020b). Horizontal shear instabilities at low prandtl number. *The Astrophysical Journal*, *901*(2), 146.

Garaud, P. (2021). Double-diffusive processes in stellar astrophysics. *arXiv preprint arXiv:2103.08072*.

Garaud, P., Gagnier, D., & Verhoeven, J. (2017). Turbulent transport by diffusive stratified shear flows: from local to global models. I. Numerical simulations of a stratified plane Couette flow. *The Astrophysical Journal*, *837*(2).

Gaurat, M., Jouve, L., Lignières, F., & Gastine, T. (2015). Evolution of a magnetic field in a differentially rotating radiative zone. *Astronomy & Astrophysics*, *580*, Article A103.

Gilman, P. A. (2018). Magnetic buoyancy and rotational instabilities in the tachocline. *The Astrophysical Journal*, *853*(1), 65.

Gilman, P. A., & Dikpati, M. (2014). Baroclinic instability in the solar tachocline. *The Astrophysical Journal*, *787*(1), 60.

Goldreich, P., & Schubert, G. (1967). Differential rotation in stars. *Astrophysical Journal, 150*, 571.

Goldstein, J., Townsend, R., & Zweibel, E. (2019). The Tayler instability in the anelastic approximation. *The Astrophysical Journal*, *881*(1), 66.

Goodman, J. (2009). Thermodynamics of Atmospheric Circulation on Hot Jupiters. *The Astrophysical Journal*, *693*(2), 1645–1649.

Goodman, J., & Dickson, E. S. (1998). Dynamical tide in solar-type binaries. *The Astrophysical Journal*, *507*(2), 938.

Gough, D. (2007). *An introduction to the solar tachocline* (D. W. Hughes, R. Rosner, & N. O. Weiss, Eds.). Cambridge University Press Cambridge.

Gough, D., & McIntyre, M. E. (1998). Inevitability of a magnetic field in the sun's radiative interior. *Nature*, *394*(6695), 755–757.

Guilet, J., & Müller, E. (2015). Numerical simulations of the magnetorotational instability in protoneutron stars - I. Influence of buoyancy. *Monthly Notices of the Royal Astronomical Society*, *450*(2), 2153–2171.

Hanasoge, S. M. (2014). Full waveform inversion of solar interior flows. *The Astrophysical Journal*, *797*(1), 23.

Harvey, K. (1992). The solar cycle (astronomical society of the pacific conference series 12).

Hathaway, D. H. (2015). The solar cycle. *Living reviews in solar physics*, *12*(1), 4.

Hawley, J. F., & Balbus, S. A. (1992). A powerful local shear instability in weakly magnetized disks. iii-long-term evolution in a shearing sheet. *The Astrophysical Journal*, *400*, 595–609.

Hawley, J. F., Gammie, C. F., & Balbus, S. A. (1995). Local three-dimensional magnetohydrodynamic simulations of accretion disks. *The Astrophysical Journal*, *440*, 742.

Hawley, J. F., Gammie, C. F., & Balbus, S. A. (1996). Local three-dimensional simulations of an accretion disk hydromagnetic dynamo. *The Astrophysical Journal*, *464*, 690.

Høiland, E. (1941). On the stability of the circular vortex. *Klasse*, *11*, 1–24.

Hollebon, J., & Fazi, F. M. (2020). Efficient hrtf representation using compact mode hrtfs. *Audio Engineering Society Convention 149*.

Hollerbach, R., Teeluck, V., & Rüdiger, G. (2010). Nonaxisymmetric magnetorotational instabilities in cylindrical taylor-couette flow. *Physical Review Letters*, *104*(4), 044502.

Howard, L. N. (1961). Note on a paper of John W. Miles. *Journal of Fluid Mechanics*, *10*(4), 509–512.

Hughes, D. W. (1988). Magnetic fields in the solar convection zone: Magnetoconvection and magnetic buoyancy. *Annual Review of Fluid Mechanics*, *20*(1), 187–223.

Hughes, D. W., Rosner, R., & Weiss, N. (2007). *The solar tachocline*. Cambridge University Press.

Hung, D., Blackman, E., Caspary, K., Gilson, E., & Ji, H. (2019). Experimental confirmation of the standard magnetorotational instability mechanism with a spring-mass analogue. *Communications Physics*, *2*, 7.

Jones, C. A., Thompson, M. J., & Tobias, S. M. (2010). The solar dynamo. *Space Science Reviews*, *152*, 591–616.

Jouve, L., Gastine, T., & Lignières, F. (2015). Three-dimensional evolution of magnetic fields in a differentially rotating stellar radiative zone. *Astronomy & Astrophysics*, *575*.

Jouve, L., Lignières, F., & Gaurat, M. (2020). Interplay between magnetic fields and differential rotation in a stably stratified stellar radiative zone. *Astronomy & Astrophysics*, *641*.

Kippenhahn, R., Weigert, A., & Weiss, A. (1990). *Stellar structure and evolution*. Springer.

Kitchatinov, L. (2014). Baroclinic instability in stellar radiation zones. *The Astrophysical Journal*, *784*(1), 81.

Knobloch, E. (1982). Nonlinear diffusive instabilities in differentially rotating stars. *Geophysical & Astrophysical Fluid Dynamics*, *22*(1-2), 133–158.

Knobloch, E., & Spruit, H. C. (1982). Stability of differential rotation in stars. *Astronomy & Astrophysics*, *113*, 261–268.

Knobloch, E., & Spruit, H. C. (1983). The molecular weight barrier and angular momentum transport in radiative stellar interiors. *Astronomy & Astrophysics*, *125*(1), 59–68.

Kosovichev, A. (2003). *What helioseismology teaches us about the sun* (Vol. 535). ISCS Symposium.

Kulenthirarajah, L., & Garaud, P. (2018). Turbulent transport by diffusive stratified shear flows: from local to global models. III. A closure model. *The Astrophysical Journal*, *864*(2).

Kumar, P., Talon, S., & Zahn, J.-P. (1999). Angular momentum redistribution by waves in the sun. *The Astrophysical Journal*, *520*(2), 859.

Kunze, E. (2003). A review of oceanic salt-fingering theory. *Progress in Oceanography*, *56*(3-4), 399–417.

Labarbe, J., & Kirillov, O. N. (2021). Diffusive instabilities of baroclinic lenticular vortices. *Physics of Fluids*, *33*(10), Article 104108.

Latter, H. N., & Papaloizou, J. (2018). Vortices and the saturation of the vertical shear instability in protoplanetary discs. *Monthly Notices of the Royal Astronomical Society*, *474*(3), 3110–3124.

Le Bars, M. (2021). Numerical study of the McIntyre instability around Gaussian floating vortices in thermal wind balance. *Physical Review Fluids*, *6*(9), Article 093801.

Leibacher, J., & Stein, R. (2018). A new description of the solar five-minute oscillation. In *Solar neutrinos* (pp. 400–401). CRC Press.

Leighton, R. B., Noyes, R. W., & Simon, G. W. (2018). Velocity fields in the solar atmosphere: I. preliminary report. In *Solar neutrinos* (pp. 381–389). CRC Press.

Lesur, G., & Longaretti, P.-Y. (2005). On the relevance of subcritical hydrodynamic turbulence to accretion disk transport. *Astronomy & Astrophysics*, *444*(1), 25–44.

Li, J., & Goodman, J. (2010). Circulation and Dissipation on Hot Jupiters. *The Astrophysical Journal*, *725*(1), 1146–1158.

Maeder, A. (1995). On the Richardson criterion for shear instabilities in rotating stars. *Astronomy & Astrophysics, v. 299, p. 84*, *299*, 84.

Maeder, A. (2008). *Physics, Formation and Evolution of Rotating Stars*. Springer Science & Business Media.

Maeder, A., & Meynet, G. (2000). The evolution of rotating stars. *Annual Review of Astronomy & Astrophysics*, *38*(1), 143–190.

Mamatsashvili, G., Stefani, F., Hollerbach, R., & Rüdiger, G. (2019). Two types of axisymmetric helical magnetorotational instability in rotating flows with positive shear. *Physical Review Fluids*, *4*(10), 103905.

Marques, J., Goupil, M., Lebreton, Y., Talon, S., Palacios, A., Belkacem, K., Ouazzani, R.-M., Mosser, B., Moya, A., Morel, P., et al. (2013). Seismic diagnostics for transport of angular momentum in stars-i. rotational splittings from the pre-main sequence to the red-giant branch. *Astronomy & Astrophysics*, *549*, A74.

Mathis, S., Palacios, A., & Zahn, J.-P. (2004). On shear-induced turbulence in rotating stars. *Astronomy & Astrophysics*, *425*(1), 243–247.

Mayne, N. J., Debras, F., Baraffe, I., Thuburn, J., Amundsen, D. S., Acreman, D. M., Smith, C., Browning, M. K., Manners, J., & Wood, N. (2017). Results from a set of three-dimensional numerical experiments of a hot Jupiter atmosphere. *Astronomy & Astrophysics*, *604*.

McIntyre, M. (1970). Diffusive destabilisation of the baroclinic circular vortex. *Geophysical & Astrophysical Fluid Dynamics*, *1*(1), 19–57.

McKee, C. F., & Ostriker, E. C. (2007). Theory of star formation. *Annual Review of Astronomy & Astrophysics*, *45*, 565–687.

Meduri, D. G., Lignières, F., & Jouve, L. (2019). Nonaxisymmetric magnetorotational instability in spherical Couette flow. *Physical Review E*, *100*(1).

Menou, K., Balbus, S. A., & Spruit, H. C. (2004). Local axisymmetric diffusive stability of weakly magnetized, differentially rotating, stratified fluids. *The Astrophysical Journal*, *607*(1), 564.

Menou, K., & Le Mer, J. (2006). Magnetorotational Transport in the Early Sun. *The Astrophysical Journal*, *650*(2), 1208–1216.

Mestel, L. (1968). Magnetic braking by a stellar wind. *Monthly Notices of the Royal Astronomical Society*, *138*(3), 359–391.

Mestel, L., & Weiss, N. O. (1987). Magnetic fields and non-uniform rotation in stellar radiatives zones. *Monthly Notices of the Royal Astronomical Society*, *226*, 123–135.

Mestel, L., & Weiss, N. (1987). Magnetic fields and non-uniform rotation in stellar radiative zones. *Monthly Notices of the Royal Astronomical Society*, *226*(1), 123–135.

Meynet, G., Ekstrom, S., Maeder, A., Eggenberger, P., Saio, H., Chomienne, V., & Haemmerlé, L. (2013). Models of rotating massive stars: Impacts of various prescriptions. In *Studying stellar rotation and convection* (pp. 3–22). Springer.

Meynet, G., & Maeder, A. (2000). Stellar evolution with rotation v: Changes in all the outputs of massive star models. *arXiv astro-ph/0006404*.

Miesch, M. S. (2005). Large-scale dynamics of the convection zone and tachocline. *Living Reviews in Solar Physics*, *2*(1), 1.

Miesch, M. S., Brown, B. P., Browning, M. K., Brun, A. S., & Toomre, J. (2010). Magnetic cycles and meridional circulation in global models of solar convection. *Proceedings of the International Astronomical Union*, *6*(S271), 261–269.

Miesch, M. S., Gilman, P. A., & Dikpati, M. (2007). Nonlinear evolution of global magnetoshear instabilities in a three-dimensional thin-shell model of the solar tachocline. *The Astrophysical Journal Supplement Series*, *168*(2), 337.

Miles, J. W. (1961). On the stability of heterogeneous shear flows. *Journal of Fluid Mechanics*, *10*(4), 496–508.

Mordasini, C., Mollière, P., Dittkrist, K.-M., Jin, S., & Alibert, Y. (2015). Global models of planet formation and evolution. *International Journal of Astrobiology*, *14*(2), 201–232.

Moyano, F., Eggenberger, P., Salmon, S., Mombarg, J., & Ekström, S. (2023). Angular momentum transport by magnetic fields in main-sequence stars with gamma doradus pulsators. *Astronomy & Astrophysics*, *677*, A6.

Nelson, R. P., Gressel, O., & Umurhan, O. M. (2013). Linear and non-linear evolution of the vertical shear instability in accretion discs. *Monthly Notices of the Royal Astronomical Society*, *435*(3), 2610–2632.

Noyes, R. W., & Leighton, R. B. (1963). Velocity fields in the solar atmosphere. ii. the oscillatory field. *Astrophysical Journal, 138*, 631.

Observatory, N. S. D. (2017). Sun erupts with significant flare [Accessed: 2024-04-12]. https://www.nasa.gov/solar-system/sun-erupts-with-significant-flare

Ogilvie, G. I., & Pringle, J. E. (1996). The non-axisymmetric instability of a cylindrical shear flow containing an azimuthal magnetic field. *Monthly Notices of the Royal Astronomical Society*, *279*(1), 152–164.

Ogilvie, G. I. (2007). Instabilities, angular momentum transport and magnetohydrodynamic turbulence. In D. W. Hughes, R. Rosner, & N. O. Weiss (Eds.), *The solar tachocline* (p. 299).

Oishi, J. S., Vasil, G. M., Baxter, M., Swan, A., Burns, K. J., Lecoanet, D., & Brown, B. P. (2020). The magnetorotational instability prefers three dimensions. *Proceedings of the Royal Society of London Series A*, *476*(2233), 20190622.

Parfrey, K. P., & Menou, K. (2007). The Origin of Solar Activity in the Tachocline. *The Astrophysical Journal Letters*, *667*(2), L207–L210.

Park, J., Prat, V., & Mathis, S. (2020). Horizontal shear instabilities in rotating stellar radiation zones. I. Inflectional and inertial instabilities and the effects of thermal diffusion. *Astronomy & Astrophysics*, *635*.

Park, J., Prat, V., Mathis, S., & Bugnet, L. (2021). Horizontal shear instabilities in rotating stellar radiation zones. II. Effects of the full Coriolis acceleration. *Astronomy & Astrophysics*, *646*, 635–648.

Park, J., Prat, V., & Mathis, S. (2019). Horizontal shear instabilities in stellar radiative zones. *Bulletin of the American Physical Society*, *64*, 635–648.

Pols, O. R. (2011). *Stellar structure and evolution.* Astronomical Institute Utrecht NY.

Prat, V., & Lignières, F. (2013). Turbulent transport in radiative zones of stars. *Astronomy & Astrophysics*, *551*.

Prialnik, D. (2000). *An introduction to the theory of stellar structure and evolution.* Cambridge University Press.

Radko, T. (2013). *Double-diffusive convection.* Cambridge University Press.

Rashid, F. Q., Jones, C. A., & Tobias, S. M. (2008). Hydrodynamic instabilities in the solar tachocline. *Astronomy & Astrophysics*, *488*(3), 819–827.

Rayleigh, L. (1880). On the stability, or instability, of certain fluid motions. *Proc. London Math. Soc.*, *9*, 57–70.

Rayleigh, L. (1917). On the dynamics of revolving fluids. *Proceedings of the Royal Society of London*, *93*(648), 148–154.

Rhodes Jr., E. J., Ulrich, R. K., & Simon, G. W. (1977). Observations of nonradial p-mode oscillations on the sun. *The Astrophysical Journal, 218*, 901–919.

Rieutord, M., & Valdettaro, L. (1997). Inertial waves in a rotating spherical shell. *Journal of Fluid Mechanics*, *341*, 77–99.

Rieutord, M., & Espinosa Lara, F. (2009). On the dynamics of a radiative rapidly rotating star. *" Communications in Asteroseismology, Proceedings of "38th Liege International Astrophysical Colloquium: Evolution and Pulsation of Massive Stars on the Main Sequence and Close to it", held on July 7-11 2008, edited by Arlette Noels, Conny Aerts, Josefina Montalban, Andrea Miglio and Maryline Briquet."*, *158*, 99.

Rogallo, R. S. (1981). Numerical experiments in homogeneous turbulence.

Rogers, T. M., & Glatzmaier, G. A. (2006). Angular momentum transport by gravity waves in the solar interior. *The Astrophysical Journal*, *653*(1), 756.

Rüdiger, G. (1989). *Differential rotation and stellar convection: Sun and solar-type stars.* Taylor & Francis.

Schatzman, E. (1993). Transport of angular momentum and diffusion by the action of internal waves. *Astronomy & Astrophysics*, *279*, 431–446.

Schmitt, R. W. (1995). The ocean's salt fingers. *Scientific American*, *272*(5), 70–75.

Schwarzschild, M. (2015). *Structure and evolution of stars*. Princeton University Press.

Sharma, P., Hammett, G. W., Quataert, E., & Stone, J. M. (2006). Shearing box simulations of the MRI in a collisionless plasma. *The Astrophysical Journal*, *637*(2), 952.

Showman, A. P., Fortney, J. J., Lian, Y., Marley, M. S., Freedman, R. S., Knutson, H. A., & Charbonneau, D. (2009). Atmospheric Circulation of Hot Jupiters: Coupled Radiative-Dynamical General Circulation Model Simulations of HD 189733b and HD 209458b. *The Astrophysical Journal*, *699*(1), 564–584.

Solanki, S. K. (2003). Sunspots: An overview. *The Astronomy & Astrophysics Review*, *11*, 153–286.

Solberg, H. (1936). Über die freien Schwingungen einer homogenen Flüssigkeitsschicht auf der rotierenden Erde. I. Mit 4 Textfiguren. *Astrophysica Norvegica*, *1*, 237.

Spiegel, E. A., & Veronis, G. (1960). On the Boussinesq approximation for a compressible fluid. *The Astrophysical Journal*, *131*, 442.

Spiegel, E. A., & Zahn, J.-P. (1970). Instabilities of differential rotation. *Comments on Astrophysics and Space Physics, Vol. 2, p. 178*, *2*, 178.

Spruit, H. C. (1999). Differential rotation and magnetic fields in stellar interiors. *Astronomy & Astrophysics*, *349*, 189–202.

Spruit, H. C. (2002). Dynamo action by differential rotation in a stably stratified stellar interior. *Astronomy & Astrophysics*, *381*(3), 923–932.

Spruit, H. C., & Knobloch, E. (1984). Baroclinic instability in stars. *Astronomy & Astrophysics, 132*, 89–96.

Staquet, C., & Sommeria, J. (2002). Internal gravity waves: From instabilities to turbulence. *Annual Review of Fluid Mechanics*, *34*(1), 559–593.

Strugarek, A., Brun, A., & Zahn, J.-P. (2011). Magnetic confinement of the solar tachocline: II. Coupling to a convection zone. *Astronomy & Astrophysics*, *532*, A34.

Sule, A., Rüdiger, G., & Arlt, R. (2005). A numerical MHD model for the solar tachocline with meridional flow. *Astronomy & Astrophysics*, *437*(3), 1061–1067.

Svestka, Z. (2012). *Solar flares* (Vol. 8). Springer Science & Business Media.

Sweet, P. (1969). Mechanisms of solar flares. *Annual Review of Astronomy & Astrophysics*, *7*(1), 149–176.

Tayler, R. J. (1994). *The stars: Their structure and evolution*. Cambridge University Press.

Taylor, G. I. (1923). Stability of a viscous liquid contained between two rotating cylinders. *Philosophical Transactions of the Royal Society of London*, *223*(605-615), 289–343.

Thompson, M. J. (2004). Helioseismology and the sun's interior. *Astronomy & Geophysics*, *45*(4), 4–21.

Tobias, S. (2002). The solar dynamo. *Philosophical Transactions of the Royal Society of London. Series A: Mathematical, Physical and Engineering Sciences*, *360*(1801), 2741–2756.

Tobias, S. (2005). The solar tachocline: Formation, stability and its role in the solar dynamo. *Fluid dynamics and dynamos in astrophysics and geophysics*, *1*, 193.

Tripathi, B., Barker, A. J., Fraser, A. E., Terry, P. W., & Zweibel, E. G. (2024). Predicting the Slowing of Stellar Differential Rotation by Instability-Driven Turbulence. *arXiv e-prints*.

Ulrich, R. K., & Rhodes Jr., E. J. (1977). The sensitivity of nonradial p mode eigenfrequencies to solar envelope structure. *Astrophysical Journal, 218*, 521–529.

Umurhan, O. M., & Regev, O. (2004). Hydrodynamic stability of rotationally supported flows: Linear and nonlinear 2D shearing box results. *Astronomy & Astrophysics*, *427*, 855–872.

Urpin, V., & Brandenburg, A. (1998). Magnetic and vertical shear instabilities in accretion discs. *Monthly Notices of the Royal Astronomical Society*, *294*(3), 399–406.

Vasil, G. M., Lecoanet, D., Augustson, K., Burns, K. J., Oishi, J. S., Brown, B. P., Brummell, N., & Julien, K. (2024). The solar dynamo begins near the surface. *arXiv e-prints*, Article arXiv:2404.07740.

Velikhov, E. (1959). Stability of an ideally conducting liquid flowing between cylinders rotating in a magnetic field. *Soviet Physics JETP*, *36*(9), 995–998.

De Vries, N. B., Barker, A. J., & Hollerbach, R. (2023). The interactions of the elliptical instability and convection. *Physics of Fluids*, *35*(2), 024116.

Watson, M. (1980). Shear instability of differential rotation in stars. *Geophysical & Astrophysical Fluid Dynamics*, *16*(1), 285–298.

Weinberg, N. N., Arras, P., Quataert, E., & Burkart, J. (2012). Nonlinear tides in close binary systems. *The Astrophysical Journal*, *751*(2), 136.

Weiss, N. O. (2007). *Sunspot structure and dynamics* (Vol. 22). Springer New York.

Weiss, N. (2010). Solar and stellar dynamos. *Proceedings of the International Astronomical Union*, *6*(S271), 247–260.

Wilson, P. R. (1994). *Solar and stellar activity cycles.* Cambridge University Press.

Wittmann, A. D., & Xu, Z. (1987). A catalogue of sunspot observations from 165 BC to AD 1684. *Astronomy & Astrophysics Supplement Series*, *70*, 83–94.

Wolff, C. L. (1983). The rotational spectrum of g-modes in the sun. *The Astrophysical Journal, Part 1, 264*, 667–676.

Yau, K., & Stephenson, F. (1988). A revised catalogue of far eastern observations of sunspots (165 bc to ad 1918). *Royal Astronomical Society, Quarterly Journal, 29*, 175–197.

Zahn, J.-P. (1974). Rotational instabilities and stellar evolution. *Symposium-International Astronomical Union*, *59*, 185–195.

Zahn, J.-P. (1992). Circulation and turbulence in rotating stars. *Astronomy & Astrophysics*, *265*, 115–132.

Zhang, K., Earnshaw, P., Liao, X., & Busse, F. H. (2001). On inertial waves in a rotating fluid sphere. *Journal of Fluid Mechanics*, *437*, 103–119.